



## Biogas fueled solid oxide fuel cells - from cell to system level

**Langnickel, Hendrik**

*Publication date:*  
2020

*Document Version*  
Publisher's PDF, also known as Version of record

[Link back to DTU Orbit](#)

### Citation (APA):

Langnickel, H. (2020). *Biogas fueled solid oxide fuel cells - from cell to system level*. Technical University of Denmark.

---

### General rights

Copyright and moral rights for the publications made accessible in the public portal are retained by the authors and/or other copyright owners and it is a condition of accessing publications that users recognise and abide by the legal requirements associated with these rights.

- Users may download and print one copy of any publication from the public portal for the purpose of private study or research.
- You may not further distribute the material or use it for any profit-making activity or commercial gain
- You may freely distribute the URL identifying the publication in the public portal

If you believe that this document breaches copyright please contact us providing details, and we will remove access to the work immediately and investigate your claim.



PhD thesis

# Biogas fueled solid oxide fuel cells - from cell to system level

## Author

**Hendrik Langnickel**

Electrochemistry

Department of Energy Conversion and Storage

Technical University of Denmark

E-mail: henlan@dtu.dk (hendrik.langnickel@alum.uol.de)

## Supervisors

**Anke Hagen, Prof. Dr. Dr.**

Professor, Electrochemistry

Department of Energy Conversion and Storage

Technical University of Denmark

E-Mail: anke@dtu.dk

**Christopher Graves, PhD**

Associate Professor, Solid State Chemistry

Department of Energy Conversion and Storage

Technical University of Denmark

E-Mail: cgra@dtu.dk

**Rasmus Olsen, M.Sc.**

Operations manager

Odense Renovation A/S

E-mail: rao@odenserenovation.dk

**Release date:** 27. March 2020



---

In really challenging times (COVID-19), I tried to do my best to complete my manuscript.

This manuscript is part of the requirements to achieve the degree of Doctor of Philosophy (PhD) at the Department of Energy Conversion and Storage, Technical University of Denmark.

**Release date:** 27. March 2020

**Technical University of Denmark**

Department of Energy Conversion and Storage  
Technical University of Denmark  
Fysikvej  
2800 Kgs. Lyngby  
Denmark  
[www.energy.dtu.dk](http://www.energy.dtu.dk)



---

*Don't keep forever on the public road, going only where others have gone. Leave the beaten track occasionally and dive into the woods. You will be certain to find something you have never seen before. Of course it will be a little thing, but do not ignore it. Follow it up, explore around it; one discovery will lead to another, and before you know it you will have something worth thinking about to occupy your mind. All really big discoveries are the result of thought.*

*Alexander Graham Bell (1847-1922)*



# **Abstract**

The use of biogas fueled solid oxide fuel cells (SOFC's) could be a promising option in order to reduce greenhouse gas emissions and to get one step further in the direction of a circular economy. The main components of biogas are CH<sub>4</sub> and CO<sub>2</sub>. Furthermore, other impurities are present in the biogas. A SOFC can convert hydrocarbon fuels like biogas directly into heat and electricity without producing NOx or small particles like in combustion engines. Additionally, different kinds of biogas compositions are feasible for a SOFC. In this thesis, different aspects of biogas fueled SOFC's are investigated from both a theoretical and experimental point of view. SOFC operation modes and poisoning effects are analyzed considering real biogas. Biogas is used from the biggest dump site of Denmark and from a wastewater plant located in Italy. Additionally, anode-off gas operation parameters for avoiding carbon formation during biogas SOFC operation are investigated. Finally, an efficiency study of biogas fueled industrial sized SOFC systems is conducted. In general, the results of this thesis show that operation of biogas fueled SOFC's is possible and high efficiencies can be achieved. Moreover, different approaches and strategies are successfully investigated in order to achieve a stable operation during real biogas fueled SOFC's operation. Thereby, the system complexity could also be reduced.



# Acknowledgements

This thesis would have not been possible without the good guidance and strong support of the following persons:

My main supervisor Anke Hagen. Many thanks for giving me the opportunity of doing my PhD in the field of solid oxide fuel cells. Thanks a lot for the good scientific support, guidance and also for the freedom to investigate my own ideas which were not considered at the beginning of the project. My second supervisor Christopher Graves. Many thanks for the good scientific discussions concerning impedance fittings and SOFC simulation. My third supervisor Rasmus Olsen and Ulrik Løenker from Odense Renovation A/S. Thanks a lot for providing the landfill gas and making everything possible in Odense. My wife Birte and my 1.5 years old son Jesper. Thank you very much Birte for your strong support and trust during the last three years. 'Danke' Jesper for remembering me that we can learn everyday new things if we want. Many thanks to the DTU Energy technician team but especially to Henrik Henriksen and Ole Hansen for the amazing support during rebuilding and setting up the test equipment. My three master students Hannah Loeper, Nils Hinzen and Daniele Reschiotto. It was a pleasure supervising you. 'Quitos' to team 'Fuel Cells and Hydrogen' at VTT in Finland. Especially many thanks to Olli Himanen, Markus Rautanen and Ville Saarinen for hosting me and supporting me during my external stay. 'Mange tak' Eva Ravn Nielsen for the warm and pleasant talk during the 'Hannover Messe 2013' and for inviting me to do my bachelor research project at DTU Energy. Without this first project I (probably) would have not done my PhD at DTU Energy. Thank you very much Doris Hoffmeyer, Lisa Langnickel and Tobias Kühnel for proofreading. Many thanks to my colleagues and previous colleagues Alexandra Ploner, Anita Voss, Daniel Bøgh Drasbæk, Florian Gellrich, Heidi Adler Bergen, Lars Nilausen Cleemann, Megha Raw, Søren Højgard Jensen and Xifu Sun for the good (scientific) discussions and help during the last three years.

**Side comment:** For remembering the sentence of my impedance course teacher about reliability of impedance fits and for increasing the chance that Jesper finds the following pages more interesting two elephants are hiding in the thesis.



# Contents

<b>1</b>	<b>Introduction</b>	<b>1</b>
<b>2</b>	<b>Fundamentals</b>	<b>3</b>
2.1	Solid oxide fuel cells (SOFC's) . . . . .	3
2.1.1	Working principle . . . . .	3
2.1.2	Fuel cell materials and properties . . . . .	4
2.2	Biogas . . . . .	5
2.2.1	Biogas composition and formation . . . . .	6
2.2.2	Energy production from biogas and the use of fuel cells . . . . .	7
2.2.3	Landfill gas from the landfill site Odense, Denmark . . . . .	8
2.3	Considerations for biogas fueled SOFC . . . . .	10
2.3.1	Internal reforming of biogas . . . . .	10
2.3.2	Carbon deposition . . . . .	12
2.3.3	Poisoning effects and handling of impurities . . . . .	14
2.4	SOFC characterization parameters and techniques . . . . .	18
2.4.1	iV-curve characteristics . . . . .	19
2.4.2	Electrochemical impedance spectroscopy . . . . .	21
2.4.3	Degradation rates . . . . .	23
2.4.4	Efficiencies and fuel utilization . . . . .	24
<b>3</b>	<b>Test facilities</b>	<b>25</b>
3.1	Single cell tests . . . . .	25
3.1.1	Main components of the rig . . . . .	25
3.1.2	Cell house setup . . . . .	26
3.1.3	Real landfill gas as fuel . . . . .	28
3.1.4	Anode off-gas recirculation . . . . .	29
3.1.5	Tested cells and standardized characterization . . . . .	30
3.1.6	Electrochemical impedance measurements and analysis . . . . .	32
3.2	Biogas fueled SOFC system site . . . . .	33

<b>4 Method development for predicting H<sub>2</sub>S effect on cell performance</b>	<b>35</b>
4.1 iV-curve sulfur poisoning . . . . .	35
4.2 Verification of the H <sub>2</sub> S iV-curve approach . . . . .	41
4.3 H <sub>2</sub> S voltage drop forecasting of cells with the same material composition . . . . .	43
4.4 Conclusion . . . . .	49
<b>5 In-situ analysis of pre-mixed landfill gas operation</b>	<b>50</b>
5.1 Anode and cathode process identification . . . . .	50
5.2 Flow rate and current density variation . . . . .	52
5.3 Landfill gas CH <sub>4</sub> content dependency . . . . .	56
5.4 Conclusion . . . . .	60
<b>6 Landfill gas fueled SOFC operation modes</b>	<b>61</b>
6.1 Cleaned landfill gas galvanostatic and potentiostatic operation . . . . .	62
6.2 Non cleaned landfill gas operation . . . . .	65
6.2.1 Galvanostatic operation . . . . .	68
6.2.2 Potentiostatic operation . . . . .	69
6.2.3 Potentiostatic operation with extra steam supply . . . . .	70
6.2.4 Impedance spectra analysis . . . . .	72
6.2.5 Anode in-plane voltage comparison . . . . .	76
6.2.6 Area specific resistance increase comparison (filter off) . . . . .	78
6.3 Cleaning method comparison after non cleaned landfill gas operation . . . . .	79
6.4 Conclusion . . . . .	80
<b>7 Durability of SOFCs with anode off-gas recirculation</b>	<b>82</b>
7.1 Carbon activity algorithm and semi 1D cell model . . . . .	82
7.2 Determination of possible operation parameters . . . . .	89
7.3 Experimental durability study . . . . .	92
7.4 Conclusion . . . . .	98
<b>8 Biogas SOFC system efficiency</b>	<b>99</b>
8.1 SOFC system data analysis scheme . . . . .	99
8.2 Electrical net power relation . . . . .	100
8.3 Biogas CH <sub>4</sub> content correlation . . . . .	104
8.4 Conclusion . . . . .	106
<b>9 Conclusion</b>	<b>107</b>

<b>10 Outlook</b>	<b>110</b>
<b>References</b>	<b>XVIII</b>
<b>List of Figures</b>	<b>XXXIII</b>
<b>List of Tables</b>	<b>XXXVIII</b>
<b>Appendix A Calculation of carbon activity and OCV considering CH<sub>4</sub> conversion in a SOFC</b>	<b>XLII</b>
A.1 Gibbs minimization method . . . . .	XLII
A.2 Determining carbon activity . . . . .	XLIV
A.3 OCV determination via Nernst equation . . . . .	XLIV
<b>Appendix B Supporting impedance figures for the CH<sub>4</sub> content pre-mixed landfill gas study (section 5.3)</b>	<b>XLVII</b>
<b>Appendix C Proceedings and articles</b>	<b>LIII</b>
C.1 Galvanostatic and potentiostatic operation of real landfill gas fueled SOFCs	LIII
C.2 New Methodology of Studying H <sub>2</sub> S Poisoning Effects on SOFC's Fueled by Carbon Containing Fuels like Biogas . . . . .	LXIV
C.3 Efficiency analysis of 50 kW <sub>e</sub> SOFC systems fueled with biogas from waste water . . . . .	LXXVI
	XIII

# 1 Introduction

For reducing emissions of greenhouse gases and moving forward in the direction of a circular economy, a responsible and efficient use of the available biomass is essential. This is even more important by bearing in mind that food production has first priority. Using anaerobic digestion, biomass can be converted into biogas, which consists out of CH<sub>4</sub>, CO<sub>2</sub> plus traces of other gases and compounds. Besides industrial biogas production, biogas is also a side product during wastewater treatment and landfilling. Environmental pollution of dump sites or wastewater treatment plans can be decreased by an efficient use of the biogas, which evolves as a side product.

A common approach for converting biogas into electricity and heat is the operation of micro turbines or combustion engines. These technologies have, however, the disadvantage of low electric efficiencies and that biogas with a low heating value can not be utilized. The low heating value corresponds to a low CH<sub>4</sub> content in the biogas, which is the case for biogas from dump sites also named landfill gas. Another disadvantage during the conversion process is the local environmental pollution by the production of nitrogen oxides and small particles. An alternative could be the use of solid oxide fuel cells (SOFC's) for the conversion of biogas into electricity and heat in a highly efficient way. A SOFC is an electrochemical device which converts the energy in hydrocarbon fuels like biogas directly into electricity and the side product heat. In relation to other fuel cell types SOFC's have the advantage that the material properties along with the operation temperatures between 650 °C and 850 °C enable the direct usage of carbon containing fuels such as biogas. On the other hand, the use of biogas as fuel for SOFC's poses challenges on the cell level but also on the system level. One of the challenges is the handling of impurities and another one the avoiding of carbon formation.

The aim of the thesis is to analyze the operation of real biogas fueled SOFC's and identify dependencies between operation conditions and SOFC performance. Simulation and experimental studies are done on both single cell and system level. Real landfill gas

from the biggest dump site of Denmark located close to Odense is used for the tests on cell level. On system level real biogas from a wastewater plant was used. In chapter two of the thesis the fundamentals for biogas fueled SOFC's are summarized. In the third chapter the test facilities are introduced. In chapter four a method is developed and evaluated for determining the poisoning effects of the impurity  $H_2S$  during biogas fueled SOFC operation. In the fifth chapter the anode processes during operating the SOFC with pre-mixed landfill gas are analyzed in detail using electrochemical impedance spectroscopy, including catalytic and electrochemical reactions. The relations between the SOFC anode processes and the total fuel flow rate, applied current density and  $CH_4$  content in the biogas are tested. In the sixth chapter an experimental study at cell level is presented which analyses the differences between the galvanostatic and potentiostatic operation mode using real landfill gas as fuel. The study includes a degradation analysis, the effect of gas cleaning and means of regeneration of the cell performance. Afterwards, in chapter seven, a model is presented which was designed in order to predict safe operation conditions of landfill gas fueled SOFC's and using anode off-gas recirculation for preventing carbon formation. The results of the theoretical study are validated and further investigated in an experimental study at cell level. Finally, in the eighth chapter the results of an efficiency study of industrial sized SOFC systems fueled with biogas from wastewater treatment are shown. The study focuses system efficiencies as function of the operation parameters electrical net power output and  $CH_4$  content in the biogas. The studies presented in the thesis involve thermodynamic considerations, efficiency calculations, voltage, current characterizations as well as electrochemical impedance measurements.

## 2 Fundamentals

In this chapter an introduction about the basics is given which are the foundation for the studies presented in the thesis. Therefore an overview about the solid oxide fuel cell (SOFC) and biogas is given.

### 2.1 Solid oxide fuel cells (SOFC's)

In this section the working principle of a solid oxide fuel cell (SOFC) is explained and the SOFC materials and properties are summarized.

#### 2.1.1 Working principle

Fuel cells are electrochemical cells which convert chemical energy into electricity and the side product heat with high efficiency. A fuel cell consists of two electrodes which are separated by an electrolyte [1, 2]. The fuel electrode is called the anode and the oxygen electrode the cathode. A electric load connects the two electrodes. The solid oxide fuel cell (SOFC) has a ceramic electrolyte and operates at a temperature range between 650 °C and 850 °C. A sketch of the working principle of a SOFC is shown in Figure 2.1. Porous electrode structures allow H<sub>2</sub>/CO to enter at the anode and O<sub>2</sub>/air at the cathode. The half-cell reactions which are taking place at the active areas, also called the triple phase boundary (TPB) of the electrodes, are given in Equations 2.1-2.2 (anode) and 2.3 (cathode). Oxygen ions are passing through the electrolyte from the cathode to the anode. Electricity is generated by the motion of electrons from the anode to the cathode via the electric load. Furthermore, due to the presence of the nickel catalyst in state-of-the-art anodes, internal reforming of hydrocarbon fuels like biogas is possible, which is further discussed in Section 2.3. The material properties of the two electrodes and electrolyte are briefly summarized in the following section.

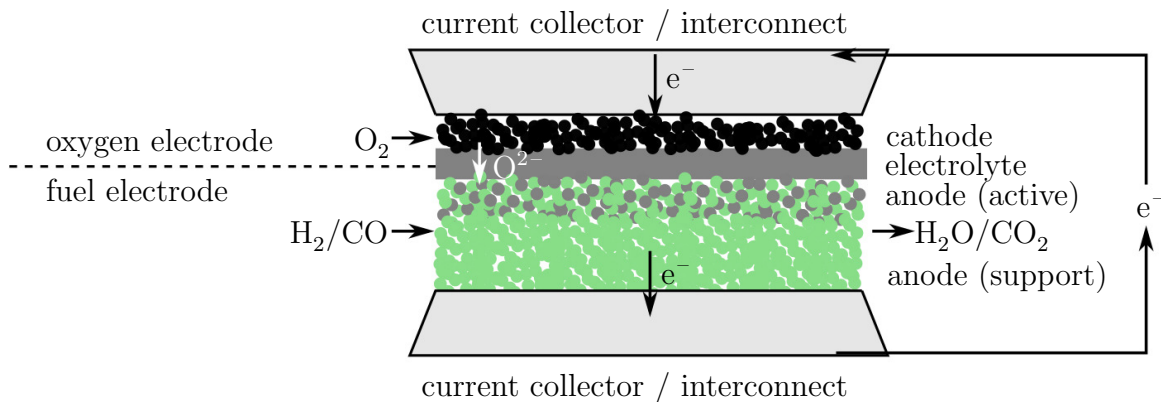


**Figure 2.1:** Working principle of a solid oxide fuel cell (SOFC).

### 2.1.2 Fuel cell materials and properties

Specific material properties are needed for the different fuel cell parts. All parts need to have chemical, phase, morphological and dimensional stability. To achieve a long SOFC lifetime, high toughness and mechanical strength properties are needed. Furthermore, to avoid cracking during operation, similar thermal expansion coefficients of the different materials are required [3].

#### Electrolyte

Yttria stabilized zirconia (YSZ) is currently the most common material for the electrolyte. Vacancies of oxygen in the YSZ crystal structure ensure the conductivity of oxygen ions without electronic conduction. Additionally, YSZ is stable in the reducing (anode) and oxidizing environment (cathode) [1]. Further details about other possible ceramic SOFC electrolytes, such as samarium doped cerium oxide (SDC) and gadolinium doped cerium oxide (GDC), can be found in literature [4].

### Anode

To ensure a good gas supply to and from the TPB (active anode site), a high porosity of the anode is needed. Furthermore, a high electron and oxygen ion conductivity is necessary. State-of-the-art anodes for anode-supported SOFC are made of a mixture of nickel and the electrolyte material YSZ to meet these requirements. The presence of YSZ also ensures a similar thermal expansion coefficient in comparison to the electrolyte. Improving the anode performance by using new materials is not the scope of this work. Therefore, it is referred to literature for further information, e.g. [5, 6].

### Cathode

Similar to the anode, a high porosity is needed to ensure a good gas supply to and from the cathode TPB. A high electron and oxygen ion conductivity is also needed. Electronically conducting or mixed ionically/electronically conducting oxides are used as cathode material. To identify the best metal oxide for the electrolyte material, the operation temperature and the ceramic fabrication methods have to be taken into consideration [4]. Lanthanum strontium cobalt oxide (LSC) or lanthanum strontium cobalt ferrite oxide (LSCF) are good options in temperature ranges from 600 °C–800 °C [3, 7]. Furthermore, to improve the electronic conductivity, the LSC or LSCF can be infiltrated with cerium gadolinium oxide (CGO). For operation temperatures above 800 °C lanthanum strontium manganite (LSM) is favorable [3].

### Barrier layer and contact layer

To prevent reactions between the two materials of the cathode and the electrolyte, a barrier layer is placed. In terms of a YSZ electrolyte and a CGO infiltrated LSC cathode, a CGO barrier layer can be used. Furthermore, a contact layer is placed at the cathode side to reduce the resistance between cathode and the current collection plate [8].

## 2.2 Biogas

In this section the biogas composition and formation is discussed. Additionally energy production from biogas and the use of fuel cells is summarized. Finally the landfill gas from the landfill site close to Odense in Denmark is introduced because this landfill gas was used for SOFC testing in this thesis (see Chapters 6 and 7)

### 2.2.1 Biogas composition and formation

Biogas evolves through anaerobic digestion of biomass (organic matter). The main components of biogas are CH<sub>4</sub> and CO<sub>2</sub> plus different impurities such as sulfur. The exact biogas composition including the impurities depends on the source of the biomass, and the biogas is typically divided into two groups depending on the source. The first group consists of biogas produced industrially with the aim of generating energy. For example, growing agricultural products like corn or straw. Research is conducted to maximize the biogas yield of the biomass and increase the amount of CH<sub>4</sub> in the biogas e.g. [9]. The second group includes biomass which is a side product of another process, such as wastewater treatment or landfilling. This thesis focuses on the use of biogas from the second group. Emphasis is made on the second group because it is available and can help to reduce green house gas emissions by using the biogas in an efficient way. An overview of the biogas composition from different waste sources is given in Table 2.1. Furthermore, energy production should never compete with food production which might not be the case for the first biogas group.

**Table 2.1:** Overview of the biogas composition from different waste sources. Adapted from Tjaden et al. [10, table 2]

composition	biogas			
	wastewater	food waste	animal waste	landfill
CH <sub>4</sub> [vol%]	50-60	50-70	45-60	40-50
CO <sub>2</sub> [vol%]	30-40	25-45	35-60	35-50
N <sub>2</sub> [vol%]	<4	<4	<4	<20
O <sub>2</sub> [vol%]	<1	<1	<1	<2
H <sub>2</sub> S [ppm]	<400	<10000	<300	<200
non H <sub>2</sub> S sulfur [ppm]	<1	<1000	<30	<30
halogens [ppm]	<0.2	<0.2	<0.2	<100
moisture [%]	≈3	≈3	≈3	≈3

Due to the fact that the impurities of biogas are highly dependent on the source and location, a more detailed overview is given by Lanzini et al. [11]. As an example, the impurities of wastewater biogas (anaerobic digester gas) and landfill gas are shown in Table 2.2. The main contaminants are sulfur compounds (mainly H<sub>2</sub>S), siloxanes,

halocarbons and hydrocarbons. As shown in Table 2.2, the amount of impurities is higher in landfill gas in comparison to wastewater biogas.

**Table 2.2:** Overview of the amount of impurities present in wastewater biogas (anaerobic digester gas) and landfill gas. Summarized from reference [11, table 9].

	wastewater biogas	landfill gas
H <sub>2</sub> S [ppm]	1.8-130	63-5400
other S-compounds [ppm]	0.15-0.66	7.5-19
siloxanes [ppm]	0.1-2.3	up to 0.7
halogens (HCl) [ppm]	0.2-1.4	11-20
halocarbons [ppm]	0-0.16	6-14
hydrocarbons (benzene, toluene, etc.) [ppm]	0.4-3	86-300

## 2.2.2 Energy production from biogas and the use of fuel cells

The study conducted by Chum et al. [12] assumes that the energy produced from biogas could be between approximately 2 800 000 and 8 300 000 TW h by 2050. In the year 2016, the total energy production from biogas was 190 TW h in Europe, from which approximately 63 TW h were electricity and 7.5 TW h were heat [13]. Around 74% of the biogas was produced by industrial plants, for example decentralized agricultural plants and methanation plants. Biogas produced from landfill accounts for around 17% and biogas from wastewater plants for approximately 9% of the total biogas production in Europe. The majority of the biogas used for energy production is converted to electricity and heat in combined heat and power (CHP) plants. In most cases, the CHP plants use conventional internal combustion engines or micro turbines for the conversion process. These technologies have the disadvantages of low electric efficiencies, nitrogen oxide formation and air pollution with small particles [14]. Additionally, only biogas with a high heating value (high CH<sub>4</sub> volume percentage) can be feed to internal combustion engines or micro turbines.

To achieve a reduction of the amount of greenhouse gas emissions and to move towards circular economy, efficient utilization of waste is necessary [15, 16]. To achieve these goals, the use of a fuel cell instead of a combustion engine for converting biogas into energy could be beneficial [17]. The different aspects of using biogas as a fuel for fuel cells

were investigated in a wide range of studies [15, 18, 19, 20, 21, 22, 23, 24, 25, 26, 27, 28]. For example, Torija et al. [18] and Van herle et al. [19] analyzed the potential of fuel cells fueled with biogas for producing electricity and heat. The positive aspects of using fuel cells to increase the waste management system efficiency and reduce the plant's emissions were analyzed for example by Gandiglio et al. [20] and Lombardi et al. [15]. Gandiglio et al. points out that the waste plant energy consumption should be reduced while consuming energy produced from the biogas internally for achieving higher plant efficiencies. Lombardi et al. suggests the use of a fuel cell system for achieving the highest emission reduction of the waste management plant in comparison to other technologies. Investigations at the cell level and successful operation of a real landfill gas fueled SOFC was presented by Hagen et al. [21]. The study by Hagen et al. proves that SOFC's can be operated with biogas also when the CH<sub>4</sub> content in the biogas is low. A SOFC short stack operated successfully for 500 h with pre-mixed dry biogas, which was passed through a cleaning unit and a pre-reformer before entering the stack, is reported by Papurello et al. [22]. An initial field test of a commercial phosphoric acid fuel cell (PAFC) system installed at a landfill side is described by Spiegel et al. [23] in 1997. The first PAFC system fueled with biogas from a wastewater plant in Europe was operated in Germany [24]. The wastewater biogas was pre-cleaned by a two-phase purification phase and an adsorption step applying an activated carbon. Additionally, a pre-reformer unit was used to convert the biogas into H<sub>2</sub> rich gas, which was entering the 200 kW PAFC system. Krumbeck et al. [25] described the operation of the first use of a molten carbonate fuel cell (MCFC) system for producing energy from wastewater biogas in Europe. The first demonstration of using a 20 kW SOFC system was conducted by Wärtsilä in Finland [26, 27]. The first industrial sized SOFC site operated with biogas from a wastewater plant is installed close to Turin in Italy and started operation in 2017 [28]. '[The aim of the installation is to demonstrate] the technical and economical practicability of SOFC systems operated at a wastewater plant' [29]. Additionally, the aim of the SOFC side installation is to illustrate the increase of the overall waste plant efficiency and reduction of the environmental plant emissions. Further information about the SOFC side setup are provided in Section 3.2. A detailed efficiency analysis of the SOFC site fueled with wastewater biogas is presented in Chapter 8.

### 2.2.3 Landfill gas from the landfill site Odense, Denmark

The largest landfill gas plant in Denmark is the former landfill located on Stige Island close to Odense. On Stige Island the operator Odense Renovation A/S is extracting

landfill gas from around  $10 \text{ m}^3$  of waste [30]. The landfill gas is collected via 160 vertical boreholes in the island. 'The total length of the boreholes is more than 2000 meters' [30]. The boreholes are connected by a pipe system with a length of around 25 km and 4 pump modules are installed for pumping the landfill gas. Each pump module can pump up to  $720 \text{ m}^3 \text{ h}^{-1}$  landfill gas from the landfill. A container of an extraction unit located on the closed landfill is shown in Figure 2.2.



**Figure 2.2:** Container of an extraction unit located at the closed landfill on Stige Island close to Odense in Denmark.

For transferring the landfill gas from the landfill side to the CHP plant, which is located 4 km away, the gas is compressed to 1 bar absolute pressure. Currently, Odense Renovation A/S is operating a gas engine for producing electricity and heat from the landfill gas. In 2019,  $\approx 4900 \text{ MW h}$  electricity and  $\approx 6000 \text{ MW h}$  heat could be produced from the annual landfill gas production of  $\approx 400 \text{ m}^3 \text{ h}^{-1}$  [31]. Due to the fact that the waste is decomposing and no new waste is added, the gas production and the  $\text{CH}_4$  content present in the landfill gas will continuously decrease over the years. Due to the decreasing  $\text{CH}_4$  content, which corresponds to a decreasing heating value in the gas, approximately a gas engine can no longer be used for producing energy at a certain point. Furthermore, a higher electric efficiency during the conversion process of landfill gas to electric energy would be profitable from a economic point of view. Due to this fact the use of a SOFC system might become interesting for Odense Renovation A/S in the near future. The use of a SOFC system instead of a gas engine could also increase the plant efficiency and reduce the environmental plant emissions. On this basis, Odense Renovation A/S provided the landfill gas for the conducted tests at cell level for first feasibility studies (see Section 3.1.3 and Chapters 6, 7).

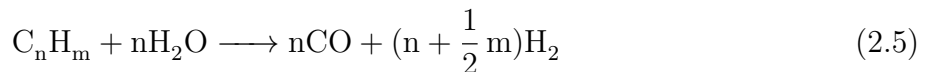
## 2.3 Considerations for biogas fueled SOFC

This chapter deals with the basics which are necessary for operation of biogas fueled SOFC's. Firstly, the internal reforming possibilities of biogas at the SOFC anode are summarized. Secondly, the possibility of carbon deposition at the SOFC anode is discussed. In the last section the poisoning effects on the SOFC anode and the handling of the impurities present in the biogas are summarized.

### 2.3.1 Internal reforming of biogas

The SOFC has the advantage that because of the nickel containing anode and the operation temperatures ( $650\text{ }^{\circ}\text{C}$ - $850\text{ }^{\circ}\text{C}$ ), direct internal reforming of carbon-containing fuels like  $\text{CH}_4$  or biogas is possible. For  $\text{CH}_4$  reforming, at least three different kinds of reforming processes have to be taken into consideration (see Eq. 2.4-2.8) [32]. The difference between the reforming process is the considered reforming agent. 'The dry reforming [(see Eq. 2.8)], which occurs with  $\text{CO}_2$  is especially interesting for biogas, as it already contains significant amounts of this reforming agent' [33]. In the presence of steam, e.g. during the steam reforming process, the water-gas shift reaction occurs. If a sufficient amount of reforming agent is not present, the risk of carbon formation is possible, which is further discussed in Section 2.3.2.

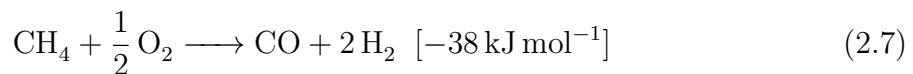
**Steam reforming:**



*Water-gas shift reaction:*



**Catalytic partial oxidation (CPO)**



### Dry reforming



In the following, the reforming reactions are further discussed from a thermodynamic point of view. The steam reforming process and the dry reforming process are endothermic, whereas the catalytic partial oxidation process is exothermic. In the case of biogas fueled SOFCs, a gas mixture of  $\text{CH}_4$ ,  $\text{CO}_2$  and  $\text{H}_2\text{O}$  (steam) is present at the fuel electrode. The steam is present because of the electrochemical reactions taking place under current and might be used as extra reforming agent. In this scenario it is not directly clear which reforming reactions are taking place. A broad range of thermodynamic based investigations have been carried out for estimating the performance and boundary conditions of hydrocarbon fueled SOFCs, e.g. [34, 35, 36]. One common procedure is to minimize the Gibbs free energy (see Eq. 2.9) of the anode gas mixture for determining the thermodynamic equilibrium. The gas mixture at thermodynamic equilibrium corresponds to the gas mixture at the anode after a 100% reforming of the carbon-containing fuel. In Equation 2.9,  $n_j$  stands for the number of moles of species  $s$ ,  $G_j^0$  for the standard Gibbs free energy of species  $j$ ,  $T$  [K] for the temperature and  $R$  [ $\text{J mol}^{-1} \text{ K}^{-1}$ ] for the universal gas constant.

$$G = \sum_s n_j \left[ G_s^0 + RT \ln \left( \frac{n_s}{\sum n_s} \right) \right] \quad (2.9)$$

To determine the gas equilibrium, commercial software such as FactSage [37] can be used. In the present study a program with the name ElchDAT was developed for estimating the gas mixture after reforming. The program is based on Gibbs minimization (Eq. 2.9) and is written in Python. Further explanations concerning the calculation process are given in Appendix A.

More detailed model-based investigations for estimating the fuel composition along the SOFC take further quantities like the energy balance, heat transfer and efficiencies into account [38, 39, 40, 41, 42, 43]. To estimate the reforming rate of  $\text{CH}_4$  at the nickel surface by using the steam reforming process (Eq. 2.4), the dependency (Eq. 2.10) derived by Achenbach and Riensche [44] can be used. As shown in Equation 2.10, the reformed rate of  $\text{CH}_4$  ( $r_{\text{CH}_4}$ ) is dependent on the partial pressure of  $\text{CH}_4$  ( $p_{\text{CH}_4}$ ), the anode cell

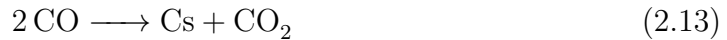
area ( $A_{\text{anode}}$ ) and the operation temperature ( $T$ ).

$$r_{\text{CH}_4} = 4274 p_{\text{CH}_4} A_{\text{anode}} e^{-82000(RT)^{-1}} \quad (2.10)$$

A similar dependency for  $\text{CH}_4$  reformation at the anode surface of a SOFC using the dry reforming process (Eq. 2.8) is not reported in literature at the current point in time.

### 2.3.2 Carbon deposition

Carbon deposition is a problem during SOFC operation because it is deactivating the reactions taking place at the anode. Carbon deposition at the SOFC anode is caused by three main reactions (Eq. 2.11-2.13) [34, 45]. Equation 2.11 defines the carbon formation because of methane cracking. In Equation 2.12 carbon is produced by CO hydrogenation. The last equation (Eq. 2.13) is called the Boudouard reaction. In this case CO is reformed to solid carbon and  $\text{CO}_2$ .



In Figure 2.3 the temperature dependency of carbon formation is shown in a Ternary phase diagram which was calculated with the commercial software FactSage [37]. Additionally a biogas consisting of 50%  $\text{CH}_4$  plus 50%  $\text{CO}_2$  and natural gas (100%  $\text{CH}_4$ ) is shown. Figure 2.3 shows that the carbon formation process is strongly dependent on the gas composition and the operation temperature. For avoiding carbon formation during operation of biogas fueled SOFCs the correct amount of extra reforming agent supply is needed. Additionally, the arriving oxygen ions at the anode (electrochemical reactions) also influencing the gas composition and supports the preventing of carbon formation [46]. Furthermore the extra reforming agent supply can be replaced by recirculating the anode exhaust gas back to the anode inlet again during operation (anode off-gas recirculation). This prevents carbon formation because the anode exhaust gas contains  $\text{H}_2\text{O}$  (steam) and  $\text{CO}_2$  [41, 47, 48]. In this case the supply of the reforming agent is only needed during the start-up and shutdown of the SOFC. The topic anode off-gas recirculation is further evaluated and discussed in Chapter 7 for landfill gas fueled SOFC's.

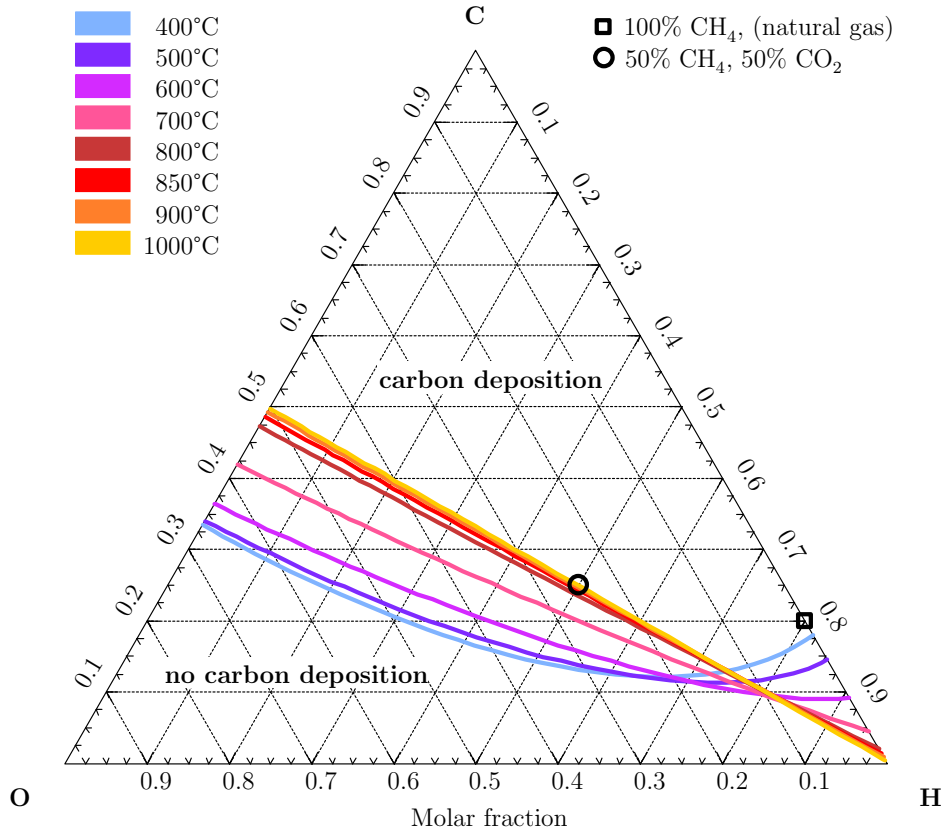


**Figure 2.3:** Ternary phase diagram of the system C-H-O showing carbon formation as function of the temperature at ambient pressure. Additionally the biogas mixture of 50% CH<sub>4</sub> plus 50% CO<sub>2</sub> and natural gas is shown [49, fig. 3].

If carbon formation is possible from a thermodynamical point of view is defined by the carbon activity. The carbon activity ( $\alpha_c$ ) can be calculated according to Equation 2.14 which is based on the Boundard reaction (Eq. 2.13). In Equation 2.14  $K_1$  stays for the equilibrium constant,  $p_{CO}$  for the CO partial pressure and  $p_{CO_2}$  for the CO<sub>2</sub> partial pressure. If the gas mixture is in equilibrium (Gibbs free energy minimum) the carbon activity based on the Boundard reaction (Eq. 2.13) is equal to the carbon activities based on the other two carbon formation reactions (Eq. 2.12, 2.11) [45, 50]. Referring to Nagata et al. [45] the lowest carbon activity value has to be considered for gas mixtures not in equilibrium.

$$\alpha_c = K_1 \frac{p_{CO}^2}{p_{CO_2}} \quad (2.14)$$

The carbon activity gives only an indication for the thermodynamical possibility of

carbon deposition. The definition is given below.

- $\alpha_c \geq 1$  Carbon formation possible
- $\alpha_c < 0$  No carbon formation possible

Determining the exact amount of carbon formed is not possible. The calculation of the carbon activity is a fast approach for identifying safe operation conditions for biogas fueled SOFC's. Therefore, this approach was implemented in the self developed software ElchDAT [51]. Further information are given in the Appendix A.

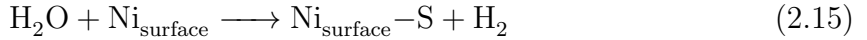
### 2.3.3 Poisoning effects and handling of impurities

The high operation temperature of SOFCs resulting in the fact that SOFCs are more robust to fuel impurities in relation to other fuel cell types. Nevertheless certain impurities which are present in the biogas are affecting the SOFC life time and performance. Therefore, it is important to know the effect of these impurities on the SOFC. The knowledge is beneficial for applying the correct biogas cleaning strategy or SOFC operation conditions. In the following the effects of the impurity sulfur are discussed in more detail because it is a very common impurity in hydrocarbon fuels and is decreasing the SOFC anode performance. While the effects of siloxane and the halogen chlorine mentioned briefly. Finally, a pre-cleaning option is shortly summarized.

#### Sulfur

The effect of the impurity sulfur has been investigated and discussed in a broad range in literature because sulfur is present in different hydrocarbon fuels. In the following the impact of sulfur poisoning on nickel based SOFC anodes is explained. The present of sulfur is preventing the catalytic reactions (reforming reactions Eq. 2.8, 2.4, water gas shift reaction 2.6) and the electrochemical reactions (see Eq. 2.1, 2.2) [21, 52, 53, 54, 55, 56, 57]. Additionally, Johnson et al. [58] showed in his SOFC anode catalysis study that the CH<sub>4</sub> dry reforming process (see Eq. 2.8) is less sensitive to H<sub>2</sub>S than the CH<sub>4</sub> steam reforming process (see Eq. 2.4). This could result in the advantage that less cleaning might be needed by using the dry reforming process. According to literature the poisoning effect of sulfur takes place by chemisorption of sulfur (S) at the anode nickel surface as shown in Equation 2.15 [59, 60]. The active sites for the reforming and

electrochemical reactions are blocked by sulfur.



As described by Hansen et al. the sulfur coverage can be defined as a function of the partial pressure ratio of  $p_{\text{H}_2\text{S}}/p_{\text{H}_2}$  ratio in the fuel and of temperature ( $T$ ) (see Eq. 2.16).

$$\theta_s = 1.45 - 9.53 * 10^{-5}T + 4.17 * 10^{-5}T - \ln \left( \frac{p_{\text{H}_2\text{S}}}{p_{\text{H}_2}} \right) \quad (2.16)$$

The definition given in Equation 2.16 is only valid for the case only  $\text{H}_2$  is present at the anode. Considering that during the electrochemical reactions of a SOFC steam is produced and than the anode gas mixture contains of  $\text{H}_2$ ,  $\text{H}_2\text{O}$  and  $\text{H}_2\text{S}$ . The results of the  $\text{H}_2\text{S}$  studies up to temperature of 850 °C conducted by Rostrup-Nielsen [61] indicate that steam has no effects on the adsorption of sulfur on the nickel catalysts. Also Matsuzaki et al. [62] could not observe changes of the overvoltage during their study of  $\text{H}_2\text{S}$  poisoning on SOFCs. In the study Matsuzaki et al. varied the  $\text{H}_2\text{O}$  (steam) content at the anode and kept the  $p_{\text{H}_2\text{S}}/p_{\text{H}_2}$  ratio constant. According to the described studies by Rostrup-Nielsen [61] and Matsuzaki et al. [62] Equation 2.15 is also valid during the present of a certain amount of steam at the SOFC anode. No quantitative correlation is reported in literature yet for the dependency of sulfur coverage and carbon containing fuels (e.g.  $\text{CH}_4$  and  $\text{CO}_2$  or  $\text{H}_2\text{O}$ ).

A sketch of the common test procedure for  $\text{H}_2\text{S}$  poisoning studies at the SOFC anode is provided in Figure 2.4. The  $\text{H}_2\text{S}$  study is normally carried out at galvanostatic conditions. The  $\text{H}_2\text{S}$  concentration in the fuel stream is increased step wise at a set current density and operation temperature followed by a step wise decrease of the  $\text{H}_2\text{S}$  concentration. The presence of  $\text{H}_2\text{S}$  results in an immediate loss of cell performance followed by a liner performance loss region which is also named long term degradation region [63]. In case of the presence of the sulfur compound Ni sulfide and  $\text{H}_2\text{S}$  a gradual performance degrease occurs after the initial performance loss [64]. The performance loss is expressed by the corresponding voltage drop ( $\Delta U$ ) [52, 59]. During the test procedure the  $\text{H}_2\text{S}$  concentration is kept constant until the cell performance degradation has reached the linear degradation regime. Additionally the current density is increased step wise and maybe also decreased again. At each current density the  $\text{H}_2\text{S}$  concentration test procedure is repeated. The immediate performance loss can be recovered to a

certain extend by reducing the  $\text{H}_2\text{S}$  amount in the fuel stream again. The magnitude of cell performance recovery is among others dependent on the fuel composition and applied current density. Furthermore, Hauch et al. [63] showed that the magnitude of the  $\text{H}_2\text{S}$  poisoning effect is also dependent on the initial cell performance. A higher  $\text{H}_2\text{S}$  poisoning effect is observed for hydrocarbon fuels in comparison to hydrogen fuel in SOFC's. [52, 56, 57, 65]. This is caused by the higher  $\text{H}_2\text{S}$  sensitivity of the reforming process (see Eq. 2.4-Eq. 2.8) in contrast to the lower  $\text{H}_2\text{S}$  sensitivity of the electrochemical reaction (see Eq. 2.1- Eq. 2.2). The reforming reactions are more poisoned with increasing sulfur amount in the fuel which results in a corresponding increasing voltage drop. The trend of the  $\text{H}_2\text{S}$  poisoning can be described approximately by an exponential dependency [21].

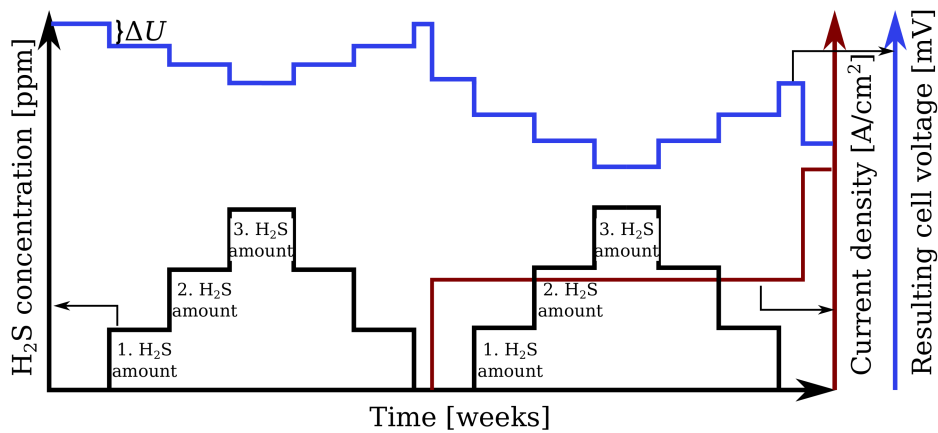


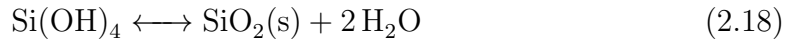
**Figure 2.4:** Illustration of the conventional steady state approach for studying sulfur poisoning at the anode of SOFC's.

Only for short term  $\text{H}_2\text{S}$  exposure tests the cell performance loss is close to 100 % reversible and the permanent cell performance loss is not detectable in cell voltage measurements. For the reversibility the  $\text{H}_2\text{S}$  concentration needs to be between 20 ppm and 30 ppm for  $\text{CH}_4$  containing fuels and up to 100 ppm for  $\text{H}_2$  fuels [21, 54, 65]. Cheng et al. [66] investigated the differences between  $\text{H}_2\text{S}$  poisoning during galvanostatic mode which is normally used for  $\text{H}_2\text{S}$  tests and potentiostatic mode. He pointed out that sulfur poisoning is leading to a higher cell performance loss during potentiostatic operation than during galvanostatic operation. This could be caused by the different amount of oxygen ions passing through the electrolyte. The poisoning effect differences during real landfill gas supply in the galvanostatic mode and potentiostatic mode is investigated in Chapter 6.

### Siloxane and halogen chlorine

As summarized by Lanzini et al. [53] only a limited amount of studies concerning biogas impurities beside of H<sub>2</sub>S studies are available in literature at the present time.

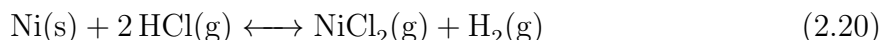
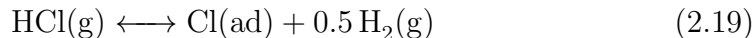
A thermodynamical investigation by Madi et al. [67, 68] indicates that siloxanes forms SiO<sub>2</sub>(s) by decomposing at high temperatures. Furthermore, he stated that nickel based SOFC anodes could be affected by formation of NiSi and Ni<sub>2</sub>Si even at low siloxane concentration. The gradual performance loss caused by siloxane on Ni-ScSz anode based cells fueled with 3% H<sub>2</sub>O in H<sub>2</sub> at 800-1000 °C and at 0.2 A cm<sup>-2</sup> was connected with SiO<sub>2</sub> formation at the porous cermet anode [64, 69]. A large amount of the SiO<sub>2</sub> close to the anode top surface and small quantities in the porous anode layer were identified. Haga et al. [64, 69] concluded that the deposition of SiO<sub>2</sub>(s) at the cell anode is the result of the reactions defined in Equations 2.17 and 2.18 [64].



Madi et al. [67, 68] saw in his experimental investigations performance degradation of Ni-YSZ SOFC single cells and short-stacks during siloxane poisoning, too. The EDX studies by Madi et al. [67, 68] found siloxane on the current collectors, the anode support and also at the TPB. Additionally the further calculations of Madi et al. [67, 68] suggest that SOFC operation at OCV and the increase of the operation temperature are two possibilities to remove a certain amount of siloxane again. The siloxane removal would result in a partly SOFC performance recovery. In his study the first recovery option operating the SOFC at *OCV* was investigated and resulted in a SOFC performance recovery to a certain extend.

In the following, the poisoning impact of chlorine (HCl) on the SOFC performance is summarized. The study of Haga et al. [64, 69] showed continuous degradation during chlorine poisoning. An explanation could be that nickel precipitates in the Ni-ScSZ anodes. The cell were fueled with were fueled with 3% H<sub>2</sub>O in H<sub>2</sub> at 800 °C and operated with 0.2 A cm<sup>-2</sup> in the studies of Haga et al.. Furthermore, Madi et al. [70] conducted a detailed electrochemical impedance study for analyzing the poisoning behavior of chlorine on the SOFC performance during H<sub>2</sub> and syngas anode supply at 750 °C. In the

study impedance response changes in the low and high frequency were observed during the SOFC was exposed to HCl. Concluding that the fuel conversion and the electrochemical reactions at the triple phase boundary (TPB) are influenced by the presence of HCl. 'This report concluded that the increase in cell resistance with exposure to HCl can be due to the presence of electronegative atoms such as Cl which hinder the adsorption of H<sub>2</sub> on Ni surfaces [Equation 2.19] and also to the formation of NiCl<sub>2</sub>(g) via [Equation 2.20], which limits the TPB reaction sites' [53].



### Cleaning strategies

As described in the previous two sections impurities like sulfur and siloxane are causing a performance loss of the SOFC. Therefore, pre-cleaning steps have to be implemented for biogas fueled SOFC's. Studies by Xiao et al. [71] and Cabrera-Codony et al. [72] showed that activated carbon filter are an efficient option to remove H<sub>2</sub>S and siloxanes. These observations are in line with the results summarized by Lanzini et al. [53]. One essential parameter for the design of the activated carbon filter is the breakthrough time. This time defines how long the filter is able to absorb the specific impurity. In case of the biogas system described in Section 3.2 two activated carbon filter are used. One filter is optimized for removing H<sub>2</sub>S while the second one is optimized for removing siloxanes. Additionally, the installation set up of the activated carbon filters is important to avoid down times of the SOFC systems during replacement of the filter before the breakthrough time of the filters is reached. Therefore, Lanzini et al. [53] recommends a 'lead-and-lag' configuration which allows the replacement of one activated carbon filter while the biogas is passed through another activated carbon filter with the same specifications.

## 2.4 SOFC characterization parameters and techniques

Aim of this part it to introduce the needed SOFC characterization parameters and techniques. First, the iV-curve characteristics are introduced. In the next section the electrochemical impedance spectroscopy technique for analyzing the SOFC performance during operation is introduced. In the last two sections definitions of the degradation rates, efficiencies and fuel utilization are presented which are possibilities for quantifying the SOFC performance.

### 2.4.1 iV-curve characteristics

An iV-curve represents the dependency between the applied current density and the corresponding voltage of bipolar electric parts. An example of an iV-curve of a SOFC fueled with dry hydrogen is given in Figure 2.5. The curve behavior is caused by three main losses: the thermodynamic losses, the ohmic losses and finally the concentration polarization. For SOFC's the thermodynamic losses related to the Nernst equation (see Eq. 2.21) are mainly influencing the iV-curve in this region and not the activation losses [73]. Besides the contribution of the electrolyte, also the electrical resistance of the electrodes contributes to the ohmic losses. The concentration polarization is occurring because at high current densities, not enough fuel/oxygen can be supplied to the reaction sides (triple phase boundaries) of the electrodes. The cell voltage while no current is flowing is defined by the Nernst equation and the maximum current density is defined by Faraday's law, which is further described in the following.

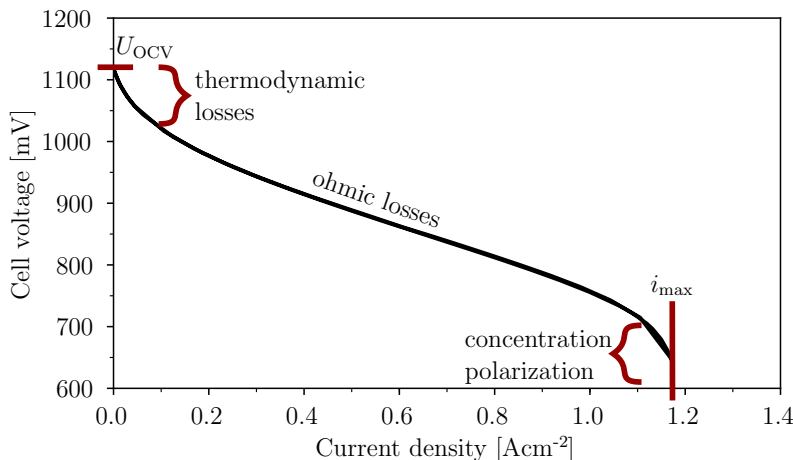


**Figure 2.5:** Example iV-curve of a SOFC fueled with dry H<sub>2</sub> operated at 850 °C.

#### Open circuit voltage

The open circuit voltage (OCV) represents the cell voltage while no current is applied and is defined by the Nernst equation. The Nernst equation describes the dependency between the cell potential  $U_{OCV}$  and the equilibrium reduction potential of an electrochemical cell. The Nernst equation for a SOFC with the half cell reactions according to Equations 2.1 and 2.3 is given in Equation 2.21. In the Equation 2.21,  $p_{H_2}$  represents the partial pressures of H<sub>2</sub> on the anode side,  $p_{H_2O}$  the partial pressure of steam at the

anode side and  $p_{O_2}$  the partial pressure of  $O_2$  on the cathode side. Additionally,  $E^0$  is the standard cell potential,  $R$  the universal gas constant,  $T$  the absolute temperature and  $F$  the Faraday constant.

$$U_{OCV} = E = E^0 - \frac{RT}{2F} * \ln \left( \frac{p_{H_2O,an}}{p_{H_2,an}\sqrt{p_{O_2,cat}}} \right) \quad (2.21)$$

For calculating the theoretical OCV of a SOFC according to the Nernst equation, the program ElchDAT [51] written in Python was developed. Further information about the determination of for example  $E^0$  is given in the appendix.

### Area specific resistance

The area specific resistance ( $ASR$ ) (see Eq. 2.23) is another parameter which is often used for quantifying the performance of a SOFC [74]. The  $ASR$  can be calculated from an iV-curve or from measurements while a constant current is applied. In Equation 2.23  $U_{OCV}$  is the cell voltage at OCV according to the Nernst potential,  $U(i)$  the cell voltage at the specific operation point and  $i$  the current density. This definition of the  $ASR$  has the advantage of representing the full polarization range of the cell performance in comparison to the deferentially derived  $ASR$  (see Eq. 2.22) [75]. For single cell testing the minimum  $ASR$  values at current densities higher than  $0.1 \text{ A cm}^{-2}$  calculated from the iV-curve measurements are compared in some cases (see Chapter 6). Only  $ASR$  values determined at the same operation conditions can be compared because the  $ASR$  is sensitive to the conditions [75]. Besides this, the change of the  $ASR$  over time  $t$  (see Eq. 2.24) can be used for comparing test scenarios (see Chapter 6).

$$ASR(i)_{\text{deriv}} = \frac{\partial U(i)}{\partial i} \quad (2.22)$$

$$ASR(t, i) = \frac{U_{OCV,t} - U(t, i)}{t, i} \quad (2.23)$$

$$\Delta ASR(t, i) = ASR(t, i) - ASR(t_{\text{start}}, i) \quad (2.24)$$

### Maximum current density

The theoretical maximum current density can be determined by combining Faraday's law (see Eq. 2.25) and the ideal gas law. Equation 2.25 expresses the linear relation

between the amount of any substance that is liberated at an electrode and the quantity of electricity passing through the electrode.  $Q$  stands for the charge,  $n$  for the amount of substance and  $z_e$  for the charge number. Expressing  $Q$  by the current  $I$  times the time  $t$  and the amount of substance  $n$  in terms of the ideal gas law (see Equation 2.26), Equation 2.27 can be derived. Equation 2.27 defines the maximum current density  $i_{\max}$  as a function of the volumetric fuel flow rate  $\dot{V}_{\text{fuel}}$  of the fuel gas and the cell area  $A$ .

$$Q = z_e n F \quad (2.25)$$

$$PV = nRT \quad (2.26)$$

$$i_{\max} = \frac{\dot{V}_{\text{fuel}} z_e p F}{RT A_{\text{cell}}} \quad (2.27)$$

## 2.4.2 Electrochemical impedance spectroscopy

Electrochemical impedance spectroscopy (EIS) is a common technique to analyze electrochemical systems [76]. In SOFC research, it is used as an in situ method for analyzing the different processes taking place at the anode and cathode during operation. To ensure a pseudo-linear voltage and current dependency, a small alternating current or voltage is used for exciting the electrochemical device. For investigations of SOFCs, it is common to measure the phase shifted current response of the corresponding sinusoidal voltage excitation signal. This is done over a selected frequency range. Based on Ohm's law, the resulting impedance can be calculated from the relation shown in Equation 2.28, with the dependency between the radial frequency and the frequency given in Equation 2.29.

$$Z = \frac{E_t}{I_t} = \frac{E_0 \sin(\omega t)}{I_0 \sin(\omega t + \phi)} \quad (2.28)$$

$$\omega = 2\pi f \quad (2.29)$$

The obtained data is often presented in a Nyquist plot and a Bode plot (see Figure 2.6). The Nyquist plot presents the imaginary part of the impedance ( $-\text{Im}(Z)$ ) against the real part of the impedance ( $\text{Re}(Z)$ ), while the Bode plot shows for example the imaginary part of the impedance ( $-\text{Im}(Z)$ ) in relation to the frequency  $f$ . Other options for a Bode plot are the magnitude ( $\text{mag}(Z)$ ) or the phase angle  $\phi$  against the frequency  $f$ . From the Nyquist plot two ohmic resistances of the cell can easily be identified, as illustrated

in Figure 2.6. The serial resistance  $R_s$  is the resistance of the different components of the cell (mainly electrolyte), while the polarization resistance  $R_p$  is the sum of the anode and cathode process losses. Beside the Bode and Nyquist plots, methods like the distributions of relaxation times (DRT) [77] were developed for separating and identifying the occurring processes in detail. Jensen et al. [78] illustrated that with the analysis of difference of impedance spectra (ADIS) the domain frequency changes corresponding to the different electrodes can be shown. '[Additionally] the Kramers-Kronig relations [79, 80, 81], which are based on the principle of causality, present a very useful tool for data validation' [82]. A broad range of impedance studies, e.g [83, 84, 85, 86, 87, 88, 89] were conducted for identifying and understanding the different processes taken place in a SOFC. This knowledge can be used for optimizing the cell performance and durability.

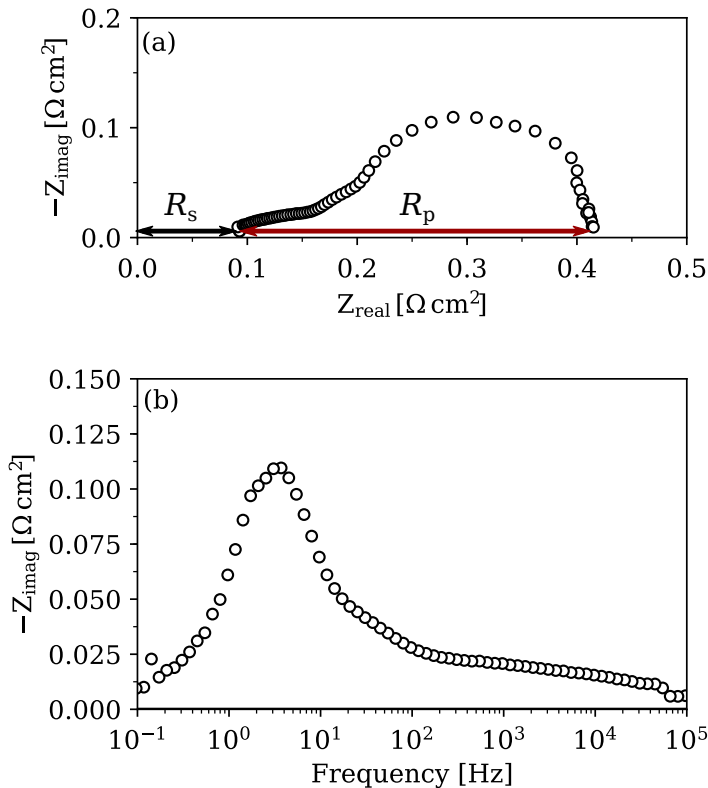


**Figure 2.6:** Example of a Nyquist (a) and Bode plot (b) for presenting an impedance measurement of a SOFC cell.

For further analysis, the impedance measurement can be modeled by an equivalent electrical circuit. Different kind of models have been developed to represent the impedance

responses of electrochemical cells [90]. Table 2.3 gives an overview of selected models used for describing the processes in a SOFC. To apply the equivalent electric circuit for modeling the measured impedance data, a complex non-linear least square fit can be done as described by Boukamp [91].

**Table 2.3:** A selection of equivalent circuit elements used for describing the impedance response of a SOFC.

element	impedance	process	reference
(R) serial resistor	$R$	contact and electrolyte resistance	
(RQ) resistor and a constant phase element in parallel	$\frac{R}{1+RQ_0(j\omega)^n}$	double layer capacitance and charge-transfer reactions in parallel	[88]
(G) Gerischer element	$\frac{R_{\text{chem}}}{\sqrt{1+j\omega t_{\text{chem}}}}$	combination of electrochemical charge-transfer and diffusion	[86]
(W) Warburg element	$R_w \frac{\tanh[(j\omega T)^\alpha]}{(j\omega T)^\alpha}$	diffusion processes	[86]
(TLM) transition line model	$\frac{R_{\text{el}} R_{\text{ion,L}}}{R_{\text{el}} + R_{\text{ion,L}}} \left( L + \frac{2\lambda}{\sinh(L/\lambda)} \right) + \lambda_{TLM} \frac{R_{\text{el}}^2 + R_{\text{ion,L}}^2}{R_{\text{el}} + R_{\text{ion,L}}} \coth \left( \frac{L}{\lambda_{TLM}} \right)$	porous electrode electrochemistry	[88]

### 2.4.3 Degradation rates

At the moment, no standards or guidelines are available for a standardized determination of the degradation rate (DR) of a SOFC. In this thesis the degradation rates of the cell voltage, current density and *ASR* have been calculated according to Equations 2.30-2.32, which are based on the description of Gemmen et al. [74, based on Eq. 8]. The degradation corresponds to a decrease of the cell voltage or current density but to an increase of the *ASR*. The degradation rates are expressed in percentage per 1000 hours. To reach the right conclusions, it is important to compare only degradation rates of tests which have been operating for the same time, because the slope of the increase in *ASR* might not be linear [74]. '[Furthermore, the] degradation rates strongly depend on operating conditions like temperature, gas composition and utilization, and current

density applied during the long-term test' [92].

$$DR(t)_U = 100 \frac{U(t_{\text{start}}) - U(t)}{U(t_{\text{start}})(t - t_{\text{start}})} \quad (2.30)$$

$$DR(t)_i = 100 \frac{i(t_{\text{start}}) - i(t)}{i(t_{\text{start}})(t - t_{\text{start}})} \quad (2.31)$$

$$DR(t)_{\text{ASR}} = 100 \frac{ASR(t_{\text{start}}) - ASR(t)}{ASR(t_{\text{start}})(t - t_{\text{start}})} \quad (2.32)$$

#### 2.4.4 Efficiencies and fuel utilization

The determination of the efficiency of a SOFC system is defined by the International Standard IEC 62282-3-200 Fuel cell technologies – Part 3 [93]. For the efficiency analysis of an industrial SOFC system (see Chapter 8), the calculations were conducted according to the IEC standard. Due to the fact that the electric efficiency was also determined for selected tests at cell level (see Chapters 6 and 7), the used definition for a biogas fueled SOFC is given in equation 2.33.  $P_{\text{cell}}$  stands for the produced electric power of the SOFC cell,  $\dot{n}_{\text{fuel}}$  the molar mass fuel flow rate,  $\text{vol}\%_{\text{CH}_4}$  the amount of  $\text{CH}_4$  present in the fuel and  $LHV_{\text{CH}_4}$  the lower heating value of  $\text{CH}_4$ .

$$\eta_{\text{el,DC,cell}} = 100 * \frac{P_{\text{cell}}}{\dot{n}_{\text{fuel}} * \text{vol}\%_{\text{CH}_4} * LHV_{\text{CH}_4}} \quad (2.33)$$

Another unit for quantifying the fuel cell performance is the fuel utilization, which is given in Equation 2.34. The fuel utilization is the ratio between the used  $\text{CH}_4$  according to the applied current density  $i$  (Faraday's law Eq. 2.25, ideal gas law Eq. 7.1) and the supplied amount of fuel.

$$FU = \frac{iRTA_{\text{cell}}}{z_e p F} * \frac{1}{\dot{n}_{\text{fuel}} * \text{vol}\%_{\text{CH}_4}} \quad (2.34)$$

# 3 Test facilities

In this chapter the two testing facilities are introduced. In the first section the single cell tests are explained while in the second section the SOFC system site is presented.

## 3.1 Single cell tests

First of all the main components of the single cell test rig are presented. Followed by the introduction of the cell house set-up, the option of real landfill gas supply as an anode fuel, the option of anode-off gas recirculation. In the last two subsections the tested cells and the electrochemical impedance measurements plus analysis are summarized.

### 3.1.1 Main components of the rig

The single cell tests were conducted at a test rig built in-house at DTU Energy. A schematic arrangement of the test rig is provided in Figure 3.1. For safety reasons, the whole setup was placed in a ventilated hood. A safety box was monitoring the H<sub>2</sub> and CO concentration in the hood, the ventilation of the hood and the temperature of the furnace the cell was operated in. In case of an alarm, the safety box could change the cell gas supply via magnetic valves (MVs) and turn off other equipment if needed. The anode and cathode gases were supplied by mass flow controllers (MFCs) as illustrated on the left (anode) and right side (cathode) in Figure 3.1. The anode could be supplied with H<sub>2</sub>, carbon-containing gases such as CH<sub>4</sub>, CO<sub>2</sub> and CO, O<sub>2</sub>, Ar and safety gas (9% H<sub>2</sub> in N<sub>2</sub>). Additionally, the possibility of real landfill gas supply was added, which is described in Section 3.1.3. To simulate the sulfur impurities in biogas, 200 ppm H<sub>2</sub>S in H<sub>2</sub> could be supplied to the anode. The cathode could be supplied with O<sub>2</sub>, air and N<sub>2</sub>. The gases were delivered to the cell via the cell house, which is explained in Section 3.1.2. To reach the operation temperature (600–850 °C of the SOFC), the cell house was placed in a furnace. Furthermore, an option for anode exhaust gas recirculation was installed (see Section 3.1.4). In safe operation mode, the test rig could be operated by the RFCcontrol (remote fuel cell control) software [94].

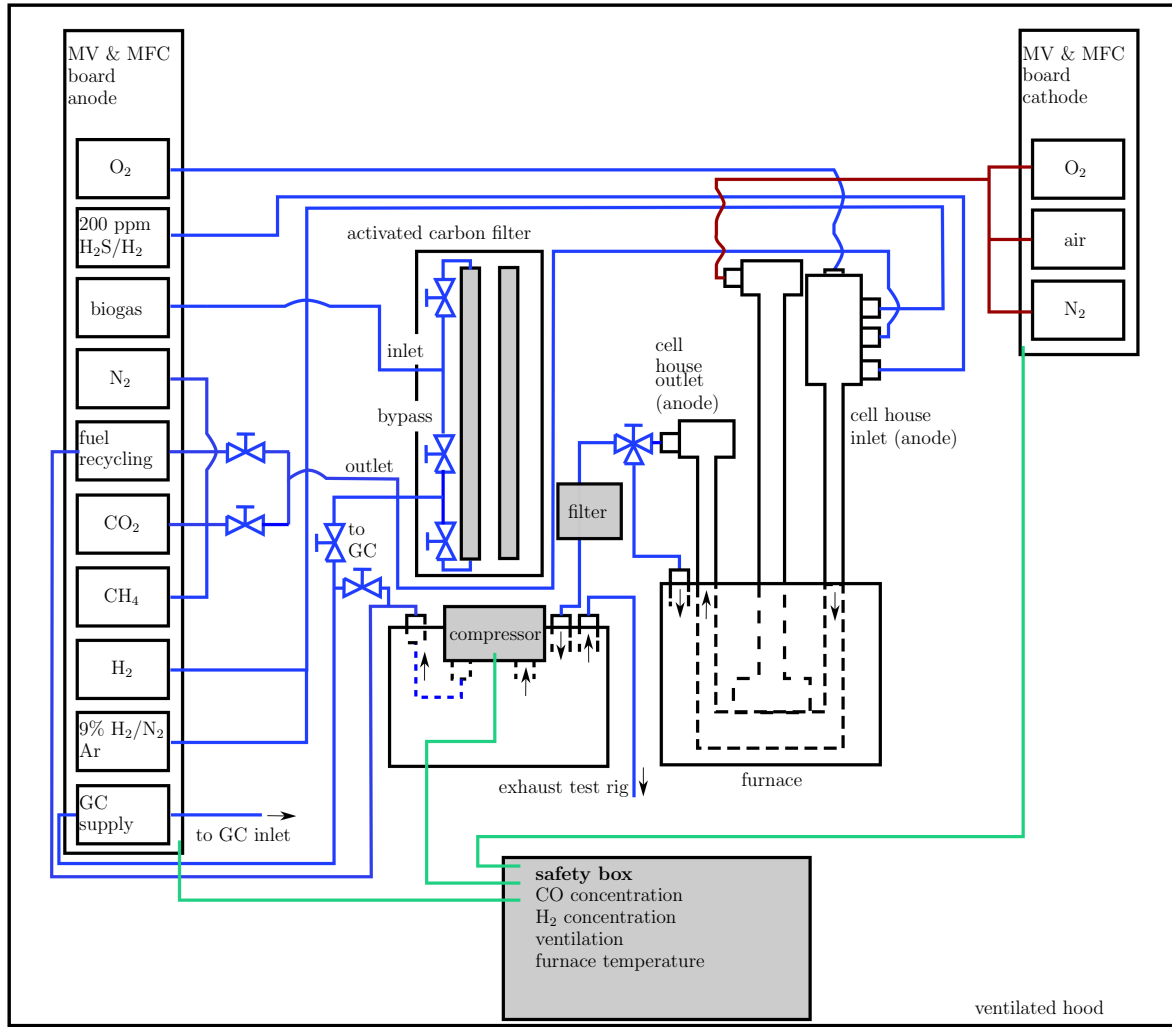


**Figure 3.1:** Schematic arrangement of the test rig.

### 3.1.2 Cell house setup

A schematic arrangement of the cell placed in the cell house is shown in Figure 3.2. The cell is placed between the bottom part and the top part of the cell house, which consists of alumina. The fuel for the anode of the cell is supplied via the bottom part of the cell house. To ensure a good electrical contact, a nickel plate is placed on top of the bottom part of the cell house. Between the nickel plate and the cell, two nickel meshes (coarse and fine) are placed to ensure distribution of the fuel and a good electrical contact. The anode side is sealed by a gold frame. The nickel plate is connected to the current collectors and voltage probes (see Figure 3.3). The cell is held in position by a duct, which also ensures the correct position on top of the cathode cell side of the top part of

the cell house. The electrical contact to the cathode is ensured by gold stripes and a gold mesh. The cathode part has no sealing. The air/O<sub>2</sub> is distributed from the center of the top part of the cell house over the cathode side through the gold stripes and the gold mesh. A weight is applied on top of the top part of the cell house to ensure a leak-tight setup. As shown in Figure 3.3, two voltage probes are placed in the cell house, one on the inlet side and one on the outlet side of the cell. This allows measurement of the potential between the two probes, which is of interest for analyzing the poisoning effects of for example sulfur along the cell. Thermocouples are placed on the sides of the top piece, at the gas inlets and at the gas outlet of the anode. Additionally, pO<sub>2</sub> sensors are installed at the inlet and outlet of the anode (not shown in Figure 3.3). The pO<sub>2</sub> sensors are based on platinum and measure the voltage of the target gases vs. air and gives a measure of the pO<sub>2</sub> using the Nernst equation. This allows conclusions about the gas compositions to be drawn and enables comparison to the OCV of the cell. Further details about cell set-ups and cell testing are provided in literature [75].

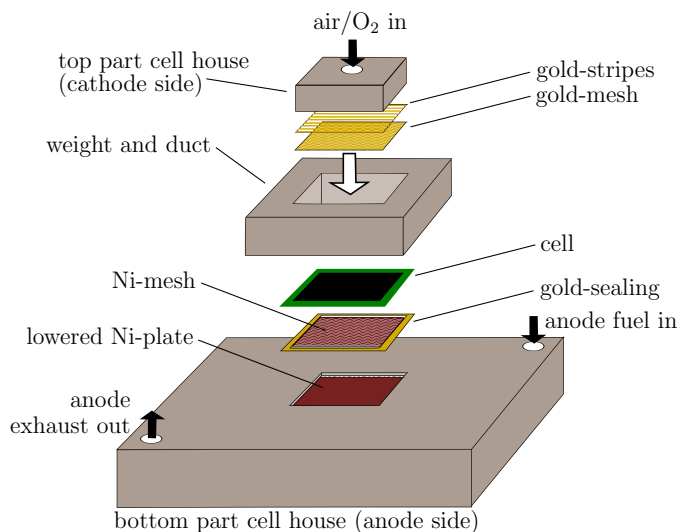


**Figure 3.2:** Schematic arrangement of the cell placed in the cell house.

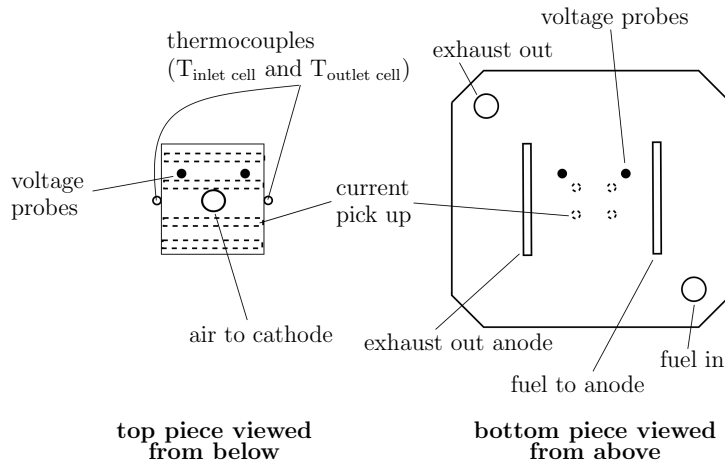


**Figure 3.3:** Cell house sketch of the top and bottom part including voltage probes, current collectors and thermocouples.

### 3.1.3 Real landfill gas as fuel

The real landfill gas was collected at the landfill site of Odense Renovation A/S located in Odense, Denmark. The approximate landfill gas composition is given in Table 3.1. The impurities of the landfill gas have not been analyzed in detail. It is only known that at least 40 ppm H<sub>2</sub> are present and a certain amount of siloxane. At the CHP plant of the landfill site, the landfill gas has an absolute pressure of 0.5 bar. To transport the landfill gas from the landfill site in Odense to the DTU Energy test facility, the gas was compressed to 15–25 bar and filled in four standard 50 L gas bottles. The bottles were connected to the single-cell test rig and the cell could be supplied with landfill gas via a mass flow controller. Using a landfill gas flow rate of 4 L h<sup>-1</sup>, a cell could be operated with real landfill gas for approximately 1000 h. To remove impurities like sulfur and siloxane as discussed in Section 2.3.3, the landfill gas could be passed through a commercial activated carbon filter (see Figure 3.1). To avoid carbon formation, the landfill gas (4 L h<sup>-1</sup>) was normally mixed with 2 L h<sup>-1</sup> CO<sub>2</sub> at room temperature before entering the cell house.

**Table 3.1:** Approximate gas composition of the landfill gas, which was collected at the dump site in Odense, Denmark. Single cells were normally fueled with  $4 \text{ L h}^{-1}$  landfill gas and  $2 \text{ L h}^{-1}$   $\text{CO}_2$  for avoiding carbon formation (dry reforming process Eq. 2.8).

$\text{CH}_4$	$\text{CO}_2$	$\text{O}_2$	$\text{N}_2$
34 vol%	22.5 vol%	1.5 vol%	42 vol%

Because only a limited amount of real landfill gas was available for the tests also pre-mixed biogas was used for selected studies (see Chapter 5). The fuel composition including the extra supply of  $\text{CO}_2$  as reforming agent is shown in Table 3.2 and is based on the real landfill gas composition.

**Table 3.2:** Pre-mixed landfill gas compositions plus extra reforming agent  $\text{CO}_2$  based on the real landfill gas composition (see Table 3.1).

$\text{CH}_4$	$\text{CO}_2$	$\text{N}_2$	extra reforming agent $\text{CO}_2$
23 vol%	15 vol%	29 vol%	33 vol%

### 3.1.4 Anode off-gas recirculation

To allow the use of the anode exhaust gas in order to prevent carbon formation during landfill gas supply, the cell test rig was modified. To recirculate the anode exhaust gas back to the inlet, an extra particle filter, a pump and an extra mass flow controller was installed in the test rig (see Figure 3.1). The anode exhaust gas could be collected in a tank before being recirculated back to the cell.

From the anode cell house exhaust to the tank, the gas is passed through a standard particle filter to protect the compressor. A scroll compressor P11H12N2.5 from Air Squared Manufacturing, Inc. was used to recirculate the anode exhaust gas and to provide the needed operation pressure for the mass flow controller. A picture of the tank and the compressor is shown in Figure 3.4. The recirculation flow rate could be set via the mass flow controller. The pump and the mass flow controller were connected to the safety box for security reasons and could be operated by the RFCcontrol software [94]. Due to the fact that the pump was operating at room temperature, a certain amount of steam was condensing during the recirculation process and collected in the particle filter.

During the experimental durability study, which is described in Chapter 7, the amount of condensed steam was around 150 mL after 150 h of recirculation. Furthermore, a small amount of carbon was found in the particle filter after each test. Due to this fact, the recirculation setup had to be maintained between each test using anode off-gas recirculation.

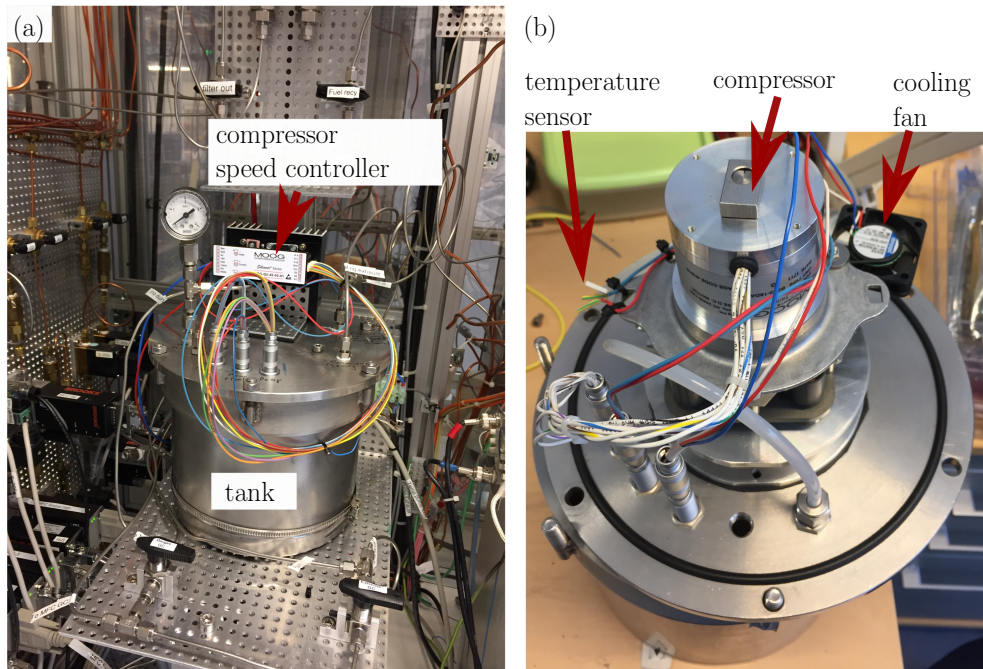


**Figure 3.4:** Picture of the anode exhaust gas tank in the test rig (a) and the scroll compressor P11H12N2.5 from Air Squared Manufacturing, Inc. (b) which is mounted inside the tank for recirculating the anode exhaust gas.

#### 3.1.5 Tested cells and standardized characterization

##### Tested cells

State-of-the-art anode supported SOFCs with a size of 5x5 cm<sup>2</sup> and an active area of 16 cm<sup>2</sup> were used for the testing. The cells were produced in-house at DTU Energy. The cells consisted of an anode support layer, an anode, an electrolyte and a cathode, as shown in Figure 3.5. Furthermore, a barrier layer was placed between the electrolyte and the cathode. Depending on the cell availability, the cell compositions were slightly different in terms of anode material and cathode material (see Table 3.3). For the different cell layers different manufacturing steps like sintering steps, tape casting and spraying are used. Further details about the cells produced in-house, including the

manufacturing process, are provided by Ramousse et al. [95].

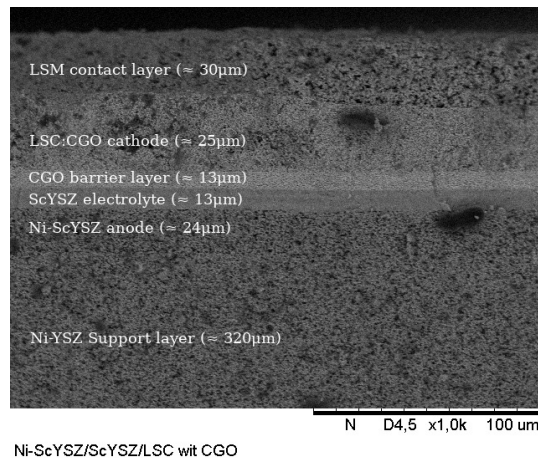


**Figure 3.5:** Electron microscope picture of a Ni-SCYSZ/ScYSZ/LSC:CGO with CGO barrier and a cathode contact layer cell cross section.

**Table 3.3:** Single-cell test compositions of the cells used in this thesis. All cell types had a CGO barrier layer between electrolyte and cathode, plus a LSM cathode contact layer.

chapter	material		
	anode	electrolyte	cathode
4	Ni-ScYSZ	YSZ	LSC-CGO
5, 6	Ni-YSZ	YSZ	LSCF-CGO
7	Ni-YSZ	YSZ	LSC-CGO

### Standardized characterization

In all tests which are described in this thesis, the cells were supplied with  $10 \text{ L h}^{-1}$  argon on the anode side and  $20 \text{ L h}^{-1}$  air on the cathode side during the heating process to  $850^\circ\text{C}$ . After the temperature was reached, the anode supply was changed to 9%  $\text{H}_2/\text{N}_2$  for around two hours to reduce the nickel from nickel oxide. Before the testing, a standardized initial characterization called 'finger print' was carried out, which was repeated before shutting down the test and between test segments if needed. 'The 'finger print' consisted of iV-curves and electrochemical impedance measurements in different steam to  $\text{H}_2$  ratios [(4%, 20%, 50%)] to the anode side and air or oxygen supply to the

cathode side to characterize the cell performance' [96]. If necessary, the measurements were also carried out at different operation temperatures ( $700\text{ }^{\circ}\text{C}$ ,  $750\text{ }^{\circ}\text{C}$ ,  $800\text{ }^{\circ}\text{C}$ ,  $850\text{ }^{\circ}\text{C}$ ).

### 3.1.6 Electrochemical impedance measurements and analysis

#### Equipment

For the electrochemical impedance measurements, Solatron workstations were used. The Solatrons were operated with the software 'Elchemea data acquisition' developed in-house [97]. Impedance spectra were normally recorded in a frequency range from 96 850 Hz to 0.02 Hz with 12 points per decade and an integration cycle of 200 to 5 depending on the frequency segment. Further equipment specifications are summarized in Table 3.4.

**Table 3.4:** Used frequency response analyzer specifications for conducting the electrochemical impedance measurements according to reference [98, 99, 100].

device	frequency	excitation signal	resolution
Solartron 1260A	10 $\mu\text{Hz}$ - 32 MHz	0-3 V or 0-60 mA	1 $\mu\text{V}$ (30 mV), 10 $\mu\text{V}$ (300 mV), 100 $\mu\text{V}$ (3 V)
Solartron 1255B	10 $\mu\text{Hz}$ - 1 MHz	0-3 V	1 $\mu\text{V}$ (30 mV), 10 $\mu\text{V}$ (300 mV), 100 $\mu\text{V}$ (3 V)
Solartron 1252a	10 $\mu\text{Hz}$ - 300 kHz	0-3 V	1 $\mu\text{V}$ (30 mV), 10 $\mu\text{V}$ (300 mV), 100 $\mu\text{V}$ (3 V)

#### Analysis

The frequency response ranges of the different processes occurring at the anode and cathode of the used type of cells are summarized in Table 3.5. Additionally, the equivalent electric circuit elements which were used for the impedance modeling are shown. The considered equivalent electric circuit is based on the work by Leonide et al. [101] and Njodzefon et al. [89, 102], with the simplification that a RQ-element is used to represent the diffusion process in the anode substrate instead of a Warburg element. 'Also, due to the high air flow rate at the cathode and the overall cathode thickness of  $<60\text{ }\mu\text{m}$  gas diffusion at the oxygen electrode [ $P_{\text{OD}}$ ] was neglected' [89]. To carry out the impedance spectra analysis, the Python based software RAVDAV [103] was used. The

software allows presenting the data in form of e.g. a DRT plot, conducting Kramers-Kronig relations for data validation and conducting CNLS fits to model the measured impedance data with equivalent electric circuits.

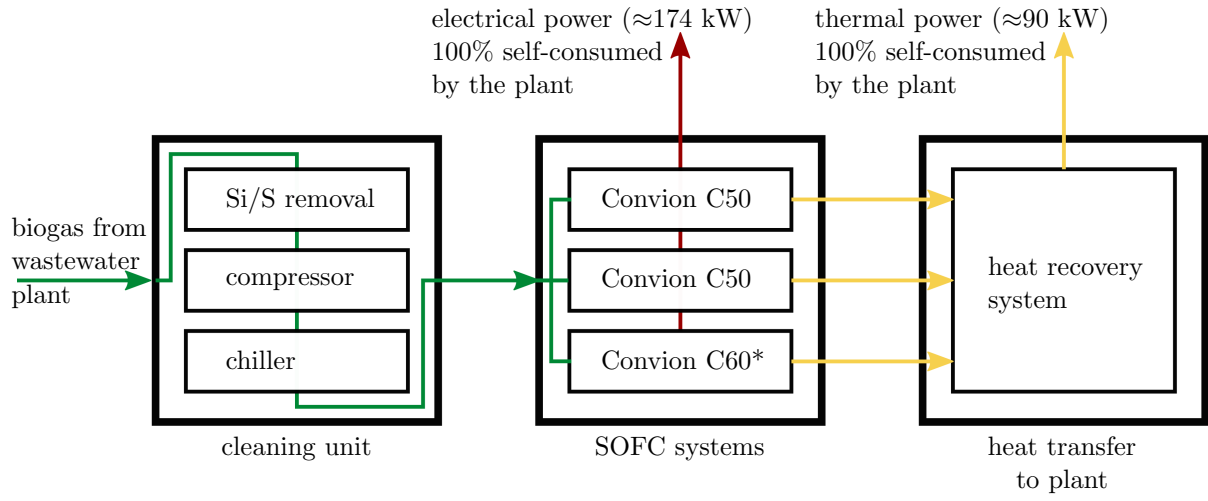
process symbol	equivalent element	frequency range	physical process description
	(L)	-	inductance of the test equipment
$R_s$	(R)	-	ohmic losses (serial resistance) across the cell (mainly electrolyte)
$P_{FP}$	(RQ)(RQ)	50-1 kHz	anode electrochemical oxidation coupled with ionic transport in the anode
$P_{OP}$	(G)	10-300 kHz	electrochemical charge transfer and diffusion at the cathode
$P_{FD}$	(RQ)	10-50 Hz	gas diffusion at the anode
$P_{FC}$	(RQ)	1-10 Hz	gas conversion at the anode
$P_{FR}$	(RQ)	0.1-1 Hz	hydrocarbon fuel reforming at the anode

**Table 3.5:** Equivalent circuit elements for the impedance fitting with corresponding frequency ranges of the considered processes occurring at the anode and cathode of the investigated cells. Adopted from reference [89, 101, 102, 104].

## 3.2 Biogas fueled SOFC system site

The biogas fueled SOFC system site is installed at the SMAT Collegno wastewater plant close to Turin in Italy. The SOFC system site can be divided into three sections as illustrated in Figure 3.6. In the first section the biogas delivered from the wastewater plant is compressed, cleaned by impregnated activated carbon filters and cooled. The filters are designed for removing the main wastewater biogas impurities sulfur and siloxanes. The second part of the plant consists of two C50 SOFC systems and one C60 SOFC system from the company Convion [105]. The electric net power output range of each system is between 40 kW and 60 kW, respectively. A heat recovery is included in the systems. By the end of 2019, the two Convion C50 systems have been in operation, while the Convion C60 system is intended to be installed in 2020. The two C50 systems differ only in the implemented SOFC stack technology and stack manufacturer supplier. The produced electricity is 100 % self-consumed by the wastewater treatment plant. The

SOFC system and plant data are monitored by different sensors at various locations on the site. More detailed descriptions about the setup and the design of the SOFC site are given in literature [106, 107].



\* currently not in operation/installed (planned to be installed in 2020)

**Figure 3.6:** Schematic setup of the biogas fueled SOFC site at the SMAT Collegno wastewater plant close to Turin in Italy.

# 4 Method development for predicting H<sub>2</sub>S effect on cell performance

**Comment:** Sections 4.1, 4.2 and 4.4 are based on the work which was presented at the 16<sup>th</sup> International Symposium on Solid Oxide Fuel Cells (SOFC-XVI), Kyoto, September 2019. As part of the conference the corresponding manuscript was published in the Ecs Transactions, 91(1):511–521, 2019 [33]. The support of the co-author is gratefully acknowledged. The paragraphs which are framed by double quotes ("") are originally from the manuscript.

An initial understanding of the effects of the impurities present in the biogas (see Table 2.2) like for example H<sub>2</sub>S on the SOFC performance is beneficial for successful operation of biogas fueled SOFC systems. As described in Section 2.3.3 a broad range of H<sub>2</sub>S studies are reported in literature. In this chapter emphasis is made on H<sub>2</sub>S poisoning effects from a different point of view. In this chapter an alternative H<sub>2</sub>S testing procedure on cell level is introduced for estimating and predicting the cell performance loss caused by H<sub>2</sub>S. One advantage of this procedure is the reduction of testing time and a more gentle handling of the tested cell as described in more detail in the following sections.

## 4.1 iV-curve sulfur poisoning

As described in Section 2.3.3 the common procedure for investigating the poisoning effects of the biogas impurity sulfur on the SOFC performance is to increase the H<sub>2</sub>S concentration in the fuel stepwise at different current densities (see Figure 2.4). The result is a cell voltage drop ( $\Delta U$ ) as function of the amount of sulfur present in the fuel stream and the applied current density.

This time consuming test procedure might result in a high permanent anode performance loss due to chemisorption of the sulfur at the anode nickel surface. The permanent anode

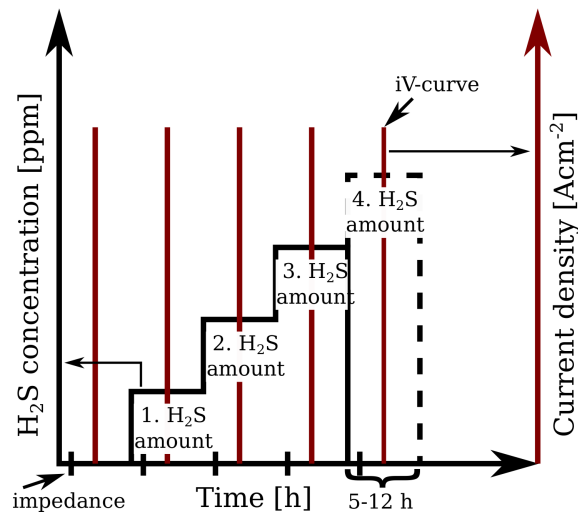


**Figure 4.1:** Experimental procedure of the short term sulfur poisoning tests at 850 °C (for gas compositions see Table 4.1).

performance loss caused by sulfur is dependent on the sulfur exposing time (see Section 2.3.3). By considering the test procedure illustrated in Figure 4.1 the sulfur exposing time can be minimized in comprising to the standard procedure (compare with Figure 2.4). This results in a smaller permanent cell performance loss. The sulfur concentration in the fuel stream is increased stepwise and at each sulfur concentration an iV-curve is conducted. This test procedure was carried out for four different fuel compositions including two different  $H_2$  in steam compositions (test (a),(b)) plus the carbon containing fuels  $CH_4$  (test (c)) and pre-mixed biogas (test (d)). Additionally, the total anode flow rate was  $24\text{ L h}^{-1}$  for test (a) while the total flow rate was  $10\text{ L h}^{-1}$  for test (b) until test (d). The detailed test specifications are provided in Table 4.1.

The recorded iV-curves as function of the sulfur concentration are shown in Figure 4.2. The OCVs of the iV-curves fueled with with  $H_2$  and steam (test (a), (b)) were not effected by the presents of sulfur. In this tests the OCVs stayed constant for all sulfur concentrations. This was expected because at OCV no catalytic reactions are taking place. Whereas during the supply of carbon containing fuels (test (c), (d)) at OCV the catalytic reforming reactions (Eq. 2.4, 2.6, 2.8) are occurring. In these tests the OCV decreased with increasing sulfur concentration. This OCV change (based on the Nernst eq. 2.21) is caused by the change of the anode gas composition because the  $CH_4$  reforming rate decreases with increasing sulfur amount. In comparison to the not poisoned case (sulfur free) a lower  $CH_4$  reforming rate results in a smaller share of  $H_2$  and CO at the anode.

In all four tests the increasing sulfur concentration resulted in a decreasing slope of the iV-curves and a decreasing maximum current density. This dependencies were larger during the carbon containing fuel tests ((c), (d)) in comparison to the H<sub>2</sub> in steam tests ((a), (b)). Considering the fact that the slope of the iV-curve shows the ASR of the cell (see Eq. 2.22) the results confirm that the electrochemical reactions were poisoned by sulfur as described in Section 2.3.3. Additionally, the lower fuel flow rate and the smaller share of H<sub>2</sub> of test (b) in comparison to test (a) results in an earlier bending down of the iV-curves at high current densities. Due to this fact the fuel starvation occurs at lower current densities for test (a) in relation to test (b) due to less available H<sub>2</sub> in the fuel even for the iV-curves recorded with sulfur free fuel (0 ppm H<sub>2</sub>S, black circles).

In case of the H<sub>2</sub> tests, the highest slope decrease occurred by increasing from 0 ppm H<sub>2</sub>S to 2 ppm H<sub>2</sub>S. Afterwards the slope change was minor during further increase of the H<sub>2</sub>S concentration. In other terms the H<sub>2</sub>S poisoning effect was saturating. Concluding that the greatest poisoning effects taking place already at low H<sub>2</sub>S concentrations. Similar tendencies are reported in literature [52] from H<sub>2</sub> studies using the conventional H<sub>2</sub>S poisoning tests at steady current density and even with other cell types. Significant

**Table 4.1:** Anode gas composition, anode total flow and applied sulfur concentration of the short term poisoning tests. Air was supplied at the cathode and tests were conducted at a operation temperature of 850 °C. Adapted from reference [33].

test	gas composition	total flow [L h <sup>-1</sup> ]	H <sub>2</sub> S Amount [ppm]
(a) H <sub>2</sub> -test (high flow)	82 vol% H <sub>2</sub> , 18 vol% H <sub>2</sub> O	24	0, 2, 10, 20
(b) H <sub>2</sub> -test	47 vol% H <sub>2</sub> , 53 vol% H <sub>2</sub> O	10	0, 2, 10, 20, 90
(c) CH <sub>4</sub> -test	29 vol% CH <sub>4</sub> , 13 vol% H <sub>2</sub> , 58 vol% H <sub>2</sub> O	10	0, 2, 10, 20
(d) Biogas-test	50 vol% biogas (60 vol% CH <sub>4</sub> , 40 vol% CO <sub>2</sub> ), 10 vol% H <sub>2</sub> , 40 vol% H <sub>2</sub> O	10	0, 2, 10, 20

diffusion losses are reflected by the bend down of the iV-curves in the  $H_2$ , the  $CH_4$  and biogas tests (see Figure 4.2(b)-(d)) with the same total flow rate of  $10\text{ L h}^{-1}$ . Additionally, in the hydrocarbon fuel tests (see Figure 4.2(c)-(d)) the starvation was caused by the small share of  $H_2$  due to the poisoning of the reforming reactions.

"The obtained results of the iV-curves were further evaluated in terms of the more common approach of determining the immediate voltage drops ( $\Delta U$ ) and *ASR* increase as consequence of the addition of sulfur. This was achieved by subtracting iV-curves under  $H_2S$  from the one without  $H_2S$  in the fuel. The results are shown in Figure 4.3 as a function of the current density. The data were taken from the measured iV-curves (see Figure 4.2) after linear interpolation as a first approximation."

Using hydrogen/steam fuel in the regime where no fuel starvation occurs (linear range in Figure 4.2 (a), (b)), the resulting cell voltage drops (delta voltage) are superimposed, i.e. the poisoning effect is the same (line (a) and (b) in Figure 4.3). The sulfur coverages as calculated according to Equation 2.16 were 0.73 and 0.76 for test (a) and (b), respectively. Obviously, these two values are very similar leading to similar degree of poisoning of the electrochemical reaction. These results indicate that the total flow rate in the range between  $24\text{ L h}^{-1}$  (test (a)) and  $10\text{ L h}^{-1}$  (test (b)) has no influence on the degree of  $H_2S$  poisoning because the ratio of  $p(H_2S)$  and  $p(H_2)$  is the determining parameter and not the flow rate. As soon as the regime of fuel starvation is reached, the poisoning effect becomes more significant, not only affecting the anode reaction but also fuel conversion and diffusion leading to the bending down of the iV-curves."

The voltage drops of test (c) ( $CH_4$ -test) and (d) (biogas-test) increased steeply with increasing current density, which points to a critical effect of fuel starvation with progressing poisoning of the reforming reaction caused by the low flow rate of hydrogen and CO. The voltage drop increased more in test (d) than in test (c). The reason for this could be the lower hydrogen amount (10 % vs. 13 %, respectively) and the larger share of  $CO_2$  in the initial fuel stream of test (d). For the tests with  $CH_4$  and biogas (test (c) and (d)), two poisoning regimes can be distinguished as function of current density, one at low current density (more flat slope) and one at high current density (steep slope). The poisoning regime at lower current densities (more flat slope) is observed in the  $H_2$  fuel as well (test (a) and (b))."

”These two regions become even more apparent when calculating the increase of *ASR* due to H<sub>2</sub>S addition [108]. In Figure 4.4 the immediate *ASR* value increases as a function of the current density are shown using the results obtained in this study. The curves were derived by taking the gradient of the immediate voltage drop curves shown in Figure 4.4 and applying a Savitzky-Golay filter for smoothing the data.”

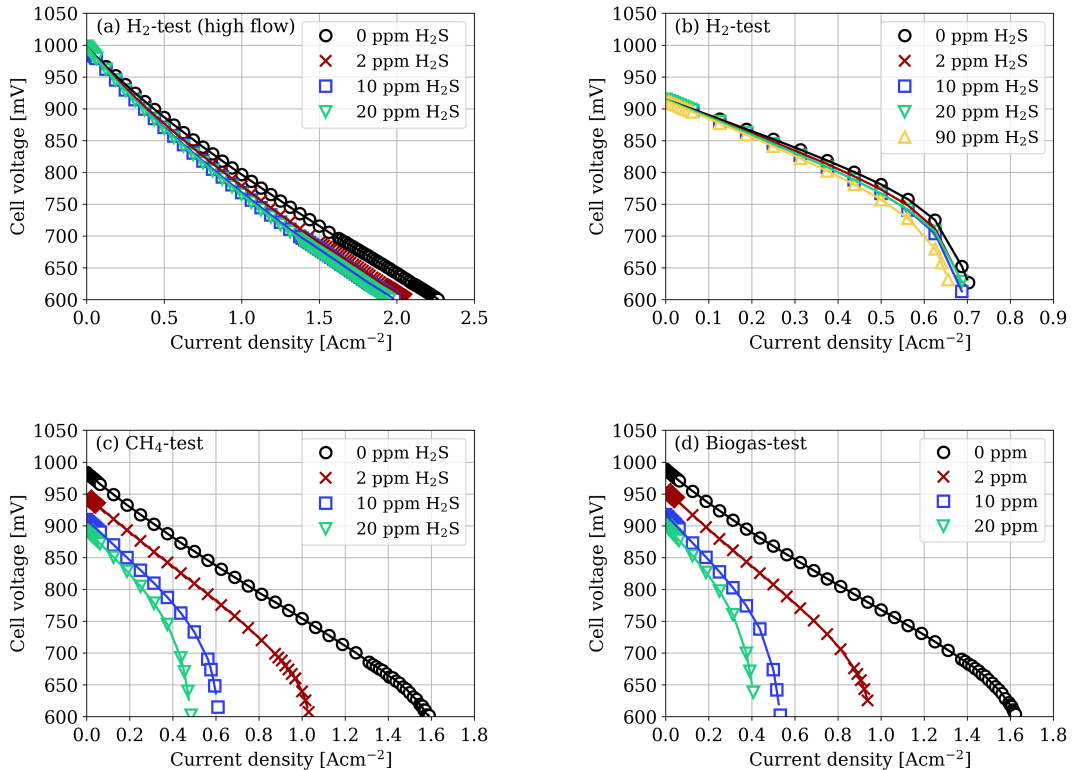


**Figure 4.2:** Linear interpolated iV-curves with various sulfur concentrations (0 ppm–90 ppm) fueled with (a) H<sub>2</sub>, (high flow), (b) H<sub>2</sub> (low flow), (c) CH<sub>4</sub> and (d) pre-mixed biogas at 850 °C and 140 L h<sup>-1</sup> air on the cathode side. Further specifications are given in Table 1. Adapted from reference [33].

”There has been a discussion of the effect of current on the sulfur poisoning, with arguments in favor of current [60, 66, 109, 110, 111, 112, 113] and against an effect [114, 115]. Interestingly, when looking at the region where the iV-curves are linear (compare to Figure 4.2(c) and (d)), there is basically no change of the immediate *ASR* increase as function of current density. In Figure 4.4 the curves (a) and (b) show no change of the *ASR* up to current density of ca. 0.5 A cm<sup>-2</sup> and curve (c) up to ca. 0.2 A cm<sup>-2</sup>.

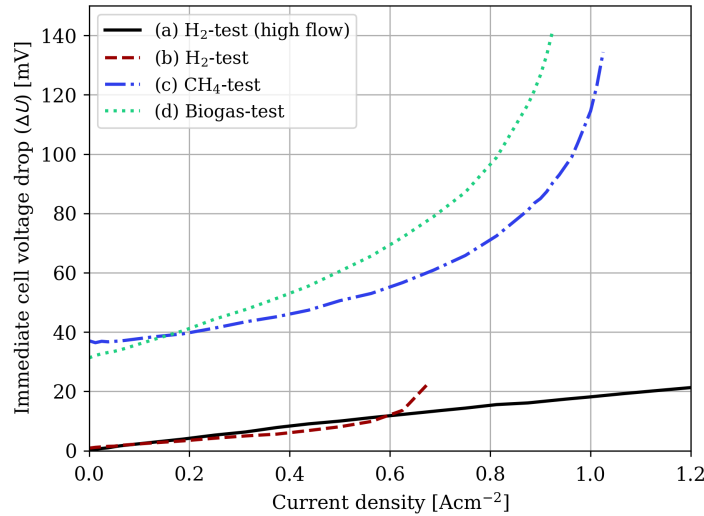


**Figure 4.3:** Immediate voltage drops for 2 ppm  $H_2S$  in relation to 0 ppm  $H_2S$  as a function of the current density in fuels (a) to (d). The curves were derived from the interpolated iV-curves shown in Figure 4.2. Adapted from reference [33].

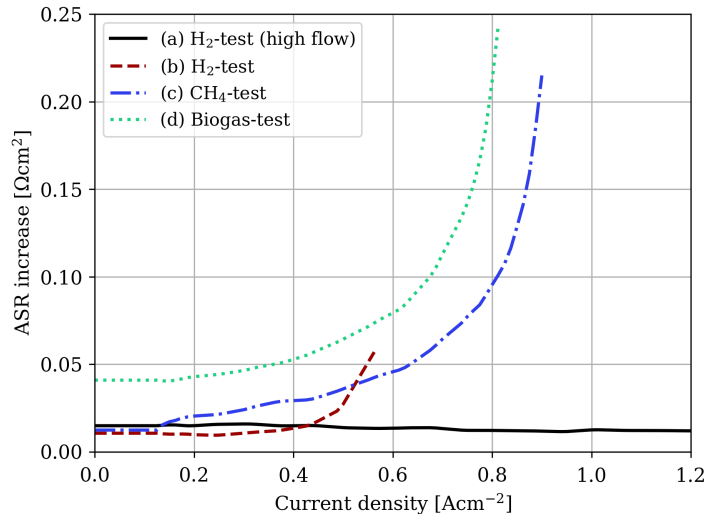


**Figure 4.4:** Area specific resistance (ASR) increase for 2 ppm  $H_2S$  in relation to 0 ppm  $H_2S$  as a function of the current density in fuels (a) to (d). Curves were derived by taking the gradient of the immediate voltage drop curves shown in Figure 4.3. Furthermore, a Savitzky-Golay filter was applied for smoothing the data. Adapted from reference [33].

On the other hand, the ASR values increase steeply at higher current density (see Figure 4.4). Hagen et al. [108] found that current has no effect on the increase of ASR due to  $H_2S$  poisoning in the low-current region, where the poisoning effect is mainly due

to poisoning of the anode polarization. However, at higher current density, where fuel starvation due to the poisoning of the reforming reaction occurs more severely, there is an increase of  $ASR$  with increasing current density. The results in this study, which were obtained through a different approach, completely support these findings.”

## 4.2 Verification of the $H_2S$ iV-curve approach

”The current study suggests that it is possible to determine cell voltage drops and increase of  $ASR$  due to  $H_2S$  poisoning by analyzing iV-curves (see Figures 4.3 and 4.4), which is significantly faster than the conventional approach that measures under steady state conditions – as long as reversible changes occur.”

”In order to validate the results and compare to values obtained with the traditional poisoning tests, a test with pre-mixed biogas as fuel was carried out following the conventional steady-state approach with a constant current density of  $0.5\text{ A cm}^{-2}$ . Figure 4.5 shows the cell voltage and the serial resistance ( $R_s$ ) and polarization resistance ( $R_p$ ) which were determined from EIS spectra over time. In the absence of sulfur, the cell voltage was 871 mV and thus close to the expected value of 868 mV from the iV-curve (see Figure 4.2 (d)). After addition of 2 ppm  $H_2S$  the cell voltage dropped (for values see Table 4.2) by 61.9 mV. This value is very close to the one calculated from the iV-curves; the relative error is only 2.2% (see Table 4.2, Figure 4.3). This confirms the validity of the cell voltage drop values obtained with the faster iV-curve approach.”

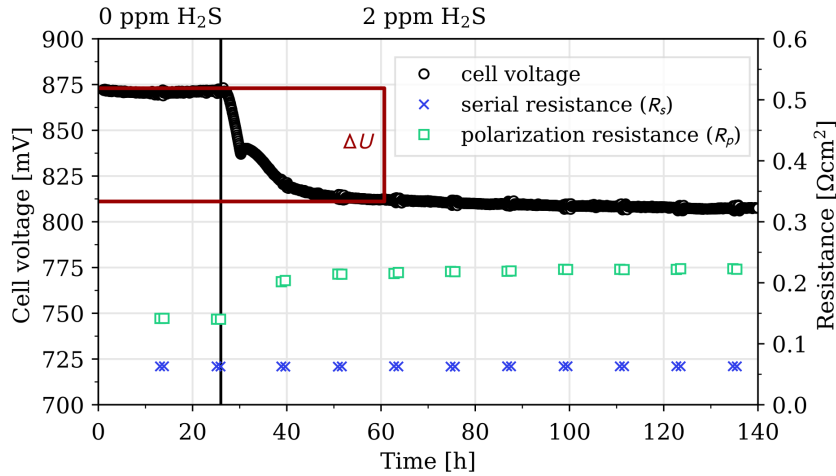


**Figure 4.5:** Steady state test with pre-mixed biogas at  $0.5 \text{ A cm}^{-2}$ ,  $850^\circ\text{C}$ . Cell voltage (black circle, left-axis) and serial resistance  $R_s$  (cross, right-axis), polarization resistance  $R_p$  (square, right-axis) before and after addition of 2 ppm  $H_2S$ . Adapted from reference [33].

**Table 4.2:** Expected (see Figure 4.2) and measured (after 61 hours of test, Figure 4.5) cell voltage drop after addition of 2 ppm  $H_2S$  to pre-mixed biogas fuel at  $850^\circ\text{C}$  and  $0.5 \text{ A cm}^{-2}$ . Adapted from reference [33].

expected voltage drop [mV]	60.9
expected voltage drop [mV]	61.9
relative error [%]	2.2

”The  $R_p$  and  $R_p$  values for the EIS recorded over time as presented in Figure 4.5 show that  $R_p$  is increasing when  $H_2S$  is added to the fuel, while  $R_s$  remains constant. This is a clear indication of a reversible poisoning effect under the applied conditions. In Figure 4.6, selected EIS spectra are shown. They confirm that the serial resistance remained constant. The  $R_p$  increased and two main contributions to this increase can be clearly identified (see Figure 4.6(b)). There is an increase of impedance at lower frequencies (4 Hz fuel conversion/diffusion) and one at higher (800 Hz, fuel electrode polarization) frequencies. The result confirms the expectations from the iV-curves in Figure 4.2(d), where a current density of  $0.5 \text{ A cm}^{-2}$  is located in a regime where the anode reaction is poisoned and also fuel starvation occurs due to poisoning of the reforming reaction.”

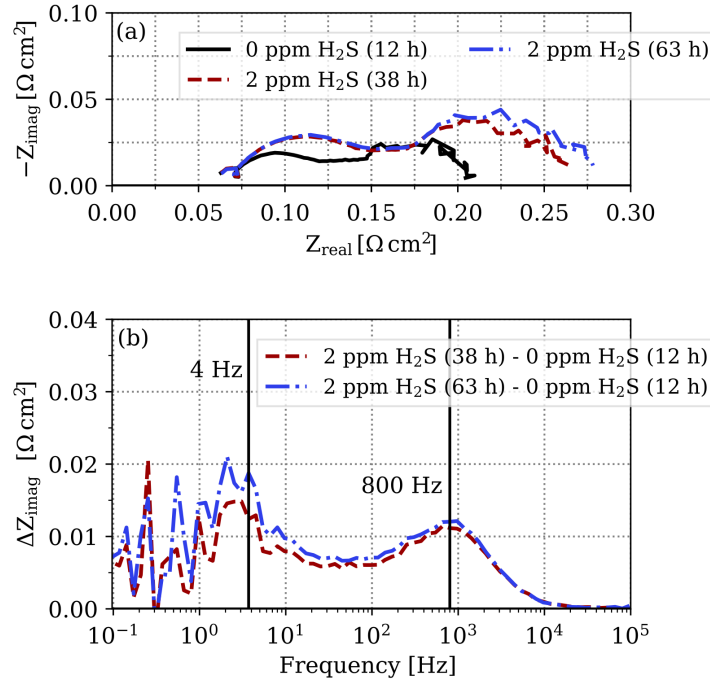


**Figure 4.6:** Nyquist (a) and differences (b) plot (bode plot) of the pre-mixed biogas before and after addition of 2 ppm  $\text{H}_2\text{S}$  sulfur in pre-mixed biogas, 850 °C, 0.5 A  $\text{cm}^{-2}$ . Adapted from reference [33].

### 4.3 $\text{H}_2\text{S}$ voltage drop forecasting of cells with the same material composition

The approach of analyzing iV-curves in the current study proved to be a fast approach leading to the same results as compared to conventional steady state testing, as validated with the test shown above (see Figure 4.5). A further advantage would be to predict the  $\text{H}_2\text{S}$  voltage drops of cells with the same anode material compositions without the need of poisoning tests of all cells with  $\text{H}_2\text{S}$ . In the following, the  $\text{H}_2\text{S}$  voltage drops of cells with the same anode compositions (referred to as 2011 test and 2014 test) are predicted considering the fast iV-curve approach test of the current study. With the 2011 and 2014 cells,  $\text{H}_2\text{S}$  poisoning tests were carried out using the conventional steady-state approach (see Table 4.4). For this evaluation, two cell tests (same anode cell composition) using  $\text{CH}_4$  containing fuel were selected because the effect of  $\text{H}_2\text{S}$  is larger as compared to tests in hydrogen fuel. Furthermore, the presence of sulfur impurities in methane containing

fuel is a more realistic case. The two selected test parameters are listed in Table 4.3. As mentioned, these poisoning tests were carried out at only one constant current density at a time and addition of one or a few  $H_2S$  concentrations.

**Table 4.3:** Selected tests from previous studies for studying the usability of the prediction method with the fast iV-curve method of the expected immediate voltage drops of the  $CH_4$ -test for other cells.

test year	cell composition (anode/electrode/cathode)	current densities [ $A\text{ cm}^{-2}$ ]			reference literature
		2 ppm $H_2S$	10 ppm $H_2S$	20 ppm $H_2S$	
2011	Ni-ScYSZ/ScYSZ/LSCF:CGO	0, 0.25, 0.5,	0, 0.25, 0.5, 1	0, 0.25, 0.5	[108]
2014	Ni-ScYSZ/ScYSZ/LSC:CGO	0	0	0	[21]

In order to be able to predict  $\Delta U$  using the iV-curves recorded in the presence and absence of  $H_2S$  from the current study, the initial iV-curves of the two cells in question are needed (see Figure 4.7(a)) together with the iV-curves from the present study. The initial performances of the cell in the present study and cell test 2014 are very similar in terms of the ASR (slope of the iV-curve). Only  $R_p$  seems slightly larger in the present cell (see Figure 4.7(b)). On the other hand, the cell 2011 test showed a significantly larger ASR (steeper slope red dashed line, Figure 4.7 bottom), mainly attributed to the serial resistance  $R_s$  (see red dashed line, Figure 4.7(b)). This is mainly caused by the different cathode material of cell 2011 in comparison to the cell in the present study and cell 2014. In order to be able to use the iV-curves in presence of  $H_2S$  from this study to predict  $\Delta U$  for the two other cells, these differences of initial cell performance have to be taken into consideration. As the  $H_2S$  poisoning affects the anode of the SOFC, this contribution was extracted. Below only the performance in relation to the anode was considered because the addition of  $H_2S$  affects the anode.

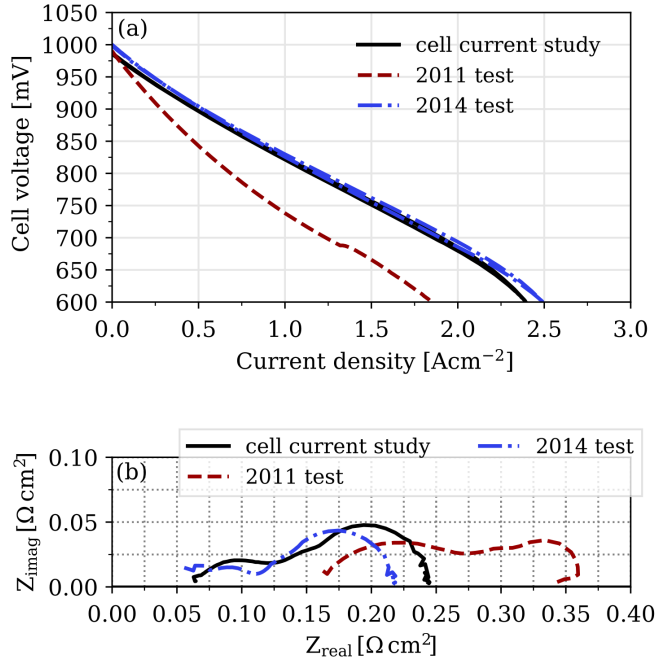


**Figure 4.7:** Nyquist impedance plot at OCV (a) and iV-curves (b) illustrating the initial cell performance ('finger print') of the cells from the present study (black lines) together with cell test 2011 (red dashed lines) and cell test 2014 (blue dashed dotted lines) for prediction of  $\Delta U$ . Fuel supply anode: 20 %  $H_2O$  in  $H_2$  (all in absence of  $H_2S$ ), Cathode supply air, Operation temperature 850 °C.

One quantity for estimating the anode cell performance is the active anode area ( $A_{\text{active}}$ ) [116, 117, 118]. In the following, the active anode area represents the nickel active area ( $CH_4$  reforming process) and the active anode area of the triple phase boundary (electrochemical reaction). As higher the value of the active anode area the better is the cell performance. Equation 4.1 assumes that the voltage drop ( $\Delta U$ ) is proportional to the active anode cell area and the supplied sulfur stream to the cell ( $\dot{n}_{H_2S}$ ).

$$\Delta U \approx A_{\text{active}} \dot{n}_{H_2S} \quad (4.1)$$

According to Equation 4.1, the voltage drop caused by  $H_2S$  is low if the value of the active anode area is low (low anode cell performance) because less active area is available which can be effected by the sulfur. In other terms, the addition of sulfur results in a high initial voltage drop for a cell with a high anode performance (high active anode area

value). Equation 4.2 defines that the anode resistance  $R_{\text{anode}}$  is inversely proportional to the value of the active anode area. A high active anode area value (high anode cell performance) results in a small initial  $R_{\text{anode}}$  value.  $R_{\text{anode}}$  is beside  $R_{\text{cathode}}$  one part of  $R_p$  and can be determined by fitting the impedance data with an equivalent circuit model.

$$A_{\text{active}} \approx \frac{1}{R_{\text{anode}}} \quad (4.2)$$

Considering Equation 4.1 and 4.2 the voltage drop ( $\Delta U$ ) is then proportional to the initial anode resistance  $R_{\text{anode}}$  and the sulfur supply  $\dot{n}_{\text{H}_2\text{S}}$  to the cell (see Eq. 4.3).

$$\Delta U \approx \frac{1}{R_{\text{anode}}} \dot{n}_{\text{H}_2\text{S}} \quad (4.3)$$

Therefore, the prediction of the H<sub>2</sub>S voltage drops of a different cell was done by considering only the initial  $R_{\text{anode}}$  values of the cells. Furthermore, a linear dependency is assumed and only the reversible H<sub>2</sub>S poisoning effect is considered. The simplified dependency between the immediate voltage drop ( $\Delta U$ ) of cell 1 and cell 2 in terms of the initial  $R_{\text{anode}}$  values of the cells is then defined in Equation 4.4. This dependency is derived from Equation 4.3 and the fact the sulfur stream to the cell is the same for both cell tests.

$$\frac{R_{\text{anode}}^{\text{cell 2}}}{R_{\text{anode}}^{\text{cell 1}}} = \frac{\Delta U^{\text{cell 1}}}{\Delta U^{\text{cell 2}}} \quad (4.4)$$

In this study the initial magnitude of  $R_{\text{anode}}$  was determined by impedance fitting from measurements carried out during the ‘finger prints’ with 20% H<sub>2</sub>O in H<sub>2</sub> on the anode side and air on the cathode side at 850 °C before the sulfur poisoning tests. The used impedance model for determining  $R_{\text{anode}}$  is described in Section 3.1.6. The determined  $R_{\text{anode}}$  values of the three cells and the corresponding ratios according to Equation 4.4 are given in Table 4.4.

**Table 4.4:** Initial  $R_{\text{anode}}$  values of the current study plus the 2011 test and 2014 test cells determined by impedance fitting (corresponding impedance data are shown in Figure 4.7).

	$R_{\text{anode}} [\Omega \text{ cm}^2]$	$R_{\text{anode}} \text{ ratio (see Eq. 4.4)}$
<b>cell current study</b>	0.138	-
<b>2011-test</b>	0.211	1.53
<b>2014-test</b>	0.142	1.03

In Figure 4.8 the expected immediate voltage drop according to the iV-curves (Figure 4.2(c)) for the sulfur concentrations 2 ppm, 10 ppm, and 20 ppm as function of the current density are shown. Furthermore, the points in figure 10 represent the steady state measured voltage drops from the cell tests 2011 and 2014 including error bars if more than one test was available at the specific conditions (see Table 4.3). The steady state measured voltage drops for the cell tests listed in Table 4.3 were determined according to Equation 4.4, by considering the initial anode performances (see Table 4.4).

The results of the steady state tests were best predicted for tests within a safe operation window which is the linear range of the curves. This is the case in the presence of 2 ppm  $H_2S$  (solid curve and circles, Figure 4.8) up to a current density of  $0.8 \text{ A cm}^{-2}$  and in the presence of larger  $H_2S$  concentrations for the region at lower current densities ( $<0.5 \text{ A cm}^{-2}$  for 10 ppm and  $<0.3 \text{ A cm}^{-2}$  for 20 ppm  $H_2S$ , see Figure 4.8). Particularly the results of all three sulfur concentrations at  $0.25 \text{ A cm}^{-2}$  (linear range) were well predicted by the iV-curve analysis. The relative errors between the predicted voltage drops derived from the iV-curves and the steady state tests illustrated in Table 4.5 are between 1.2 % and 20.5 % and thus rather small considering the simplified assumptions mentioned previously to compare test results from cells with different initial cell performance.



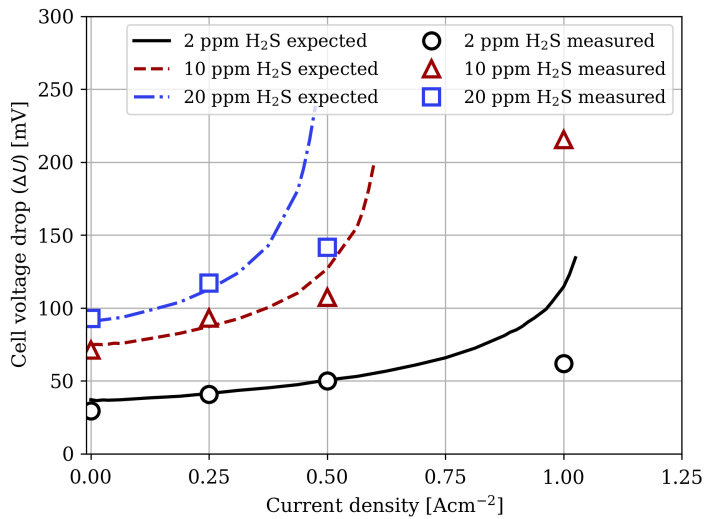


**Figure 4.8:** Immediate voltage drop determined from the iV-curves in this study (lines) and measured voltage drops from 2011 plus 2011 cell tests (see Table 3) recorded with the steady state method (data points).

When increasing the  $H_2S$  concentration – particularly in combination with high current density - the assumed linear dependency between the  $H_2S$  voltage drop and the anode resistance for deriving Equation 4.4 is reaching a limit. Because in this current density ranges the dependency between these two parameters is not linear anymore. Furthermore, the fuel starvation effect due to the large degree of reforming reaction poisoning is a major consequence and has to be included for a more precise prediction. The presented prediction method is valid for the linear range of the iV-curves. The prediction limit can be deduced from the delta cell voltage (flat slope) and the delta ASR (zero slope) relation to the current density.

**Table 4.5:** Relative error between immediate voltage drop determined from the iV-curves and measured voltage drops from previous steady state tests carried out at DTU Energy (see Figure 4.8 and Table 4.3).

	relative error [%]		
	2 ppm $H_2S$	10 ppm $H_2S$	20 ppm $H_2S$
0 $A\text{ cm}^{-2}$	20.5	4.8	1.4
0.25 $A\text{ cm}^{-2}$	1.2	6.6	4.0
0.5 $A\text{ cm}^{-2}$	1.3	not in linear range	
1 $A\text{ cm}^{-2}$		not in linear range	

## 4.4 Conclusion

”A new approach of testing SOFC in regard to sulfur poisoning was introduced. This approach is significantly less time consuming as compared to the traditional steady state approach of starting SOFC operation, adding of a certain H<sub>2</sub>S concentration, observing a steady state response, removing the H<sub>2</sub>S and awaiting recovery, followed by the H<sub>2</sub>S addition of the next concentration and later on other variations of operating parameters such as current density. In this study it was demonstrated that a fast approach is to compare iV-curves recorded at a certain H<sub>2</sub>S concentration in the fuel with sulfur free conditions. The comparison of the iV-curves with and without sulfur allows for the calculation of the well-known voltage drop due to H<sub>2</sub>S poisoning. The values are the same as obtained by the traditional steady state approach. Therefore, from recording iV-curves at a set of relevant conditions, the initial H<sub>2</sub>S cell voltage drop ( $\Delta U$ ) can be retrieved and used to define safe operating windows in the presence of sulfur impurities in the fuel. Because this method is much faster than the conventional steady state approach, overall cell degradation is much less probable to interfere with the actual poisoning effects.”

The approach can also be used for predicting the H<sub>2</sub>S voltage drops of cells with the same anode material composition, when taking into consideration potential differences of initial performance. In that way, the cell voltage drops as measure for the degree of H<sub>2</sub>S poisoning can be obtained as function of operating parameters. This has the big advantage that there is no need for poisoning tests estimating H<sub>2</sub>S voltage drops of cells with the same material composition. Only an initial iV-curve in H<sub>2</sub> is needed.

”The magnitudes of the voltage drops were seen to change with current density. In addition to a general increase of the voltage drop with increasing current density, also the differentiation between two major poisoning regimes, one at low and one at higher current densities was possible. These regimes are related to the poisoning of the anode reaction and the increase of fuel starvation due to poisoning of the methane reforming reaction, respectively. Apart from evaluating the cell voltage drop as parameter for the degree of H<sub>2</sub>S poisoning, also the increase of *ASR* was evaluated based on the iV-curves. It was shown that the *ASR* increase due to H<sub>2</sub>S poisoning is independent on the current density as long as there is no severe fuel starvation. In the operating regime of severe fuel starvation, the *ASR* increase grows with increasing current density.”

# 5 In-situ analysis of pre-mixed landfill gas operation

To gain an initial understanding of the anode processes taking place during landfill gas fueled SOFC operation, an impedance parameter study was conducted, starting by identifying the different frequency ranges of the processes taking place during landfill gas fueled operation. In the next steps, the dependency of the impedance on flow rate and current density were analyzed. Finally, the impedance response change due to varying CH<sub>4</sub> content in the landfill gas is investigated.

## 5.1 Anode and cathode process identification

To identify the different processes, a 'finger print' was conducted at 750 °C as described in Section 3.1.5. Additionally, two further conditions were tested (see Table 5.1) to determine the impedance response of the reforming process during pre-mixed landfill gas supply. The first one is a mixture of 30 % CH<sub>4</sub> plus 70 % CO<sub>2</sub> and the second one of 9 % H<sub>2</sub>O (steam) in H<sub>2</sub>. The second setting is chosen according to the theoretically produced steam (Gibbs free energy minimization) after reformation of the CH<sub>4</sub>+CO<sub>2</sub> mixture. The calculations were carried out with ElchDAT [33].

**Table 5.1:** Flow composition used to identify the reforming process in the impedance response.

anode supply	cathode supply	temperature
30 vol% CH <sub>4</sub> , 70 vol% CO <sub>2</sub> (20 L h <sup>-1</sup> )	air (140 L h <sup>-1</sup> )	750 °C
91 vol% H <sub>2</sub> , 9 vol% H <sub>2</sub> O (20 L h <sup>-1</sup> )	air (140 L h <sup>-1</sup> )	750 °C

In Figure 5.1, the impedance measurement results of the conducted 'finger print' at 750 °C and the extra conducted measurements described in Table 5.1 are shown. As the relative Kramers-Kronig residuals plot shows (see Figure 5.1(b)), the measurement

data have a lower quality due to noise in the measurements at the lowest and highest applied frequencies. Especially the low frequency noise was caused by the measurement setup. The Nyquist plot in Figure 5.1(a) indicates that  $R_s$  is the same for all tests except for the one where  $\text{CH}_4$  was used. The  $R_s$  value of the  $\text{CH}_4$  test is greater because the internal reforming of  $\text{CH}_4$  is an endothermic process and therefore the corresponding temperature decrease results in a higher serial resistance. Additionally, the polarization resistances of the tests with steam in  $\text{H}_2$  are decreasing with increasing steam content. These observations are in line with other experimental studies, e.g. [119]. As described by Mogensen et al. [120], the change in the polarization resistance is dependent on both the used raw materials and the fabrication process of the cell. Furthermore, the  $R_p$  values of the  $\text{O}_2$  cathode supply are smaller in comparison to the air cathode supply during the same anode fuel supply. Differences in the Nyquist plots during  $\text{H}_2\text{O}$  (steam) in  $\text{H}_2$  anode supply correspond to frequency changes around 1 Hz and 100 kHz, as shown

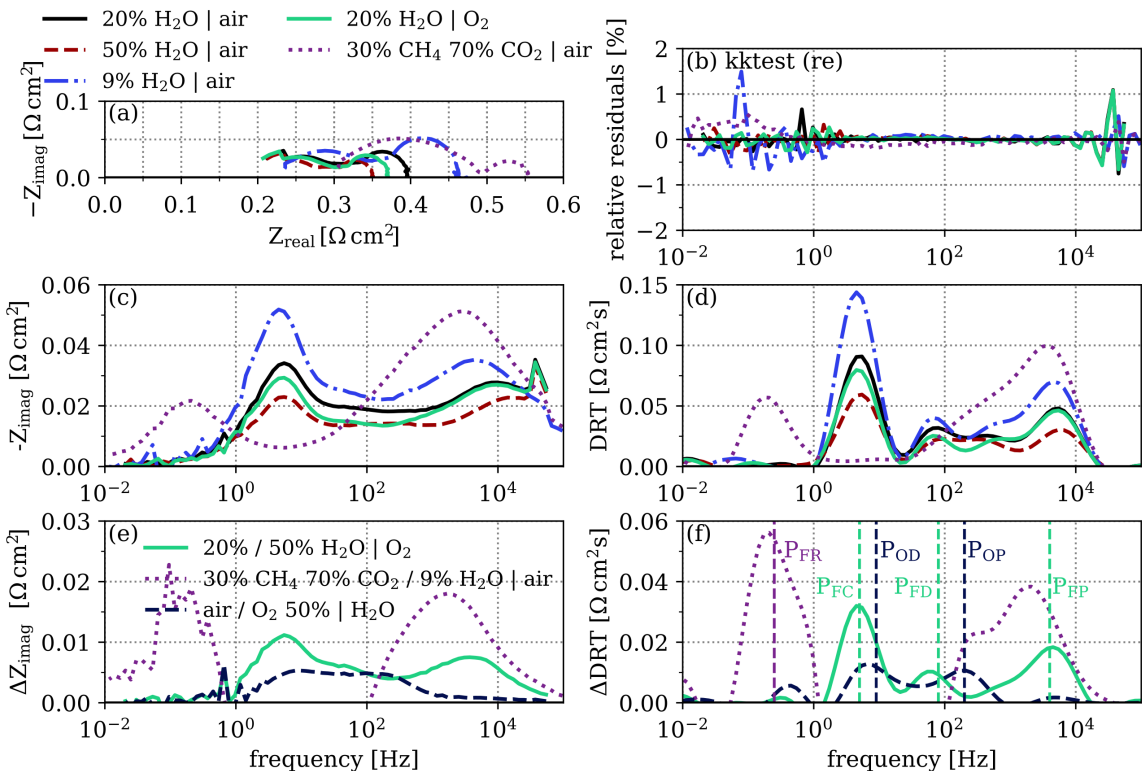


**Figure 5.1:** Selected impedance measurements of the initial finger print and pre-mixed biogas supply (see Table 5.1) for identification of the different processes. (a) Nyquist plot; (b) Kramers-Kronig data validation test; (c) Bode plot; (d) DRT plot; (e) Bode difference blot; (f) DRT difference plot. Operated at 750 °C.

by the Bode plot and DRT plot (see Figure 5.1(c) and (d)). For the CH<sub>4</sub>+CO<sub>2</sub> test, one peak at low frequency and one peak at high frequency are visible in the Bode and DRT plots (see purple dotted line Figures 5.1(c) and (d)).

The frequency ranges of the different anode and cathode processes can be identified by the use of Bode and DRT difference plots (see Figure 5.1(e) and (f)), as illustrated by Graves et al. [119]. The green line represents the difference between 20 % H<sub>2</sub>O (steam) in H<sub>2</sub> and 50 % H<sub>2</sub>O (steam) in H<sub>2</sub>. The amount of H<sub>2</sub>O (steam) present at the anode is effecting the frequency range between 1 Hz and 100 kHz, as shown in the Bode plot (see Figure 5.1(e)). This is in line with the observations discussed before for the normal Bode plot (compare with Figure 5.1(c)). The dashed blue line in Figure 5.1(e) represents the change between air and O<sub>2</sub> cathode supply during constant anode supply. The frequency range changes are occurring between 1 Hz and 10 kHz and are overlapping with the frequency range of the steam change at the anode. Differences between the impedance measurement of the CH<sub>4</sub>+CO<sub>2</sub> mixture and the 9 % H<sub>2</sub>O (steam) in H<sub>2</sub> (dotted purple line) are occurring in the low frequency range (<1 Hz) and the high frequency range (100 Hz-10 kHz) to 100 kHz. A sharper differentiation can be obtained by the DRT difference plot (see Figure 5.1(f)). The peaks of the three plots can be assigned to the anode and cathode processes described in Section 3.1.6. The three peaks of the difference plot of the steam concentration change at the anode (green line) correspond to the anode fuel conversion response ( $P_{FC}$ , 5 Hz), the anode fuel diffusion process ( $P_{FD}$ , 80 Hz) and the anode fuel polarization ( $P_{FP}$ , 40 kHz). The peak in the low frequency range of the purple dashed line represents the anode fuel reformation process during hydrocarbon fuel supply ( $P_{FR}$ , 0.25 Hz). The two cathode processes are represented by the two peaks of the dashed blue line, which are the oxygen diffusion process ( $P_{OD}$ , 9 Hz) and the oxygen polarization process ( $P_{OP}$ , 200 Hz). As explained in Section 3.1.6, the oxygen diffusion process is neglected in the analysis of impedance spectra, which were recorded during air supply on the cathode side.

## 5.2 Flow rate and current density variation

As a next step, the impedance response of pre-mixed landfill gas fueled SOFC as function of the total anode fuel rate and the applied current density are analyzed. The settings are shown in Table 5.2. The pre-mixed landfill gas composition was based on the real landfill gas composition and extra CO<sub>2</sub> was added to avoid carbon formation, as described in

Section 3.1.3. The total flow rate dependency investigations were conducted because the real landfill gas supplied tests (see Chapters 6 and 7) were recorded at a low total fuel flow rate ( $6 \text{ L h}^{-1}$ ), but the landfill gas  $\text{CH}_4$  content dependency (see Section 5.3) could only be investigated at high flow rates. The latter is caused by mass flow controller limitations in the test rig.

**Table 5.2:** Settings for the quantities flow rate and current density for analyzing the corresponding impedance response change during pre-mixed landfill gas supply.

quantity	step size	further settings
fuel flow rate [ $\text{L h}^{-1}$ ]	6; 10; 15; 20; 25; 30	temperature: $750 \text{ }^\circ\text{C}$ current density: $0 \text{ A cm}^{-2}$ (OCV)
current density [ $\text{A cm}^{-2}$ ]	0 (OCV); 0.125; 0.375; 0.5	temperature: $750 \text{ }^\circ\text{C}$ total flow rate: $6 \text{ L h}^{-1}$ anode fuel composition: 23 vol% $\text{CH}_4$ cathode fuel composition: air

The impedance measurements of the flow variation test are shown in a Nyquist plot (a) and DRT plot (b) in Figure 5.4. The serial resistance ( $R_s$ ) is increasing with increasing flow rate because the fuel is acting as a kind of cooling gas for the anode cell surface. With a higher fuel flow rate more heat can be transferred away from the cell. The lower cell temperature then causes a higher  $R_s$  value. Additionally, the polarization resistance ( $R_p$ ) first decreases and then increases again with increasing fuel flow rate. Furthermore, the second arc (low frequencies) is decreasing with increasing fuel flow rate. For a more detailed understanding about the processes which are dependent on the fuel flow rate a DRT difference plot is shown in Figure 5.4(b). The impedance response of three anode processes are mainly affected by the flow rate. In all three cases the resistance magnitude is more affected than the response frequency range. The highest effect of the fuel rate is recognized for the reforming process ( $P_{\text{FR}}$ ). The reforming process resistance is decreasing with increasing flow rate because more fuel for the reforming process is available. Additionally, also the fuel diffusion process ( $P_{\text{FD}}$ ) and fuel polarization process ( $P_{\text{FP}}$ ) are affected with a lower magnitude. For both processes the change in the DRT plot (see Figure 5.4(b)) is increasing with increasing fuel flow rate. This indicates that more diffusion in the anode substrate and more fuel polarization at the active sides of the anode are occurring with higher amounts of fuel present at OCV. In a next step, the impedance response measurements as a function of the applied current density is

analyzed. The corresponding Nyquist plot (a) and the DRT plot (b) are shown in Figure 5.3. In this case the  $R_s$  stays constant for all applied current density but the  $R_p$  varies with increasing current densities. Similar to the observations during the flow dependency analysis,  $R_p$  is first decreasing and then increasing again with increasing current density which is a similar behavior as observed during the flow dependency analysis (compare Figure 5.2(a)). This time the two processes fuel reforming ( $P_{FR}$ ) and fuel polarization ( $P_{FP}$ ) are changing with the change of current density as illustrated in Figure 5.3(b). In this case the resistance of the  $P_{FP}$  processes is decreasing with increasing current density because at higher current densities more electrochemical reactions are taking place at the active anode sides. Additionally, the  $P_{FR}$  frequency response is shifting to higher frequencies with increasing current density indicating that the reforming process

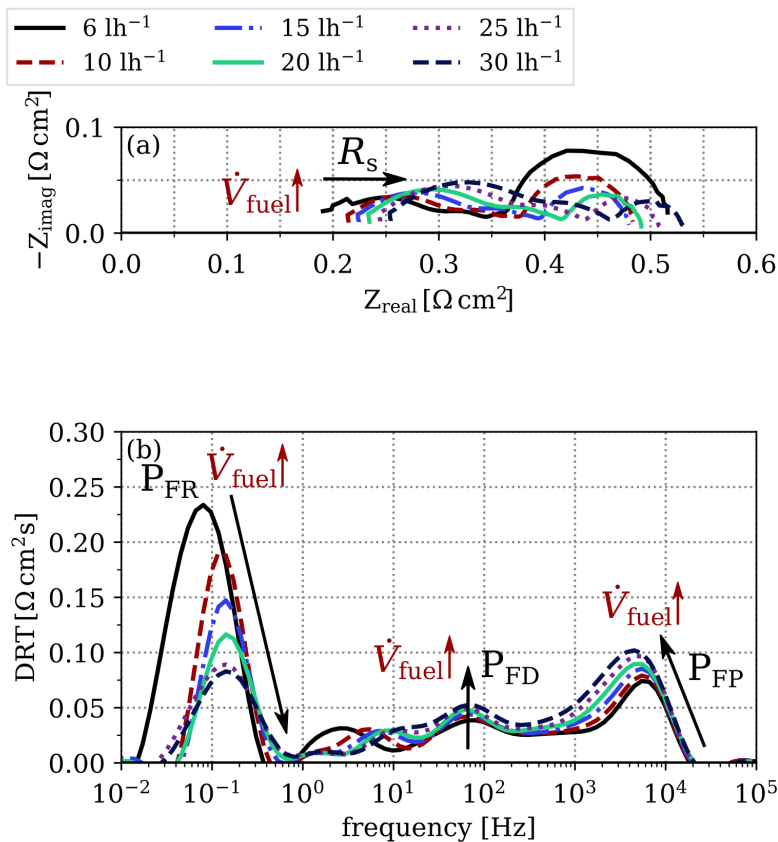


**Figure 5.2:** Nyquist plot (a) and DRT plot (b) as function of the volumetric fuel flow rate ( $\dot{V}_{fuel}$ ) during fueling the anode with anode pre-mixed landfill gas and extra  $\text{CO}_2$ . Cathode was supplied with air and tests were done at  $750^\circ\text{C}$

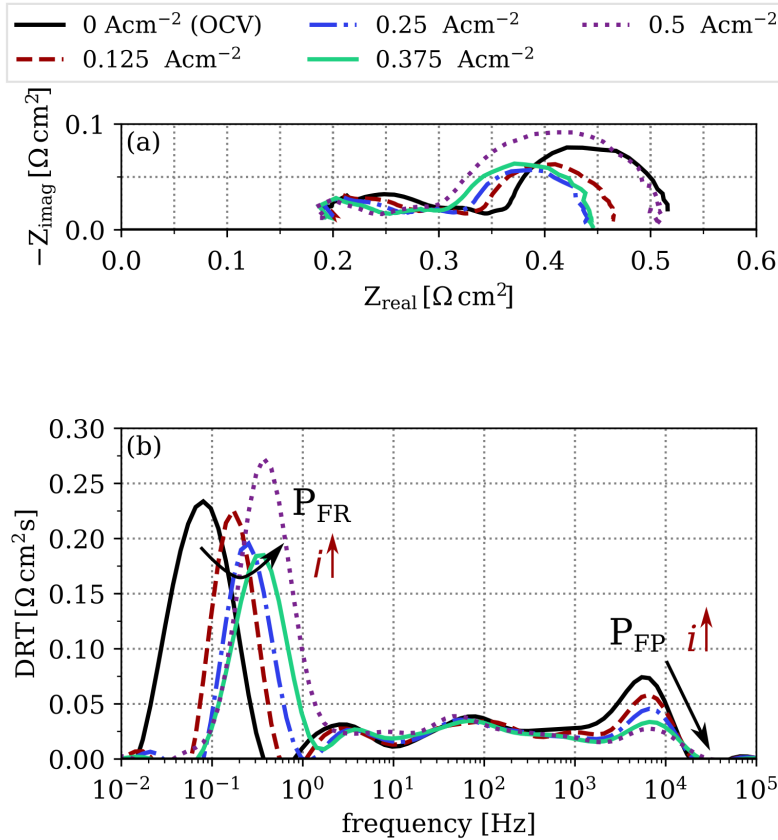


**Figure 5.3:** Nyquist plot (a) and DRT plot (b) as function of the current density ( $i$ ) during fueling the anode with anode pre-mixed landfill gas and extra CO<sub>2</sub>. Cathode was supplied with air and tests were done at 750 °C.

is occurring faster at higher current densities. First, the  $P_{\text{FR}}$  resistance decreases while current density increases until the latter reaches 0.375 A cm<sup>-2</sup>. Afterwards, the  $P_{\text{FR}}$  resistance increased again. The  $P_{\text{FR}}$  resistance at 0.5 A cm<sup>-2</sup> is even  $\approx 22\%$  higher than the corresponding resistance value during the 0 A cm<sup>-2</sup> (OCV) measurement. This increase explains the  $R_p$  increase between the 0.375 A cm<sup>-2</sup> and 0.5 A cm<sup>-2</sup> measurements (compare Figure 5.3(a)). This result shows that the  $P_{\text{FR}}$  is dependent on the amount of oxygen ions/steam present at the anode which is in turn dependent on the applied current density. The observed dependency of the  $P_{\text{FR}}$  is usually reported for the fuel conversion process  $P_{\text{FC}}$  in literature [84]. One theory could be that, in the presented case, the  $P_{\text{FR}}$  is an overlap of the  $P_{\text{FR}}$  and the  $P_{\text{FC}}$  process. Assuming that the previous process frequency response analysis was accurate (see Section 5.1), this explanation is probably not realistic. Another explanation for the observed dependencies could be that

first the reformation process speed is increasing because more reforming agent is available with increasing current density and second the converted H<sub>2</sub>,CO is further used by the electrochemical reactions (see Eq. 2.1, 2.2). At a current density of 0.5 A cm<sup>-2</sup> the concentration polarization losses are occurring already because of the low total anode flow rate of 6 L h<sup>-1</sup>. The low fuel flow rate results in a shortage of fuel supply and therefore initially in an increase of the P<sub>FR</sub> resistance at higher current densities.

### 5.3 Landfill gas CH<sub>4</sub> content dependency

For understanding, the impedance response change was caused by a lower CH<sub>4</sub> reforming rate during real landfill gas supply (see Chapters 6 and 7) this was simulated at OCV. Therefore, the cell was fueled with pre-mixed landfill gas and extra CO<sub>2</sub> supply in order to avoid carbon formation. Starting with the 23 vol% of CH<sub>4</sub> present in the pre-mixed landfill gas CO<sub>2</sub> fuel mixture, the CH<sub>4</sub> amount was decreased step wise down to 5 vol% (see Table 5.3). The 23 vol% corresponds to the amount of CH<sub>4</sub> present in the premixedl landfill gas and CO<sub>2</sub> reforming agent mixture (see Section 3.1.3). To keep the total anode fuel flow rate constant, the amount of CH<sub>4</sub> was replaced by the equivalent amount of N<sub>2</sub> via mass flow controller. The total flow rate was chosen to be 25 L h<sup>-1</sup> to ensure the possibility of reducing the CH<sub>4</sub> content in the calibration limits of the mass flow controller ranges.

**Table 5.3:** Settings for analyzing the impedance response as function of the CH<sub>4</sub> content present in the pre-mixed landfill gas

vol% CH <sub>4</sub> step size	further settings
23; 20; 15; 10; 5	temperature: 750 °C total flow rate: 25 L h <sup>-1</sup>
CH <sub>4</sub> was replaced by N <sub>2</sub> to keep the fuel flow rate constant.	

For a better comparison between the CH<sub>4</sub> test and the tests described in the previous section, the results are shown in a Nyquist plot (a) and a DRT plot (b) in Figure 5.4. First of all, one can notice that R<sub>s</sub> is decreasing with decreasing CH<sub>4</sub> content present in the anode fuel mixture. This is caused by the fact that with less CH<sub>4</sub> present in the fuel less CH<sub>4</sub> reforming according to Equation 2.8 can take place. With decreasing amount of reforming less energy (heat) from the surrounding is needed. Due to this fact, the operation temperature is slightly increasing with decreasing amount of CH<sub>4</sub>.

reforming and therefore  $R_s$  is decreasing. Additionally,  $R_p$  is decreasing for the  $\text{CH}_4$  amounts 23 vol% to 10 vol% and then increasing again for the 5 vol%  $\text{CH}_4$  scenario. The DRT difference plot in Figure 5.4 indicates that the  $P_{\text{FR}}$  process at low frequencies and the  $P_{\text{FP}}$  process at high frequencies are mainly dependent on the  $\text{CH}_4$  amount present in the fuel. The magnitude of the  $P_{\text{FR}}$  slightly increases for the 23 vol% plus 20 vol%  $\text{CH}_4$  scenarios and than decrease for the 15 vol% plus 10 vol%  $\text{CH}_4$  scenarios with a kind of linear trend. For the lowest  $\text{CH}_4$  amount of 5 vol% present in the fuel stream the  $P_{\text{FR}}$  resistance is the highest in comparison to the measurement recorded with lower  $\text{CH}_4$  amount. The increase of the  $P_{\text{FR}}$  at the lowest  $\text{CH}_4$  amounts might be caused by the fact that a sufficient amount of  $\text{CH}_4$  is not available for the total active anode side area. Additionally, the  $P_{\text{FR}}$  process response frequency is shifted to higher frequencies with decreasing  $\text{CH}_4$  amount present in the inlet fuel stream. This can be correlated with the temperature increase in accordance to a decreased reforming of  $\text{CH}_4$ . Therefore, at higher temperatures the reforming process occurs faster. For the purpose of analyzing the dependency of the different anode processes in regard to the amount of  $\text{CH}_4$  present in the pre-mixed landfill gas, the impedance measurements were fitted with an equivalent electric circuit using the batch fitting approach according to Gaves et al. [119]. The considered electrical circuit model is described in Section 3.1.6. For the latter, the resistance change of the  $P_{\text{FR}}$ , the  $P_{\text{FP}}$  plus  $R_s$  and  $P_{\text{FR}}$  frequency change with changing  $\text{CH}_4$  content were considered for the initial model parameter guesses. Additionally, no cathode degradation was assumed because of the short total test time of around 24 hours. Therefore, the resistance of the process  $P_{\text{OP}}$  was assumed to be constant for all impedance measurements. An overview about the model parameters which were kept constant and which were varied during the batch fitting is provided in Table 5.4.

**Table 5.4:** Parameters which were varied and kept constant during the advanced impedance batch fitting of the pre-mixed landfill gas  $\text{CH}_4$  content variation analysis.

parameter	process					
	$R_s$	$P_{\text{FR}}$	$P_{\text{FC}}$	$P_{\text{FD}}$	$P_{\text{OP}}$	$P_{\text{FP}}$
$R_{xx}$	d	d	d	d	e	d
$f_{xx}$	-	d	e	e	e	e
$n_{xx}$	-	e	e	e	e	e

e: parameter equal for all impedance measurements

d: parameter dependent on single impedance measurement

The resistance values of the different processes as function of the  $\text{CH}_4$  content in the

pre-mixed landfill gas determined by the impedance batch fitting are shown in Figure 5.5. The results of the individual impedance fits can be found in the appendix B. In Figure 5.5 the black squares represent the  $R_s$  values. As already discussed previously,  $R_s$  is dependent on the  $\text{CH}_4$  content in the inlet fuel stream (compare with Figure 5.4). The representation in Figure 5.5 clearly indicates that the dependency between  $R_s$  and the amount of  $\text{CH}_4$  in the landfill gas is linear.  $R_s$  increased from  $0.21 \Omega \text{cm}^2$  up to  $0.25 \Omega \text{cm}^2$  with increasing  $\text{CH}_4$  amount in the anode fuel.  $R_p$  (red circles) represents the sum of the process resistances  $R_{\text{FR}}$ ,  $R_{\text{FC}}$ ,  $R_{\text{FD}}$ ,  $R_{\text{OP}}$  and  $R_{\text{FP}}$ . The trend of  $R_p$  shown in Figure 5.5 goes in line with the tendencies of the Nyquist plot in Figure 5.4(a) which was discussed above. The value of  $R_p$  is first decreasing and then increasing with rising  $\text{CH}_4$  content in the pre-mixed landfill gas. The resistance values of  $R_p$  are between

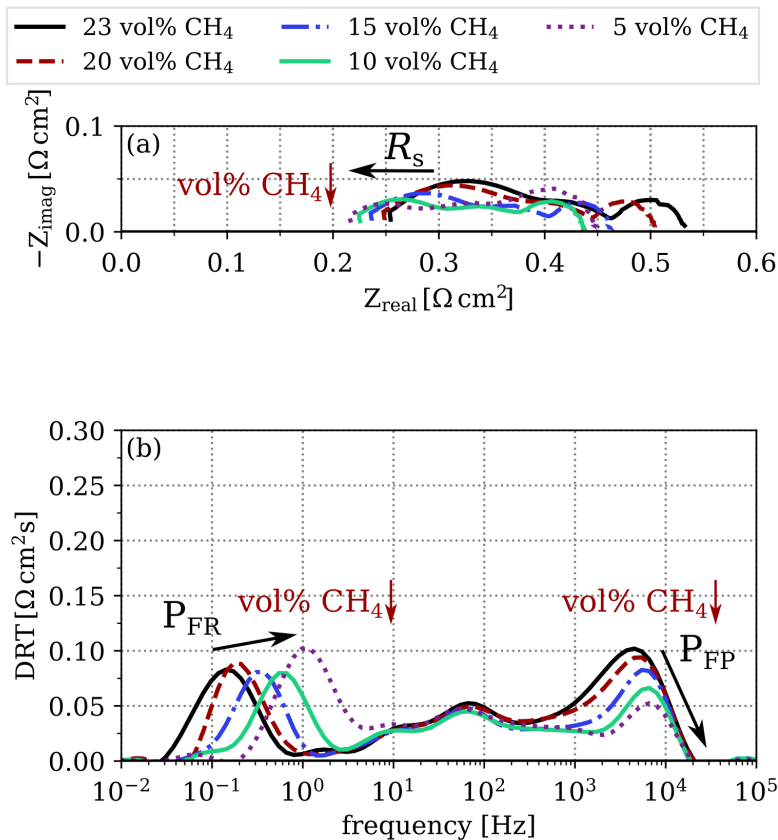


**Figure 5.4:** Nyquist plot (a) and DRT plot (b) as function of the amount of  $\text{CH}_4$  in the landfill gas (vol%  $\text{CH}_4$ ). Anode was supplied with pre-mixed landfill gas and extra  $\text{CO}_2$ .  $\text{CH}_4$  amount was replaced by  $\text{N}_2$  for a constant fuel flow rate. Cathode was supplied with air and tests were done at  $750^\circ\text{C}$ .

$0.2 \Omega \text{ cm}^2$  and  $0.28 \Omega \text{ cm}^2$ . Due to the fact that this is an anode fuel composition study, the cathode resistance value  $R_{\text{OP}}$  stays constant during  $\text{CH}_4$  variation on the anode side. Additionally, the resistance  $R_{\text{FC}}$  stayed constant and seems to be independent from the  $\text{CH}_4$  content in the fuel. At  $\text{CH}_4$  amounts between 5 vol% to 10 vol%, the  $R_p$  decreasing trend is dominated by the decreasing trend of the  $R_{\text{FD}}$  (orange triangle left) and  $R_{\text{FR}}$  (yellow triangle up) while  $R_{\text{FP}}$  (blue triangle down) is increasing in this  $\text{CH}_4$  concentration range. First, at  $\text{CH}_4$  contents greater than 10 vol% the  $R_p$  trend is dominated by the approximately linear increase of  $R_{\text{FP}}$ . Second, at  $\text{CH}_4$  contents above 10 vol%  $R_{\text{FD}}$  and  $R_{\text{FR}}$  stay constant with values of  $0.06 \Omega \text{ cm}^2$  and  $0.07 \Omega \text{ cm}^2$ . Afterwards the resistances are increasing up to values of  $0.07 \Omega \text{ cm}^2$  to  $0.08 \Omega \text{ cm}^2$ .  $R_{\text{FP}}$  increased from  $0.07 \Omega \text{ cm}^2$  up to  $0.13 \Omega \text{ cm}^2$  with rising  $\text{CH}_4$  amount in the pre-mixed landfill gas. The analysis shows that the three anode processes  $P_{\text{FR}}$ ,  $P_{\text{FD}}$ ,  $P_{\text{FP}}$  and the serial resistance  $R_s$  are dependent on the amount of  $\text{CH}_4$  present in the landfill gas. In all cases the temperature change caused by the changing  $\text{CH}_4$  reforming rate has an effect on the process speeds and resistances.

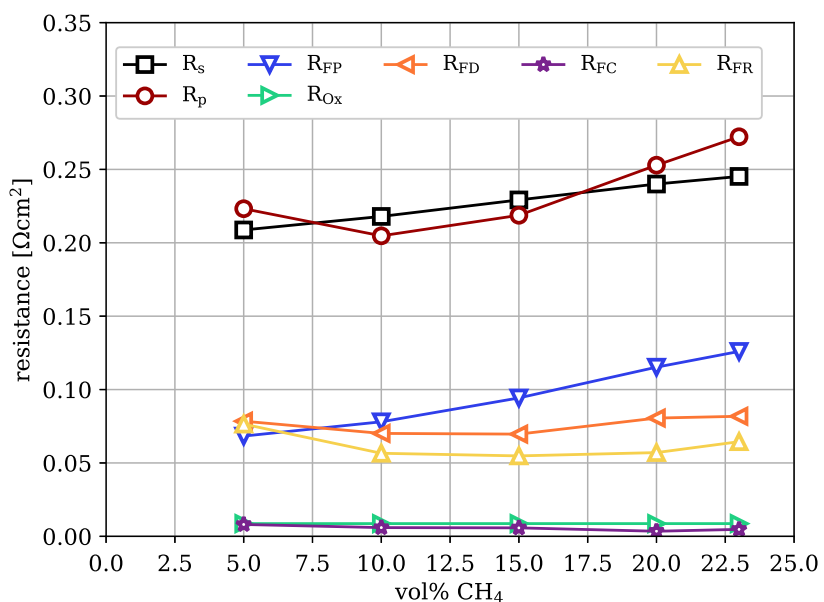


**Figure 5.5:** Anode and cathode resistances from the impedance batch fittings as function of the  $\text{CH}_4$  [vol%] amount present in the pre-mixed biogas (see Figure 5.4). Corresponding  $\chi^2$  error of the impedance batch fit is  $2.95 \times 10^{-7}$ . Further information about the single impedance measurement fit results are provided in the Appendix B.



## 5.4 Conclusion

In this chapter an electrochemical impedance study of pre-mixed landfill gas fueled SOFC cells at 750 °C was presented. The aim of the conducted study was to get a better understanding of the following operation parameters: total anode fuel flow rate, applied current density and the CH<sub>4</sub> amount present in the landfill gas. This knowledge provides the basis for drawing more detailed conclusions of the conducted tests with real landfill gas supply which are presented in Chapters 6 and 7. At the beginning of the analysis the frequency ranges of the different anode and cathode process were determined by analyzing an initial 'finger print' plus extra measurements conducted with a CH<sub>4</sub> CO<sub>2</sub> gas mixture. The parameter analyses showed that mainly the three anode processes P<sub>FR</sub>, P<sub>FD</sub>, P<sub>FP</sub> and the resistance R<sub>s</sub> are influenced by the parameter anode fuel flow rate, applied current density and CH<sub>4</sub> content in the landfill gas. The influence of the CH<sub>4</sub> content in the landfill gas on the impedance response was further investigated by applying an equivalent circuit model via impedance batch fitting. With the help of this approach, it could be shown that R<sub>FD</sub> and R<sub>FR</sub> are increasing linearly with rising CH<sub>4</sub> content in the landfill gas. Additionally, the values of R<sub>FR</sub> and R<sub>FD</sub> are first decreasing followed by a constant period with rising CH<sub>4</sub> content in the landfill gas. Finally, at high CH<sub>4</sub> contents the values of R<sub>FR</sub> and R<sub>FD</sub> are increasing again.

# 6 Landfill gas fueled SOFC operation modes

**Comment:** Parts of the Sections 6.1, 6.2 and 6.3 are based on the work which was presented at the 13<sup>th</sup> European SOFC & SOEC Forum 2018, Lucerne, July 2018. As part of the conference the corresponding manuscript was published in the conference proceedings [96]. The support of the co-authors is gratefully acknowledged. The paragraphs which are framed by double quotes ("") are originally from the manuscript.

As a next step a durability study with real landfill gas was conducted for analyzing the cell performance and behavior especially during operation with non cleaned landfill gas. During the study three sister cells (see Table 3.3 for cell compositions) were fueled with real landfill gas by using the internal dry reforming process (Eq. 2.8). The landfill gas was collected at the landfill site in Odense as described in Section 3.1.3. '[In this study] the landfill gas was passed or by-passed through a commercial activated carbon filter before entering the cell [(see Section XX)]. In case of by-passing the filter, different operation modes were investigated with the aim to restore the original performance of the cell. Furthermore, the degradation behavior was studied in two operation modes: galvanostatic and potentiostatic' [96]. The first cell was used for tests in the galvanostatic mode (see Figure 6.1) while the other cells were used for two tests in the potentiostatic mode (see Figure 6.2 and 6.5). The aim of the second potentiostatic test was to investigate the differences of the steam partial pressure at the anode between the galvanostatic mode and the potentiostatic mode in relation to the poisoning effects of the landfill gas impurities. '[In the test procedure Figures 6.1, 6.2 and 6.5] the lower coordinate system shows the operation mode over the operation time. The state of passing or by-passing the landfill gas through the activated carbon filter during landfill gas supply is shown in the middle diagram. The top diagram illustrates the current density over the operation time' [96]. '[All] tests were framed by ‘finger prints’ after start up, i.e. before the durability test period and after it, i.e. before shutdown of the cell testing'

[96]. The cathode was supplied with air during the landfill gas fueled durability tests. Section 6.1 of this chapter contains the durability test segments of the first two cells in galvanostatic and potentiostatic mode with passing the landfill gas through the activated carbon filter. Followed by Section 6.2 about the galvanostatic test and the two potentiostatic test segments during by passing the activated carbon filter. Finally, in Section 6.3 cleaning methods are compared which were applied after the tests with by passed activated carbon filter.

## 6.1 Cleaned landfill gas galvanostatic and potentiostatic operation

As mentioned previously the test procedure of the galvanostatic test and the first potentiostatic test (see Figure 6.1 and 6.2) can be divided into two segments. In this section the procedure and the corresponding results of the first segments are presented.

"In the first segment the anode side of the cell was supplied with landfill gas plus the reforming agent CO<sub>2</sub> passing the fuel through the activated carbon filter for cleaning. In the galvanostatic mode a current density of 0.5 A cm<sup>-2</sup> was applied and in the potentiostatic mode a cell voltage of 765 mV. These settings were selected to obtain in both cases a similar power output of approximately 0.4 W cm<sup>-2</sup>."

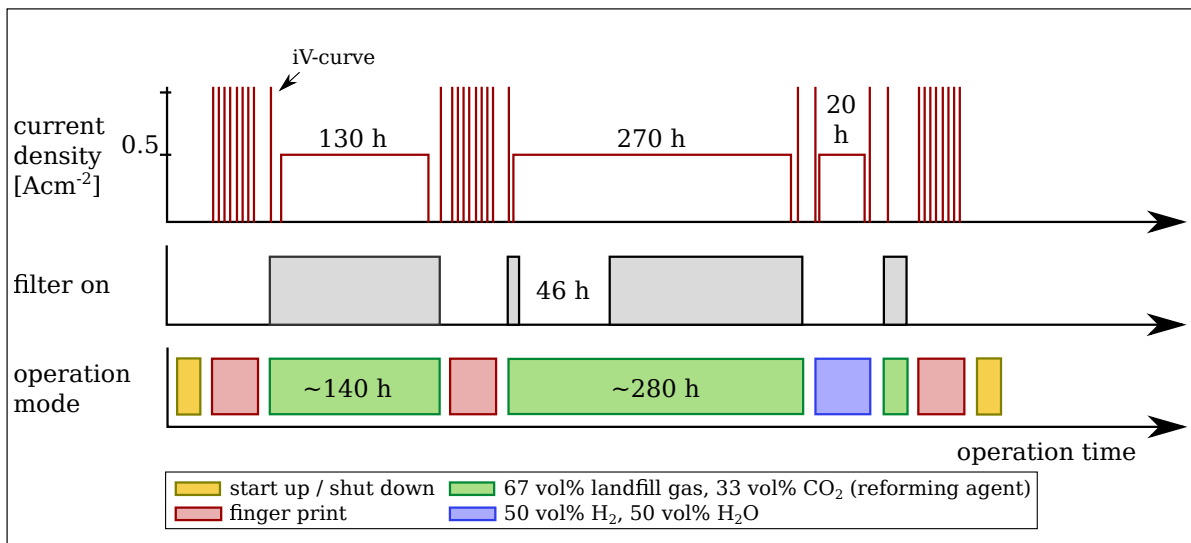


**Figure 6.1:** Test procedure for the galvanostatic operation mode with real landfill gas and additional CO<sub>2</sub> at 750 °C with 0.5 A cm<sup>-2</sup>. Modified from reference [96].

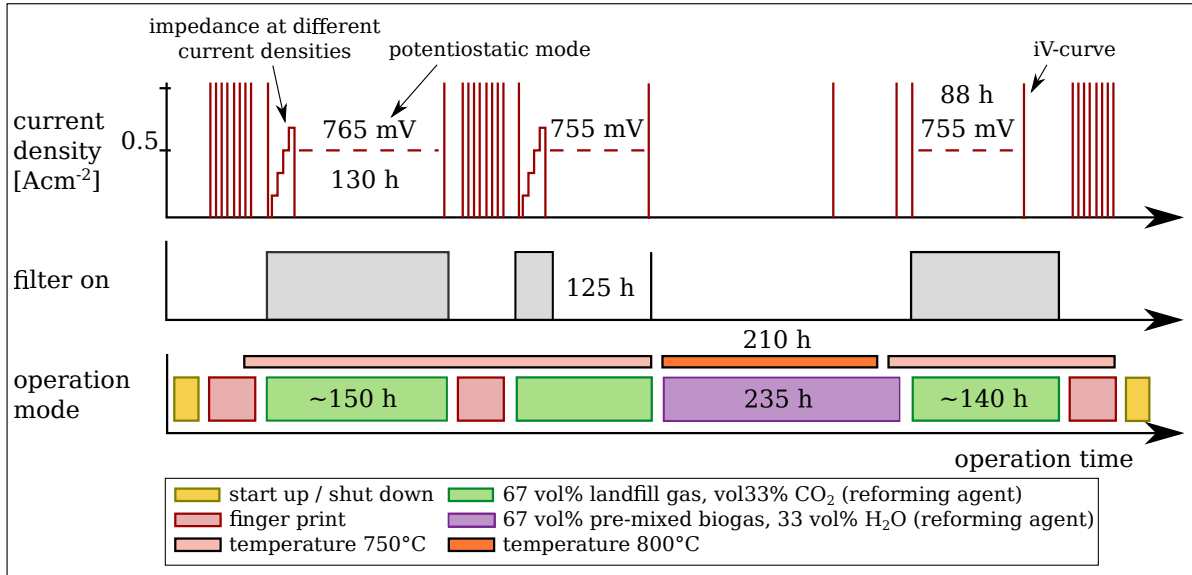


**Figure 6.2:** Test procedure for the potentiostatic operation mode with real landfill gas and additional CO<sub>2</sub> (or steam) at 750 °C and 800 °C with 765 mV in the first part and 755 mV in the second part. Modified from reference [96]

The results of the galvanostatic (a)-(c) and potentiostatic mode test are shown in Figure 6.3. The cell voltage (black line) started with a value of  $\approx 797$  mV and dropped slightly over the operation time of 130 h. The voltage drop corresponds to a degradation rate of 1.1 %/1000h assuming a linear behavior and an area specific resistance (*ASR*) increase of 3.9 %/1000h. The value of the pO<sub>2</sub> sensor at the outlet of the cell (green line) stayed constant which indicates that the gas composition had not changed during the operation time. In Figure 6.3(b) the corresponding serial resistance ( $R_s$ ) (black dots) and polarization resistance ( $R_p$ ) (blue dots) plus the applied current density of 0.5 A cm<sup>-2</sup> (red line) are illustrated. The constant  $R_s$  and  $R_p$  with values of  $\approx 0.19 \Omega \text{ cm}^2$  and  $\approx 0.22 \Omega \text{ cm}^2$  respectively is consistent with the very low degradation observed in the DC measurements. The measured cell voltage and applied current density correspond to an electric efficiency of [ $\approx 45\%$ ] during the landfill gas fueled operation, using the definition of the electric efficiency according to [Equation 2.33]. In Figure 6.3(c) the cell temperature at the inlet (black line) and outlet (blue line) are shown. These temperatures stayed constant with values of 745 °C at the inlet and 750 °C at the outlet. The temperature difference between inlet and outlet indicates that the endothermic dry reforming process was mainly occurring at the inlet side of the cell. This statement is supported by the fact that during tests with SOFCs fueled with an H<sub>2</sub>/H<sub>2</sub>O mixture this temperature difference was not detected. The observations of the potentiostatic testing were similar

in comparison to the galvanostatic testing as shown in the graphs of Figure 6.3(d)-(f). But due to the different operation modes the current density decreased slightly instead of the cell voltage. The decrease of the current density corresponds to a degradation rate of 2.2 %/1000h and an *ASR* increase of 8.4 %/1000h. The small fluctuations of the cell voltage (black line, Figure 6.3(d)) and current density (red line, Figure 6.3(e)) are the result of small potentiostatic operation adjustments.”

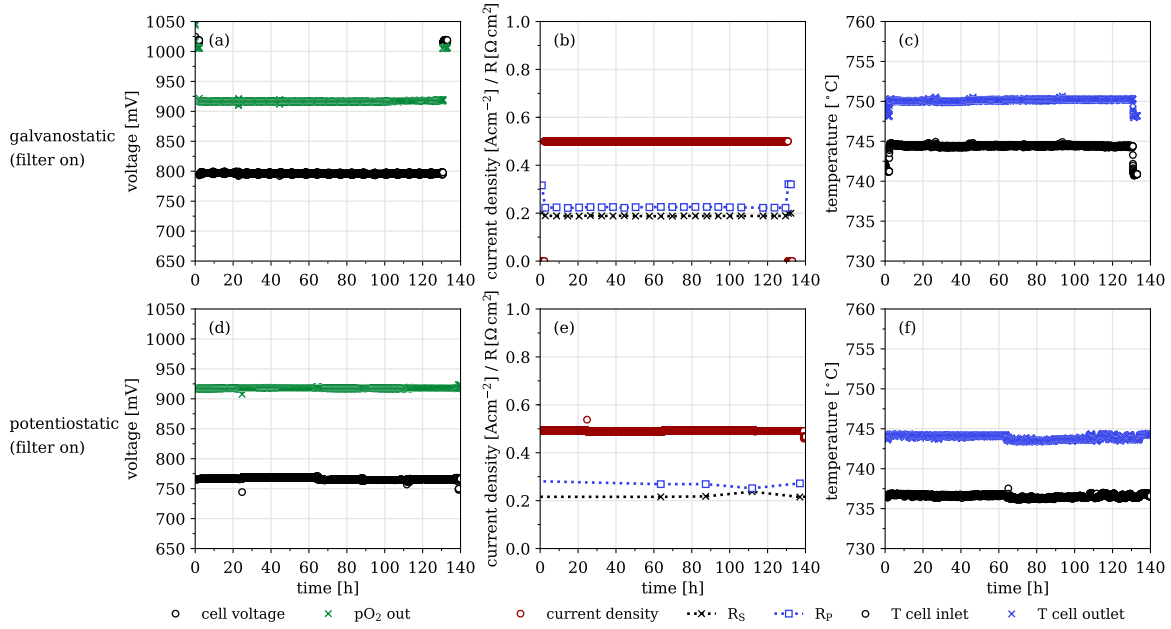


**Figure 6.3:** Test results of the galvanostatic (a)-(c) and potentiostatic (d)-(f) operation using cleaned landfill gas. Plot (a), (d): Cell voltage,  $p\text{O}_2$  sensor at outlet of the cell; Plot (b), (e): Serial resistance ( $R_s$ ), Polarization resistance ( $R_p$ ) obtained from impedance spectra during operation, and current density; Plot (c), (f): Cell temperature at fuel inlet and outlet. Adapted from reference [96].

”The *ASR* values of the cells were determined from the iV-curves recorded before and after the operation and are illustrated in Figure 6.4. The minimum *ASR* value found at current densities higher than  $0.1 \text{ A cm}^{-2}$  was considered. The *ASR* values of the cell in the galvanostatic test are shown on the left side and the *ASR* values of the potentiostatic test on the right side. The *ASR* values before the degradation tests were slightly different for the two cells with values of  $0.45 \Omega \text{ cm}^2$  for the cell in the galvanostatic test and  $0.5 \Omega \text{ cm}^2$  for the potentiostatic test. This can be explained by a higher initial *ASR* for the specific cell used in the potentiostatic test in comparison to the galvanostatic test.

This assumption is supported by the higher values of  $R_s$  and  $R_p$  as indicated in Figure 6.3(e). The  $ASR$  values had increased only slightly after the potentiostatic operation mode, by 6 %, whereas the  $ASR$  value did not change significantly after the galvanostatic operation mode. This confirms the observations of the cell voltage and current density over time in Figure 6.3.”

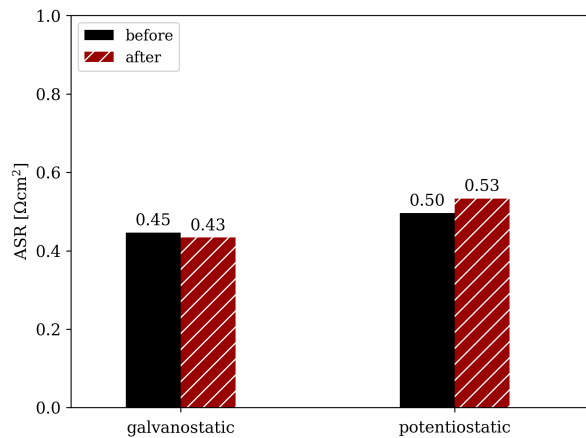


**Figure 6.4:** Comparison of the area specific resistance ( $ASR$ ) determined from the iv-curves before and after the galvanostatic/potentiostatic operation with cleaned landfill gas via the activated carbon filter. Adapted from reference [96].

## 6.2 Non cleaned landfill gas operation

The effect of by-passing the activated carbon filter for a certain time during real landfill gas plus  $CO_2$  supply was studied during the second test segments of the galvanostatic and the first potentiostatic test.

”In case of the galvanostatic operation the activated carbon filter was by-passed for 46 h before the fuel was passed through the filter again. The total operation time with landfill gas was  $\approx 270$  h. In the potentiostatic test, the activated carbon filter was by-passed for  $\approx 125$  h before the fuel was passed through the activated carbon filter again for an iV-curve and impedance recording. Afterwards, different regeneration strategies were applied with the aim to improve the cell performance again, as summarized in Table 6.1 plus illustrated in the Figures 6.1 and 6.2. In the case of galvanostatic operation the anode was fueled with a mixture of 50 vol%  $H_2$  and 50 vol%  $H_2O$  for 20 h at a current density of  $0.5 A\ cm^{-2}$  and  $750^\circ C$ . In the potentiostatic operation test, the cell was supplied with a pre-mixed biogas composition similar to the real landfill gas (but without

impurities) and the reforming agent steam instead of CO<sub>2</sub>, the operation temperature was increased to 800 °C for 210 h and the cell was operated at OCV. After the regeneration treatments, the cells were again supplied with landfill gas through the activated carbon filter plus CO<sub>2</sub> to validate the regeneration approach. In the galvanostatic test only an iV-curve and an impedance measurement were recorded because of a limited availability of landfill gas, while in the potentiostatic test the cell was operated in the potentiostatic mode for additional 88 h.” As mentioned at the beginning of the chapter

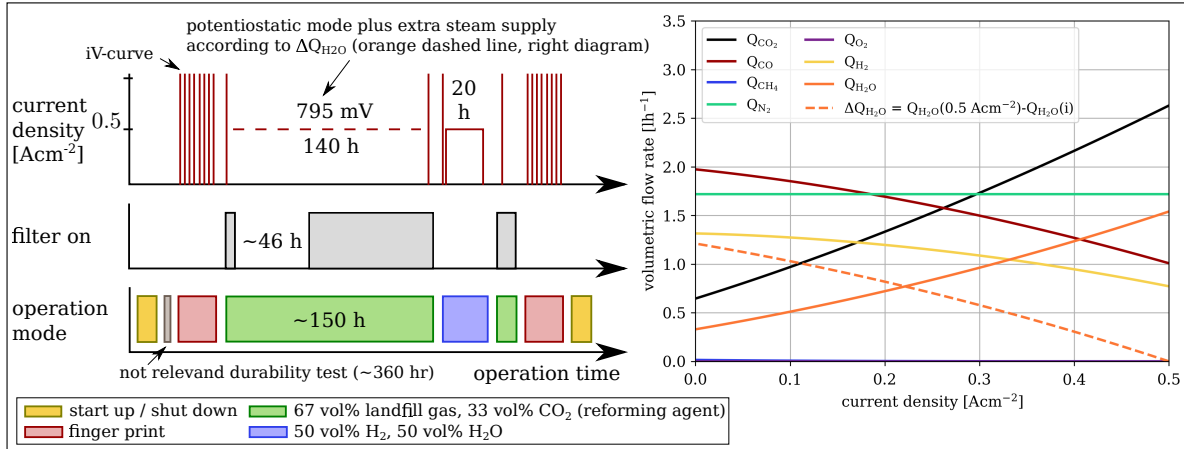


**Figure 6.5:** Test procedure for the potentiostatic operation mode with additional steam supply fueled with real landfill gas and additional CO<sub>2</sub> at 750°C (left side). Theoretical volumetric flow rates of the gas species at the outlet of the anode as function of the applied current density (right side). Inlet fuel 4 L h<sup>-1</sup> landfill gas plus 2 L h<sup>-1</sup> extra CO<sub>2</sub>. Thermodynamic calculations were based on Gibbs free energy minimization (see Eq. 2.9) plus Faraday’s law (see Eq. 2.25) and calculated with ElchDAT [51]. Dashed orange line represents the steam flow rate which was added step wise via mass flow controller during potentiostatic operation according to the applied current density.

a second potentiostatic test was carried out with by-passing the activated carbon filter (see Figure 6.5). The test was carried out for investigating the dependency between the cell performance during poisoning and the steam present at the anode. Therefore, the test was carried out in the potentiostatic mode and additional steam was added via mass flow controller to compensate the missing steam at the anode caused by the lower current density. This approach should ensure a similar steam partial pressure at the anode during potentiostatic operation as during galvanostatic operation. For estimating the amount of steam present at the anode thermodynamic calculations based on Gibbs free energy minimization and Faradays law were conducted. On the right side of Figure 6.5 the volumetric gas flows of the present species at the anode as function of the current

density are shown. The dashed orange line represents the amount of steam which had to be added manually via mass flow controller during potentiostatic operation in terms of the measured current density. As lower the current density as higher the additional added steam flow rate. Due to mass flow controller limitations the extra steam was added step-wise. For better comparison the filter by-passing time and the cleaning method was the same as for the galvanostatic test (compare Figures 6.2 and 6.5, see Table 6.1). This time no impedance measurements were recorded to avoid negative influences between the extra steam supply and the impedance measurements.

**Table 6.1:** Testing conditions for the regeneration approach after fueling the cell with landfill gas plus CO<sub>2</sub> and by-passed activated carbon filter. Modified from reference [96].

test part	regeneration approach			
	anode fuel composition	current density	temperature	regeneration time
galvanostatic	50 vol% H <sub>2</sub> , 50 vol% H <sub>2</sub> O	0.5 A cm <sup>-2</sup>	750 °C	20 h
potentiostatic	pre-mixed biogas plus steam (25 vol% CH <sub>4</sub> , 16 vol% CO <sub>2</sub> , 26 vol% N <sub>2</sub> , 33 vol% H <sub>2</sub> O)	0 A cm <sup>-2</sup>	800 °C	210 h
potentiostatic with extra steam supply	50 vol% H <sub>2</sub> , 50 vol% H <sub>2</sub> O	0.5 A cm <sup>-2</sup>	750 °C	20 h

Firstly, the results over operation time of the test segments during by-passed activated carbon filter are discussed in the following (see Sections 6.2.1, 6.2.2 and 6.2.3). Secondly, the selected impedance measurements recorded in the galvanostatic mode and potentiostatic mode are discussed. Thirdly, the anode in-plane voltage trends (see Section 6.2.5) and the ASR increase trends (see Section 6.2.6) of the three test segments are compared for evaluating the during by-passed activated carbon filter more in detail.

### 6.2.1 Galvanostatic operation

Figure 6.6 shows the results of the galvanostatic operation mode without cleaning the landfill in the first period of the operation. As the nature of the specific impurities was not known, a carbon filter was used which should remove all impurities. Using landfill gas without cleaning, the cell voltage (black line, Figure 6.6(a)) started to decrease slowly and after approximately 20 h more rapidly. After 48 h of operating the SOFC, the cell voltage had dropped by 80 mV which corresponds to an increase of the  $R_p$  by  $0.15 \Omega \text{cm}^2$  as shown in Figure 6.6(b) (blue dots). Previous dedicated studies on the sulfur poisoning in methane containing fuel show typically a fast cell voltage drop followed by an overall degradation or stable cell voltage, depending on sulfur concentration, temperature etc. [21, 54, 63]. The rather slow time scale and continuous trend for the cell voltage decrease in this study indicates that there are other impurities than sulfur present in the landfill, which have a poisoning effect. In order to counteract this severe degradation, the landfill was again passed through the activated carbon filter. Still, the cell voltage decreased even further in the following 25 h to 686 mV and the  $R_p$  increased to  $0.51 \Omega \text{cm}^2$ . Afterwards, the cell started to recover slowly. After 270 h the cell voltage had recovered to 92 % and  $R_p$  was still 35 % higher than at the beginning. The serial resistance  $R_s$  stayed constant (black dots Figure 6.6(b)) during the whole operation time. The temperature at the fuel inlet side (black line Figure 6.6(c)) of the cell increased from  $745^\circ\text{C}$  to  $748^\circ\text{C}$  during the time the cell voltage decreased and afterwards decreased again to  $746^\circ\text{C}$ . Taking into account that the reforming process is an endothermal process and therefore less energy (heat) is needed from the environment by a decreasing reforming activity. Furthermore,

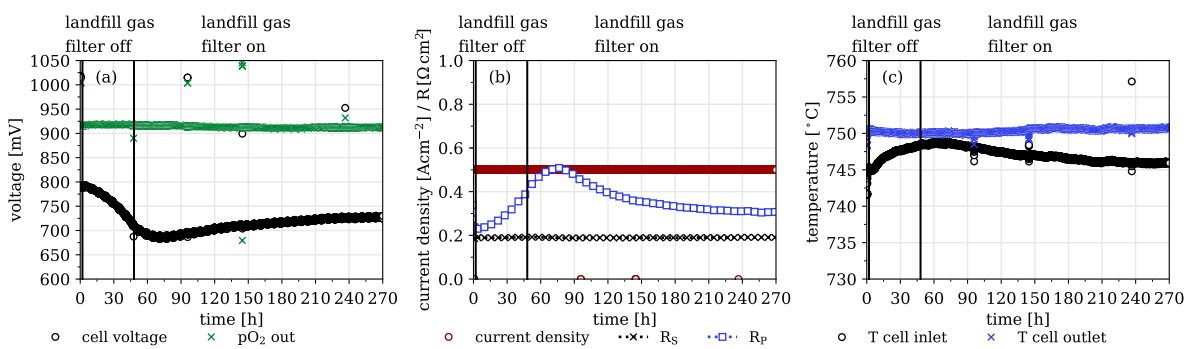


**Figure 6.6:** Test results of the galvanostatic operation without cleaning of the landfill gas. Plot (a): Cell voltage,  $p\text{O}_2$  sensor at outlet of the cell; Plot (b): Serial resistance ( $R_s$ ), Polarization resistance ( $R_p$ ) obtained from impedance spectra during operation, current density; Plot (c): Cell temperature inlet and outlet. Adapted from reference [96].

the cell inlet temperature increase was not caused by the lower electrical power output which results in a higher thermal power output because the cell outlet temperature did not increase. Additionally, the value of the  $pO_2$  out sensor slightly decreased during the first 200 h of operation which indicates that the outlet gas composition had changed to a small degree towards a lower amount of  $H_2$  and a higher amount of  $CH_4$  (see Figure 6.6(a)). These findings point suggest that the dry reforming process was affected by the poisoning caused by the impurities of the landfill gas.”

### 6.2.2 Potentiostatic operation

”The results of operating the cell with real landfill gas in the potentiostatic mode without cleaning is illustrated in Figure 6.7. The operation time can be divided into three parts. During the first 125 h the cell is fueled with landfill gas plus  $CO_2$  and the filter is by-passed. The current density decreased rapidly from approximately  $0.5\text{ A cm}^{-2}$  to  $0.2\text{ A cm}^{-2}$  in the first 50 h. Afterwards the current density decreased at a slower rate down to  $0\text{ A cm}^{-2}$ . During that time  $R_p$  increased rapidly whereas  $R_s$  stayed approximately constant. As the current density approached zero, the potentiostatic controller was not able to maintain the set voltage of 755 mV, as seen in the fluctuating cell voltage with progressing operation time. The  $pO_2$  value measured at the fuel outlet of the cell increased by 44 mV in the first 75 h which can be explained by the decreasing current density, causing a decreasing amount of steam on the anode side and a corresponding higher  $pO_2$  voltage value. Afterwards, the value of the  $pO_2$  sensor at the outlet decreased rapidly which could indicate that the  $pO_2$  sensor was affected by the impurities, too. Similar to the observations during the galvanostatic test the temperature at the cell inlet increased during the time the filter was turned off. Following this degradation period, a number of approaches were tested to regenerate the cell performance. In the following 235 h the fuel supply was changed from real landfill gas to pre-mixed biogas and using steam as reforming agent instead of  $CO_2$ . Furthermore, the operation temperature was increased from  $750^\circ\text{C}$  to  $800^\circ\text{C}$  in order to facilitate desorption of impurities and no current was applied. In this period the cell voltage and the  $pO_2$  out values increased rapidly in the first 20 h, and then both approached the theoretical value of 1005 mV. After 280 h of regeneration at OCV and pre-mixed biogas supply, the cell voltage was 1003 mV. The  $R_s$  decreased from  $0.25\Omega\text{ cm}^2$  to  $0.19\Omega\text{ cm}^2$  when the temperature was increased from about  $750^\circ\text{C}$  to  $800^\circ\text{C}$ .  $R_p$  decreased again immediately and stabilized at a value of approximately  $0.29\Omega\text{ cm}^2$ . The cell inlet temperature decreased with a steep slope at the beginning and then slowly from approximately  $790^\circ\text{C}$  to  $780^\circ\text{C}$  in

a time period of 155 h, whereas the cell temperature at the outlet stayed constant at around 792 °C. The mentioned observations indicate that the poisoning of the cell could be regenerated to a certain degree. From the fast decrease of  $R_p$  and fast cell voltage increase at the beginning of the regeneration it can be concluded that the electrochemical reaction rates at the triple face boundary recovered fast, while the reforming process recovered more slowly as the previously described temperature trend indicates. The reforming process can take place on the electrochemically inactive nickel particles in the thick cell support layer, far from the electrolyte. Poisoning of this layer is expected to occur first and thereby result in a greater density of accumulated impurities than in the electrochemically active zone near the electrolyte, which could explain the longer desorption time period. In the last period, a stable operation was achieved during fueling the cell with cleaned landfill gas plus the reforming agent CO<sub>2</sub>. But the current density was 20 % lower than at the beginning of the test at the same 755 mV potentiostatic operation point, i.e. a full regeneration was not achieved.”

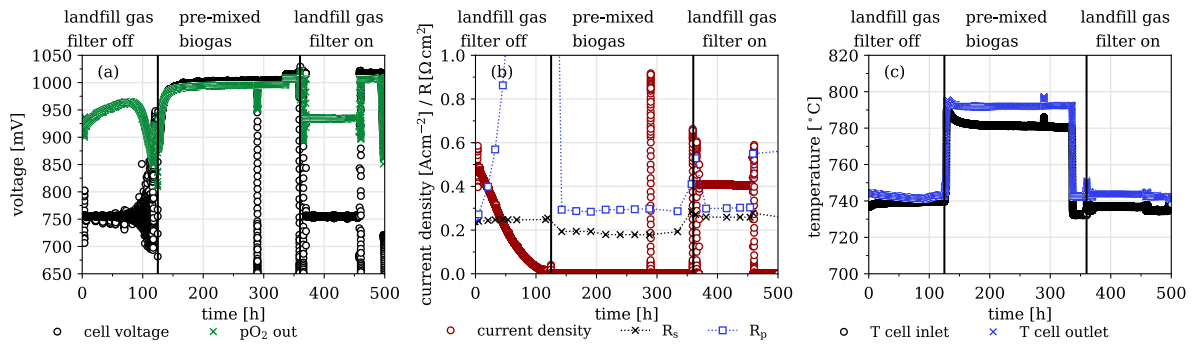


**Figure 6.7:** Test results of the potentiostatic operation without cleaning of the landfill gas. Plot (a): Cell voltage,  $p\text{O}_2$  sensor at outlet of the cell; Plot (b): Serial resistance ( $R_s$ ), Polarization resistance ( $R_p$ ) obtained from impedance spectra during operation, current density; Plot (c): Cell temperature inlet and outlet. Adapted from reference [96].

### 6.2.3 Potentiostatic operation with extra steam supply

The results of the potentiostatic operation with extra steam supply during by-passing the activated carbon filter are shown in Figure 6.8. In the first 20 % after by-passing the filter similar observations were made as during the first potentiostatic test (compare with Figure 6.7). The current density (red line, Figure 6.8(b)) decreased while the cell voltage stayed constant (black line, Figure 6.8(a)). The potential at the  $p\text{O}_2$  out sensor increased also (green line, Figure 6.8(a)). The temperature at the cell inlet (black line,

Figure 6.8(c)) was higher than at the cell outlet (blue line, Figure 6.8(c)) which was the opposite during the first potentiostatic test.

After 30 h of operation the current density had decreased from  $0.5 \text{ A cm}^{-2}$  down to  $0.4 \text{ A cm}^{-2}$  which corresponds to a decrease of steam of  $0.3 \text{ L h}^{-1}$ . After the missing amount of steam was added manually via mass flow controller (Figure 6.8(b), black line) the current density increased by  $0.03 \text{ A cm}^{-2}$  directly. Followed by the same decreasing behavior as before the steam was introduced. After  $0.35 \text{ A cm}^{-2}$  the steam amount was increased again according to Figure 6.5 but no effect of the steam was detected. The current density decreased further afterwards. After 46 h by-passing the filter the filter was passed again and the current density stopped decreasing and started increasing again after 9 h. When the current density had reached a value of  $0.35 \text{ A cm}^{-2}$  the extra amount of steam was reduced again. The current density started to recover slightly slower after the extra steam amount was lower. After 130 h the current density had recovered by 78 %. A determination of the effect of the extra steam supply on the  $p\text{O}_2$  outlet potential was difficult to detect. The  $p\text{O}_2$  outlet potential showed first an increasing behavior until a maximum was reached followed by a decrease during the activated carbon filter was by-passed. This dependency was also observed during the first potentiostatic test. The only dependency which was noted is that the  $p\text{O}_2$  outlet potential reached the maximum and stayed stable for a certain time after the extra steam supply was increased the second time. When the filter was passed again the  $p\text{O}_2$  out potential decreased again and reached approximately the same value as before the by-passing of the filter. Afterwards, the  $p\text{O}_2$  potential started to increase again and showed a similar trend than the current density. Furthermore, a temperature increase of around  $1^\circ\text{C}$  at the cell inlet and outlet was measured after the first extra steam supply was added. Afterwards the temperature at the cell inlet decreased and increased again with a similar trend as the current density. The cell outlet temperature stayed constant after the temperature increase and started decreasing slightly after the filter was passed again. At around 130 h of operation the cell inlet temperature was slightly above the temperature at the beginning of this experiment. The cell outlet temperature was approximately the same as before the filter was by-passed. A reason for the different temperature behavior at the cell inlet and outlet could be a misplacement of the temperature sensors. The temperature probes were not at the correct position for measuring temperature changes due to poisoning of reforming processes like during the previous tests. In this case the inlet cell temperature was representing the amount of heat generated due to the applied current density.

In general similar observations were made during the second potentiostatic test in comparison to the first potentiostatic test and to the galvanostatic test in terms of cell performance recovery after passing the filter again. Moreover by manually increasing the partial pressure of steam at the anode according to the current density the poisoning effects of the landfill gas impurities could not be prevented or slowed down.

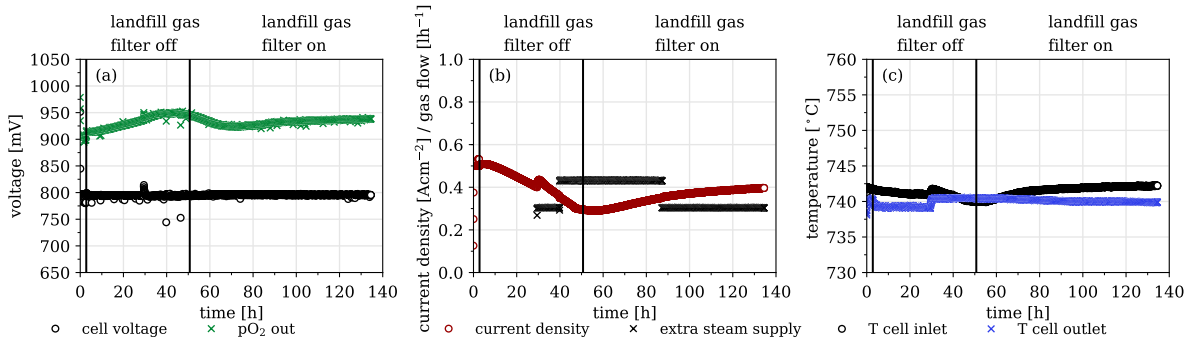


**Figure 6.8:** Test results of the potentiostatic operation without cleaning of the landfill gas and extra steam supply according to Figure 6.5. Plot (a): Cell voltage,  $p_{O_2}$  sensor at outlet of the cell; Plot (b): Extra steam supply volumetric flow, current density; Plot (c): Cell temperature inlet and outlet.

#### 6.2.4 Impedance spectra analysis

The impedance spectra recorded during by-passed activated carbon filter in the operation modes galvanostatic (compare Figure 6.6) and potentiostatic (compare Figure 6.7) are discussed in more detail in this section. In Figure 6.9 selected impedance spectra recorded during galvanostatic operation are shown in a Nyquist plot (a) and a DRT plot (b). The increasing and then decreasing trend of  $R_p$  of the impedance spectra shown in the Nyquist plot (see Figure 6.9(a)) is in line with the described dependencies of Figure 6.6(b). The DRT plot shown in Figure 6.9(b) allows to give conclusions about the landfill gas impurities poisoning and recovery of the anode processes. The four anode process peaks are following two trends an increasing and then decreasing trend or only an increasing trend. At the low frequency the  $P_{FR}$  peak is first slightly decreasing and then increasing during the activated carbon filter is by-passed. Even after passing the fuel through the filter again the  $P_{FR}$  peak increases further for a certain time and then decreases again. After 148 h of operation the  $P_{FR}$  peak is even 10.5 % lower than at the beginning of the test (orange and black line Figure 6.9(b)). Additionally the  $P_{FR}$  peak is shifted to higher frequencies as function of the operation time. The observation of

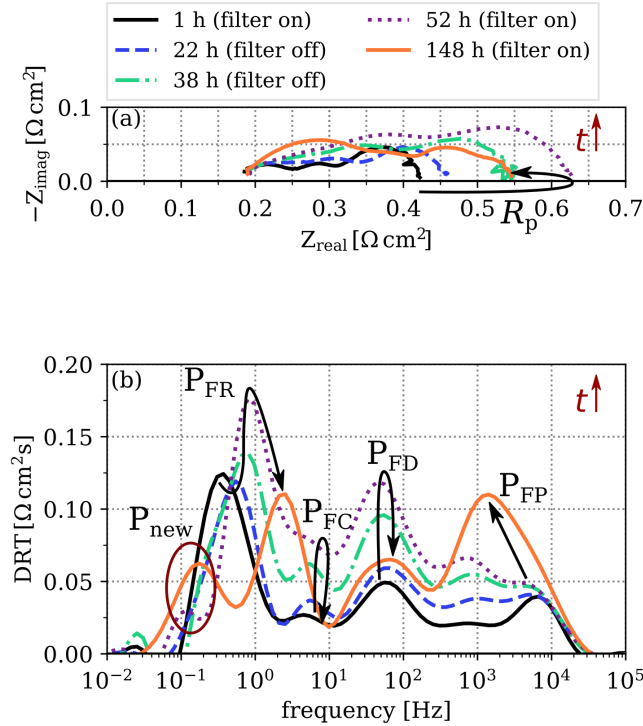


**Figure 6.9:** Selected impedance measurements over operation time ( $t$ ) recorded in the galvanostatic mode during real landfill gas plus extra  $\text{CO}_2$  and by-passed activated carbon filter for a certain amount of time (see Figures 6.1 and 6.6). Plot (a): Nyquist plot; Plot (b): DRT plot.

the frequency shift and the increase of  $P_{\text{FR}}$  peak at the beginning are indicating that the impurities preventing the reforming of  $\text{CH}_4$  by blocking the active anode sides. This conclusion is based on the dependencies of the landfill gas  $\text{CH}_4$  content impedance study which is described in Section 5.3. Furthermore, the decrease of the  $P_{\text{FR}}$  peak indicates that the  $\text{CH}_4$  reforming rate could be recovered by passing the landfill gas through the activated carbon filter again. Due to the fact that the  $P_{\text{FR}}$  is even lower after 148 h of operation time than at the beginning the  $\text{CH}_4$  reforming rate was maybe even further increased. Concluding that an activation of the active anodes sides might occurred. The second and third process with similar increasing and than decreasing trends over time are the  $P_{\text{FC}}$  and  $P_{\text{FD}}$  process. In this cases the process peaks are not shifted to a higher frequency. An increase of the  $P_{\text{FD}}$  process peak was also observed during the total flow rate variation study (see Section 5.2) but not during the  $\text{CH}_4$  content variation study (see Section 5.3). The increase of the  $P_{\text{FD}}$  peak in the total anode fuel flow rate variation study was caused by the increase of fuel available at the anode with

increasing anode fuel flow rate. In this case a higher amount of fuel present at the anode could be caused by the blocking of the active anode sides by the landfill gas impurities which would explain the similar impedance response behaviors in comparison to the total anode fuel flow rate study (see Section 5.2). The corresponding peak of the  $P_{FP}$  is increasing with increasing operation time and showing no recovery effects after the activated filter is passed again. The increase of the  $P_{FD}$  process peak was also noted during the anode fuel flow rate dependency study (see Section 5.2). This indicates that also in this case a higher amount of fuel is present at the TPB because the landfill gas impurities are prohibiting the electrochemical reactions. Summarized that the  $R_p$  value is only recovering to a certain extend after supplying the cell with cleaned landfill gas again because only the anode processes  $P_{FR}$ ,  $P_{FC}$  and  $P_{FD}$  but not the anode process  $P_{FP}$ . Additionally another process peak called  $P_{new}$  in Figure 6.9 can be noted in the low frequency range in the impedance spectra recorded at an operation time of 52 h and 148 h. One explanation could be that this peak is an uncertainty of the DRT plot. Another explanation might be that the peak reflects the permanent cell performance loss caused by the permanent presence of the landfill gas impurities at the active anode sides.

In Figure 6.10 selected impedance spectra of the potentiostatic mode during by-passed filter are shown in an Nyquist plot (a) and DRT plot (b). Considering the fact that during the potentiostatic operation the current density decreased during by-passed activated carbon filter (see Figure 6.10(b)) only impedance spectra recorded at the same current density can be compared. The full lines in Figure 6.10 show the reference impedance measurements at the specific current density which were recorded while the activated carbon filter was passed (see Figure 6.2) The dotted lines represent the corresponding impedance measurements recorded at the specific current density during the activated filter was by-passed in the potentiostatic operation mode. The reference measurements (full lines) show a similar trend change with increasing current than the measurements of the impedance current variation study reported in Section 5.2. At the beginning of by-passing the filter in the potentiostatic mode no differences between the recorded impedance measurement at  $0.5 \text{ A cm}^{-2}$  (dotted black line, Figure 6.10) and the reference measurement (full black line) are observed. Afterwards with the value of  $R_p$  rises with increasing operation time and corresponding decreasing current density. Additionally, the DRT plot in Figure 6.10(b) shows that the peaks of the four anode processes  $P_{FR}$ ,  $P_{FC}$ ,  $P_{FD}$  and  $P_{FP}$  are increasing with operation time which was also observed during the operation in the galvanostatic mode (compare Figure 6.9(b)). But the increasing

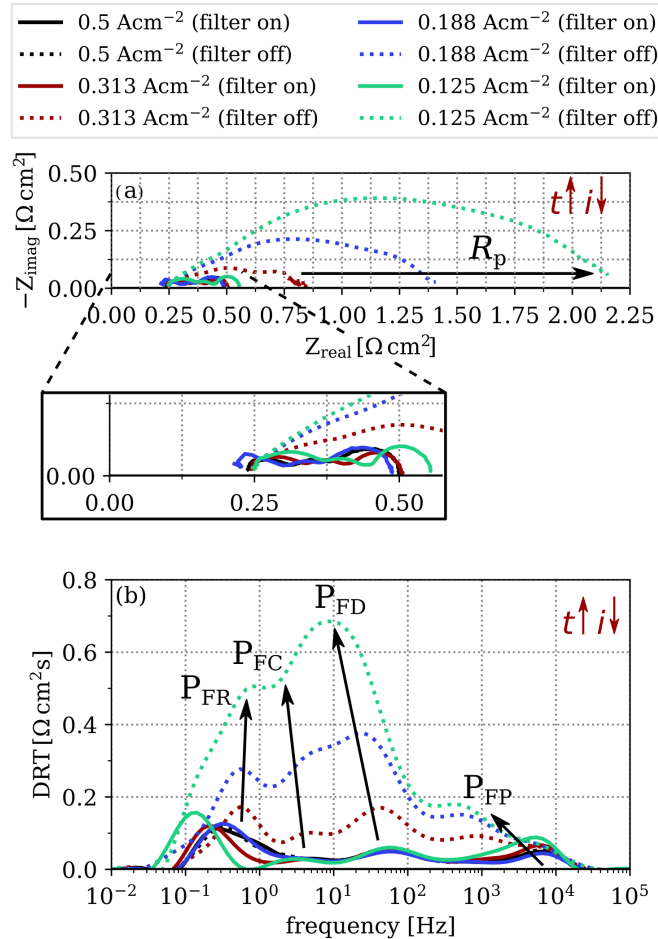


**Figure 6.10:** Selected impedance measurements (dotted lines) over operation time ( $t$ ) recorded in the potentiostatic mode during real landfill gas plus extra  $\text{CO}_2$  and by-passed activated carbon filter (see Figures 6.2 and 6.7). Full lines show the reference impedance measurements recorded at the same current density ( $i$ ) and fuel passed through the cleaning filter as illustrated in Figure 6.2. Plot (a): Nyquist plot; Plot (b): DRT plot.

magnitudes are different in this case. In the potentiostatic mode the highest increase in the DRT plot is noted for the  $P_{\text{FP}}$  and  $P_{\text{FC}}$  process while for the galvanostatic mode the highest increase is noted for the  $P_{\text{FR}}$ . A small part of the anode process peaks are caused by the decreasing current as noted by comparing the dotted lines with the full lines in Figure 6.10(b). Taking the results of the potentiostatic test with extra steam supply into account (see Section 6.2.3) the reason for the higher increasing magnitude of the anode process peaks in the potentiostatic mode in comparison to the galvanostatic mode might be not the amount of steam present at the anode. Another possible explanation is prohibiting of the landfill gas impurity deposition to a certain extend by the

electrochemical reactions occurring at the TFB. Due to the constant current density in the galvanostatic mode and the decreasing current density in the potentiostatic mode during by-passing the filter a higher electrochemical reaction rate is occurring in the galvanostatic mode. This relation might result in a lower landfill gas impurities deposition in the galvanostatic mode. This would be in line with H<sub>2</sub>S impurity comparison tests conducted in the potentiostatic and potentiostatic mode reported in literature as explained in Section 2.3.3.

### 6.2.5 Anode in-plane voltage comparison

One option for analyzing the poisoning effects of the landfill gas impurities along the cell is the measurement of the anode in-plane voltage. In Figure 6.11 the normalized anode in-plane voltages including the corresponding cell voltage/current density curves of the galvanostatic (filter off) test and the potentiostatic test with extra steam (filter off) are shown. In terms of the galvanostatic operation the in-plane voltage decreased linear for the operation time the filter was by-passed. After the filter was passed again the in-plane voltage increased linear for approximately the same time the filter was by-passed. Additionally the curve increased with the same absolute slope as it was decreasing before. Afterwards the voltage in-plane curve increase started to slow down until a maximum was reached at approximately 160 h of operation time. At least for the time the filter was by-passed the in-plane voltage trend represents the first derivative trend of the corresponding cell voltage trend (black line, Figure 6.11(b)). This dependency was also reported in literature for H<sub>2</sub>S poisoning of the water gas shift [57]. During the recovering process (filter on) the dependency was not observed anymore. Underlining the fact that beside sulfur also other impurities in the landfill gas as for example siloxanes are poisoning the anode reactions. In terms of the potentiostatic test with extra steam supply the trend of the in-plane voltage (red line, Figure 6.11(a)) was the same as the trend of the corresponding current density trend (red line, Figure 6.11(b)). For this test the in-plane voltage was not representing the first derivative of the current density during by-passing the filter as observed for the galvanostatic test. The manually change of the anode gas composition by adding extra steam could be the explanation for the different behavior.

The in-plane voltage of the potentiostatic test (without extra steam supply) and the corresponding current density trend is shown in Figure 6.12. In this case the in-plane voltage (black line) was representing the first derivative of the current density (red line)

again to a certain attend. The current density was decreasing continuously from around  $0.5 \text{ A cm}^{-2}$  down to  $0 \text{ A cm}^{-2}$  during the 120 h the filter was by-passed. While the corresponding in-plane voltage (black line) was first exponentially decreasing to a minimum which was reached at 60 h of by-passing the filter and then increasing again.

In general the in-plane voltages showed for the tests without extra steam supply a similar behavior as during  $\text{H}_2\text{S}$  poisoning [57]. The different in-plane behavior after passing the filter again might illustrate that the non-permanent degradation by sulfur was recovered but the deposition of other impurities like for example siloxanes were more permanent. This is supported by the corresponding cell voltage and current density trends.

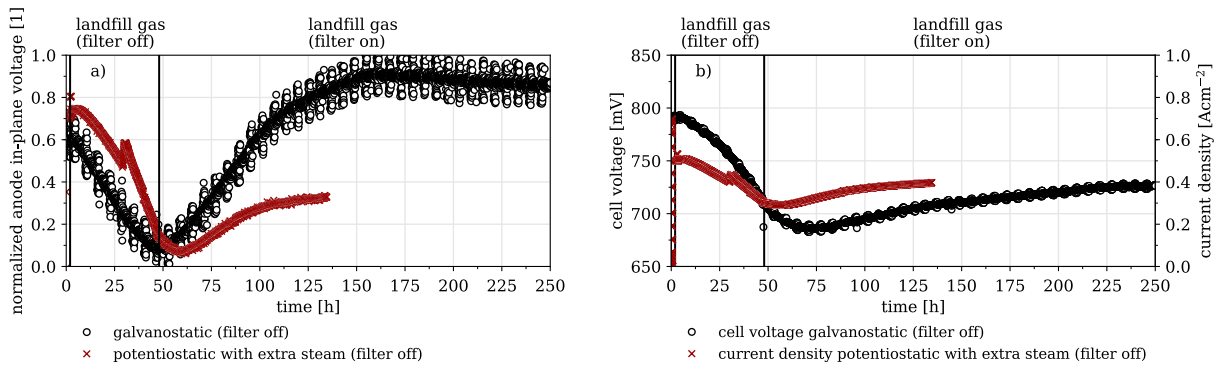


**Figure 6.11:** Normalized in-plane voltages and corresponding cell voltage/current density curves of the galvanostatic test (filter off) and the potentiostatic test with extra steam supply (filter off). Plot a) Normalized anode in-plane voltages; Plot b) Cell voltage galvanostatic test (filter off) and current density potentiostatic test with extra steam (filter off).

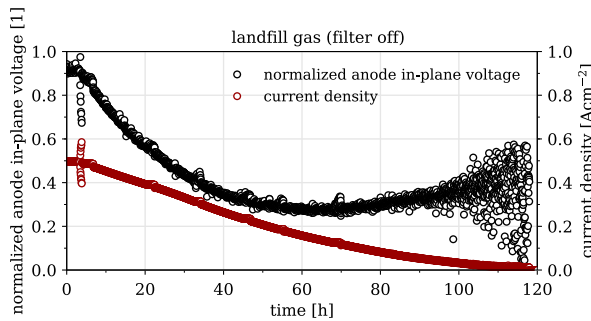


**Figure 6.12:** Normalized in-plane voltage and corresponding current density of the potentiostatic test (filter off).

### 6.2.6 Area specific resistance increase comparison (filter off)

In the next step the effect of not cleaning the landfill gas during the operation modes galvanostatic, potentiostatic and potentiostatic plus extra steam are compared by the *ASR* increase. The *ASR* increase ( $\Delta ASR$ ) shown in Figure 6.13 was calculated according to Equation 2.24.

In Figure 6.13 all three curves show an exponential type behavior with the difference that the *ASR* during the two potentiostatic operation tests increased faster than during the galvanostatic operation. After 40 h of operation the *ASR* in the potentiostatic modes increased by  $0.48 \Omega \text{cm}^2$  and  $0.21 \Omega \text{cm}^2$  whereas the *ASR* in galvanostatic operation increased by  $0.12 \Omega \text{cm}^2$ . The lower *ASR* increase during potentiostatic operation with extra steam in comparison to the normal potentiostatic operation results from a better initial cell performance. The first addition of extra steam caused immediately an *ASR* decrease of  $0.05 \Omega \text{cm}^2$  (green curve). Afterwards, the *ASR* increase continued like before the extra addition of steam. The second addition of extra steam was showing no effect on the *ASR*. These observations are in line with the results shown in Figures 6.8 and 6.11.

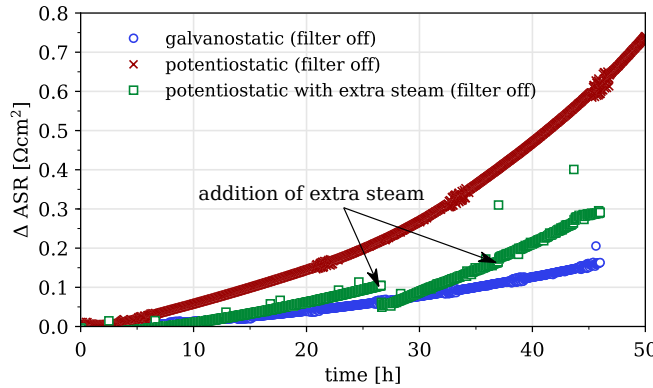


**Figure 6.13:** Area specific resistance increase ( $\Delta ASR$ ) of the cells after turning of the filter during landfill gas supply. Blue line illustrates the galvanostatic operation the red line the potentiostatic operation and the green line the potentiostatic operation with extra steam supply.

'This indicates that the potentiostatic operation mode is more affected during the time the landfill gas was not cleaned than the galvanostatic operation mode' [96]. A manual

increase of steam partial pressure at the anode during potentiostatic mode could not reduce the poisoning effects. An explanation could be that during galvanostatic operation the oxygen ions passed through the electrolyte prevented the poisoning effect to a certain extend and not the resulting higher steam partial pressure. During potentiostatic operation the current density was lowered over time to achieve a constant cell voltage. By lowering the current density the amount of passing oxygen ions through the electrolyte was also lowered which might result in a faster deposition of the landfill gas impurities. Similar conclusions were made by Cheng et al. [66] in terms of  $\text{H}_2\text{S}$  poisoning during galvanostatic and potentiostatic operation.

## 6.3 Cleaning method comparison after non cleaned landfill gas operation

The  $ASR$  values determined from the  $iV$ -curves [based on Equation 2.23] before the operation without gas cleaning, after it and after attempted regeneration (see Table 6.1) are shown in Figure 6.14' [96]. The initial  $ASR$  was  $0.44 \Omega \text{cm}^2$  during the galvanostatic test and the potentiostatic test with extra steam. During the potentiostatic test the initial  $ASR$  was  $0.53 \Omega \text{cm}^2$ .

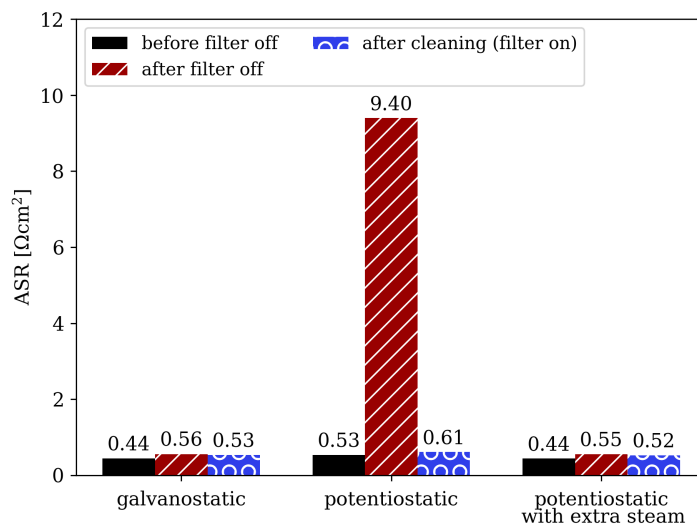


**Figure 6.14:** Comparison of the cell  $ASR$  determined from the  $iv$ -curves with and without cleaning of the galvanostatic and the two potentiostatic tests.

The  $ASR$  increased 27% in the galvanostatic test and 25% in the potentiostatic test with extra steam after the cells were operated for 46 h without cleaned landfill gas plus

$\text{CO}_2$ . In the galvanostatic case the cell was operated for 222 h with cleaned landfill gas plus  $\text{CO}_2$  afterwards. Whereas in the potentiostatic case with extra steam the cell was only operated for 102 h with cleaned landfill gas plus  $\text{CO}_2$  subsequently due to limitations of real landfill gas supply. 'In the potentiostatic test the  $ASR$  increased 1774 % after 125 h of operation without cleaned landfill gas plus  $\text{CO}_2$ ' [96].

## 6.4 Conclusion

The aim of the study presented in this chapter was to investigate the operation of SOFC cells fueled with real landfill gas supply and extra  $\text{CO}_2$  for internal dry reforming conditions. 'The operation modes galvanostatic and potentiostatic were compared with and without cleaning the landfill gas via an activated carbon filter upstream of the cell' [96]. Moreover the steam partial pressure at the anode was investigated during potentiostatic operation for a further comparison with the galvanostatic operation.

In general this study pointed out that it is possible to operate a cell with real landfill gas and  $\text{CO}_2$  in galvanostatic and potentiostatic operation modes. In both cases the SOFC performance was stable during the time the landfill gas was cleaned. In terms of the tests with landfill gas fueled SOFCs without cleaning the results indicate that the cell performance during potentiostatic operation was more affected than during galvanostatic operation."

A manual increase of the anode steam partial pressure during potentiostatic operation could not reduce the performance gap between the galvanostatic and potentiostatic operation while operating without cleaned landfill gas. An explanation for this dependency could be the decreasing amount of oxygen ions on the anode side during potentiostatic operation as the degradation led to decreasing current density. The differences of the impurity poisoning effects on the anode processes in the galvanostatic mode and potentiostatic mode were analyzed using the recorded impedance measurements. For a better understanding about the process dependencies the results of the pre-mixed landfill gas impedance study explained in Chapter 5 could be used. Additionally the anode in-plane voltage trends were compared for a more detailed understanding about the cell performance loss caused by the landfill gas impurities along the cell.

"Even though the degradation in potentiostatic mode was larger, it is less detrimental to

the cell, because the current density (power output) is lowered and no critically low voltages occur as during degradation in galavanostatic mode. The cell voltage trends while feeding not cleaned landfill to the SOFC indicate the presence of different impurities [like for example siloxanes,] probably in addition to sulfur. Additionally, two different regeneration strategies were applied. The tests showed that the cell performance was recovered to a certain degree by supplying the cell with a H<sub>2</sub>/H<sub>2</sub>O mixture and operating under current density or by using steam as a reforming agent instead of CO<sub>2</sub> and operating at OCV in addition to a higher operation temperature.”

# **7 Durability of SOFCs with anode off-gas recirculation**

Avoiding the permanent supply of extra reforming agent during the biogas fueled SOFC operation would simplify the SOFC system maintenance and reduce costs. As described in Section 2.3.2, anode off-gas recirculation is one option to avoid carbon formation during biogas fueled SOFC operation and also no permanent external reforming agent supply is needed. The anode exhaust gas consists to a certain amount of the reforming agents steam and CO<sub>2</sub>. Additionally, the presence of the O<sub>2</sub> ions at the anode, coming through the electrolyte during operating under current, influences the possibility of carbon formation at the anode. The following chapter investigates the option of anode off-gas recirculation for preventing carbon formation at the SOFC anode during landfill gas supply. Firstly, the semi 1D cell model including an algorithm for determining stable carbon activity conditions is presented. Secondly, the model was used for determining possible operation conditions. Finally, an experimental durability study was conducted in order to proof the possible operation conditions determined by the simulation approach.

## **7.1 Carbon activity algorithm and semi 1D cell model**

To estimating operation conditions for biogas fueled SOFC's by considering anode off-gas recirculation for avoiding carbon formation a semi 1D cell model and an algorithm was developed. The semi 1D cell model is based on the assumptions and simplifications listed below.

- considers a thermodynamic perspective (Gibbs free energy reactor).
- equal current density distribution along the cell.
- thermal energy interaction with the surroundings is neglected.

- heat exchange along the cell caused by e.g. reforming reactions and electrochemical reactions is not considered.
- assuming same reforming rate ( $r_{\text{CH}_4}$ ) for the  $\text{CH}_4$  steam reforming and  $\text{CH}_4$  dry reforming process.

The structure of the implemented program can be divided into two main sections. On the one hand side the algorithm for determining a stable carbon activity along the cell by considering anode off-gas recirculation (see Figure 7.2) and on the other hand side the semi 1D cell model which is used for calculating the carbon activity along the cell (see Figure 7.1) in each algorithm step. The step number of the algorithm step is given by the variable  $j$  while the position along the cell is defined by the variable  $k$ . The inlet and outlet parameters of the designed program are summarized in Table 7.1. The algorithm was implemented in the programming language Python and is based on the self developed program ElchDAT (see Appendix A).

**Table 7.1:** Input and output parameters of the developed model for determining the carbon activity along the SOFC during biogas supply and anode off-gas recirculation.

input parameter
inlet biogas composition (volumetric fraction)
$\Phi_{\text{CH}_4}, \Phi_{\text{CO}_2}, \Phi_{\text{CO}}, \Phi_{\text{N}_2}, \Phi_{\text{H}_2}, \Phi_{\text{H}_2\text{O}}, \Phi_{\text{O}_2}$
inlet volumetric flow biogas $\dot{V}_{\text{biogas}} [\text{L h}^{-1}]$
extra volumetric flow $\text{CO}_2$ (beginning) $\dot{V}_{\text{CO}_2,extra} [\text{L m}^{-1}]$
fuel utilization ( $FU$ ) [%] /
current density ( $i$ ) [ $\text{A cm}^{-2}$ ]
anode off-gas recirculation ( $aogr$ ) [%]
operation temperature ( $T_{op}$ ) [ $^{\circ}\text{C}$ ]
cell area ( $A_{cell}$ ) [ $\text{cm}^2$ ]
number of sub cells ( $n_{cell}$ ) [1]
simulation tolerance ( $Tol$ ) [1]
output parameter
output molar flow of each sub cell $k$
$\dot{n}_{\text{CH}_4}(k,j), \dot{n}_{\text{CO}_2}(k,j), \dot{n}_{\text{CO}}(k,j), \dot{n}_{\text{N}_2}(k,j), \dot{n}_{\text{H}_2}(k,j), \dot{n}_{\text{H}_2\text{O}}(k,j), \dot{n}_{\text{O}_2}(k,j)$
output molar fraction of each sub cell $k$
$x_{\text{CH}_4}(k,j), x_{\text{CO}_2}(k,j), x_{\text{CO}}(k,j), x_{\text{N}_2}(k,j), x_{\text{H}_2}(k,j), x_{\text{H}_2\text{O}}(k,j), x_{\text{O}_2}(k,j)$
carbon activity of each sub cell $k$ $\alpha_c(k,j)$
carbon activity mean value cell of the cell $\alpha_{c,cell}(j)$

As shown in Figure 7.1 the semi 1D cell model divides the cell into  $n_{cell}$  sub cells and considers the inlet fuel biogas (green arrow), the extra reforming agent  $\text{CO}_2$  (grey arrow) at the beginning and the anode exhaust gas (orange arrow) which can be recirculated. Additionally, the blue arrows are indicating the  $\text{O}_2$  supply through the cathode. As mentioned previously, the position of the sub-cell is indicated by the variable  $k$ . The inlet gas composition is at the position  $k = 0$  while the cell outlet composition is at  $k = n_{cell}$ . Each sub-cell is simulated as a thermodynamic reforming reactor in which Gibbs free energy minimization is used to determine the gas composition after reformation. As shown in Table 7.1, the inlet biogas composition is defined by the molar fractions of the

gas species present in the biogas. In the simulation, the gas species CH<sub>4</sub>, CO<sub>2</sub>, CO, N<sub>2</sub>, H<sub>2</sub>, H<sub>2</sub>O and O<sub>2</sub> are considered. The constant molar flow rates of the considered species ( $\dot{n}_{XX}(k = 0, j)$ ) of the entering gas composition at the position  $k = 0$  was calculated from the volumetric flow rates ( $\dot{V}_{XX}$ ) by using the ideal gas law as defined in Equation 7.1. For this calculation the mass flow controller temperature ( $T_{MFC}$ ) instead of the SOFC operation temperature ( $T_{op}$ ) has to be used.

$$\dot{n}_{XX}(k = 0, j) = \frac{p\dot{V}_{XX}}{RT_{MFC}} \quad (7.1)$$

The volumetric flow rates needed for Equation 7.1 are calculated based on Equations 7.2 and 7.3 because for the volumetric CO<sub>2</sub> flow the extra addition of the reforming agent CO<sub>2</sub> in the first simulation step ( $j = 0$ ) has to be considered.

$$\dot{V}_{XX}(k = 0, j) = \Phi_{XX}\dot{V}_{Biogas} \quad (7.2)$$

$$\dot{V}_{CO_2}(k = 0, j = 0) = \Phi_{CO_2}\dot{V}_{Biogas} + \dot{V}_{CO_2,extra} \quad (7.3)$$

As mentioned previously and shown in Figure 7.1, the gas composition of each sub-cell after reforming is determined by Gibbs free energy minimization (see Eq. 2.9) as further explained in Appendix A. The molar flows of the considered species which are used for the Gibbs free energy minimization process are the outlet flows of the previous sub-cell ( $\dot{n}_{XX}$ ). For the gas species O<sub>2</sub> the equivalent amount of O<sub>2</sub> according to the applied current density ( $i$ ) has to be added as defined in Equation 7.4. The total O<sub>2</sub> molar flow rate ( $\dot{n}_{O_2,F\ total}$ ) according to the applied current density ( $i$ ) is based on Faraday's law (see Eq. 2.25) and shown in Equation 7.5. Additionally, a linear current distribution along the cell is assumed which results in an equal distribution of the corresponding O<sub>2</sub> shown in Equation 7.6.

$$\dot{n}_{O_2,Gibbs\ in}(k, j) = \dot{n}_{O_2}(k - 1) + \dot{n}_{O_2,F}(k, j) \quad (7.4)$$

$$\dot{n}_{O_2,F\ total}(i) = \frac{iA_{cell}}{z_e F} \quad (7.5)$$

$$\dot{n}_{O_2,F}(k, j) = \frac{1}{n_{sub\ cells}}\dot{n}_{O_2,F\ total} \quad (7.6)$$

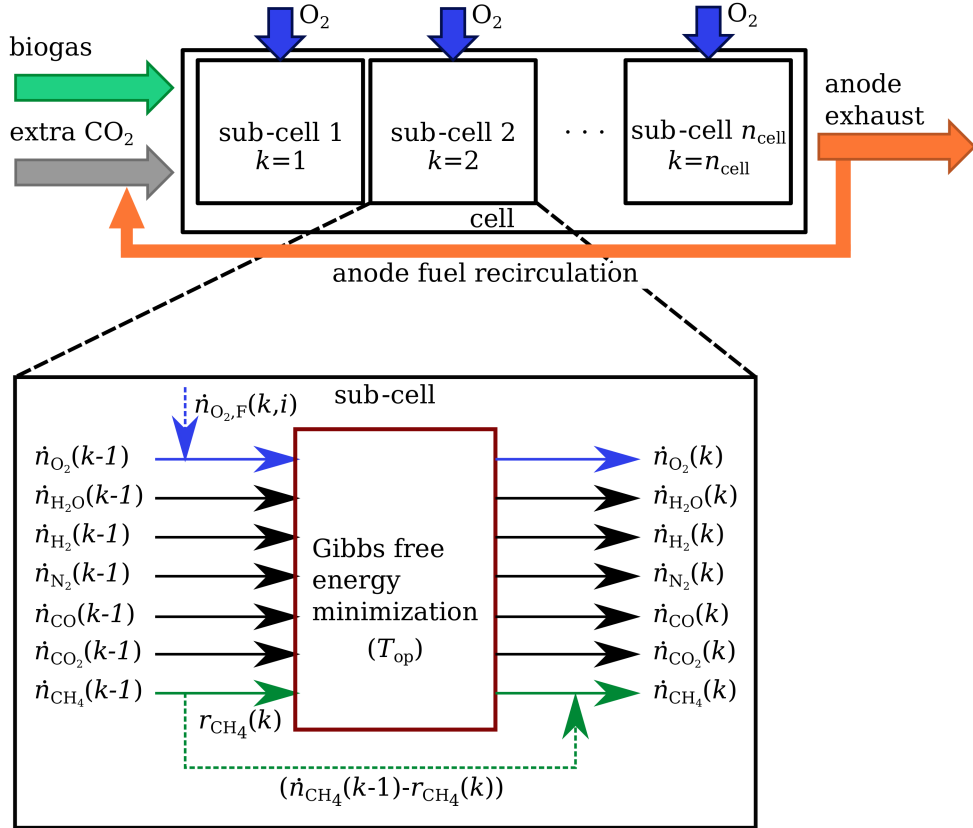


**Figure 7.1:** Schematic sketch of the thermodynamic semi-1D cell model for studying anode off-gas recirculation to avoid carbon formation of landfill gas fueled solid oxide fuel cells.

Additionally, a reforming rate of CH<sub>4</sub> was considered. The reforming rate of each sub-cell is based on the reforming rate definition (see Eq. 2.10) for steam reforming (see Eq. 2.4) at the SOFC anode. For this model the assumption was made that the equation is also valid for the dry reforming process (see Eq. 2.8). Equation 7.7 defines the CH<sub>4</sub> reforming rate  $r_{CH_4}$ .

$$r_{CH_4}(k, j) = 4274 p_{CH_4}(k-1) A_{\text{cell}} e^{-82000(RT_{\text{op}})^{-1}} \quad (7.7)$$

As shown in Figure 7.1 and defined in Equation 7.9, the CH<sub>4</sub> molar flow rate of each sub-cell ( $\dot{n}_{CH_4}(k, j)$ ) is the sum of the CH<sub>4</sub> molar flow rate determined by Gibbs free energy minimization and the CH<sub>4</sub> amount which was not considered for the reforming

process.

$$\dot{n}_{\text{CH}_4, \text{Gibbs in}}(k, j) = r_{\text{CH}_4}(k, j) \quad (7.8)$$

$$\dot{n}_{\text{CH}_4}(k) = \dot{n}_{\text{CH}_4, \text{Gibbs out}}(k, j) + (\dot{n}_{\text{CH}_4(k-1,j)} - r_{\text{CH}_4}(k, j)) \quad (7.9)$$

For the cases the simulation step  $j$  is greater 1 the anode off-gas recirculated gas has to be taken into consideration (see Figure 7.2). The molar flow rates of the gases present in the anode off-gas have to be added to the entering molar flow rates of the first sub-cell ( $k = 1$ ). The anode off-gas molar flow rates  $\dot{n}_{\text{XX,aofg}}$  are calculated according to Equation 7.10 considering the gas species of the last sub-cell ( $k = n_{\text{cell}}$ ) of the previous simulation step ( $j = j - 1$ ) and the recirculation rate ( $aofg_{\text{aofg}}$ ).

$$\dot{n}_{\text{XX,aogr}}(k = 1, j > 1) = \dot{n}_{\text{XX}}(k = n_{\text{cell}}, j = j - 1) \frac{aofg_{\text{rate}}}{100} \quad (7.10)$$

The carbon activity ( $\alpha_c(k, j)$ ) of each sub-cell and during each simulation step ( $j$ ) based on the Boundard reaction (see Eq. 2.13 and 2.14). The exact determination process is also further described in Appendix A. The mean values ( $\alpha_{c, \text{cell}}$ ) of the carbon activity values along the cell for each simulation step are calculated according to Equation 7.11.

$$\alpha_{c, \text{cell}}(j) = \frac{1}{n_{\text{cell}}} \sum_{k=1}^{n_{\text{cell}}} \alpha_c(k, j) \quad (7.11)$$

In each step of the carbon activity determination algorithm (see Figure 7.2), the carbon activity relative error  $E(j)$  is calculated considering the carbon activities of the first sub-cell of the steps  $j$  and  $j - 1$  as defined in Equation 7.12. If  $E(j)$  is smaller than the allowed simulation tolerance  $Tol$ , the calculation process is finished which means that the simulation has determined a stable gas distribution and carbon activity along the cell.

$$Err(j) = \frac{|\alpha_c(k = 1, j) - \alpha_c(k = 1, j - 1)|}{\alpha_c(k = 1, j)} \quad (7.12)$$

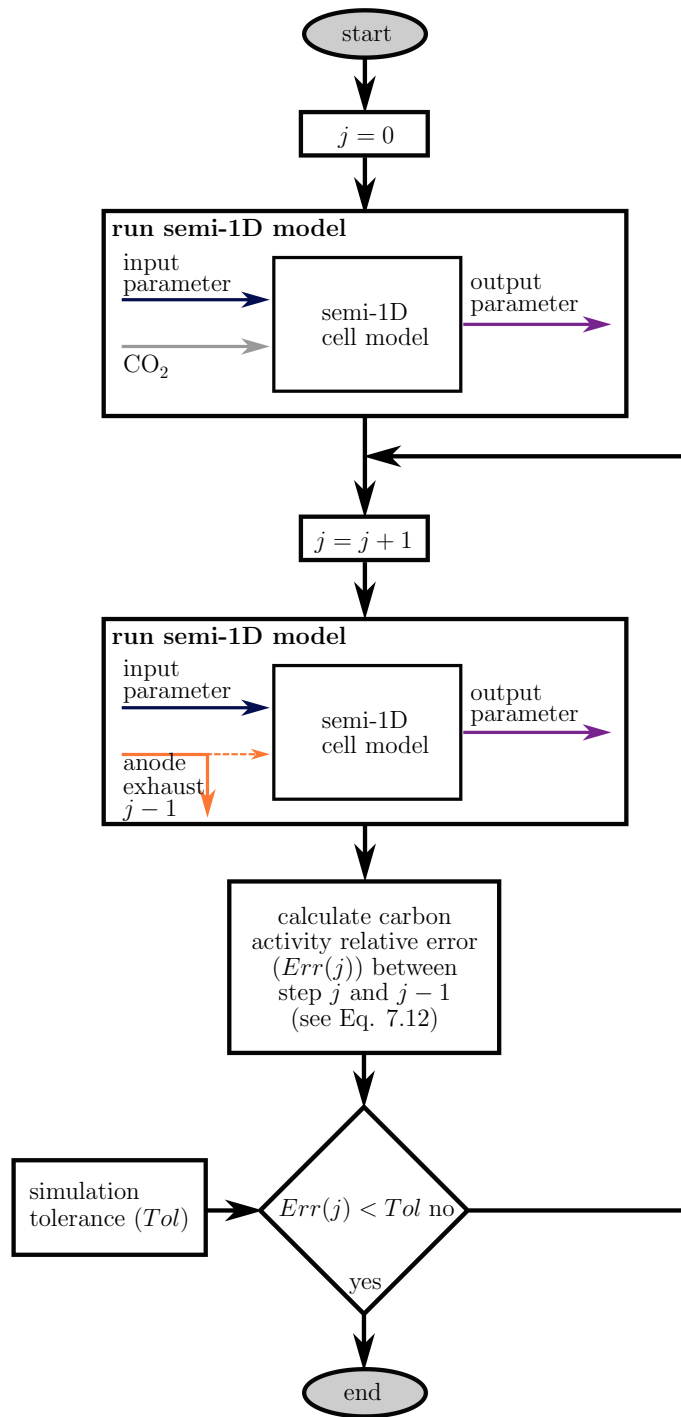


**Figure 7.2:** Illustration of the algorithm to run the semi-1D SOFC model for evaluating anode off-gas recirculation to avoid carbon formation during biogas supply.

## 7.2 Determination of possible operation parameters

For analyzing the effect of anode off-gas recirculation during landfill gas fueled SOFC, a parameter study was conducted. Therefore, the input parameter of the semi 1D cell model simulation were varied (see Table 7.2). The fuel recirculation was increased step wise from 10 % to 50 % and the current density was increased step wise from  $0.1 \text{ A cm}^{-2}$  to  $0.5 \text{ A cm}^{-2}$ . The other parameters like e.g. the operation temperature of  $750^\circ\text{C}$  and the number of sub-cells of 30 were kept constant as summarized in Table 7.2.

**Table 7.2:** Parameters of the simulation study for determining possible operation conditions for landfill gas fueled SOFCs considering anode off-gas recirculation for preventing carbon formation.

parameter	value
current density ( $i$ ) [ $\text{A cm}^{-2}$ ]	0.1, 0.3, 0.5
anode off-gas recirculation rate ( $aogr$ )[%]	10, 30, 50
inlet biogas composition	landfill gas (34 vol% $\text{CH}_4$ , 23 vol% $\text{CO}_2$ , 43 vol% $\text{N}_2$ )
inlet volumetric flow biogas ( $\dot{V}_{\text{biogas}}$ ) [ $\text{L h}^{-1}$ ]	4
extra volumetric flow $\text{CO}_2$ (beginning) [ $\text{L h}^{-1}$ ]	2
cell area ( $A_{\text{cell}}$ ) [ $\text{cm}^2$ ]	16
number of sub-cells [1] ( $n_{\text{cell}}$ )	30
simulation tolerance ( $Tol$ )	0.001

The results of the semi 1D-model simulations conducted with the parameters according to Table 7.2 are shown in Figures 7.3 and 7.4. In Figure 7.3 the carbon activity along the cell is represented as function of the anode off-gas recirculation (10 % blue line, 30 % red line, 50 % black line). Furthermore, from Figures 7.3(a) to 7.3(c) the dependency of the carbon activity and the current density is shown ( $0.1, 0.3, 0.5 \text{ A cm}^{-2}$ ). The lowest carbon activity values are at the cell inlet for a current density of  $0.1 \text{ A cm}^{-2}$  while for the current densities  $0.3 \text{ A cm}^{-2}$  and  $0.5 \text{ A cm}^{-2}$  the lowest carbon activity values are at the cell inlet and outlet. The carbon activity curve increases steeply in the first quarter of the cell until a maximum is reached. Afterwards, the carbon activity decreases continuously to the cell outlet. The absolute slope while the carbon activity is decreasing is smaller than the absolute slope while the carbon activity is increasing at the inlet area of the

cell. The anode fuel recirculation rate is influencing the maximum carbon activity and the slopes of the carbon activity trend. As lower the anode fuel recirculation rate the higher is the maximum carbon activity in the cell. The absolute values of the increasing and decreasing slopes of the carbon activity trend are increasing with decreasing anode off-gas recirculation rate. The applied current density is not changing the general curve trend but lowering all curves by a certain factor with increasing current density (compare Figure 7.3(a)-(c)). The conducted study indicates that, from a thermodynamic point of view, carbon formation occurs during all three fuel recirculation rates at a applied current current density of  $0.1 \text{ A cm}^{-2}$  (see Figure 7.3(a)). For the scenarios with applied current densities of  $0.3 \text{ A cm}^{-2}$  and  $0.5 \text{ A cm}^{-2}$  no carbon formation would occur at the cell from a thermodynamic point of view.

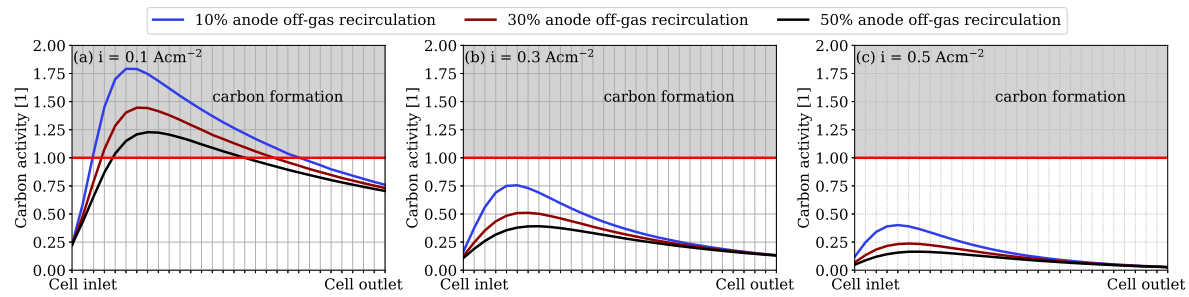


**Figure 7.3:** Carbon activity along the cell as function of the anode off-gas recirculation rate and applied current density determined with the semi 1D cell model.

For providing a better understanding of the carbon activity trends the corresponding molar fractions of the present gas species along the cell are shown in Figure 7.4. From left to right the current density is increased in the same steps as in Figure 7.3 and from top to bottom the anode off-gas recirculation rate is increased according to Table 7.2. In all scenarios the molar fraction of  $\text{CH}_4$ ,  $\text{CO}_2$ ,  $\text{H}_2\text{O}$  is exponentially declining close to the cell inlet while the molar fractions of  $\text{CO}$  and  $\text{H}_2$  are exponentially increasing. After around the first quarter of the cell the molar fraction of the  $\text{CH}_4$  decreases further with a linear slope. The molar fractions of  $\text{CO}_2$  and  $\text{H}_2\text{O}$  reach a minimum in the first quarter of the cell and increase linearly again afterwards. The linear slope increases with increasing current density.

The minimum and maximums are reached in the first quarter of the cell which corresponds to the area with the highest carbon activity (compare with Figure 7.3). This dependencies clearly show that the carbon activity is the highest at the point were the  $\text{CO}_2$  and  $\text{H}_2\text{O}$  concentrations are the lowest. The results show that the  $\text{CO}_2$  and  $\text{H}_2\text{O}$

concentrations at the cell inlet are higher with increasing anode off-gas recirculation. Furthermore, the curve trends indicate that the carbon activity is mainly dependent on the anode off-gas recirculation rate and on the O<sub>2</sub> amount of oxygen along the cell. At the inlet the anode off-gas recirculation rate has a higher effect on the carbon activity while closer to the cell outlet the carbon activity is more dependent on the amount of O<sub>2</sub> defined by the current density (see Eq. 7.4). Furthermore, in a more realistic case of a non linear current density distribution along the cell, the current density would be higher at the inlet which would result in an even lower carbon activity close to the cell inlet and probably to a slightly higher carbon activity at the cell outlet.

Moreover, the molar fraction trends of the species along the cell are similar to the trends presented by Janardhanan [121, fig. 10]. In his study Janadhanan presents the results of a detailed multi-physics biogas fueled SOFC model considering biogas reforming kinetics, electrochemical properties and species transport. This indicates that the results of the simplified semi-1D model approach are to a certain extend reliable.

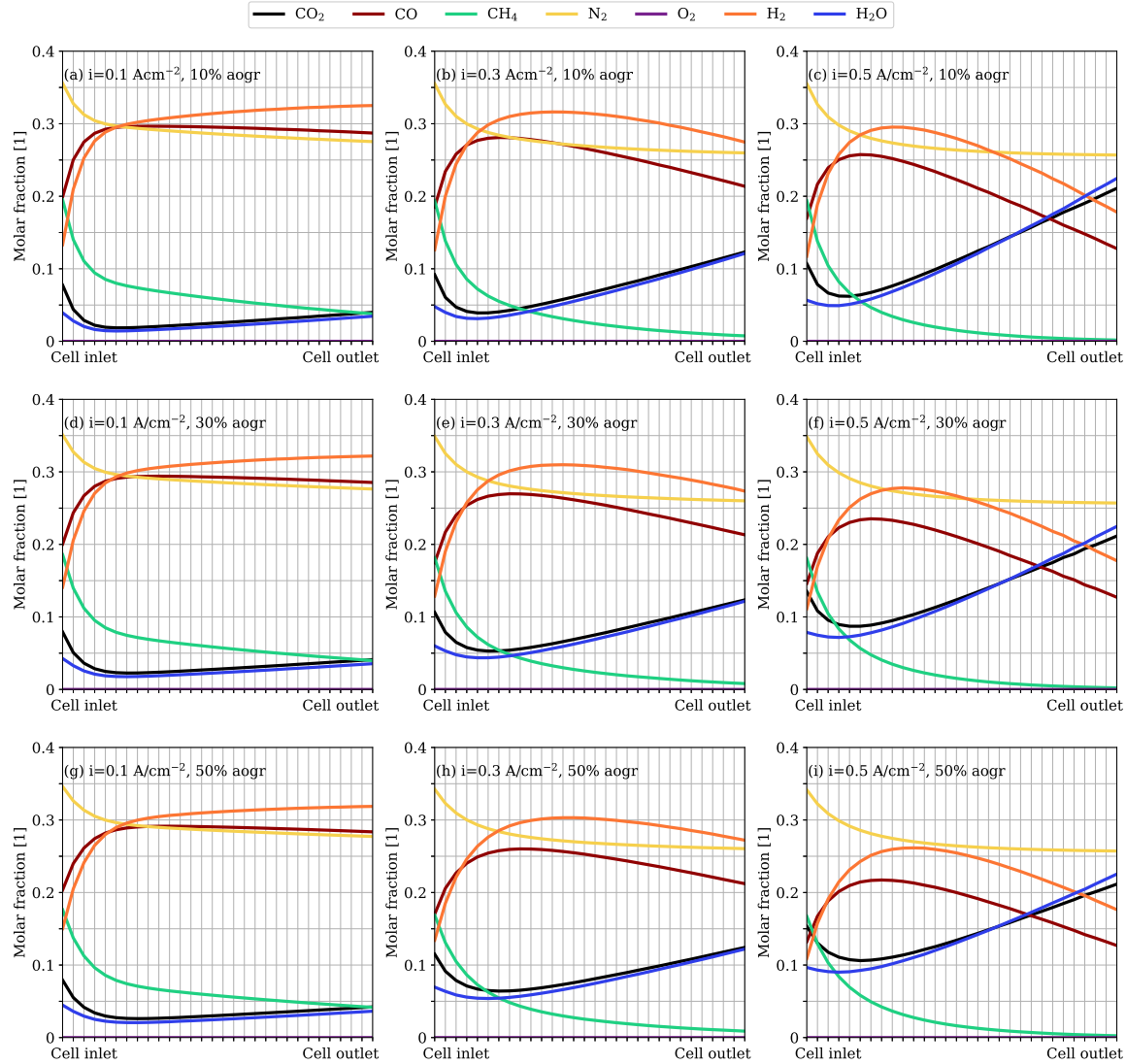


**Figure 7.4:** Molar fractions of the gases present along the cell as function of the anode off-gas recirculation rate (aogr) and applied current density ( $i$ ) determined with the semi 1D cell model.

### 7.3 Experimental durability study

Based on the theoretical simulation study described in the previous section, an experimental study was conducted for proving the results of the simulation and investigating the performance of landfill gas fueled SOFCs with anode off-gas recirculation. To ensure no carbon formation all tests were operated at a current density of  $0.5 \text{ A cm}^{-2}$ .

As shown in Table 7.3, five tests using two sister cells were conducted at an operation temperature of 750 °C. Further information about the cells is provided in Section 3.1.5. Four tests were conducted with pre-mixed biogas (composition similar to real landfill gas, see Section 3.1.3) and one test with real landfill gas which was pre-cleaned by an activated carbon filter, as described in Section 3.1.3. The used set up for realizing the fuel recirculation is described in Section 3.1.4. The anode was supplied with  $4 \text{ L h}^{-1}$  and for approximately 5 minutes with  $2 \text{ L h}^{-1}$  extra CO<sub>2</sub>. After the fuel recirculation flow was stable for around 5 – 10 minutes, the extra CO<sub>2</sub> supply was turned off. The operation time listed in Table 7.3 only considers the time while the cell is operated with fuel recirculation and without the extra CO<sub>2</sub> supply at the beginning. During all tests the cathode was supplied with air. Before and after each test segment a 'finger print' plus an impedance measurement and an iV-curve recorded with pre-mixed landfill gas supply were conducted for comparison reasons. The first test was operated with  $4 \text{ L h}^{-1}$  pre-mixed landfill gas supply and  $2 \text{ L h}^{-1}$  extra CO<sub>2</sub> for approximately 360 h hours and was used as a reference test. In order to get a good estimation of the long term durability during operation with anode fuel operation, the 50 % fuel recirculation test was conducted for around 600 h. The other tests conducted with pre-mixed landfill gas and real landfill gas with fuel recirculation rates of 30 % and 10 % were operated for around 150 h. This allows a direct comparison at least for the last three tests. The different operation test length was also caused by the maintenance requirements of the fuel recirculation set up as mentioned in Section 3.1.4.

**Table 7.3:** Settings of the conducted landfill gas fueled single cell tests with anode off-gas recirculation to avoid carbon formation.

	landfill gas type	anode off-gas recirculation rate [%]	test length [h]
1 (cell 1)	pre-mixed	0, ( $2 \text{ L h}^{-1}$ extra CO <sub>2</sub> )	≈ 360
2 (cell 1)	pre-mixed	50	≈ 600
3 (cell 2)	pre-mixed	30	≈ 150
4 (cell 2)	pre-mixed	10	≈ 150
5 (cell 2)	real	30	≈ 150

anode supply: landfill gas flow  $4 \text{ L h}^{-1}$  plus  $2 \text{ L h}^{-1}$  extra CO<sub>2</sub> at the beginning  
cathode supply: air; operation temperature 750 °C

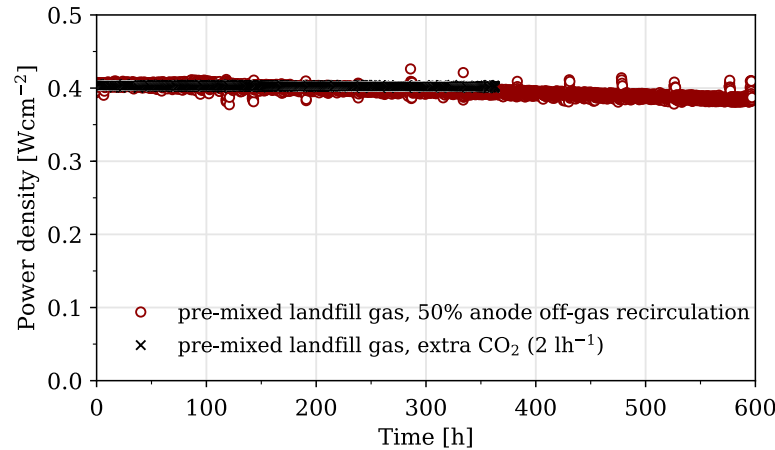


**Figure 7.5:** Power density over time of the pre-mixed landfill gas plus  $\text{CO}_2$  (reference test) and pre-mixed landfill gas with 50 % anode off-gas recirculation.

The power density as function of the operation time for the reference test (extra  $\text{CO}_2$  supply) (black crosses) and the test with 50 % fuel recirculation (red circles) is shown in Figure 7.5. First of all, the results show that the cell could be operated successfully with 50 % and no extra  $\text{CO}_2$  supply for 600 h. The higher power density fluctuation of the test with anode off-gas recirculation in comparision to the reference test was caused by the pump of the anode off-gas recirculation test set-up (see Section 3.1.4). Both tests start at an power density of approximately  $0.4 \text{ W cm}^{-2}$ . Afterwards, both power density curves are decreasing continuously. The power density decrease of the reference curve corresponds to a degradation rate of  $1.0\%/\text{1000h}$  while the decrease of the 50 % recirculation test corresponds to an degradation rate of  $8.4\%/\text{1000h}$ . This test results give a first indication for the usage of anode off-gas recirculation having an effect on the cell performance. The power density trends over operation time of the pre-mixed landfill gas tested, conducted with 30 % (blue circles) and 10 % (orange crosses) anode off-gas recirculation rate, are shown in Figure 7.6. Also with this fuel recirculation rates the cell was operated successfully for the operation time of approximately 150 h. The lower power density of the 10 % anode off-gas recirculation test in comparison to the 30 % anode off-gas recirculation test was caused by a cell leakage which occurred between the recording of the two test scenarios. Additionally, the test conducted with real landfill gas and an anode off-gas recirculation rate of 30 % (orange crosses) is shown in Figure 7.6. Also in this case the cell could be operated successfully for a time of 150 h and the lower power density was again caused by the cell leakage.

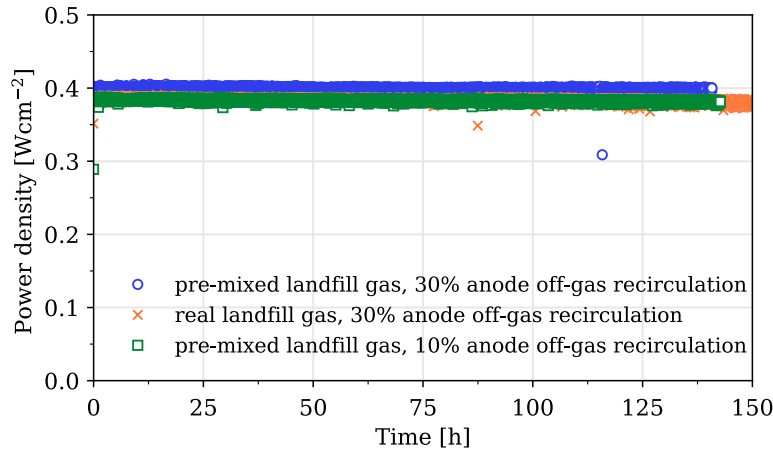


**Figure 7.6:** Power density over time of the pre-mixed landfill gas tests with 30 % and 10 % anode off-gas recirculation plus the real landfill gas test with 30 % anode off-gas recirculation.

For a better comparison of the conducted tests with different anode off-gas recirculation rates the degradation rate was calculated according to Equation 2.30. As mentioned in Section 2.4.3, the degradation rate is dependent on the considered test length. Therefore, the degradation rate was calculated for the first 150 h of each test. The determined degradation rates are shown as function of the fuel recirculation rate for the different anode fuels in Figure 7.7. The lowest degradation rate of 1 %/1000h was calculated for the pre-mixed landfill gas CO<sub>2</sub> reference test (black bar). The degradation rates of the pre-mixed landfill gas with anode off-gas recirculation tests increased continuously from 5.4 %/1000h up to 8.4 %/1000h with increasing anode off-gas recirculation rate (10 %-50 %). Additionally, the degradation rate of the 30 % fuel recirculation test conducted with real landfill gas supply was 4.7 %/1000h higher than the corresponding pre-mixed landfill gas test (compare red striped and blue white circle bar at 30 %). One explanation for the dependency between the degradation rate and the used anode off-gas recirculation could be the impurities present in the gas mixtures. Usually, the cell is exposed once to the impurities present in the gas (reference test). In case of anode off-gas recirculation a certain amount of the impurities are also recirculated and getting into contact with cell more than once. This assumption would also be in line with the fact that the degradation rate of the real landfill gas test was higher. As mentioned in previous Sections (see Section 2.3.3, 6.2), the amount of impurities in real landfill gas is much higher than in pre-mixed landfill gas by using industrial gas quality. The higher degradation rate

of the real landfill gas supply test is also an indication for the fact that the activated carbon filter was only able to remove the impurities to a certain extend. Additionally, impurities of the anode off-gas recirculation set up like for example from the pump could also have an influence on the degradation rates during anode off-gas recirculation operation. That the impurities present in the gas have an effect on the degradation rate during the use of anode off-gas recirculation is also reported by Hauch et al. [122] for solid oxide electrolysis operation. Hauch et al. could proof this theory by installing an extra half cell filter in the recirculation loop. A similar approach was tried for the presented landfill gas scenario but unfortunately, due to problems with carbon formation in the set-up, this investigation was not successful.

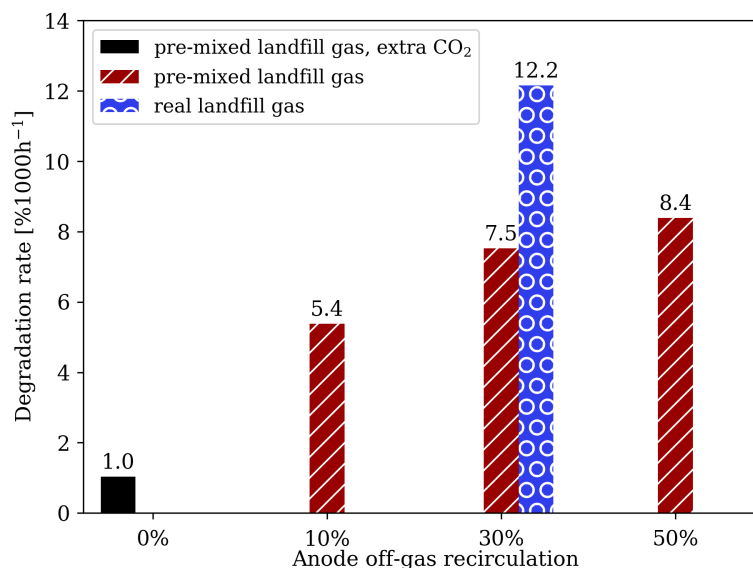


**Figure 7.7:** Degradation rates as function of the applied anode off-gas recirculation rate of the pre-mixed and real landfill gas cell tests.

To get an idea about the anode processes which were effected most during the recirculation tests, the impedance measurements recorded in pre-mixed landfill gas recorded prior and after the 50 % recirculation test are shown in Figure 7.8. The Nyquist plot in Figure 7.8(a) indicates that the value of  $R_p$  increased by around 19 % while  $R_s$  increased only marginal. The DRT plot in 7.8 shows that the increase of  $R_p$  was mainly caused by the resistance increases of the anode processes  $P_{FP}$  and  $P_{FD}$ . Additionally, the resistance of the  $P_{FR}$  increased marginal. The highest increase in the frequency range of the  $P_{FP}$  points out that the electrochemical reactions taking place at the triple phase boundary are most effected due to the impurity recirculation. Due to the fact that the  $P_{FR}$  only

increased marginally the CH<sub>4</sub> reforming processes were not really influenced.

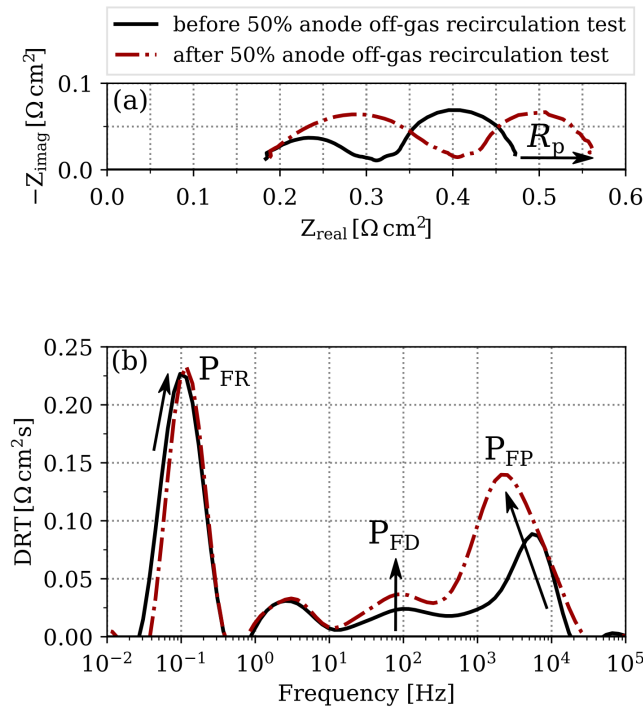


**Figure 7.8:** Nyquist plots (a) and DRT plot (b) of the impedance measurements recorded in pre-mixed landfill gas prior and after the 600 h test with 50 % anode off-gas recirculation.

In the next analyzing step the electric efficiency of the different tests are compared which are given in Table 7.4. The electric efficiency was calculated according to Equation 2.33 for the first 150 h of operation. The electric efficiencies mean values of the five tests were between 47.7 % and 45.2 %. The electric efficiencies of the 50 % and 30 % pre-mixed landfill gas anode off-gas recirculation tests were slightly higher than the electric efficiency of the reference test operated with extra CO<sub>2</sub>. This shows that anode off-gas recirculation has a positive effect on the electric efficiency because, beside the reforming agents (steam, CO<sub>2</sub>), also the H<sub>2</sub> present at the cell outlet (compare Figure 7.4) is recirculated. The around 2 % lower electric efficiencies of the fourth and fifth test were caused by the cell leakage as discussed previously.

**Table 7.4:** Electric efficiency mean values of the anode off-gas recirculation tests

electric efficiency (mean value) ( $\eta_{el,DC,cell}$ , Eq. 2.33)	
1) pre-mixed biogas and CO <sub>2</sub> , 0 % aogr	47.0 %
2) pre-mixed landfill gas, 50 % aogr	47.7 %
3) pre-mixed landfill gas, 30 % aogr	47.3 %
4) pre-mixed landfill gas, 10 % aogr	45.2 %
5) real landfill gas, 30 % aogr	45.4 %

aogr: anode off-gas recirculation

## 7.4 Conclusion

In this chapter a simulation and an experimental study was presented in order to analyze the option of anode off-gas recirculation to prevent carbon formation for landfill gas fueled SOFC's. In the first step an algorithm and a semi-1D SOFC model was developed for determining possible operation conditions. The model divides the cell into sub-cells and calculates the anode gas composition after reforming by using Gibbs free energy minimization. In a second step, a parameter study for a landfill gas fueled SOFC was conducted. In the study the anode off-gas recirculation rate and the applied current density was varied. The results showed that the carbon activity along the cell can be lowered by both increasing the anode off-gas recirculation rate and the applied current density. Additionally, the molar fraction trends of the gas species along the cell indicated that, at the cell inlet, the carbon activity is more dependent on the anode off-gas recirculation rate and in contrast, closer to the cell outlet, more on the applied current density.

# 8 Biogas SOFC system efficiency

**Comment:** This analysis was conducted during an external research stay in the 'Hydrogen and Fuel Cells Team' at VTT Technical Research Centre of Finland Ltd, Finland. This chapter is based on the corresponding article [29] which was developed during the research stay. The support of the co-authors is gratefully acknowledged. The paragraphs which are framed by double quotes ("") are originally from the manuscript.

In the last part of the previous chapter the electric efficiencies of landfill gas fueled cells and using anode fuel recirculation were discussed (see Table 7.4). On system level a common way to avoid carbon formation during supplying carbon containing fuels like biogas is the use of anode fuel recirculation, too. On system level the recirculation can be realized by the use of an ejectors or new options like steam driven recirculation micro fans [123]. As a final step this chapter is investigating the electric and total efficiency on system level. Therefore data from industrial sized SOFC systems fueled with real biogas from waste water were analyzed. Emphasis is put on the dependencies between system efficiencies and the electric net power output plus the CH<sub>4</sub> content variation in the biogas.

## 8.1 SOFC system data analysis scheme

The set up of the industrial sized SOFC site fueled with biogas from waste water is described in Section 3.2. "The data has been recorded from beginning of October 2017 until the end of 2019. For the analysis the data were interpolated to one hour time steps. Results like the electric and total efficiencies of the C50 systems were calculated according to the international standard IEC 62282-3-200 for stationary fuel cell power systems. In addition stable operation conditions for the C50 systems were defined based on the guideline as well [93]. An overview about the data analysis is given in Figure 8.1." Firstly the electric and total efficiencies of the two SOFC systems as function of the time were calculated. In a second step all measurements points with an electric net

power output ( $P_{\text{electric net}}(t)$ ) greater than zero were selected. Afterwards stable operation segments of the SOFC systems were determined. Stable operation was defined allowing a variation of  $\pm 2\%$  for the operation parameters electric net power output ( $P_{\text{electric net}}(t)$ ), thermal power output ( $P_{\text{thermal}}(t)$ ) and biogas fuel mass flow rate ( $\dot{m}_{\text{biogas}}(t)$ ) during an operation time segment. The minimum allowed length of a time segment was 4 h. The system efficiency data of the selected time segments according to the second and third step in Figure 8.1 were analyzed as function of  $P_{\text{electric net}}$  and the  $\text{CH}_4$  content in the biogas. These dependencies are presented and discussed in the following two sections.

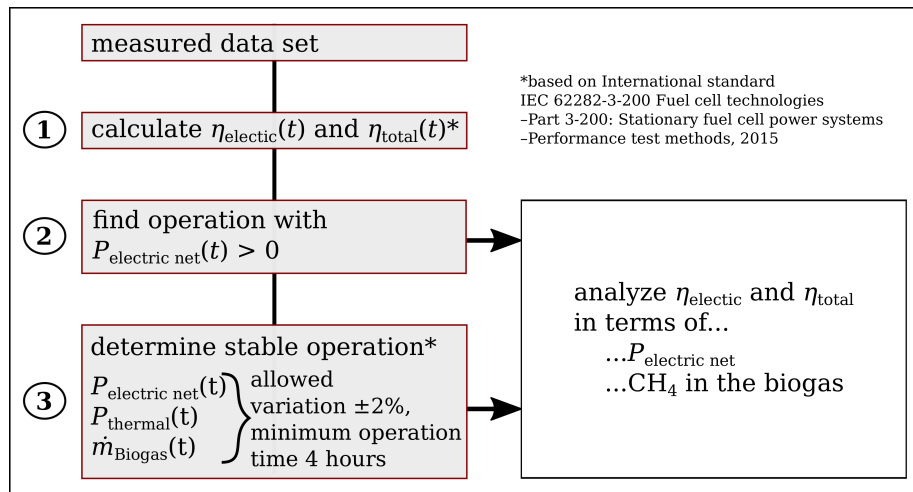


**Figure 8.1:** Illustration of the data analysis procedure which is based on the International standard IEC 62282-3-200 Fuel cell technologies – Part 3-200: Stationary fuel cell power systems – Performance test methods, 2015 [93]. Modified from reference [29].

## 8.2 Electrical net power relation

"The first system and the second system have been operating in total for 9113 h providing electricity and heat to the plant."

"In Figure 8.2 the data analysis results of the first system are shown. In Figure 8.2(a) the total electric efficiency and the total efficiency in terms of the electric net power output from 0 to 55 kW are illustrated. The red squares in Figure 8.2(a) represent the mean values of the electric efficiencies of the corresponding electric net power output segment during stable operation. The SOFC system was operated stable in an electric net power output range between 25 kW and 55 kW. In this range the electric efficiency

stayed stable between 50 % and 55 %. The black crosses show the total efficiency mean values which were between 67 % and 87 % during stable operation. The larger deviation of the total efficiency in comparison to the electric efficiency was caused by heat recovery flow rates not being optimized in the beginning of the operation. The stable and high electric efficiencies over the operating net power output range (25-55 kW) illustrate an advantage of fuel cell technology in comparison to micro turbines and internal combustion engines. The results show that power modulation according to the site demand is possible with high efficiencies using SOFC systems. The decreasing efficiencies (black dashed and dotted lines) during non-stable operation at electric net power outputs lower than 25 kW are caused by lower fuel utilization.”

”In Figure 8.2(b) the normalized distribution of the electric net power output is shown. Two main electric net power output operation regions can be identified. The first one between 50 kW and 55 kW with 77 % of the stable operation time which corresponds to 442 h. And the second one between 25 kW and 30 kW at which system one was operating for around 12 % of the stable operation time. The rest of the time the system was operating in the range 45 kW to 50 kW and 30 kW to 35 kW.”

”During stable operation the electric efficiency was between 45 % and 60 %. (see Figure 8.2(c)). For the majority of the time (79 %) the electric efficiency was between 50 % and 55 %. Around 2 % of the time the electric efficiency was even higher with values between 55 % and 60 %. The total efficiency variation was with values from 65 % up to 95 % broader than the variation of the electric efficiency. Three main areas can be identified in terms of the total efficiency of the first system. Firstly, the total efficiency was between 75 % and 85 % for 70 % of the stable operation time. Secondly, 17 % of the stable operation time the total efficiency was between 65 % and 75 %. Finally for 12 % of the stable operation time the first system reached a total efficiency between 85 % and 95 %.”

”In Figure 8.3 the data analysis of the second system is illustrated. Similar to the first system, the electric efficiency stayed stable with values in the range of 48 % to 53 % (red squares Figure 8.3(a)). The total efficiency stayed steady between 85 % and 92 % (black crosses, Figure 8.3(a)). The maximum achieved electrical net power output during stable operation was 45 kW. The lower electric net power output was caused by the fact that the systems were not identical in terms of the stack implementation. The

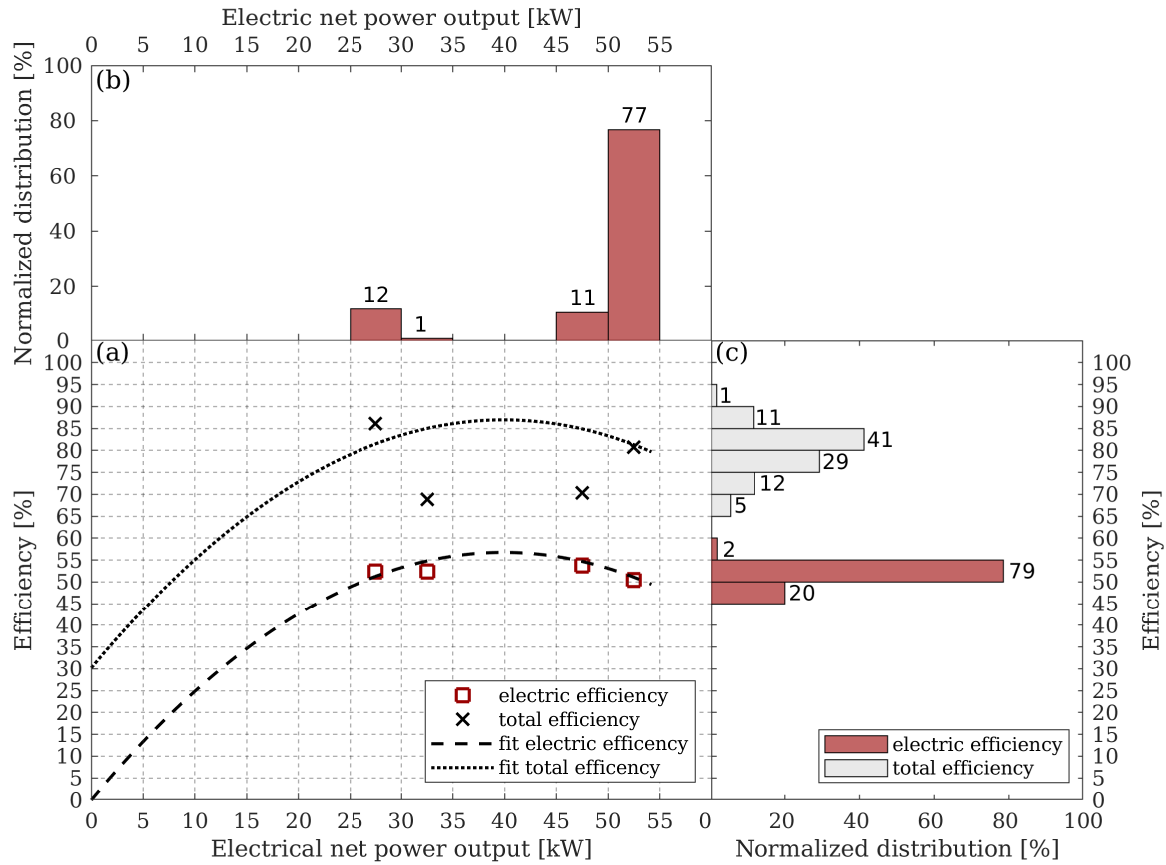


**Figure 8.2:** Electric and total efficiencies of the first Convion C50 SOFC system as function of the electrical net power output and corresponding normalized distributions. (a) Electric (red squares) and total (black crosses) efficiency mean values for electrical net power output segments during stable operation. Segments are represented by the vertical dashed lines. Black dashed and dotted lines represent second order polynomial fits of the electric and total efficiencies for electric net power output values greater zero. (b) Normalized distribution of the electric net power output. (c) Normalized distribution of the electric and total efficiencies. Combined standard uncertainties were around 3% for the electric and around 6% for the total efficiency. Adapted from reference [29].

stacks were from different manufacturers and the number of stacks implemented in the hot box were different. The similar achieved efficiencies of the systems are an indication for similar stack performances. The lower net power output of the second system was due to a lower number of stacks implemented in the hot box in comparison to the first system. The dashed and dotted black lines which represent the electric efficiency and total efficiency as a function of the electrical net power output have a similar shape as the corresponding lines of the first system (compare Figure 8.2(a)).”

The normalized distribution of the electric net power output shown in Figure 8.3(b) illustrates that the second system was operated for around 69 % ( $\approx 1040$  h) of the stable operation time between 40 kW to 45 kW. The rest of the time the unit was operated in the ranges 35-40 kW and 25-30 kW. This shows that the second system was operating more at one specific electric net power output than the first system which was operating in a larger range. Around 59 % of the stable operation time the electric efficiency of

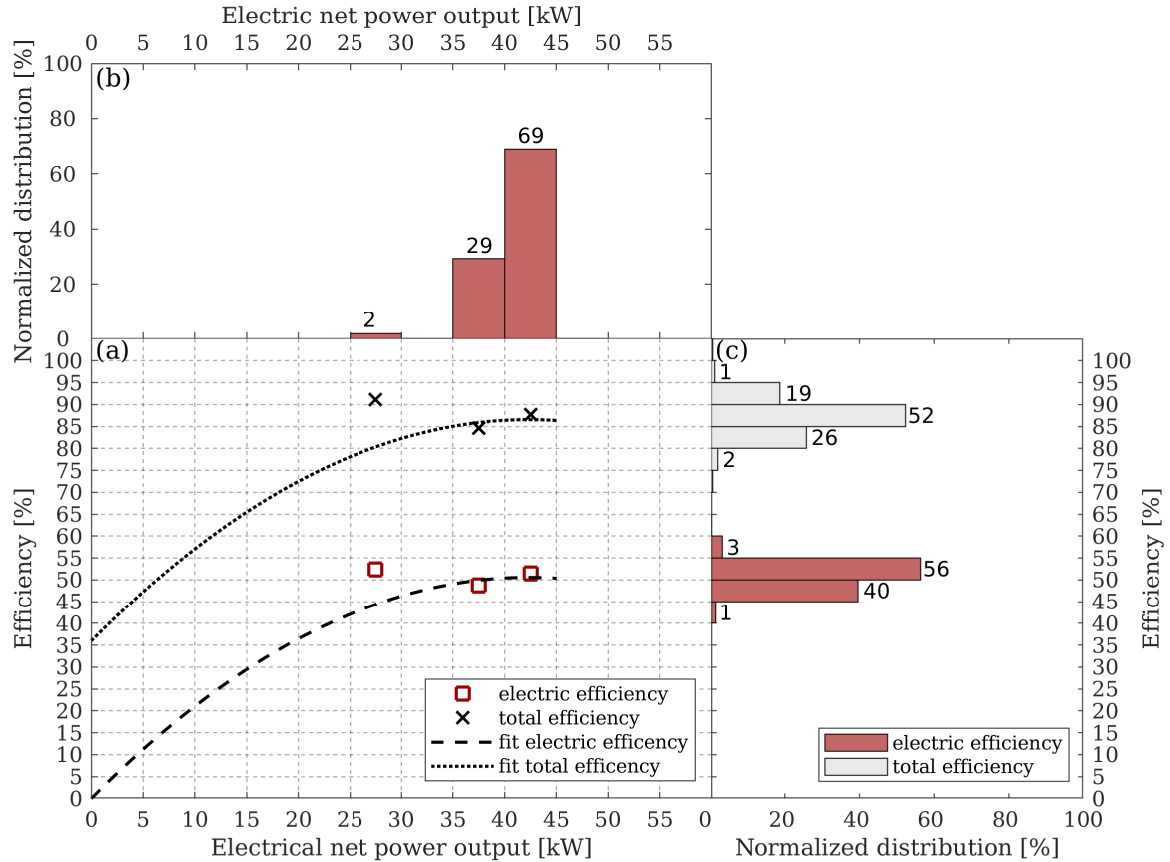


**Figure 8.3:** Electric and total efficiencies of the second Conyon C50 SOFC system as function of the electrical net power output and corresponding normalized distributions. (a) Electric (red squares) and total (black crosses) efficiency mean values for electrical net power output segments during stable operation. Segments are represented by the vertical dashed lines. Black dashed and dotted lines represent second order polynomial fits of the electric and total efficiencies for electric net power output values greater zero. (b) Normalized distribution of the electric net power output. (c) Normalized distribution of the electric and total efficiencies. Combined standard uncertainties were around 3% for the electric and around 6% for the total efficiency. Adapted from reference [29].

the second system was between 50 %-60 % (see Figure 8.3(c)). This is similar with the observed electric efficiency distribution of system one. The rest of the operation time the electric efficiency was mainly between 45 % and 50 %. A similar behavior can be observed for the total efficiency of system one: for 52 % of the stable operation time the total efficiency was between 85 % and 90 %. The rest of the time the total efficiency was mainly between 80-85 % and 90-95 %. Therefore it can be stated that the second system was operating steadier at a higher total efficiency as the first system.”

”In general the second system was operating more stable at one specific operation point than the first system. In terms of the electric efficiency similar values could be achieved. Concerning the total efficiencies the values of the second system were around 5 to 10 % higher compared to the first system. This shows that the system maturity in terms of operation monitoring and controlling was improved from the first system to the second system. Additionally the site operation was improved with less interruptions caused by the site auxiliary equipment and more optimized heat recovery loop control, which resulted in a more stable total efficiency of the second system in comparison to the first system. These are good indications for future installations.”

### 8.3 Biogas CH<sub>4</sub> content correlation

”System efficiency as a function of CH<sub>4</sub> content of the fuel gas was analyzed for both systems (see Figure 8.1). Due to the fact that the systems were supplied with biogas from the same source both systems were considered together in this case. The CH<sub>4</sub> content in the biogas was variating from 58 % up to 71 % as shown in Figure 8.4. The mean values of the electric efficiency (red squares in Figure 8.4(a)) and total efficiency (black crosses in Figure 8.4(a)) stayed constant with values around 50 % to 52 % and 82 % to 88 % respectively. This indicates that high electric and total efficiencies can be achieved by the SOFC systems with varying CH<sub>4</sub> content in biogas. This is supported by the normalized distribution plots of the system efficiencies shown in Figure 8.4(c). The electric efficiency was for 97 % of the stable operation time between 45 % and 55 %. Furthermore, the total efficiency was for 72 % of the stable operation time between 80 % and 90 %. Additionally, the normalized CH<sub>4</sub> content distribution in Figure 8.4(b) shows that the CH<sub>4</sub> content was mainly between 60 % and 65 % in the biogas during the stable operation time.”

Additionally, the electric efficiencies of the SOFC systems fueled with waste water biogas were around 5-15 % higher than the electric efficiencies of the pre-mixed and real landfill gas fueled cell tests (see Sections 6.1 and 7.3). An explanation for this dependency is the more optimized design, set up and control strategies of the SOFC system in relation to the cell testing set up. Considering the dependency between the efficiencies and the  $CH_4$  content in the waste water biogas (see Figure 8.4) a optimized SOFC system fueled with biogas from landfill instead from waste water would be able to achieve electric efficiencies of 50-60 %, too. In other terms the  $\approx$ 10-25 % lower  $CH_4$  content in landfill gas in comparison to waste water biogas would not results in lower system efficiencies.

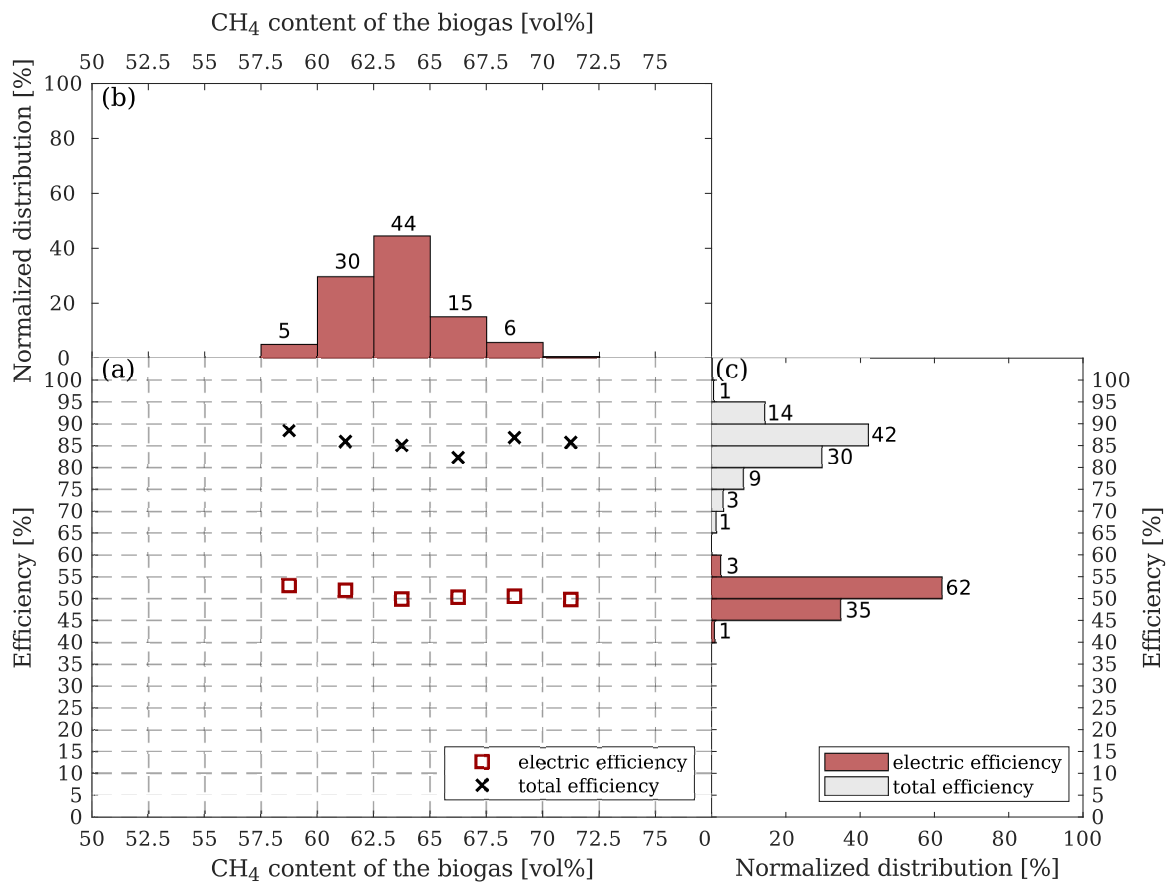


**Figure 8.4:** Electric and total efficiencies of both Convion C50 systems as function of the  $CH_4$  content of the biogas and corresponding normalized distributions. (a) Electric (red squares) and total (black crosses) efficiency mean values for  $CH_4$  content of the biogas segments during stable operation. Segments are represented by the vertical dashed lines. (b) Normalized distribution of the  $CH_4$  content of the biogas. (c) Normalized distribution of the electric and total efficiencies. Combined standard uncertainties were around 3% for the electric and around 6% for the total efficiency. Adapted from reference [29].

## 8.4 Conclusion

As a concluding step of this thesis which contains mainly investigations on cell level a study on system level was presented. "[In this study] electric and total efficiency data of two industrial sized Convion C50 SOFC systems installed at the same waste water plant were presented. During stable operation the SOFC systems were operating in an electric net power output range between 25 kW and 55 kW. The two SOFC systems fed with biogas were constantly achieving high electric efficiencies in the range of 50 % to 55 % and total system efficiencies in the range of 80 % to 90 %. Moreover it was shown that the high electric and high total efficiencies were independent of the CH<sub>4</sub> content in the biogas."

"This study points out that high electric and total efficiencies can be achieved with biogas fed SOFC systems. The high efficiencies are stable at varying electric net power output and changing CH<sub>4</sub> content of the biogas. This is a clear advantage of the SOFC technology in comparison to micro turbines and combustion engines." Especially the constant system efficiencies during variating CH<sub>4</sub> content allows to operate SOFC systems fueled with biogas while the biogas has a low amount of CH<sub>4</sub> (e.g. landfill gas) or during fluctuating CH<sub>4</sub> content in the biogas. In these scenarios the use of micro turbines or combustion engines would not be possible. "The results underline the fact that fuel cell systems are able to perform power modulation according to the power demand, while achieving constant high efficiencies. In addition the improvement of the site and system maturity which was achieved during this investigation are promising indications for further installations."

## 9 Conclusion

The aim of the thesis was to investigate real biogas fueled solid oxide fuel cells. Therefore, real landfill gas from the biggest dump site of Denmark was used. Four studies were conducted at cell level using pre-mixed and real landfill gas. In addition, a fifth parameter study of an industrial sized SOFC system fueled with biogas from wastewater treatment was carried out. Possibilities for determining and avoiding the consequences of the two main challenges during biogas fueled SOFC operation were investigated in more detail. These key challenges are the SOFC performance loss caused by impurities present in the biogas and the possibility of carbon formation during the CH<sub>4</sub> reforming process occurring at the SOFC anode.

The first experiential study presented in this thesis introduces a faster and cheaper method in order to determine the SOFC performance loss caused by the presence of the biogas impurity H<sub>2</sub>S. The method is based on iV-curve recording and allows for a fast evaluation of a large parameter space, thereby avoiding interference of the results by irreversible cell degradation due to long exposure of the cell to H<sub>2</sub>S. The method delivers the performance loss expressed by the cell voltage drop as a function of the H<sub>2</sub>S concentration in the fuel stream and the applied current density. Conditions of safe and critical poisoning effects can be determined. Up to current densities, which are affected by the concentration polarization, a linear dependency between the cell voltage drop caused by H<sub>2</sub>S and the current density was observed; these can be considered safe conditions. In this regime the voltage drop of cells with the same anode composition can be predicted to a certain extend by considering the initial cell performance determined in H<sub>2</sub>S free fuel. The advantage of the presented approach is that testing time can be reduced and the effect of H<sub>2</sub>S poisoning can be estimated for cells even without exposure to H<sub>2</sub>S.

The second study was dedicated a detailed evaluation of anode reactions in the specific gas compositions of landfill, including catalytic (e.g., reforming) and electrochemical reactions. Electrochemical impedance spectroscopy was used and a fuel representing the

real landfill (pre-mixed landfill). To avoid carbon formation extra CO<sub>2</sub> was added to the fuel. The study showed the processes at the SOFC anode in relation to the total anode fuel flow rate, current density and the CH<sub>4</sub> content present in the biogas. The parameters are affecting the reforming process, the fuel diffusion process and the fuel polarization process at the SOFC anode. This knowledge was further used to understand the anode processes in the next studies. The effect of operating the SOFC in galvanostatic and potentiostatic mode was studied by using real landfill gas. This degradation study included gas cleaning and cell regeneration. Successful operation of landfill gas fueled SOFC's was demonstrated in both operation modes and when the gas is cleaned in a carbon filter. When the gas is not cleaned the poisoning effects caused a decrease of power output, which could be recovered to a certain extend after cleaning the gas again. The poisoning could be recovered to a certain extend but not fully. This is probably due to the existence of several impurities in the real landfill. Additionally, the effect of poisoning was higher when operating in the potentiostatic mode. The investigations illustrated that the electrochemical reaction rate and not the partial pressure of steam at the anode are the reason for the different observations during galvanostatic and potentiostatic operation. Additionally, the cell performance can be recovered to a certain extend by supplying H<sub>2</sub>/H<sub>2</sub>O mixtures under current or increasing the operation temperature during pre-mixed biogas supply.

Based on the gained results at cell level, strategies for real operation were investigated, particularly the option of anode off-gas recirculation for preventing carbon formation. Pre-mixed and real landfill gas was used for this study at cell level. This option can reduce the need of external gas supply and reduces system operation costs. The developed theoretical model showed that the applied current density and the anode off-gas recirculation rate are affecting the probability of carbon formation. Successful durability tests with anode fuel recirculation rates of 10%-50% at a current density of 0.5 A cm<sup>-2</sup> and pre-mixed or real landfill gas supply were conducted at cell level. The results showed that the degradation rates are increasing at higher anode off-gas recirculation rates. This might be caused by recirculating impurities which are coming from the set-up. A solution could be the use of an additional filter for improving the SOFC lifetime. The electric DC efficiencies were between 45 % and 48 % with a testing set-up which was not optimized for achieving high electric efficiencies. With optimized industrial sized SOFC systems the efficiencies can be up to 15 % higher. This was shown in the concluding system efficiency study of industrial sized SOFC systems fueled with real biogas from

---

wastewater. The study illustrated the advantages of SOFC systems in comparison to Carnot cycle driven engines. The advantages are high electric (50-55 %) and total (80-90 %) efficiencies, which are constant during changing electric net power output and CH<sub>4</sub> content in the biogas.

# 10 Outlook

The study has shown the potential and advantages of using biogas (landfill gas) as fuel for SOFC's. Further developments should aim at increasing the SOFC live time when fueled with biogas and optimizing operation strategies.

Further research, especially with the focus on real biogas fueled SOFC's, would be favorable. At cell level, further experimental studies could be conducted for developing regeneration approaches, which can be applied after the SOFC anode was exposed to impurities present in the biogas. An additional topic could be the further investigation of anode off-gas recirculation during real landfill gas supply at the stack level for gaining a better understanding of the occurring stack performance degradation and finding possibilities for reduction of the degradation.

Moreover, simple and cheap methods as well as diagnostic tools for real time determination of needed quantities like the CH<sub>4</sub> concentration or the impurity concentration in the biogas are needed. Preferentially, quantities which are already monitored during operation like for example cell voltages and temperature changes in the system, could be used. For the diagnostics the measured quantities should be combined with thermodynamic models in order to detect changes during occurrence.

The real time methods would allow the SOFC system to react in time for preventing system failures and rapid degradation of the SOFC performance. Furthermore, the implementation of these methods would allow to apply performance regeneration approaches during operation. An advantage of these methods would be the reduction of specialized measurement equipment, which would lower costs. Additionally, the down times of the SOFC systems could be reduced because less failures would occur.

# References

- [1] James Larminie. *Fuel cell systems explained*. Chichester [u.a.] : Wiley, 2003.
- [2] Klaus-Dieter Kreuer. *Fuel Cells, Fuel Cells*. Springer New York, 2013.
- [3] A.Boudghene Stambouli and E Traversa. Solid oxide fuel cells (SOFCs): a review of an environmentally clean and efficient source of energy. *Renewable and Sustainable Energy Reviews*, 6(5):433–455, oct 2002.
- [4] R. Staniforth, John ; Ormerod. Implications for using biogas as a fuel source for solid oxide fuel cells: Internal dry reforming in a small tubular solid oxide fuel cell. *Catalysis Letters*, 2002, Vol.81(1), pp.19-23, 81(1):19, 2002.
- [5] D. B. Drasbæk, M. L. Traulsen, R. A. Walker, and P. Holtappels. Testing novel nickel and cobalt infiltrated STN anodes for carbon tolerance using in situ raman spectroscopy and electrochemical impedance spectroscopy. *Fuel Cells*, may 2019.
- [6] Daniel Bøgh Drasbæk, Marie Lund Traulsen, Bhaskar Reddy Sudireddy, and Peter Holtappels. Combining transition metals – an approach towards high-performing coking tolerant solid oxide fuel cell anodes. *ECS Transactions*, 91(1):1953–1961, jul 2019.
- [7] Jimmi Nielsen, Per Hjalmarsson, Martin Hangaard Hansen, and Peter Blennow. Effect of low temperature in-situ sintering on the impedance and the performance of intermediate temperature solid oxide fuel cell cathodes. *Journal of Power Sources*, 245:418–428, jan 2014.

- [8] Zhenguo Yang, Guanguang Xia, Prabhakar Singh, and Jeffry W. Stevenson. Electrical contacts between cathodes and metallic interconnects in solid oxide fuel cells. *Journal of Power Sources*, 155(2):246–252, apr 2006.
- [9] Beatriz Molinuevo-Salces, Søren U. Larsen, Birgitte Kiær Ahring, and Hinrich Uellendahl. Biogas production from catch crops. *Conference Proceedings of the 22nd Eu Biogas Conference*, 2014.
- [10] B. Tjaden, M. Gandiglio, A. Lanzini, M. Santarelli, and M. Järvinen. Small-scale biogas-sofc plant: Technical analysis and assessment of different fuel reforming options. *Energy and Fuels*, 28(6):4216–4232, 2014.
- [11] Andrea Lanzini, Hossein Madi, Vitaliano Chiodo, Davide Papurello, Susanna Maisano, Massimo Santarelli, and Jan Van Herle. Dealing with fuel contaminants in biogas-fed solid oxide fuel cell (sofc) and molten carbonate fuel cell (mcfc) plants: Degradation of catalytic and electro-catalytic active surfaces and related gas purification methods. *Progress in Energy and Combustion Science*, 61:150–188, 2017.
- [12] Helena Chum, A Faaij, J Moreira, G Berndes, P Dhamija, H Dong, and M Mapako. Bioenergy ipcc special report on renewable energy sources and climate change mitigation ed o edenhofer et al, 2011.
- [13] EurObserv’ER. Biogas barometer 2017. <https://www.eurobserv-er.org/pdf/biogas-barometer-2017-en/>, 2017. Accessed: 2018-02-01.
- [14] Jerzy Merkisz and Jacek Pielecha. *Particulate Matter Emissions during Engine Start-Up*, pages 47–60. Springer International Publishing, Cham, 2015.
- [15] Lidia Lombardi, Ennio Carnevale, and Andrea Corti. Greenhouse effect reduction and energy recovery from waste landfill. *Energy*, 31(15):3208–3219, 2006.
- [16] Antti Niskanen, Hanna Varri, Jouni Havukainen, Ville Uusitalo, and Mika Horttula.

- tanainen. Enhancing landfill gas recovery. *Journal of Cleaner Production*, 55:67–71, 2013. CO<sub>2</sub> savings landfill.
- [17] E. Rillo, M. Gandiglio, A. Lanzini, S. Bobba, M. Santarelli, and G. Blengini. Life cycle assessment (lca) of biogas-fed solid oxide fuel cell (sofc) plant. *Energy*, 126:585–602, 2017.
- [18] S. Torija, A. Castillo-Castillo, and N. P. Brandon. The prospects for biogas integration withfuel cells in the united kingdom. *Fuel Cells*, 16(1):55–79, 2016.
- [19] J Van herle, Y Membrez, and O Bucheli. Biogas as a fuel source for sofc co-generators. *Journal of Power Sources*, 127(1-2):300–312, 2004.
- [20] Marta Gandiglio, Andrea Lanzini, Alicia Soto, Pierluigi Leone, and Massimo Santarelli. Enhancing the energy efficiency of wastewater treatment plants through co-digestion and fuel cell systems. *Frontiers in Environmental Science*, 5, 2017.
- [21] A. Hagen, A. Winiwarter, H. Langnickel, and G. Johnson. Sofc operation with real biogas. *Fuel Cells*, 17(6):854–861, 2017.
- [22] D. Papurello, R. Borchiellini, P. Bareschino, V. Chiodo, S. Freni, A. Lanzini, F. Pepe, G. A. Ortigoza, and M. Santarelli. Performance of a solid oxide fuel cell short-stack with biogas feeding. *Applied Energy*, 125:254–263, 2014.
- [23] Ronald J. Spiegel, J. C. Trocciola, and J. L. Preston. Test results for fuel-cell operation on landfill gas. *Energy*, 22(8):777–786, 1997.
- [24] Ulrich Langnickel. First european fuel cell application using digester gas. *Fuel Cells Bulletin*, 2000.
- [25] M. Krumbeck, T. Klinge, and B. Döding. First european fuel cell installation with anaerobic digester gas in a molten carbonate fuel cell. *Journal of Power Sources*, 157(2):902–905, 2006.

- [26] Erkko Fontell. Fuel cell fed with landfill biogas provides power. *Industrial Bioprocessing*, 30(4):10, 2008.
- [27] M Noponen, T Hottinen, and C Sandstrom. Wfc20 biogas unit operation. In *Proceedings of the 9th European Solid Oxide Fuel Cell Forum*, pages 2–90, 2010.
- [28] DEMOSOFC. Demosofc project official website. <http://www.demosofc.eu/>, November 2019. Accessed: 2019-11-14.
- [29] H Langnickel, M Rautanen, M Gandiglio, M Santarelli, T Hakala, M Acri, and J Kiviahio. Efficiency analysis of 50 kwe sofc systems fueled with biogas from waste water. *Journal of Power Sources Advances*, submitted 2020.
- [30] Odense Renovation A/S. Gas extraction landfill odense renovation. <https://www.odensewaste.com/landfill/landfill-aftercare/gas-extraction/>, 2020. Accessed: 2020-02-04.
- [31] LFG Consult Aps. Økonomiberegninger ved forskellige scenarier for udskiftning af gasmotor pÅ deponigasanlÆgget stige Ø og odense nord. Technical report, LFG Consult Aps, 2019.
- [32] JR Rostrup-Nielsen, J Sehested, and JK Norskov. Hydrogen and synthesis gas by steam- and co2 reforming. *Advances in Catalysis*, 47:65–139, 2002.
- [33] H. Langnickel and A. Hagen. New methodology of studying h2s poisoning effects on sofc's fueled by carbon containing fuels like biogas. *Ecs Transactions*, 91(1):511–521, 2019.
- [34] P. Tsakaras and A. Demin. Thermodynamic analysis of a solid oxide fuel cell system fuelled by ethanol. *Journal of Power Sources*, 102(1-2):210–217, 2001.
- [35] K Sasaki and Y Teraoka. Equilibria in fuel cell gases - i. equilibrium compositions and reforming conditions. *Journal of the Electrochemical Society*, 150(7):A878–A884, 2003.

- [36] Qiong Sun, Keqing Zheng, and Meng Ni. Thermodynamic analysis of methane-fueled solid oxide fuel cells considering co electrochemical oxidation. *Chinese Journal of Chemical Engineering*, 22(9):1033–1037, 2014.
- [37] C.W. Bale, E. Bélisle, P. Chartrand, S.A. Dechterov, G. Eriksson, A.E. Gheribi, K. Hack, I.-H. Jung, Y.-B. Kang, J. Melançon, A.D. Pelton, S. Petersen, C. Robelin, J. Sangster, P. Spencer, and M-A. Van Ende. FactSage thermochemical software and databases, 2010–2016. *Calphad*, 54:35–53, sep 2016.
- [38] Marco Sorrentino, Ashraf Mandourah, Thomas F. Petersen, Yann G. Guezennec, Michael J. Moran, and Giorgio Rizzoni. A 1-d planar solid oxide fuel cell model for simulation of sofc-based energy systems. *American Society of Mechanical Engineers, Advanced Energy Systems Division (publication) Aes*, 44:IMECE2004-60927, 205–214, 2004.
- [39] K. Wang, D. Hissel, M.C. Péra, N. Steiner, D. Marra, M. Sorrentino, C. Pianese, M. Monteverde, P. Cardone, and J. Saarinen. A review on solid oxide fuel cell models. *International Journal of Hydrogen Energy*, 36(12):7212 – 7228, 2011.
- [40] X. Zhang and Y. M. Wu. A control-oriented dynamic model adapted to variant steam-to-carbon ratios for an sofc with exhaust fuel recirculation. *Fuel Cells*, 11(2):200–211, 2011.
- [41] M. P. Heddrich, M. Jahn, A. Michaelis, R. Naeke, and A. Weder. Sofc system design using ideal efficiency modeling-model and experimental implementation. *Fuel Cells*, 13(4):612–622, 2013.
- [42] Dario Marra. *Models for Solid Oxide Fuel Cell Systems : Exploitation of Models Hierarchy for Industrial Design of Control and Diagnosis Strategies*. London : Springer, London, 1st ed. 2016 edition, 2016.
- [43] Stefano Ubertini Roberto Bove. *Modeling Solid Oxide Fuel Cells, MODELING SOLID OXIDE FUEL CELLS*. Springer Netherlands, 2008.

- [44] E ACHENBACH and E RIENSCHE. Methane steam reforming kinetics for solid oxide fuel-cells. *Journal of Power Sources*, 52(2):283–288, 1994. steam reforming dependeny phCH<sub>4</sub> arrhenius.
- [45] Susumu Nagata, Akihiko Momma, Tohru Kato, and Yasuhiro Kasuga. Numerical analysis of output characteristics of tubular SOFC with internal reformer. *Journal of Power Sources*, 101(1):60–71, oct 2001.
- [46] Joon-Ho Koh, Byoung-Sam Kang, Hee Chun Lim, and Young-Sung Yoo. Thermo-dynamic analysis of carbon deposition and electrochemical oxidation of methane for SOFC anodes. *Electrochemical and Solid-State Letters*, 4(2):A12, 2001.
- [47] Baskakov, Volkova, Volkova, Munts, and Ershov. Performance evaluation method of sofc power unit with anode off-gas recirculation, performance evaluation method of sofc power unit with anode off-gas recirculation. *Ecs Transactions*, 78(1):2621–2631, 2017.
- [48] Roland Peters, Robert Deja, Ludger Blum, Jari Pennanen, Jari Kiviahio, and Tuomas Hakala. Analysis of solid oxide fuel cell system concepts with anode recycling. *International Journal of Hydrogen Energy*, 38(16):6809–6820, 2013.
- [49] Anke Hagen, Hendrik Langnickel, and Xiufu Sun. Operation of solid oxide fuel cells with alternative hydrogen carriers. *International Journal of Hydrogen Energy*, 44(33):18382–18392, 2019.
- [50] W. Sangtongkitcharoen, S. Assabumrungrat, V. Pavarajarn, N. Laosiripojana, and P. Praserthdam. Comparison of carbon formation boundary in different modes of solid oxide fuel cells fueled by methane. *Journal of Power Sources*, 142(1-2):75–80, mar 2005.
- [51] H. Langnickel and D Hoffmeyer. Elchdat - electrochemistry data analysis tool, 2019.

- [52] Jens Foldager Bregnbaalle Rasmussen and Anke Hagen. The effect of h<sub>2</sub>s on the performance of ni-ysz anodes in solid oxide fuel cells. *Journal of Power Sources*, 191(2):534–541, 2009.
- [53] A. Lanzini, D. Ferrero, D. Papurello, and M. Santarelli. Reporting degradation from different fuel contaminants in ni-anode sofcs. *Fuel Cells*, 17(4):423–433, 2017.
- [54] Anke Hagen, Jens Foldager Bregnbaalle Rasmussen, and Karl Tor Sune Thydén. Durability of solid oxide fuel cells using sulfur containing fuels. *Journal of Power Sources*, 196(17):7271–7276, 2011.
- [55] A. Weber, S. Dierickx, A. Kromp, and E. Ivers-Tiffée. Sulfur poisoning of anode-supported sofcs under reformate operation. *Fuel Cells*, 13(4):487–493, 2013.
- [56] Dimitrios K. Niakolas. Sulfur poisoning of ni-based anodes for solid oxide fuel cells in h/c-based fuels. *Applied Catalysis A: General*, 486:123–142, 2014.
- [57] Anke Hagen. Sulfur poisoning of the water gas shift reaction on anode supported solid oxide fuel cells. *Electrochemical Society. Journal*, 160(2):F111–F118, 2013.
- [58] P. ; Norrman K. ; Ozkan U. S. ; Hagen A. Johnson, G. B. ; Hjalmarsson. Biogas catalytic reforming studies on nickel-based solid oxide fuel cell anodes. *Fuel Cells, April 2016, Vol.16(2), pp.219-234*, 16(2):219, 2016.
- [59] K. Sasaki, K. Susuki, A. Iyoshi, M. Uchimura, N. Imamura, H. Kusaba, Y. Teraoka, H. Fuchino, K. Tsujimoto, Y. Uchida, and N. Jingo. H 2s poisoning of solid oxide fuel cells. *Journal of the Electrochemical Society*, 153(11):009611JES, A2023–A2029, 2006.
- [60] J. Bøgild Hansen and J. Rostrup-Nielsen. *Sulfur poisoning on Ni catalyst and anodes*, chapter 65. Wiley Online Library, 2009.
- [61] Jens R. Rostrup-Nielsen. Some principles relating to the regeneration of sulfur-poisoned nickel catalyst. *Journal of Catalysis*, 21(2):171 – 178, 1971.

- [62] Y Matsuzaki and I Yasuda. The poisoning effect of sulfur-containing impurity gas on a sofc anode: Part i. dependence on temperature, time, and impurity concentration. *Solid State Ionics*, 132(3-4):261–269, 2000.
- [63] Anne Hauch, Anke Hagen, Johan Hjelm, and Tania Ramos. Sulfur poisoning of sofc anodes: Effect of overpotential on long-term degradation. *Journal of the Electrochemical Society*, 161(6):F734–F743, F734–F743, 2014.
- [64] K. Haga, S. Adachi, Y. Shiratori, K. Itoh, and K. Sasaki. Poisoning of sofc anodes by various fuel impurities. *Solid State Ionics*, 179(27-32):1427–1431, 2008.
- [65] Jens Foldager Bregnbaalle Rasmussen and Anke Hagen. The effect of h<sub>2</sub>s on the performance of sofcs using methane containing fuel. *Fuel Cells*, 10(6):1135–1142, 2010.
- [66] Zhe Cheng, Shaowu Zha, and Meilin Liu. Influence of cell voltage and current on sulfur poisoning behavior of solid oxide fuel cells. *Journal of Power Sources*, 172(2):688–693, 2007.
- [67] Hossein Madi, Andrea Lanzini, Stefan Diethelm, Davide Papurello, Jan Van herle, Matteo Lualdi, Jørgen Gutzon Larsen, and Massimo Santarelli. Solid oxide fuel cell anode degradation by the effect of siloxanes. *Journal of Power Sources*, 279:460–471, apr 2015.
- [68] H. Madi, S. Diethelm, S. Poitel, C. Ludwig, and J. Van herle. Damage of siloxanes on ni-YSZ anode supported SOFC operated on hydrogen and bio-syngas. *Fuel Cells*, 15(5):718–727, sep 2015.
- [69] K. Haga, Y. Shiratori, K. Ito, and K. Sasaki. Chemical degradation and poisoning mechanism of cermet anodes in solid oxide fuel cells. *Ecs Transactions*, 25(2):2031–2038, 2009.
- [70] Hossein Madi, Andrea Lanzini, Davide Papurello, Stefan Diethelm, Christian Ludwig, Massimo Santarelli, and Jan Van herle. Solid oxide fuel cell anode degradation

- by the effect of hydrogen chloride in stack and single cell environments. *Journal of Power Sources*, 326:349–356, sep 2016.
- [71] Yonghou Xiao, Shudong Wang, Diyong Wu, and Quan Yuan. Experimental and simulation study of hydrogen sulfide adsorption on impregnated activated carbon under anaerobic conditions. *Journal of Hazardous Materials*, 153(3):1193–1200, 2008.
- [72] Alba Cabrera-Codony, Miguel A. Montes-Morán, Manuel Sánchez-Polo, Maria J. Martín, and Rafael Gonzalez-Olmos. Biogas upgrading: Optimal activated carbon properties for siloxane removal. *Environmental Science and Technology*, 48(12):7187–7195, 2014.
- [73] Wolfgang G. Bessler and Stefan Gewies. Gas concentration impedance of solid oxide fuel cell anodes. *Journal of The Electrochemical Society*, 154(6):B548, 2007.
- [74] Randall S. Gemmen, Mark C. Williams, and Kirk Gerdes. Degradation measurement and analysis for cells and stacks. *Journal of Power Sources*, 184(1):251–259, sep 2008.
- [75] Anne Hauch and Mogens Bjerg Mogensen. Testing of electrodes, cells and short stacks. *Cism International Centre for Mechanical Sciences*, 574:31–76, 2017.
- [76] Andrzej Lasia. *Electrochemical impedance spectroscopy and its applications*. Springer, 2014. Impedance course.
- [77] H. Schichlein, A.C. Müller, M. Voigts, A. Krügel, and E. Ivers-Tiffée. Deconvolution of electrochemical impedance spectra for the identification of electrode reaction mechanisms in solid oxide fuel cells. *Journal of Applied Electrochemistry*, 32(8):875–882, Aug 2002.
- [78] Søren Højgaard Jensen, Anne Hauch, Peter Vang Hendriksen, Mogens Bjerg Mogensen, Nikolaos Bonanos, and Torben Jacobsen. A method to separate process

- contributions in impedance spectra by variation of test conditions. *Journal of the Electrochemical Society*, 154(12):B1325–B1330, B1325–B1330, 2007.
- [79] R. de L. Kronig. On the theory of dispersion of x-rays. *J. Opt. Soc. Am.*, 12(6):547–557, Jun 1926.
- [80] HA Kramers. Die dispersion und absorption von röntgenstrahlen. *Phys. Z.*, 30:522–523, 1929.
- [81] Hendrik W Bode et al. Network analysis and feedback amplifier design. *van Nostrand New York*, 1945.
- [82] BA Boukamp. Electrochemical impedance spectroscopy in solid state ionics: recent advances. *Solid State Ionics*, 169(1-4):65–73, apr 2004.
- [83] Qiu An Huang, Rob Hui, Bingwen Wang, and Jiujun Zhang. A review of ac impedance modeling and validation in sofc diagnosis. *Electrochimica Acta*, 52(28):8144–8164, 2007.
- [84] S. Primdahl and Mogens Bjerg Mogensen. Gas conversion impedance: A test geometry effect in characterization of solid oxide fuel cell anodes. *Electrochemical Society. Journal*, 145:2431–2438, 1998.
- [85] Søren Højgaard Jensen, Anne Hauch, Peter Vang Hendriksen, and Mogens Mogensen. Advanced test method of solid oxide cells in a plug-flow setup. *Journal of the Electrochemical Society*, 156(6):B757–B764, 2009.
- [86] A. Leonide, Y. Apel, and E. Ivers-Tiffée. Sofc modeling and parameter identification by means of impedance spectroscopy. *Ecs Transactions*, 19(20):81–109, 2009.
- [87] A. Kromp, A. Leonide, André Weber, and E. Ivers-Tiffée. Electrochemical analysis of reformatte-fuelled anode supported sofc. *Journal of the Electrochemical Society*, 158(8):B980–B986, 2011.

- [88] Tania Ramos, Martin Søgaard, and Mogens Bjerg Mogensen. Electrochemical characterization of ni/scysz electrodes as sofc anodes. *Journal of The Electrochemical Society*, 161(4):F434–F444, 2014.
- [89] Jean-Claude Njodzefon, Christopher R Graves, Mogens B Mogensen, André Weber, and Johan Hjelm. Kinetic studies on state of the art solid oxide cells: A comparison between hydrogen/steam and reformate fuels. *Journal of The Electrochemical Society*, 163(13):F1451–F1462, 2016.
- [90] Mark E Orazem and Bernard Tribollet. *Electrochemical impedance spectroscopy*. Wiley,, 2008.
- [91] BA Boukamp. A nonlinear least-squares fit procedure for analysis of immittance data of electrochemical systems. *Solid State Ionics*, 20(1):31–44, 1986.
- [92] A. Weber. FUEL CELLS – SOLID OXIDE FUEL CELLS | life-limiting considerations. In *Encyclopedia of Electrochemical Power Sources*, pages 120–134. Elsevier, 2009.
- [93] International standard iec 62282-3-200 fuel cell technologies –part 3-200: Stationary fuel cell power systems – performance test methods, November 2015.
- [94] Søren Koch, Karin Vels Hansen, Martin Nielsen, Jens V. T Høgh, and DTU Energy. Rfccontrol. <https://www.elchemea.com/RFCcontrol/>, 2020. Accessed: 2020-01-14.
- [95] S. Ramousse, M. Menon, K. Brodersen, J. Knudsen, U. Rahbek, and P. H. Larsen. Manufacturing of anode-supported sofc's: Processing parameters and their influence. *Ecs Transactions*, 7(1):317–327, 2007.
- [96] Hendrik Langnickel, Christopher Graves, and Anke Hagen. Galvanostatic and potentiostatic operation of real landfill gas fueled sofc's. *Proceedings of the 13th European Sofc & Soe Forum 2018*, 2018.

- [97] Søren Koch, Karin Vels Hansen, Martin Nielsen, Jens V. T Høgh, and DTU Energy. Elchemea data acquisition. <https://www.elchemea.com/elchemea/>, 2020. Accessed: 2020-02-03.
- [98] AMETEK Scientific Instruments. 1260a impedance analyzer. <https://www.ameteksi.com/products/frequency-response-analyzers/1260a-impedance-analyzer>, 2020. Accessed: 2020-02-03.
- [99] AMETEK Scientific Instruments. 1255b frequency response analyzer. <https://www.ameteksi.com/products/frequency-response-analyzers/1255b-frequency-response-analyzer>, 2020. Accessed: 2020-02-03.
- [100] AMETEK Scientific Instruments. 1252a frequency response analyzer specifications. <https://www.ameteksi.com/support-center/legacy-products/1252a-frequency-response-analyzer>, 2020. Accessed: 2020-02-03.
- [101] A. Leonide, V. Sonn, André Weber, and E. Ivers-Tiffée. Evaluation and modeling of the cell resistance in anode-supported solid oxide fuel cells. *Journal of the Electrochemical Society*, 155(1):B36–B41, 2008.
- [102] Jean-Claude Njodzefon. *Electrode Kinetics and Gas Conversion in Solid Oxide Cells*. phdthesis, Technical University of Denmark, 2015.
- [103] Christopher R Graves. Ravdav data analysis software, version 0.9.7, 2012.
- [104] Alexandra Ploner. *Solid Oxide Fuel Cell Degradation Studies-Accelerated Testing and Lifetime Prediction*. PhD thesis, Technical University of Denmark, 2018.
- [105] Convion. Convion fuel cell - official website. <http://convion.fi/products/>, November 2019. Accessed: 2019-11-14.
- [106] Marta Gandiglio, Andrea Lanzini, Massimo Santarelli, Marco Acri, Tuomas Hakala, and Markus Rautanen. Results from an industrial size biogas-fed sofc plant (the demosofc project). *International Journal of Hydrogen Energy*, 2019.

- [107] M. Santarelli, M. Gandiglio, M. Acri, T. Hakala, M. Rautanen, and A. Hawkes. Results from industrial size biogas-fed sofc plant (demosofc project). *Ecs Transactions*, 91(1):107–116, 2019.
- [108] Anke Hagen, Gregory B. Johnson, and Per Hjalmarsson. Electrochemical evaluation of sulfur poisoning in a methane-fuelled solid oxide fuel cell: Effect of current density and sulfur concentration. *Journal of Power Sources*, 272:776–785, 2014.
- [109] John Bøgild Hansen. *Direct reforming fuel cells*, chapter 13, pages 409–450. Elsevier, 2011.
- [110] Shaowu Zha, Zhe Cheng, and Meilin Liu. Sulfur poisoning and regeneration of ni-based anodes in solid oxide fuel cells. *Journal of the Electrochemical Society*, 154(2):B201–B206, 2007.
- [111] Zhe Cheng. *Investigations into the interactions between sulfur and anodes for solid oxide fuel cells*. PhD thesis, Georgia Institute of Technology, 2008.
- [112] E. Brightman, D. G. Ivey, D. J L Brett, and N. P. Brandon. The effect of current density on h<sub>2</sub>s-poisoning of nickel-based solid oxide fuel cell anodes. *Journal of Power Sources*, 196(17):7182–7187, 2011.
- [113] D. S. Monder and K. Karan. Coverage dependent thermodynamics for sulfur poisoning of ni based anodes. *ECS Transactions*, 57(1):2449–2458, oct 2013.
- [114] S. J. Xia and V. I. Birss. Deactivation and recovery of ni-YSZ anode in h<sub>2</sub> fuel containing h<sub>2</sub>s. *ECS Proceedings Volumes*, 2005-07:1275–1283, jan 2005.
- [115] Tomoo Yoshizumi, Chie Uryu, Toshihiro Oshima, Yusuke Shiratori, Kohei Ito, and Kazunari Sasaki. Sulfur poisoning of SOFCs:dependence on operational parameters. ECS, 2011.
- [116] Peter Stanley Jørgensen, Søren Lyng Ebbehøj, and Anne Hauch. Triple phase boundary specific pathway analysis for quantitative characterization of solid oxide cell electrode microstructure. *Journal of Power Sources*, 279:686–693, 2015.

- [117] Zhenjun Jiao, Naoki Shikazono, and Nobuhide Kasagi. Quantitative characterization of sofc nickel-ysz anode microstructure degradation based on focused-ion-beam 3d-reconstruction technique. *Journal of the Electrochemical Society*, 159(3):B285–B291, B285–B291, 2012.
- [118] D. Simwonis, F. Tietz, and D. Stöver. Nickel coarsening in annealed ni/8ysz anode substrates for solid oxide fuel cells. *Solid State Ionics*, 132(3):241–251, 2000.
- [119] Christopher R. Graves and Johan Hjelm. Advanced impedance modeling of solid oxide electrochemical cells. *Proceedings of 11th European Sofc and Soe Forum 2014*, 2014.
- [120] M Mogensen. Progress in understanding SOFC electrodes. *Solid State Ionics*, 150(1-2):123–129, sep 2002.
- [121] Vinod M. Janardhanan. Internal reforming of biogas in sofc: a model based investigation. *Journal of Solid State Electrochemistry*, 19(10):2981–2990, 2015.
- [122] A Hauch, T. L. Skafte, R. Küngas, M. L. Traulsen, and S. H. Jensen. Co<sub>2</sub> electrolysis –how gas purity and over-potential affect detrimental carbon deposition. *Proceedings of the 13th European Sofc & Soe Forum 2018*, 2018.
- [123] Patrick Hubert Wagner, Zacharie Wuillemin, David Constantin, Stefan Diethelm, Jan Van herle, and Jürg Schiffmann. Experimental characterization of a solid oxide fuel cell coupled to a steam-driven micro anode off-gas recirculation fan. *Applied Energy*, 262:114219, mar 2020.
- [124] M.B. Cutlip and M. Shacham. *Problem solving in chemical engineering with numerical methods*. 1999.
- [125] V. Chiodo, A. Galvagno, A. Lanzini, D. Papurello, F. Urbani, M. Santarelli, and S. Freni. Biogas reforming process investigation for sofc application. *Energy Conversion and Management*, 98:252–258, 2015.

## References

---

- [126] Y Matsuzaki and I Yasuda. Electrochemical oxidation of h-2 and co in a h-2-h<sub>2</sub>o-co-co<sub>2</sub> system at the interface of a ni-ysz cermet electrode and ysz electrolyte. *Journal of the Electrochemical Society*, 147(5):1630–1635, 2000.
- [127] Bonnie J McBride. *Thermodynamic data for fifty reference elements*. National Aeronautics and Space Administration, Glenn Research Center, 2001.

# List of Figures

2.1	Working principle of a solid oxide fuel cell (SOFC). . . . .	4
2.2	Container of an extraction unit located at the closed landfill on Stige Island close to Odense in Denmark. . . . .	9
2.3	Ternary phase diagram of the system C-H-O showing carbon formation as function of the temperature at ambient pressure. Additionally the biogas mixture of 50% CH <sub>4</sub> plus 50% CO <sub>2</sub> and natural gas is shown [49, fig. 3].	13
2.4	Illustration of the conventional steady state approach for studying sulfur poisoning at the anode of SOFC's. . . . .	16
2.5	Example iV-curve of a SOFC fueled with dry H <sub>2</sub> operated at 850 °C. . . . .	19
2.6	Example of a Nyquist (a) and Bode plot (b) for presenting an impedance measurement of a SOFC cell. . . . .	22
3.1	Schematic arrangement of the test rig. . . . .	26
3.2	Schematic arrangement of the cell placed in the cell house. . . . .	27
3.3	Cell house sketch top and bottom part . . . . .	28
3.4	Picture of the anode exhaust gas tank in the test rig (a) and the scroll compressor P11H12N2.5 from Air Squared Manufacturing, Inc. (b) which is mounted inside the tank for recirculating the anode exhaust gas. . . . .	30
3.5	Electron microscope picture of a Ni-SCYSZ/ScYSZ/LSC:CGO with CGO barier and a cathode contact layer cell cross section. . . . .	31
3.6	Schematic setup of the biogas fueled SOFC site at the SMAT Collegno wastewater plant close to Turin in Italy. . . . .	34
4.1	Experimental procedure of the short term sulfur poisoning tests at 850 °C (for gas compositions see Table 4.1). . . . .	36
4.2	Linear interpolated iV-curves with various sulfur concentrations. . . . .	39
4.3	Immediate voltage drops for 2 ppm H <sub>2</sub> S in relation to 0 ppm H <sub>2</sub> S as a function of the current density. . . . .	40

4.4	Area specific resistance ( <i>ASR</i> ) increase for 2 ppm H <sub>2</sub> S in relation to 0 ppm H <sub>2</sub> S as a function of the current density. . . . .	40
4.5	Steady state test with pre-mixed biogas at 0.5 A cm <sup>-2</sup> , 850 °C. Cell voltage (black circle, left-axis) and serial resistance $R_s$ (cross, right-axis), polarization resistance $R_p$ (square, right-axis) before and after addition of 2 ppm H <sub>2</sub> S. Adapted from reference [33]. . . . .	42
4.6	Nyquist (a) and differences (b) plot (bode plot) of the pre-mixed biogas before and after addition of 2 ppm H <sub>2</sub> S sulfur in pre-mixed biogas, 850 °C, 0.5 A cm <sup>-2</sup> . Adapted from reference [33]. . . . .	43
4.7	Nyquist impedance plot at OCV (a) and iV-curves (b) illustrating the initial cell performance ('finger print') of the cells from the present study (black lines) together with cell test 2011 (red dashed lines) and cell test 2014 (blue dashed dotted lines) for prediction of $\Delta U$ . Fuel supply anode: 20 % H <sub>2</sub> O in H <sub>2</sub> (all in absence of H <sub>2</sub> S), Cathode supply air, Operation temperature 850 °C. . . . .	45
4.8	Immediate voltage drop determined from the iV-curves in this study (lines) and measured voltage drops from 2011 plus 2011 cell tests (see Table 3) recorded with the steady state method (data points). . . . .	48
5.1	Selected impedance measurements of the initial finger print and pre-mixed biogas supply. . . . .	51
5.2	Nyquist plot and DRT plot as function of the volumetric fuel flow rate during fueling the anode with pre-mixed landfill gas and extra CO <sub>2</sub> . . .	54
5.3	Nyquist plot and DRT plot as function of the current density during fueling the anode with anode pre-mixed landfill gas and extra CO <sub>2</sub> . . . .	55
5.4	Nyquist plot and DRT plot as function of the amount of CH <sub>4</sub> in the landfill gas . . . . .	58
5.5	Anode and cathode resistances from the impedance batch fittings as function of the CH <sub>4</sub> amount present in the pre-mixed biogas. . . . .	59
6.1	Test procedure for the galvanostatic operation mode with real landfill gas and additional CO <sub>2</sub> at 750 °C with 0.5 A cm <sup>-2</sup> . Modified from reference [96]. . . . .	62
6.2	Test procedure for the potentiostatic operation mode with real landfill gas and additional CO <sub>2</sub> (or steam) at 750 °C and 800 °C with 765 mV in the first part and 755 mV in the second part. Modified from reference [96]	63

6.3 Test results of the galvanostatic (a)-(c) and potentiostatic (d)-(f) operation using cleaned landfill gas. Plot (a), (d): Cell voltage, $pO_2$ sensor at outlet of the cell; Plot (b), (e): Serial resistance ( $R_s$ ), Polarization resistance ( $R_p$ ) obtained from impedance spectra during operation, and current density; Plot (c), (f): Cell temperature at fuel inlet and outlet. Adapted from reference [96]. . . . .	64
6.4 Comparison of the area specific resistance ( $ASR$ ) determined from the iv-curves before and after the galvanostatic/potentiostatic operation with cleaned landfill gas via the activated carbon filter. Adapted from reference [96]. . . . .	65
6.5 Test procedure for the potentiostatic operation mode with additional steam supply fueled with real landfill gas and additional CO <sub>2</sub> at 750°C (left side). Theoretical volumetric flow rates of the gas species at the outlet of the anode as function of the applied current density (right side). Inlet fuel 4 L h <sup>-1</sup> landfill gas plus 2 L h <sup>-1</sup> extra CO <sub>2</sub> . Thermodynamic calculations were based on Gibbs free energy minimization (see Eq. 2.9) plus Faraday's law (see Eq. 2.25) and calculated with ElchDAT [51]. Dashed orange line represents the steam flow rate which was added step wise via mass flow controller during potentiostatic operation according to the applied current density. . . . .	66
6.6 Test results of the galvanostatic operation without cleaning of the landfill gas. Plot (a): Cell voltage, $pO_2$ sensor at outlet of the cell; Plot (b): Serial resistance ( $R_s$ ), Polarization resistance ( $R_p$ ) obtained from impedance spectra during operation, current density; Plot (c): Cell temperature inlet and outlet. Adapted from reference [96]. . . . .	68
6.7 Test results of the potentiostatic operation without cleaning of the landfill gas. Plot (a): Cell voltage, $pO_2$ sensor at outlet of the cell; Plot (b): Serial resistance ( $R_s$ ), Polarization resistance ( $R_p$ ) obtained from impedance spectra during operation, current density; Plot (c): Cell temperature inlet and outlet. Adapted from reference [96]. . . . .	70
6.8 Test results of the potentiostatic operation without cleaning of the landfill gas and extra steam supply according to Figure 6.5. Plot (a): Cell voltage, $pO_2$ sensor at outlet of the cell; Plot (b): Extra steam supply volumetric flow, current density; Plot (c): Cell temperature inlet and outlet. . . . .	72

6.9	Selected impedance measurements over operation time ( $t$ ) recorded in the galvanostatic mode during real landfill gas plus extra $\text{CO}_2$ and by-passed activated carbon filter for a certain amount of time. . . . .	73
6.10	Selected impedance measurements (dotted lines) over operation time ( $t$ ) recorded in the potentiostatic mode during real landfill gas plus extra $\text{CO}_2$ and by-passed activated carbon filter . . . . .	75
6.11	Normalized in-plane voltages and corresponding cell voltage/current density curves of the galvanostatic test (filter off) and the potentiostatic test with extra steam supply (filter off). . . . .	77
6.12	Normalized in-plane voltage and corresponding current density of the potentiostatic test (filter off). . . . .	77
6.13	Area specific resistance increase ( $\Delta ASR$ ) of the cells after turning of the filter during landfill gas supply. Blue line illustrates the galvanostatic operation the red line the potentiostatic operation and the green line the potentiostatic operation with extra steam supply. . . . .	78
6.14	Comparison of the cell $ASR$ determined from the iv-curves with and without cleaning of the galvanostatic and the two potentiostatic tests. . . . .	79
7.1	Schematic sketch of the thermodynamic semi-1D cell model for studying anode off-gas recirculation to avoid carbon formation of landfill gas fueled solid oxide fuel cells. . . . .	86
7.2	Illustration of the algorithm to run the semi-1D SOFC model for evaluating anode off-gas recirculation to avoid carbon formation during biogas supply. . . . .	88
7.3	Carbon activity along the cell as function of the anode off-gas recirculation rate and applied current density determined with the semi 1D cell model.	90
7.4	Molar fractions of the gases present along the cell as function of the anode off-gas recirculation rate (aogr) and applied current density ( $i$ ) determined with the semi 1D cell model. . . . .	92
7.5	Power density over time of the pre-mixed landfill gas plus $\text{CO}_2$ (reference test) and pre-mixed landfill gas with 50% anode off-gas recirculation. . . . .	94
7.6	Power density over time of the pre-mixed landfill gas tests with 30 % and 10 % anode off-gas recirculation plus the real landfill gas test with 30 % anode off-gas recirculation. . . . .	95
7.7	Degradation rates as function of the applied anode off-gas recirculation rate of the pre-mixed and real landfill gas cell tests. . . . .	96

7.8 Nyquist plots (a) and DRT plot (b) of the impedance measurements recorded in pre-mixed landfill gas prior and after the 600 h test with 50 % anode off-gas recirculation. . . . .	97
8.1 Illustration of the SOFC system data analysis procedure. . . . .	100
8.2 Electric and total efficiencies of the first Convion C50 SOFC system as function of the electrical net power output. . . . .	102
8.3 Electric and total efficiencies of the second Convion C50 SOFC system as function of the electrical net power output. . . . .	103
8.4 Electric and total efficiencies of both Convion C50 systems as function of the CH <sub>4</sub> content of the biogas. . . . .	105
B.1 Impedance measurement and corresponding equivalent electric circuit fit (batch fitting) including the single equivalent elements of the cell processes taking place (according to table 2.3) during 5 vol% CH <sub>4</sub> present in the pre-mixed landfill gas plus CO <sub>2</sub> fuel mixture (see section 5.3 and table 5.3). (a) Nyquist plot; (b) DRT plot; (c) Relative residuals plot of the fit result and the measured impedance data. Corresponding $\chi^2$ error of the impedance batch fit is $2.95 \times 10^{-7}$ . . . . .	XLVIII
B.2 Impedance measurement and corresponding equivalent electric circuit fit (batch fitting) including the single equivalent elements of the cell processes taking place (according to table 2.3) during 10 vol% CH <sub>4</sub> present in the pre-mixed landfill gas plus CO <sub>2</sub> fuel mixture (see section 5.3 and table 5.3). (a) Nyquist plot; (b) DRT plot; (c) Relative residuals plot of the fit result and the measured impedance data. Corresponding $\chi^2$ error of the impedance batch fit is $2.95 \times 10^{-7}$ . . . . .	XLIX
B.3 Impedance measurement and corresponding equivalent electric circuit fit (batch fitting) including the single equivalent elements of the cell processes taking place (according to table 2.3) during 15 vol% CH <sub>4</sub> present in the pre-mixed landfill gas plus CO <sub>2</sub> fuel mixture (see section 5.3 and table 5.3). (a) Nyquist plot; (b) DRT plot; (c) Relative residuals plot of the fit result and the measured impedance data. Corresponding $\chi^2$ error of the impedance batch fit is $2.95 \times 10^{-7}$ . . . . .	L

- B.4 Impedance measurement and corresponding equivalent electric circuit fit (batch fitting) including the single equivalent elements of the cell processes taking place (according to table 2.3) during 20 vol% CH<sub>4</sub> present in the pre-mixed landfill gas plus CO<sub>2</sub> fuel mixture (see section 5.3 and table 5.3). (a) Nyquist plot; (b) DRT plot; (c) Relative residuals plot of the fit result and the measured impedance data. Corresponding  $\chi^2$  error of the impedance batch fit is  $2.95 \times 10^{-7}$ . . . . . LI
- B.5 Impedance measurement and corresponding equivalent electric circuit fit (batch fitting) including the single equivalent elements of the cell processes taking place (according to table 2.3) during 23 vol% CH<sub>4</sub> present in the pre-mixed landfill gas plus CO<sub>2</sub> fuel mixture (see section 5.3 and table 5.3). (a) Nyquist plot; (b) DRT plot; (c) Relative residuals plot of the fit result and the measured impedance data. Corresponding  $\chi^2$  error of the impedance batch fit is  $2.95 \times 10^{-7}$ . . . . . LII

# List of Tables

2.1	Overview of the biogas composition from different waste sources. Adapted from Tjaden et al. [10, table 2] . . . . .	6
2.2	Overview of the amount of impurities present in wastewater biogas (anaerobic digester gas) and landfill gas. Summarized from reference [11, table 9]. . . . .	7
2.3	A selection of equivalent circuit elements used for describing the impedance response of a SOFC. . . . .	23
3.1	Approximate gas composition of the landfill gas, which was collected at the dump site in Odense, Denmark. Single cells were normally fueled with $4 \text{ L h}^{-1}$ landfill gas and $2 \text{ L h}^{-1} \text{ CO}_2$ for avoiding carbon formation (dry reforming process Eq. 2.8). . . . .	29
3.2	Pre-mixed landfill gas compositions plus extra reforming agent $\text{CO}_2$ based on the real landfill gas composition (see Table 3.1). . . . .	29
3.3	Single-cell test compositions of the cells used in this thesis. All cell types had a CGO barrier layer between electrolyte and cathode, plus a LSM cathode contact layer. . . . .	31
3.4	Used frequency response analyzer specifications for conducting the electrochemical impedance measurements according to reference [98, 99, 100].	32
3.5	Equivalent circuit elements for the impedance fitting with corresponding frequency ranges of the considered processes occurring at the anode and cathode of the investigated cells. Adopted from reference [89, 101, 102, 104].	33
4.1	Anode gas composition, anode total flow and applied sulfur concentration of the short term poisoning tests. Air was supplied at the cathode and tests were conducted at a operation temperature of $850^\circ\text{C}$ . Adapted from reference [33]. . . . .	37

4.2	Expected (see Figure 4.2) and measured (after 61 hours of test, Figure 4.5) cell voltage drop after addition of 2 ppm H <sub>2</sub> S to pre-mixed biogas fuel at 850 °C and 0.5 A cm <sup>-2</sup> . Adapted from reference [33]. . . . .	42
4.3	Selected tests from previous studies for studying the usability of the prediction method with the fast iV-curve method of the expected immediate voltage drops of the CH <sub>4</sub> -test for other cells. . . . .	44
4.4	Initial $R_{\text{anode}}$ values of the current study plus the 2011 test and 2014 test cells determined by impedance fitting (corresponding impedance data are shown in Figure 4.7). . . . .	47
4.5	Relative error between immediate voltage drop determined from the iV-curves and measured voltage drops from previous steady state tests carried out at DTU Energy (see Figure 4.8 and Table 4.3). . . . .	48
5.1	Flow composition used to identify the reforming process in the impedance response. . . . .	50
5.2	Settings for the quantities flow rate and current density for analyzing the corresponding impedance response change during pre-mixed landfill gas supply. . . . .	53
5.3	Settings for analyzing the impedance response as function of the CH <sub>4</sub> content present in the pre-mixed landfill gas . . . . .	56
5.4	Parameters which were varied and kept constant during the advanced impedance batch fitting of the pre-mixed landfill gas CH <sub>4</sub> content variation analysis. . . . .	57
6.1	Testing conditions for the regeneration approach after fueling the cell with landfill gas plus CO <sub>2</sub> and by-passed activated carbon filter. Modified from reference [96]. . . . .	67
7.1	Input and output parameters of the developed model for determining the carbon activity along the SOFC during biogas supply and anode off-gas recirculation. . . . .	84
7.2	Parameters of the simulation study for determining possible operation conditions for landfill gas fueled SOFCs considering anode off-gas recirculation for preventing carbon formation. . . . .	89
7.3	Settings of the conducted landfill gas fueled single cell tests with anode off-gas recirculation to avoid carbon formation. . . . .	93

7.4 Electric efficiency mean values of the anode off-gas recirculation tests . . .	98
--	----

# A Calculation of carbon activity and OCV considering CH<sub>4</sub> conversion in a SOFC

Hendrik Langnickel, DTU Energy

E-Mail: henlan@dtu.dk, hendrik.langnickel@alum.uol.de

Version 2, March 2020

## A.1 Gibbs minimization method

For determining the hydrogen production of the internal reforming of e.g CH<sub>4</sub> in the anode of the SOFC the Gibbs minimisation method according to equation A.1 can be used as it is described by Cultip and Schacham [124]. The assumption for this method is that a system is beneficial from a thermodynamic point of view when its differential is zero for a set temperature and pressure [125]. Where  $n_j$  stays for the amount of molecules of specie  $j$  and  $\mu_j$  stays for the chemical potential of specie  $j$ .  $\mu_j$  is defined in terms of the standard gibbs free energy  $G_j^0$ , the temperature  $T[K]$ , the universal gas constant  $R[\frac{JK}{mol}]$  and the chemical activity  $a_j[]$  for each considered species.

$$G = \sum_j n_j \mu_j \quad (\text{A.1})$$

$$\mu_j = G_j^0 + RT \ln(a_j) \quad (\text{A.2})$$

Considering the ideal gas limit  $a_j$  is defined according to equation A.3. Where  $p[Pa]$  is the wanted pressure and  $p^0[Pa]$  is the reference pressure (atmospheric).  $y_j$  is the molar

fraction of specie  $j$  as defined in equation A.4.

$$a_j = \frac{p}{p^0} y_j \quad (\text{A.3})$$

$$y_j = \frac{n_j}{\sum n_j} \quad (\text{A.4})$$

According to equation A.1 and considering equation A.2-A.4 equation A.5 can be derived.

$$\frac{G}{RT} = \sum_j n_j \left[ \frac{G_j^0}{RT} + \ln \left( \frac{n_j}{\sum n_j} \right) \right] \quad (\text{A.5})$$

Equation A.5 can be minimized using a numerical solver and considering the linear equality constrains for atomic mass conversation (see eq. A.6).  $x$  defines the amount of moles of the species which are taken into account. Considering the species CO<sub>2</sub>, CO, CH<sub>4</sub>, N<sub>2</sub>, O<sub>2</sub>, H<sub>2</sub> and H<sub>2</sub>O the matrix  $A_{eq}$  defines for each specie the oxygen, the hydrogen, the carbon and the nitrogen (see eq. A.7).

$$A_{eq}x = b \quad (\text{A.6})$$

$$A_{eq} = \begin{pmatrix} 2 & 1 & 0 & 0 & 2 & 0 & 1 \\ 0 & 0 & 4 & 0 & 0 & 2 & 2 \\ 1 & 1 & 1 & 0 & 0 & 0 & 0 \\ 0 & 0 & 0 & 1 & 0 & 0 & 0 \end{pmatrix} \quad (\text{A.7})$$

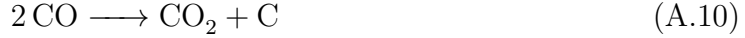
Additionally, the lower boundaries for the moles numbers have to be defined (see eq. A.8). Furthermore the initial guess for the solver is needs to be defined (see eq. A.9).

$$LB = \begin{bmatrix} 0 & 0 & 0 & 0 & 0 & 0 \end{bmatrix} \quad (\text{A.8})$$

$$x_0 = \begin{bmatrix} 10^{-3} & 10^{-3} & 10^{-3} & 10^{-3} & 10^{-3} & 10^{-3} & 10^{-3} \end{bmatrix} \quad (\text{A.9})$$

## A.2 Determining carbon activity

According to reaction A.10 the possibility of carbon formation can be expressed in terms of the carbon activity  $\alpha_c$  [34].



$\alpha_c$  is defined in terms of the partial pressures  $p_{\text{CO}}$ ,  $p_{\text{CO}_2}$  and equilibrium constant  $K_1$  (see eq. A.11).  $K_1$  is expressed in terms of the standard gibbs free energy  $G_{Ca}^0$ , the temperature  $T$  and the universal gas constant  $R$  (see eq. A.12). According to reaction A.10  $G_{Ca}^0$  is defined as shown in equation A.13. If  $\alpha_c = 1$  the system is in equilibrium but the amount of carbon formation is unknown. But from the thermodynamic point of view if  $\alpha_c < 1$  no carbon formation is possible.

$$\alpha_c = K_1 \frac{p_{\text{CO}}^2}{p_{\text{CO}_2}} \quad (\text{A.11})$$

$$K_1 = \exp\left(\frac{-G_{Ca}^0}{RT}\right) \quad (\text{A.12})$$

$$G_{Ca}^0 = G_{\text{CO}_2}^0 + G_C^0 - 2G_{\text{CO}}^0 \quad (\text{A.13})$$

## A.3 OCV determination via Nernst equation

As shown by Matsuzaki and Yasuda [126] that the electrochemical oxidation rate of  $H_2$  is around 2-3 times higher than the rate of CO only the Nernst potential (OCV) for the  $H_2$  electrochemical oxidation rate is calculated in the present case.

In the following the Nernst equation is derived. This equation gives a relation between the cell potential  $E$  and the equilibrium reduction potential of an electrochemical cell. Firstly the cell potential (open circuit voltage [OCV])  $E$  or also called the electromotive force is defined for the case of equilibrium conditions as the external work per unit charge transferred [? ]. Due to this  $E$  is related to the change of the molar Gibbs free energy  $\Delta G$  as it is shown below.

$$E = \frac{\Delta G}{z_e F} \quad (\text{A.14})$$

Where  $z_e$  is the charge number and  $F$  the Faraday constant. The change of the Gibbs free energy is related to the process of the chemical reaction. Due to this  $\Delta G$  can be

expressed as follows:

$$\Delta G = \Delta G^0 + RT * \ln \prod_i a_i^{v_i} \quad (\text{A.15})$$

In this case  $\Delta G^0$  is the change of the Gibbs free energy under standard conditions,  $R$  is the universal gas constant,  $T$  is the absolute temperature,  $a$  is the activity of the corresponding reactant and  $v$  stoichiometry coefficient. From equation A.14 and A.15 and the fact that the standard potential  $E^0$  can be expressed as  $-\frac{\Delta G^0}{z_e F}$  the general Nernst equation can be derived.

$$E = E^0 - \frac{RT}{z_e F} * \ln \prod_i a_i^{v_i} \quad (\text{A.16})$$

Due to the fact that the stoichiometry coefficient is positive for the oxidation (ox) and negative for the reduction (red) of the redox reaction the equation A.16 can be simplified as follows.

$$E = E^0 - \frac{RT}{z_e F} * \ln \left( \frac{a_{\text{ox}}}{a_{\text{red}}} \right) \quad (\text{A.17})$$

Because the activity of a substance is quite difficult to determine normally the proportional quantities partial pressure  $p_i$  or molar fraction  $\chi_i$  are used instead. In terms of the partial pressure the Nernst equation would be arranged as follows for a SOFC.

$$E = E^0 - \frac{RT}{2F} * \ln \left( \frac{pH_2O_{an}}{pH_{2,an} * \sqrt{pO_{2,cat}}} \right) \quad (\text{A.18})$$

Nevertheless it needs to be considered that  $E_0$  is also temperature dependent as it can be seen in the following where  $E_0$  is determined.

### Determining $E^0$

As already mentioned above  $E^0$  is defined as follows.

$$E^0 = -\frac{\Delta G^0}{z_e F} \quad (\text{A.19})$$

Due to this fact  $\Delta G^0$  needs to be determined which is the difference between  $\Delta G$  of the product and the reactant of the chemical reaction.

$$\Delta G^0 = \sum \Delta G_{ox}^0 - \sum \Delta G_{red}^0 \quad (\text{A.20})$$

For determining  $\Delta G_{ox/red}^0$  the following thermodynamic relation, which is only valid at constant temperature can be used.

$$\Delta G_{ox/red}^0 = \Delta H_{ox/red}^0 - T\Delta S_{ox/red}^0 \quad (\text{A.21})$$

In the case of an ideal gas the change of Enthalpy  $\Delta H^0$  and the change of Entropy  $\Delta S^0$  are defined as shown below.

$$\Delta H^0 = \int_{T_0}^T c_p dT \quad (\text{A.22})$$

$$\Delta S^0 = \int_{T_0}^T \frac{c_p}{T} dT \quad (\text{A.23})$$

Where  $c_p$  is the specific heat capacity at constant pressure. Due to the fact that  $c_p$  is temperature dependent  $c_p$  can for example be expressed in terms of a 4<sup>th</sup> order temperature-dependent polynomial. The coefficients of this polynomial are derived by numerical calculations as it is done by McBride et al. [127] for example.



## B Supporting impedance figures for the CH<sub>4</sub> content pre-mixed landfill gas study (section 5.3)

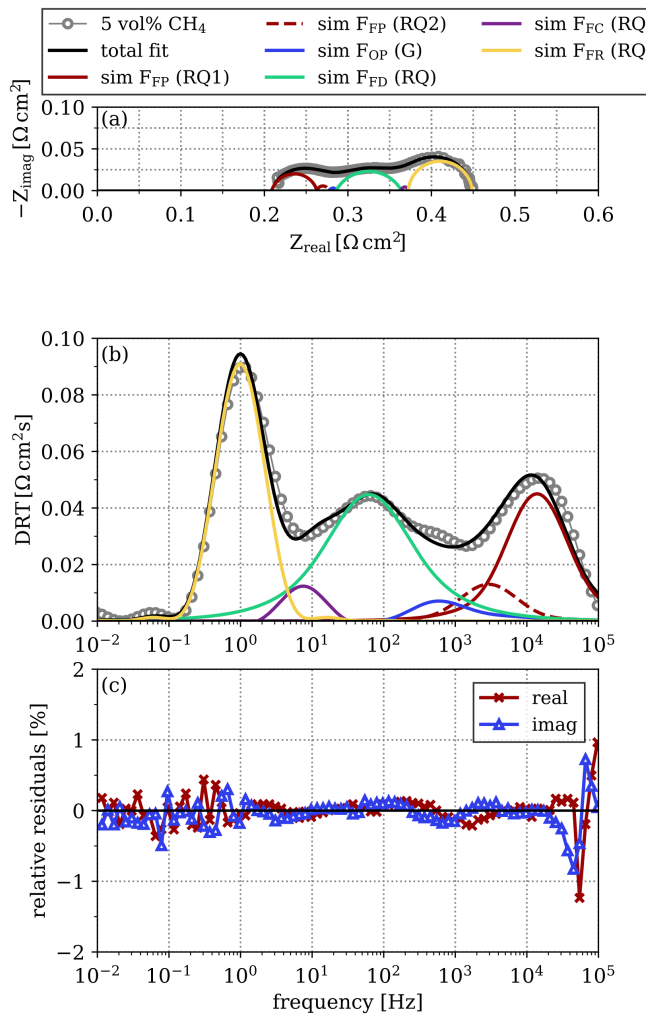


**Figure B.1:** Impedance measurement and corresponding equivalent electric circuit fit (batch fitting) including the single equivalent elements of the cell processes taking place (according to table 2.3) during 5 vol% CH<sub>4</sub> present in the pre-mixed landfill gas plus CO<sub>2</sub> fuel mixture (see section 5.3 and table 5.3). (a) Nyquist plot; (b) DRT plot; (c) Relative residuals plot of the fit result and the measured impedance data. Corresponding  $\chi^2$  error of the impedance batch fit is  $2.95 \times 10^{-7}$ .

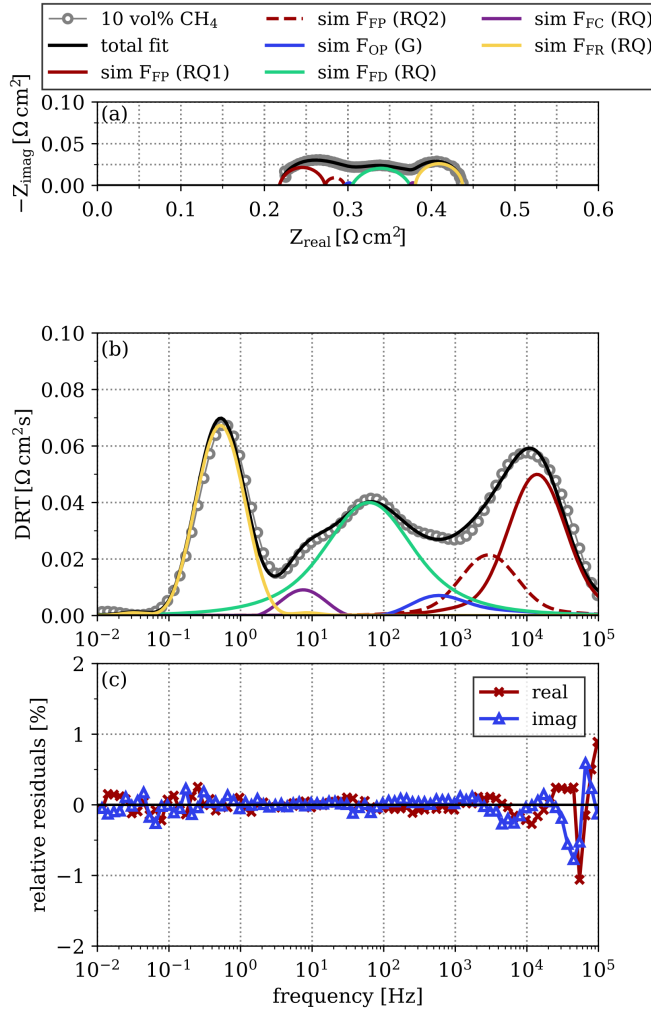


**Figure B.2:** Impedance measurement and corresponding equivalent electric circuit fit (batch fitting) including the single equivalent elements of the cell processes taking place (according to table 2.3) during 10 vol% CH<sub>4</sub> present in the pre-mixed landfill gas plus CO<sub>2</sub> fuel mixture (see section 5.3 and table 5.3). (a) Nyquist plot; (b) DRT plot; (c) Relative residuals plot of the fit result and the measured impedance data. Corresponding  $\chi^2$  error of the impedance batch fit is  $2.95 \times 10^{-7}$ .

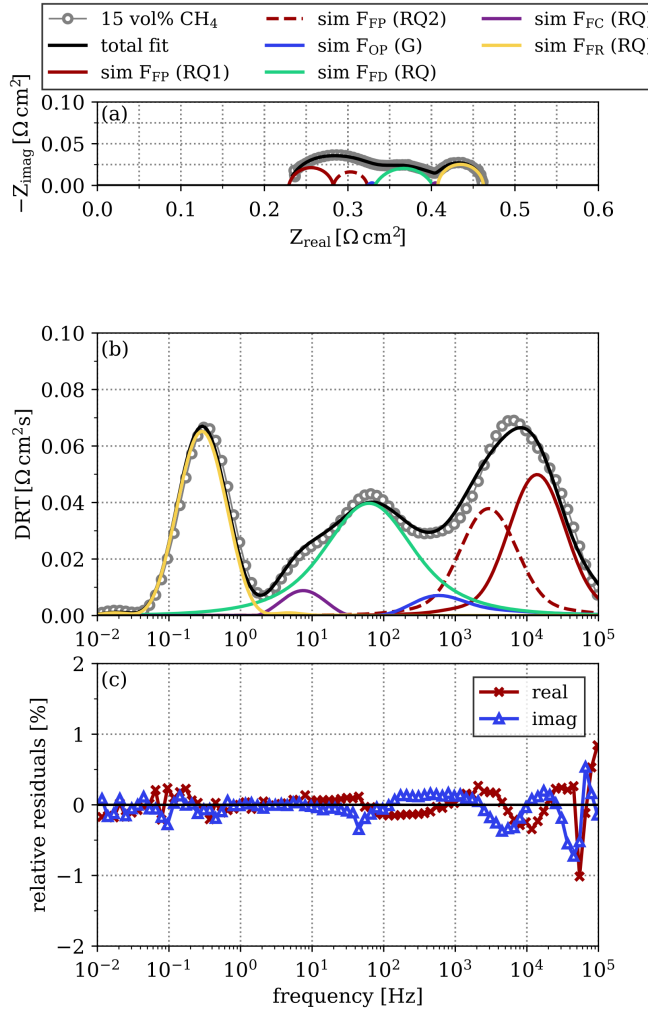


**Figure B.3:** Impedance measurement and corresponding equivalent electric circuit fit (batch fitting) including the single equivalent elements of the cell processes taking place (according to table 2.3) during 15 vol%  $\text{CH}_4$  present in the pre-mixed landfill gas plus  $\text{CO}_2$  fuel mixture (see section 5.3 and table 5.3). (a) Nyquist plot; (b) DRT plot; (c) Relative residuals plot of the fit result and the measured impedance data. Corresponding  $\chi^2$  error of the impedance batch fit is  $2.95 \times 10^{-7}$ .

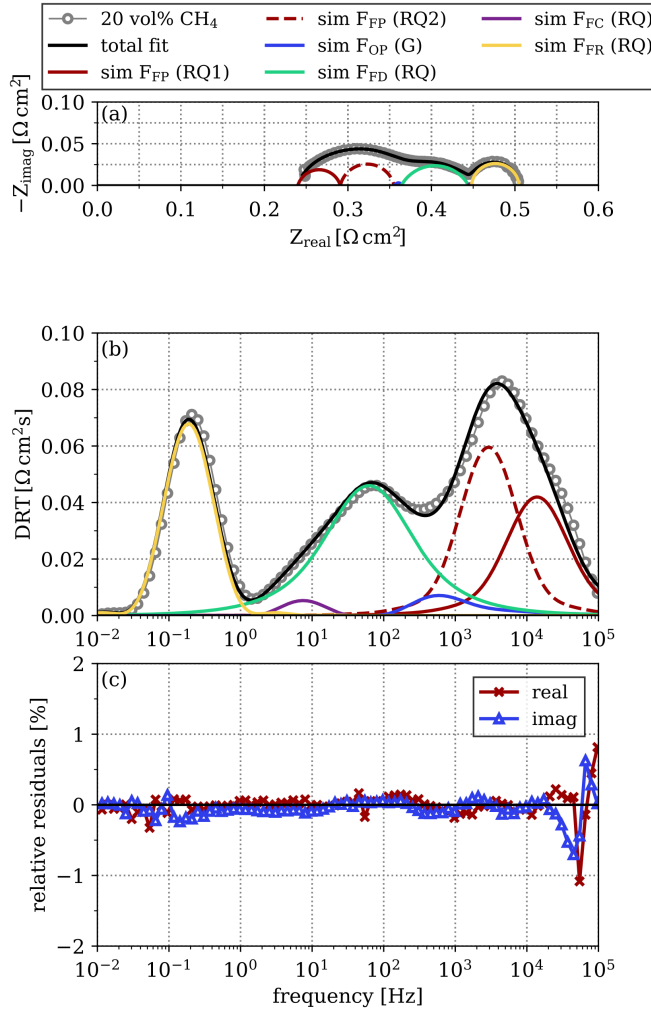


**Figure B.4:** Impedance measurement and corresponding equivalent electric circuit fit (batch fitting) including the single equivalent elements of the cell processes taking place (according to table 2.3) during 20 vol% CH<sub>4</sub> present in the pre-mixed landfill gas plus CO<sub>2</sub> fuel mixture (see section 5.3 and table 5.3). (a) Nyquist plot; (b) DRT plot; (c) Relative residuals plot of the fit result and the measured impedance data. Corresponding  $\chi^2$  error of the impedance batch fit is  $2.95 \times 10^{-7}$ .

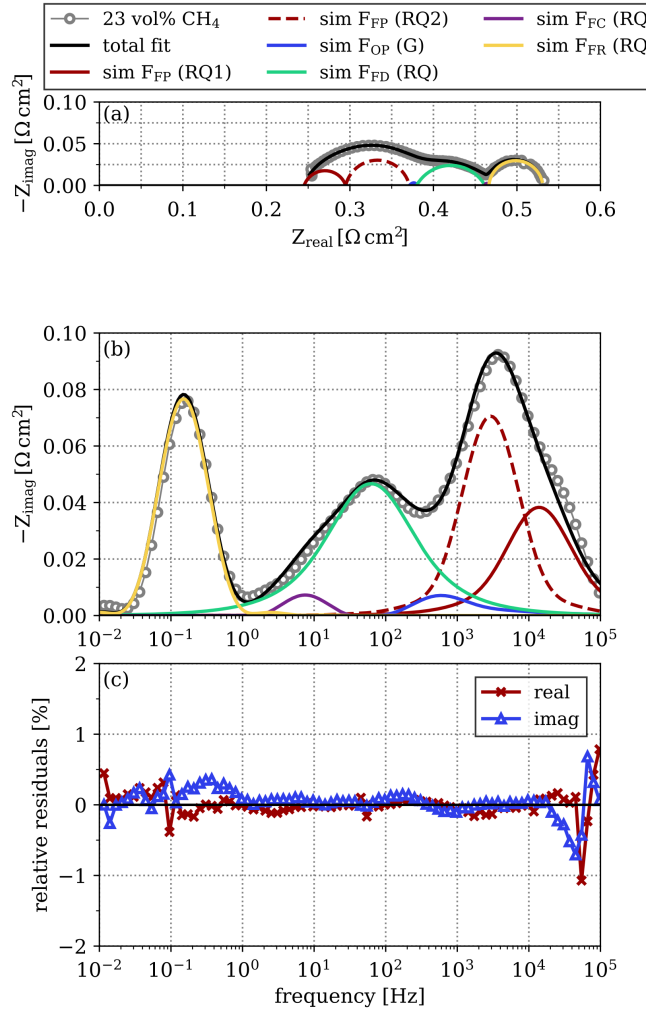


**Figure B.5:** Impedance measurement and corresponding equivalent electric circuit fit (batch fitting) including the single equivalent elements of the cell processes taking place (according to table 2.3) during 23 vol%  $\text{CH}_4$  present in the pre-mixed landfill gas plus  $\text{CO}_2$  fuel mixture (see section 5.3 and table 5.3). (a) Nyquist plot; (b) DRT plot; (c) Relative residuals plot of the fit result and the measured impedance data. Corresponding  $\chi^2$  error of the impedance batch fit is  $2.95 \times 10^{-7}$ .

## **C Proceedings and articles**

### **C.1 Galvanostatic and potentiostatic operation of real landfill gas fueled SOFCs**

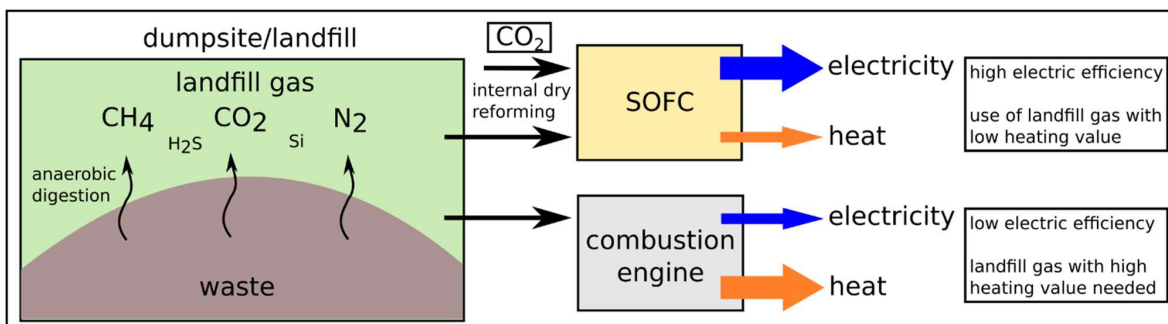
B1305

## Galvanostatic and potentiostatic operation of real landfill gas fueled SOFCs

Hendrik Langnickel, Christopher Graves, Anke Hagen

Department of Energy Conversion and Storage,  
Technical University of Denmark,  
Risø Campus, Frederiksborgvej 399,  
4000 Roskilde, Denmark  
Tel.: +45-9351-12822  
henlan@dtu.dk

### Abstract



One option to utilize landfill gas with a low heating value and to increase the electrical efficiency could be the use of solid oxide fuel cells (SOFCs). SOFCs are able to convert hydrogen or carbon containing fuels like landfill gas directly into electricity and byproduct heat. To prevent degradation of the SOFC it is important to avoid carbon formation. Therefore, a reforming agent like steam or carbon dioxide (dry reforming) is necessary. Landfill gas has the advantage that it contains a certain amount of the needed carbon dioxide already. Furthermore, a pre-cleaning of landfill gas might be required to avoid high degradation rates due to impurities in the landfill.

In the present work, planar 16 cm<sup>2</sup> SOFC cells were operated at 750 °C for a few hundred hours with real landfill gas from one of the largest Danish landfill sites, with an additional carbon dioxide reforming agent. The cell performance was analyzed and compared in galvanostatic vs potentiostatic operation modes and with vs without gas cleaning through an activated carbon filter.

In both the galvanostatic and potentiostatic operation modes, no significant changes in the power output were observed when the filter was used. When gas cleaning was not used, both operation modes showed a decline in the power output. After the first 40 hours the power density had dropped by ~0.034 W/cm<sup>2</sup> in the galvanostatic operation mode and by ~0.18 W/cm<sup>2</sup> in the potentiostatic mode.



## Introduction

Biogas derived from biomass is an attractive option to produce electricity and heat. In 2016 the total electricity production from biogas was 62500 GWh in the European Union which is an increase by 2% in comparison to 2015 [1]. The produced electricity corresponded to a primary biogas production of approximately 16.1 Mtoe in 2016. The main components of biogas are CH<sub>4</sub>, CO<sub>2</sub>, N<sub>2</sub> and impurities like sulfur or siloxanes. The biogas composition is dependent on the biomass source. Most common biomass sources are livestock manure, crops, landfill, sewage sludge, and food waste.

Landfill gas is one biogas type and amounted to around 17.2% of the total biogas production of the European Union in 2016 [1]. Landfill gas is the result of anaerobic digestion of municipal solid waste. Solid oxide fuel cell (SOFC) are able to convert biogas from different sources into electricity and heat. SOFCs have the advantage of a higher electric efficiency and biogas with a low CH<sub>4</sub> content is suitable as fuel. The integration of biogas fueled fuel cells was analyzed for example by M. Gandiglio et al. [2] for the case of an SOFC system utilizing biogas from wastewater treatment or by S. Torija et al. [3] from a more general point of few. Furthermore A. Hagen and co-workers were able to operate a state of the art SOFC cell with real landfill gas [4]. To achieve a high performance and a suitable lifetime of the SOFC, the degradation rate needs to be as low as possible. In the case of SOFC fueled with landfill gas the degradation rate is mainly dependent on poisoning by impurities like sulfur that are present in the landfill. The different effects due to poisoning of for example sulfur or siloxane have been described by various authors [5-8]. Depending on the impurity tolerance of the specific SOFC, biogas cleaning steps need to be implemented. Furthermore, a reforming agent like steam or carbon dioxide is needed to avoid carbon formation when feeding methane (and CO<sub>2</sub>) directly. The amount of carbon formation is dependent on the ratio between CH<sub>4</sub> and the reforming agent coupled with the operation temperature. The reforming agent carbon dioxide has two advantages. First, carbon dioxide is already to a certain amount present in the landfill gas and second, G. Johnsen et al. [9] could show through studies of SOFC anodes that the dry reforming process is more robust to sulfur poisoning in comparison to steam reforming.

This study focuses on the operation of state of the art anode supported SOFC cells fueled with real landfill gas from the biggest landfill site in Denmark using internal dry reforming. The landfill gas was passed or by-passed through a commercial activated carbon filter before entering the cell. In case of by-passing the filter, different operation modes were investigated with the aim to restore the original performance of the cell. Furthermore the degradation behavior was studied in two operation modes: galvanostatic and potentiostatic.

## 1. Experimental

Planar SOFC cells with an active area of 16 cm<sup>2</sup> were used. The cells consisted of Ni-YSZ/YSZ/LSCF-CGO:LSM and were placed in an alumina test house equipped with gas supplies, cell voltage probes, current collectors, temperature sensors and pO<sub>2</sub> sensors. The pO<sub>2</sub> sensor is based on platinum and measures the voltage of the target gasses vs. air and gives thus a measure of the pO<sub>2</sub> using the Nernst equation. This allowed conclusions about the gas compositions and enables comparison to the open circuit voltage (OCV) of the cell. A detailed description of the test set up is given in reference [10]. The landfill gas was mixed with the reforming agent CO<sub>2</sub> before entering the cell house. The fuel composition is shown in table 1. The impurities of the landfill gas have not been

analyzed in detail. It is only known that at least 40 ppm H<sub>2</sub>S are present and a certain amount of siloxane.

Table 1: Fuel composition consisting of the landfill gas and the additional reforming agent (RA) CO<sub>2</sub> to avoid carbon formation.

component	landfill gas				CO <sub>2</sub> RA
	CH <sub>4</sub>	CO <sub>2</sub>	O <sub>2</sub>	N <sub>2</sub>	
amount	23 vol%	15 vol%	1 vol%	28 vol%	33 vol%

The landfill gas fuel was either passed through a commercial activated carbon filter or bypassed it. The operation temperatures were 750°C and 800°C. Two cells from the same production batch were tested in long-term operation, one in galvanostatic mode and the other in potentiostatic mode. The test procedure is shown in figure 1 for the galvanostatic mode and for the potentiostatic mode in figure 2. In both figures the lower coordinate system shows the operation mode over the operation time. The state of passing or bypassing the landfill gas through the activated carbon filter during landfill gas supply is shown in the middle diagram. The top diagram illustrates the current density over the operation time. Both tests were framed by ‘finger prints’ after start up, i.e. before the durability test period and after it, i.e. before shutdown of the cell testing. The ‘finger print’ consisted of iv-curves and electrochemical impedance measurements in different steam to hydrogen ratios to the anode side and air or oxygen supply to the cathode side to characterize the cell performance. During the durability test the cathode was supplied with air. Both tests can be divided into two segments. In the first segment the anode side of the cell was supplied with landfill gas plus the reforming agent CO<sub>2</sub> passing the fuel through the activated carbon filter for cleaning. In the galvanostatic mode a current density of 0.5 A/cm<sup>2</sup> was applied and in the potentiostatic mode a cell voltage of 765 mV. These settings were selected to obtain in both cases a similar power output of approximately 0.4 W/cm<sup>2</sup>.

In the second test segment the cell was supplied with real landfill gas plus CO<sub>2</sub> and the activated carbon filter was by-passed for a certain amount of time. In case of the galvanostatic operation the activated carbon filter was by-passed for 46 hours before the fuel was passed through the filter again. The total operation time with landfill gas was ~270 hours. In the potentiostatic test, the activated carbon filter was by-passed for ~125 hours before the fuel was passed through the activated carbon filter again for an iv-curve and impedance recording. Afterwards, different regeneration strategies were applied with the aim to improve the cell performance again, as summarized in table 2 plus illustrated in the figures 1 and 2. In the case of galvanostatic operation the anode was fueled with a mixture of 50 vol% H<sub>2</sub> and 50 vol% H<sub>2</sub>O for 20 hours at a current density of 0.5 A/cm<sup>2</sup> and 750 °C. In the potentiostatic operation test, the cell was supplied with a pre-mixed biogas composition similar to the real landfill gas (but without impurities) and the reforming agent steam instead of CO<sub>2</sub>, the operation temperature was increased to 800 °C for 210 hours and the cell was operated at OCV. After the regeneration treatments, the cells were again supplied with landfill gas through the activated carbon filter plus CO<sub>2</sub> to validate the regeneration approach. In the galvanostatic test only an iv-curve and an impedance measurement were recorded because of a limited availability of landfill gas, while in the potentiostatic test the cell was operated in the potentiostatic mode for additional 88 hours. During all test segments impedance spectra and iv-curves were recorded regularly to enable analyzing the detailed cell performance (see figures 1 and 2). For data analysis the software RAVDAV was used [11].

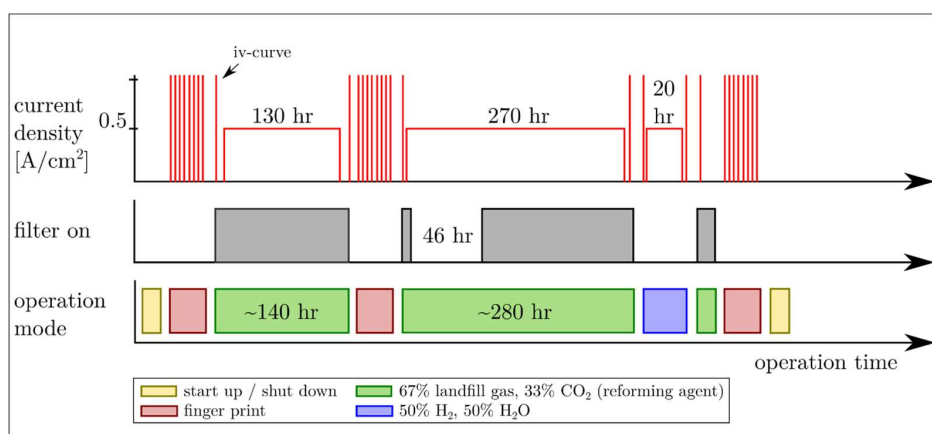


Figure 1: Test procedure for the galvanostatic operation mode with real landfill gas and additional CO<sub>2</sub> at 750°C with 0.5 A/cm<sup>2</sup>.

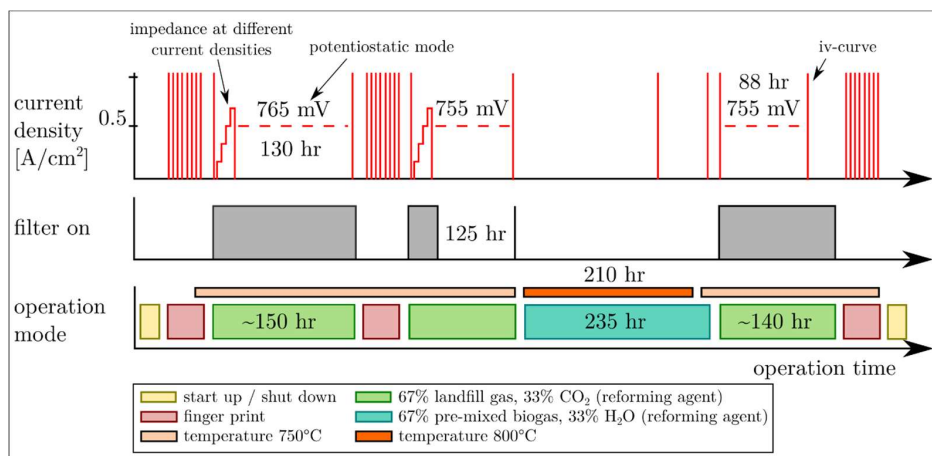


Figure 2: Test procedure for the potentiostatic operation mode with real landfill gas and additional CO<sub>2</sub> (or steam) at 750°C and 800°C with 765 mV in the first part and 755 mV in the second part.

Table 2: Testing conditions for the regeneration approach after fueling the cell with landfill gas plus CO<sub>2</sub> and by-passed activated carbon filter.

Test part	Regeneration approach			
	Fuel composition anode	Current density	Temperature	Regeneration time
Galvanostatic	50 vol% H <sub>2</sub> , 50 vol% H <sub>2</sub> O	0.5 A/cm <sup>2</sup>	750°C	20 hours
Potentiostatic	Pre-mixed biogas plus steam (CH <sub>4</sub> 25 vol%, CO <sub>2</sub> 16 vol%, N <sub>2</sub> 26 vol%, H <sub>2</sub> O 33 vol%)	0 A/cm <sup>2</sup>	800°C	210 hours

## 2. Results and discussion

### SOFC operation using landfill gas with cleaning

Figure 3 shows the results of the tests in galvanostatic (a-c) and potentiostatic (d-f) modes and applying landfill gas cleaning through the activated carbon filter. The cell voltage

(black line) started with a value of  $\sim 797$ mV and dropped slightly over the operation time of 130 hours. The voltage drop corresponds to a degradation rate of 1.1%/1000 h assuming a linear behavior and an area specific resistance (ASR) increase of 3.9%/1000 h. The value of the pO<sub>2</sub> sensor at the outlet of the cell (green line) stayed constant which indicates that the gas composition had not changed during the operation time. In figure 3b the corresponding serial resistance ( $R_s$ ) (black dots) and polarization resistance ( $R_p$ ) (blue dots) plus the applied current density of 0.5 A/cm<sup>2</sup> (red line) are illustrated. The constant  $R_s$  and  $R_p$  with values of  $\sim 0.19$   $\Omega$ cm<sup>2</sup> and  $\sim 0.22$   $\Omega$ cm<sup>2</sup> respectively is consistent with the very low degradation observed in the DC measurements. The measured cell voltage and applied current density correspond to an electric efficiency of 60% during the landfill gas fueled operation, using the definition of the electric efficiency according to reference [12, eq. 13]. In figure 3c the cell temperature at the inlet (black line) and outlet (blue line) are shown. These temperatures stayed constant with values of 745°C at the inlet and 750°C at the outlet. The temperature difference between inlet and outlet indicates that the endothermal dry reforming process was mainly occurring at the inlet side of the cell. This statement is supported by the fact that during tests with SOFCs fueled with an H<sub>2</sub>/H<sub>2</sub>O mixture this temperature difference was not detected. The observations of the potentiostatic testing were similar in comparison to the galvanostatic testing as shown in the graphs of figure 3d-f. But due to the different operation modes the current density decreased slightly instead of the cell voltage. The decrease of the current density corresponds to a degradation rate of 2.2%/1000 h and an ASR increase of 8.4%/1000 h. The small fluctuations of the cell voltage (black line, figure 3d) and current density (red line, figure 3e) are the result of small potentiostatic operation adjustments.

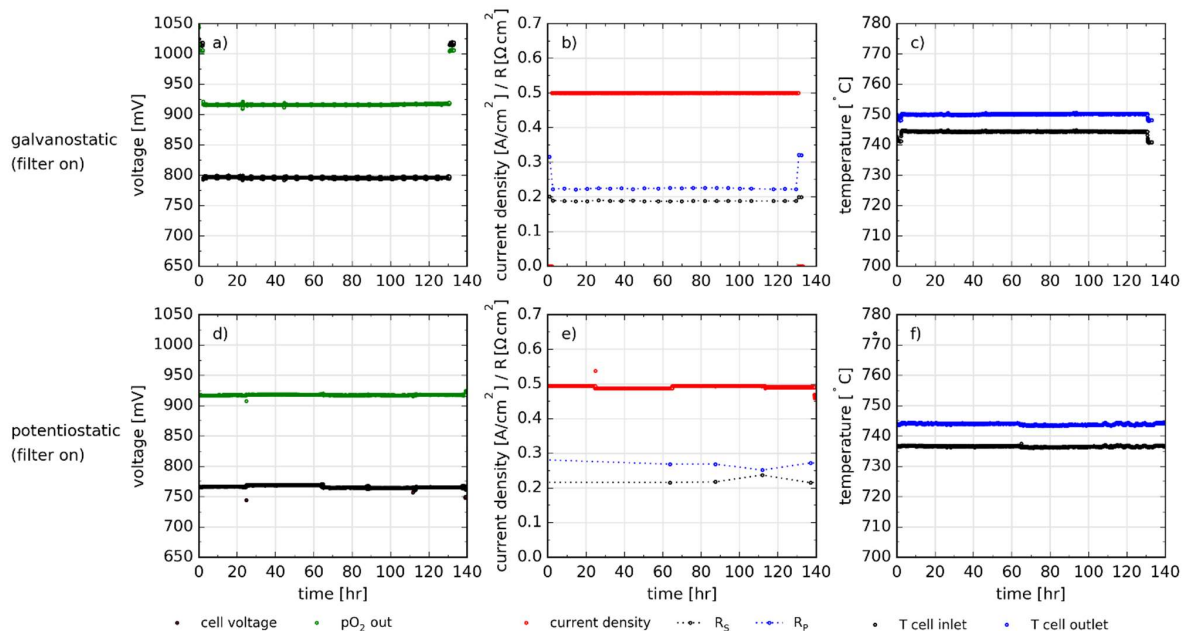


Figure 3: Test results of the galvanostatic (a-c) and potentiostatic (d-f) operation using cleaned landfill gas. Plot a), d): Cell voltage, pO<sub>2</sub> sensor at outlet of the cell; Plot b), e): Serial resistance ( $R_s$ ), Polarization resistance ( $R_p$ ) obtained from impedance spectra during operation, and current density; Plot c), f): Cell temperature at fuel inlet and outlet.

The ASR values of the cells were determined from the iv-curves recorded before and after the operation and are illustrated in figure 4. The minimum ASR value found at current densities higher than 0.1 A/cm<sup>2</sup> was considered. The ASR values of the cell in the

galvanostatic test are shown on the left side and the ASR values of the potentiostatic test on the right side.

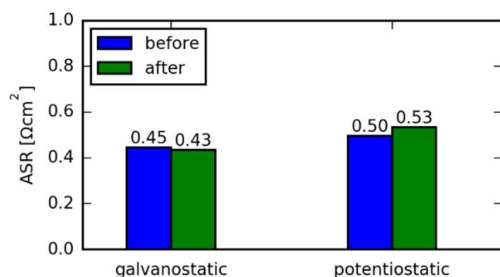


Figure 4: Comparison of the area specific resistance (ASR) determined from the iv-curves before and after the galvanostatic/potentiostatic operation with cleaned landfill gas via the activated carbon filter.

The ASR values before the degradation tests were slightly different for the two cells with values of  $0.45 \Omega\text{cm}^2$  for the cell in the galvanostatic test and  $0.5 \Omega\text{cm}^2$  for the potentiostatic test. This can be explained by a higher initial ASR for the specific cell used in the potentiostatic test in comparison to the galvanostatic test. This assumption is supported by the higher values of  $R_s$  and  $R_p$  as indicated in figure 3e. The ASR values had increased only slightly after the potentiostatic operation mode, by 6%, whereas the ASR value did not change significantly after the galvanostatic operation mode. This confirms the observations of the cell voltage and current density over time in figure 3.

### SOFC operation with landfill gas without cleaning

Figure 5 shows the results of the galvanostatic operation mode without cleaning the landfill in the first period of the operation. As the nature of the specific impurities was not known, a carbon filter was used which should remove all impurities. Using landfill gas without cleaning, the cell voltage (black line, figure 5a) started to decrease slowly and after approximately 20 hours more rapidly. After 48 hours of operating the SOFC, the cell voltage had dropped by 80 mV which corresponds to an increase of the  $R_p$  by  $0.15 \Omega\text{cm}^2$  as shown in figure 5b (blue dots). Previous dedicated studies on the sulfur poisoning in methane containing fuel show typically a fast cell voltage drop followed by an overall degradation or stable cell voltage, depending on sulfur concentration, temperature etc. [4,6,8]. The rather slow time scale and continuous trend for the cell voltage decrease in this study indicates that there are other impurities than sulfur present in the landfill, which have a poisoning effect. In order to counteract this severe degradation, the landfill was again passed through the activated carbon filter. Still, the cell voltage decreased even further in the following 25 hours to 686 mV and the  $R_p$  increased to  $0.51 \Omega\text{cm}^2$ . Afterwards, the cell started to recover slowly. After 270 hours the cell voltage had recovered to 92% and  $R_p$  was still 35% higher than at the beginning. The serial resistance  $R_s$  stayed constant (black dots figure 5b) during the whole operation time. The temperature at the fuel inlet side (black line figure 5c) of the cell increased from  $745^\circ\text{C}$  to  $748^\circ\text{C}$  during the time the cell voltage decreased and afterwards decreased again to  $746^\circ\text{C}$ . Taking into account that the reforming process is an endothermal process and therefore less energy (heat) is needed from the environment by a decreasing reforming activity. Furthermore the cell inlet temperature increase was not caused by the lower electrical power output which results in a higher thermal power output because the cell outlet temperature did not increase. Additionally, the value of the  $\text{pO}_2$  out sensor slightly decreased during the first 200 hours of operation which indicates that the outlet gas composition had changed to a small degree towards a lower amount of  $\text{H}_2$  and a higher amount of  $\text{CH}_4$  (see figure 5a).

These findings point suggest that the dry reforming process was affected by the poisoning caused by the impurities of the landfill gas.

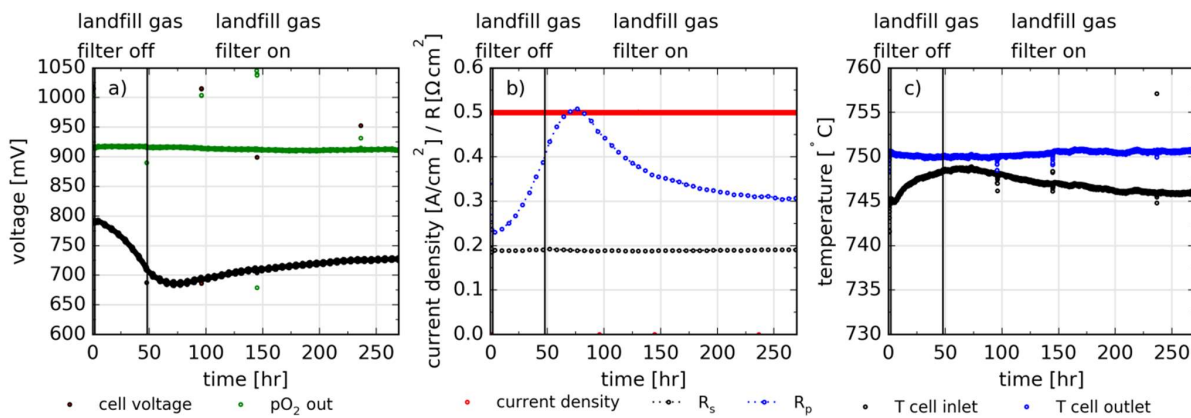


Figure 5: Test results of the galvanostatic operation without cleaning of the landfill gas.

Plot a): Cell voltage, pO<sub>2</sub> sensor at outlet of the cell; Plot b): Serial resistance ( $R_s$ ), Polarization resistance ( $R_p$ ) obtained from impedance spectra during operation, current density; Plot c): Cell temperature inlet and outlet.

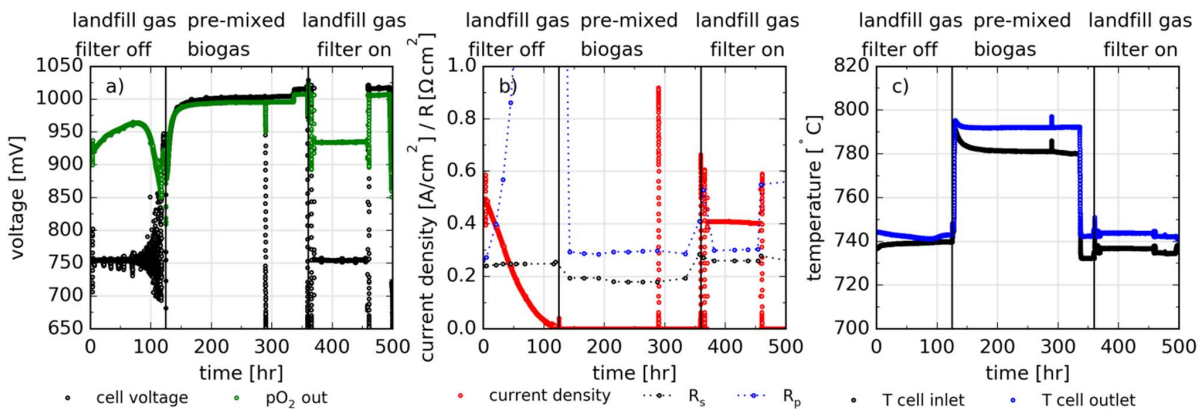


Figure 6: Test results of the potentiostatic operation without cleaning of the landfill gas.

Plot a): Cell voltage, pO<sub>2</sub> sensor at outlet of the cell; Plot b): Serial resistance ( $R_s$ ), Polarization resistance ( $R_p$ ) obtained from impedance spectra during operation, current density; Plot c): Cell temperature inlet and outlet.

The results of operating the cell with real landfill gas in the potentiostatic mode without cleaning is illustrated in figure 6. The operation time can be divided into three parts. During the first 125 hours the cell is fueled with landfill gas plus CO<sub>2</sub> and the filter is by-passed. The current density decreased rapidly from approximately 0.5 A/cm<sup>2</sup> to 0.2 A/cm<sup>2</sup> in the first 50 hours. Afterwards the current density decreased at a slower rate down to 0 A/cm<sup>2</sup>. During that time R<sub>p</sub> increased rapidly whereas R<sub>s</sub> stayed approximately constant. As the current density approached zero, the potentiostatic controller was not able to maintain the set voltage of 755 mV, as seen in the fluctuating cell voltage with progressing operation time. The pO<sub>2</sub> value measured at the fuel outlet of the cell increased by 44 mV in the first 75 hours which can be explained by the decreasing current density, causing a decreasing amount of steam on the anode side and a corresponding higher pO<sub>2</sub> voltage value. Afterwards, the value of the pO<sub>2</sub> sensor at the outlet decreased rapidly which could indicate that the pO<sub>2</sub> sensor was affected by the impurities, too. Similar to the observations during the galvanostatic test the temperature at the cell inlet increased during the time the

filter was turned off. Following this degradation period, a number of approaches were tested to regenerate the cell performance. In the following 235 hours the fuel supply was changed from real landfill gas to pre-mixed biogas and using steam as reforming agent instead of CO<sub>2</sub>. Furthermore the operation temperature was increased from 750 °C to 800 °C in order to facilitate desorption of impurities and no current was applied. In this period the cell voltage and the pO<sub>2</sub> out values increased rapidly in the first 20 hours, and then both approached the theoretical value of 1005 mV. After 280 hours of regeneration at OCV and pre-mixed biogas supply, the cell voltage was 1003 mV. The R<sub>s</sub> decreased from 0.25 Ωcm<sup>2</sup> to 0.19 Ωcm<sup>2</sup> when the temperature was increased from about 750 °C to 800 °C. R<sub>p</sub> decreased again immediately and stabilized at a value of approximately 0.29 Ωcm<sup>2</sup>. The cell inlet temperature decreased with a steep slope at the beginning and then slowly from approximately 790 °C to 780 °C in a time period of 155 hours, whereas the cell temperature at the outlet stayed constant at around 792 °C. The mentioned observations indicate that the poisoning of the cell could be regenerated to a certain degree. From the fast decrease of R<sub>p</sub> and fast cell voltage increase at the beginning of the regeneration it can be concluded that the electrochemical reaction rates at the triple face boundary recovered fast, while the reforming process recovered more slowly as the previously described temperature trend indicates. The reforming process can take place on the electrochemically inactive nickel particles in the thick cell support layer, far from the electrolyte. Poisoning of this layer is expected to occur first and thereby result in a greater density of accumulated impurities than in the electrochemically active zone near the electrolyte, which could explain the longer desorption time period. In the last period, a stable operation was achieved during fueling the cell with cleaned landfill gas plus the reforming agent CO<sub>2</sub>. But the current density was 20% lower than at the beginning of the test at the same 755 mV potentiostatic operation point, i.e. a full regeneration was not achieved.

To compare the effect of not cleaning the landfill gas in terms of the galvanostatic operation and potentiostatic operation mode, the ASR increase is illustrated in figure 7. In this case the ASR increase was calculated according to equation 1, where OCV stays for the open circuit voltage which stayed constant over time, u for the cell voltage at time t in V, i for the current density at time t in A/cm<sup>2</sup> and ASR<sub>start filter off</sub> is the ASR value at the beginning of turning of the filter during landfill gas supply.

$$\text{ASR increase}(t) = (\text{OCV} - u(t)) * i(t)^{-1} - \text{ASR}_{\text{start filter off}} \quad [\Omega\text{cm}^2] \quad (\text{eq. 1})$$

In figure 7 both curves show an exponential type behavior with the difference that the ASR during potentiostatic operation increased faster than during galvanostatic operation. After 40 hours of operation the ASR in potentiostatic mode increased by 0.48 Ωcm<sup>2</sup> whereas the ASR in galvanostatic operation increased by 0.12 Ωcm<sup>2</sup>. This indicates that the potentiostatic operation mode is more affected during the time the landfill gas was not cleaned than the galvanostatic operation mode. An explanation could be the dependency between current density and the conversion of steam at the anode. During potentiostatic operation the current density was lowered over time to achieve a constant cell voltage. By lowering the current density the production of steam is also lowered. As a consequence, the partial steam pressure at the active anode area is lower which might result in a faster deposition of the landfill gas impurities.

The ASR values determined from the iv-curves before the operation without gas cleaning, after it and after attempted regeneration (see table 2) are shown in figure 8. The initial ASR was 0.44 Ωcm<sup>2</sup> during the galvanostatic test and 0.53 Ωcm<sup>2</sup> during the potentiostatic

test. In the galvanostatic test, the ASR increased 27% after the cell was operated for 46 hours without cleaned landfill gas plus CO<sub>2</sub> followed by 222 hours with cleaned landfill gas plus CO<sub>2</sub>. In the potentiostatic test the ASR increased 1774% after 125 hours of operation without cleaned landfill gas plus CO<sub>2</sub>.

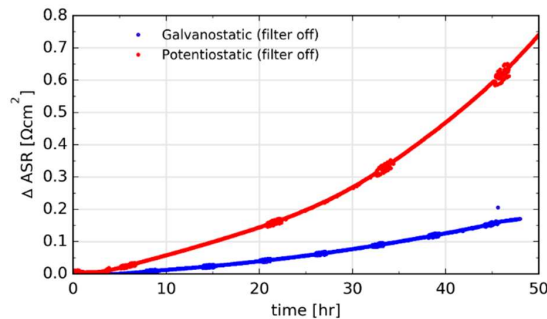


Figure 7: Area specific resistance increase of the cells after turning of the filter during landfill gas supply. Blue line illustrates the galvanostatic operation and the red line the potentiostatic operation.

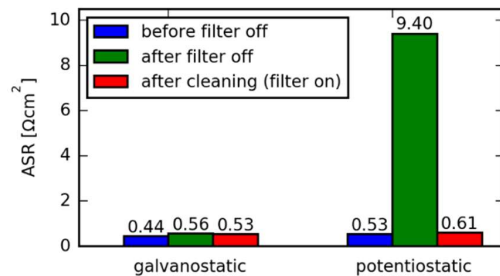


Figure 8: Comparison of the cell ASR determined from the iv-curves with and without cleaning of the galvanostatic and potentiostatic tests.

After the attempted regeneration treatments (as illustrated in table 2), the ASR decreased 5% in the galvanostatic test and 94% in the potentiostatic test. The decrease of ASR in both cases show that the supply of an H<sub>2</sub>/H<sub>2</sub>O mixture at a current density of 0.5 A/cm<sup>2</sup> (galvanostatic mode) and the supply of pre-mixed biogas plus steam at OCV in addition with an increase of operation temperature (potentiostatic test) yielded an improvement of the cell performance, i.e. a successful regeneration. These observations match with the voltage, current density and temperature dependencies illustrated in figure 6 and 7.

### 3. Conclusion

The presented work investigated the operation of state of the art solid oxide fuel cells fueled with real landfill gas and the reforming agent CO<sub>2</sub>, i.e. operation under dry reforming conditions. The operation modes galvanostatic and potentiostatic were compared with and without cleaning the landfill gas via an activated carbon filter upstream of the cell. In general this study pointed out that it is possible to operate a cell with real landfill gas and CO<sub>2</sub> in galvanostatic and potentiostatic operation modes. In both cases the SOFC performance was stable during the time the landfill gas was cleaned. In terms of the tests with landfill gas fueled SOFCs without cleaning the results indicate that the cell performance during potentiostatic operation was more affected than during galvanostatic operation. An explanation for this dependency could be the decreasing amount of steam on the anode side during potentiostatic operation as the degradation led to decreasing



current density. Even though the degradation in potentiostatic mode was larger, it is less detrimental to the cell, because the current density (power output) is lowered and no critically low voltages occur as during degradation in galvanostatic mode. The cell voltage trends while feeding not cleaned landfill to the SOFC indicate the presence of different impurities, probably in addition to sulfur. Additionally, two different regeneration strategies were applied. The tests showed that the cell performance was recovered to a certain degree by supplying the cell with a H<sub>2</sub>/H<sub>2</sub>O mixture and operating under current density or by using steam as a reforming agent instead of CO<sub>2</sub> and operating at OCV in addition to a higher operation temperature.

## Acknowledgment

The authors are very grateful to Ulrik Lønkjær and Rasmus Olsen from Odense Renovation for providing real biogas from the landfill unit in Odense. We also thank Nils Hintzen, Ole Hansen and Henrik Henriksen from DTU Energy for technical assistance.

## References

- [1] EurObserv'ER, "Biogas Barometer 2017," 01-Feb-2018. [Online]. Available: <https://www.eurobserv-er.org/pdf/biogas-barometer-2017-en/>.
- [2] M. Gandiglio, A. S. Mehr, A. Lanzini, and M. Santarelli, "DESIGN, ENERGY MODELING AND PERFORMANCE OF AN INTEGRATED INDUSTRIAL SIZE BIOGAS SOFC SYSTEM IN A WASTEWATER TREATMENT PLANT," Proceedings of the Asme 14th Fuel Cell Science, Engineering, and Technology Conference, 2016, 2016.
- [3] S. Torija, A. Castillo-Castillo, and N. P. Brandon, "The Prospects for Biogas Integration with Fuel Cells in the United Kingdom," *Fuel Cells*, vol. 16, no. 1, pp. 55–79, 2016.
- [4] A. Hagen, A. Winiwarter, H. Langnickel, and G. Johnson, "SOFC Operation with Real Biogas," *Fuel Cells*, vol. 17, no. 6, pp. 854–861, 2017.
- [5] Matsuzaki, Y. & Yasuda, I.: The poisoning effect of sulfur-containing impurity gas on a SOFC anode: Part I. Dependence on temperature, time, and impurity concentration. In: *Solid State Ionics* 132 (2000), Nr. 3-4, S. 261-269
- [6] A. Hauch, A. Hagen, J. Hjelm, and T. Ramos, "Sulfur Poisoning of SOFC Anodes: Effect of Overpotential on Long-Term Degradation," *Journal of the Electrochemical Society*, vol. 161, no. 6, pp. F734-NaN-F743, 2014.
- [7] K. Haga, S. Adachi, Y. Shiratori, K. Itoh, and K. Sasaki, "Poisoning of SOFC anodes by various fuel impurities," *Solid State Ionics*, vol. 179, no. 27–32, pp. 1427–1431, 2008.
- [8] A. Hagen, J. F. B. Rasmussen, and K. T. S. Thydén, "Durability of solid oxide fuel cells using sulfur containing fuels," *Journal of Power Sources*, vol. 196, no. 17, pp. 7271–7276, 2011.
- [9] G. B. Johnson, P. Hjalmarsson, K. Norrman, U. S. Ozkan, and A. Hagen, "Biogas Catalytic Reforming Studies on Nickel-Based Solid Oxide Fuel Cell Anodes," *Fuel Cells*, vol. 16(2), pp. 219–234, 2016.
- [10] A. Hauch and M. B. Mogensen, "Testing of Electrodes, Cells and Short Stacks," Cism International Centre for Mechanical Sciences, vol. 574, pp. 31–76, 2017.
- [11] Graves, C.: RAVDAV data analysis software, version 0.9.7, 2012.
- [12] V. Chioldo et al., "Biogas reforming process investigation for SOFC application," *Energy Conversion and Management*, vol. 98, pp. 252–258, 2015.

## **C.2 New Methodology of Studying H<sub>2</sub>S Poisoning Effects on SOFC's Fueled by Carbon Containing Fuels like Biogas**

# **New Methodology of Studying H<sub>2</sub>S Poisoning Effects on SOFC's Fueled by Carbon Containing Fuels like Biogas**

H. Langnickel<sup>a</sup>, A. Hagen<sup>a</sup>

<sup>a</sup> Department of Energy Conversion and Storage, Technical University of Denmark, Risø Campus, Frederiksborgvej 399, 4000 Roskilde, Denmark

Solid oxide fuel cells are an option to convert carbon containing fuels like natural gas or biogas into electricity with high efficiency. Natural gas consists mainly of CH<sub>4</sub> and is based on fossil fuels nowadays but can be based on renewable sources in the future. Biogas is a renewable source and consists of 40%-70% CH<sub>4</sub> and 30%-60% CO<sub>2</sub>. One advantage of the SOFC is that direct internal reforming of these fuels is possible. Impurities like sulfur components, which are present in both fuels, can have negative effects on the internal reforming of the fuel in the SOFC and the electrochemical reaction. These effects have been widely investigated. The current study presents a new, time efficient approach to investigate sulfur poisoning. It is possible to predict the effect of H<sub>2</sub>S expressed as the well-known voltage drop occurring due to sulfur exposure via the evaluation of iV-curves taken with and without sulfur.

## **Introduction**

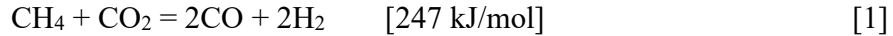
Electricity production is moving towards using entirely renewable energy sources. Due to the fluctuating nature of these sources, technologies are needed that produce electricity and heat with high efficiency using stable sources, which are independent on solar and wind. Such sources can be carbon containing fuels like for example natural gas and biogas. Natural gas consists mainly of CH<sub>4</sub> and is based on fossil fuels at the moment. But it might be obtained based on renewable sources in the future, for example through electrolysis using electricity from wind or solar (e-gas). Biogas consists mainly of: 40%-70% CH<sub>4</sub> and 30%-60% CO<sub>2</sub> and is derived from biomass (1), which is a renewable source. The electricity production from biomass was 62500 GWh in the European Union in 2016, which was an increase by around 2% from 2015 to 2016 (2). According to H. Chum et al. (3) the energy produced from biomass could lie between 100 and 300 EJ by 2050 worldwide.

In commercial biogas power plants biogas is burned off with rather low electric efficient combustion engines. For some biogas compositions, for example from landfill sources, the heating value is even too low to be compatible with combustion engines. Due to their fuel flexibility, solid oxide fuel cells (SOFC) are able to convert this fuel with low heating value into electricity with efficiencies over 50%.

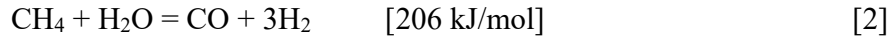
In order to avoid the thermodynamically preferred carbon formation, methane needs to be converted to H<sub>2</sub> and CO using a reforming agent like steam, CO<sub>2</sub> or O<sub>2</sub>. State-of-

the-art SOFC anodes contain nickel, which catalysis this reaction at the typical operating temperatures of 700 - 850 °C. The following reforming reactions, which normally occur, were considered in this study (4):

Dry reforming:



Steam reforming:

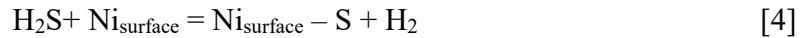


Water-gas shift reaction:



The dry reforming (eq.: [1]), which occurs with CO<sub>2</sub> is especially interesting for biogas, as it already contains significant amounts of this reforming agent.

All these catalytic reactions can be affected by impurities in the natural gas and biogas. Among various species, sulfur compounds have attracted special attention because they are known poisons (table 8.5 in ref. (5)). In addition to the catalytic reactions (reforming, water gas shift) of natural gas and biogas, sulfur has a poisoning effect on the electrochemical reaction in a SOFC (6) (7) (8) (9) (10). The poisoning effect of sulfur is believed to occur via chemisorption (eq.: [4]) of sulfur (S) at the nickel surface of the SOFC anode, thus blocking active sites for the reforming and the electrochemical reactions (11) (12).



Sulfur poisoning studies in SOFCs are typically carried out by starting the SOFC operation in a certain fuel composition followed by addition of H<sub>2</sub>S with different concentrations over different time periods until a steady state cell voltage is reached, often followed by a removal of H<sub>2</sub>S from the fuel to observe the recovery. The general observations include an initial drop of the cell voltage after introducing sulfur in the feed of the fuel stream (6) (11). This immediate loss of performance is reversible to a certain degree and the magnitude is a function of operating parameters such as temperature, fuel composition and applied current density. When comparing hydrogen and hydrocarbon fuels, the poisoning effect is larger for the latter, i.e. the reforming process is more sensitive to sulfur poisoning than the electrochemical reaction (6) (10) (13) (14). With increasing sulfur amount the reforming reaction is more and more poisoned and the voltage drop increased. These effects behave in an approximately exponential way and are reversible under conditions of a short term (24 h) exposure to sulfur and H<sub>2</sub>S concentrations in the ppm range below ca. 50 in methane containing fuel and below ca. 100 ppm in hydrogen fuel (8) (14) (15).

Such an approach is very time consuming and has to be repeated for all potential operating conditions such as current density, temperature and fuel composition. It also bears the risk of gradual degradation of the cell and might require several tests of fresh cells necessary to obtain the correct correlation of p(H<sub>2</sub>S) to cell voltage drop. The current study is aimed at investigating the effects of sulfur on the SOFC performance using a new approach. Based on results obtained following conventional studies, the

sulfur poisoning effect is evaluated in terms of iV-curves – a standard SOFC characterization tool, while varying the fuel composition. The target parameter for correlation is the well-known cell voltage drop.

## Experimental

### Cell and Test Setup

An anode supported planar Ni-ScYSZ/ScYSZ/LSCF:CGO cell with a CGO barrier layer was used. The cell had a total size of  $5 \times 5 \text{ cm}^2$  with an active area of  $16 \text{ cm}^2$ . The cell was placed in an alumina test house, sandwiched between gas distribution plates (see figure 1). A nickel plate (anode side) and gold stripes (cathode side) were used for current collection. Platinum voltage probes were connected. On the anode side a Ni-mesh was placed between the nickel plate and the anode side of the cell to ensure the gas supply and a good contact. The Ni-mesh was framed by a gold sealing. The equivalent mesh on the cathode side was a gold-mesh without a sealing. Further details about the test set up are given in reference (16).

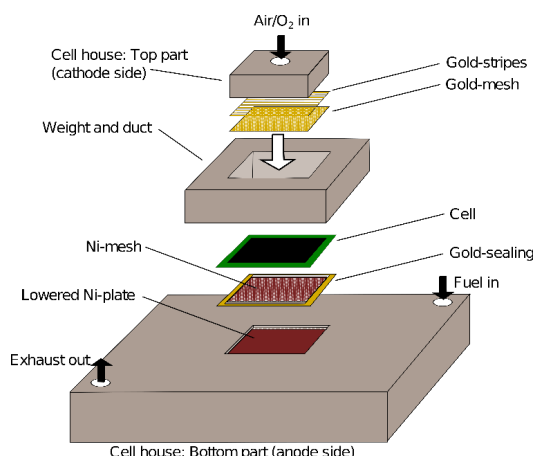


Figure 1. Sketch of the cell test house.

### Test Procedure

**Start-Up Procedure.** The cell was heated to  $850 \text{ }^\circ\text{C}$  fueled with argon to the anode side and air to the cathode side. After  $850 \text{ }^\circ\text{C}$  was reached, argon was changed to 9% H<sub>2</sub> in N<sub>2</sub> for 2h to reduce the nickel oxide to nickel in the anode. Afterwards, the anode gas was changed to pure hydrogen and a standard electrochemical characterization of the performance of the cell ('fingerprint') was done at open circuit voltage (OCV), at  $750 \text{ }^\circ\text{C}$ ,  $800 \text{ }^\circ\text{C}$ , and  $850 \text{ }^\circ\text{C}$ . The 'fingerprint' contained iV-curves and electrochemical impedance spectra (EIS) in hydrogen with up to 20% humidification. This procedure was repeated after the sulfur poisoning studies.

**Sulfur Poisoning Tests.** Four different anode gas compositions were used (see table 1). The first two tests differed in the degree of humidification of hydrogen and total flow rate, whereas the last two cases included methane and pre-mixed biogas (60% CH<sub>4</sub>, 40% CO<sub>2</sub>) in the feed. To avoid carbon deposition, a biogas to steam ratio of 0.6 was chosen based

on thermodynamic calculations. The cathode gas supply was fixed to 140 l/h air during all tests. The experimental procedure is shown in figure 2. Three to four different sulfur concentrations were applied from a bottle containing 200 ppm H<sub>2</sub>S in H<sub>2</sub>. The sulfur was added to the fuel stream by substituting the corresponding H<sub>2</sub> flow by the 200 ppm H<sub>2</sub>S in H<sub>2</sub> until a steady state of the OCV was reached (between 5 and 12 h). For each sulfur concentration, an EIS was recorded initially, followed by iV-curves. The data were analyzed with programs written in Python and for the impedance data the software RAVDAV (17) was used.

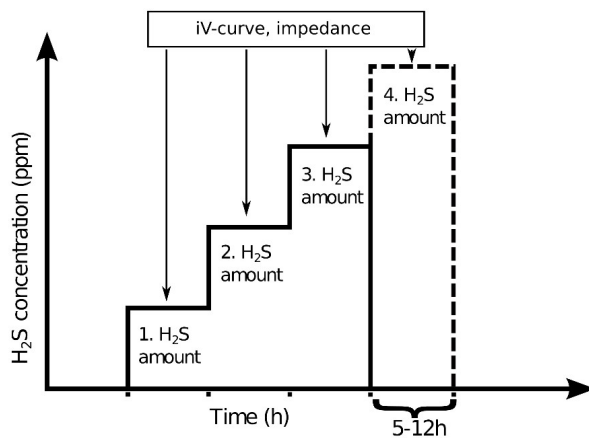


Figure 2. Experimental procedure of the short term sulfur poisoning tests at 850 °C (for gas composition see table 1).

**TABLE I.** Gas composition, total flow and applied sulfur concentration of the short term poisoning tests.

Test	Gas Composition	Total Flow [l/h]	H <sub>2</sub> S Amount [ppm]
a) H <sub>2</sub> -test (high flow)	82 vol% H <sub>2</sub> , 18 vol% H <sub>2</sub> O	24	0, 2, 10, 20
b) H <sub>2</sub> -test	47 vol% H <sub>2</sub> , 53 vol% H <sub>2</sub> O	10	0, 2, 10, 20, 90
c) CH <sub>4</sub> -test	29 vol% CH <sub>4</sub> , 13 vol% H <sub>2</sub> , 58 vol% H <sub>2</sub> O	10	0, 2, 10, 20
d) Biogas-test	50 vol% biogas (60 vol% CH <sub>4</sub> , 40 vol% CO <sub>2</sub> ), 10 vol% H <sub>2</sub> , 40 vol% H <sub>2</sub> O	10	0, 2, 10, 20

For validation of the iV analysis approach, a long-term test was done with pre-mixed biogas at a current density of 0.5 A/cm<sup>2</sup>. After ca. 25 h, a sulfur concentration of 2 ppm was applied for the next ca. 220 h. Then the H<sub>2</sub>S supply was removed from the fuel stream. EIS measurements were done every 12 h under current.

## Results and Discussion

### Sulfur Poisoning iV-Curves

In figure 3 iV-curves are shown as a function of sulfur concentration. In the tests shown in figure 3a) and b) hydrogen and steam where used as fuel. At OCV, this gas composition (hydrogen/steam) is not affected by the presence of sulfur, because no catalytic reactions occur. This results therefore in the same OCV at all sulfur concentrations, as expected. In tests shown in figure 3c) and d), methane containing fuel

was used. In the presence of steam and  $\text{CO}_2$ , methane reforming reaction (reactions 1-3) occur at OCV, which are purely catalytic reactions as long as no current is applied. Sulfur is affecting these catalytic reactions and therefore the gas composition in the SOFC anode. This is reflected in a change of the OCV (according to the Nernst relation). Specifically, the OCV decreased as the sulfur concentration was increased. This illustrates a smaller methane conversion and thus a smaller share of  $\text{H}_2$  and  $\text{CO}$  in the fuel as compared to the sulfur free, not poisoned case.

Evaluating the iv-trends, the slope increased and the maximum current density decreased with increasing sulfur concentration in all four tests, also the ones with hydrogen/steam and no methane. This proofs that the electrochemical reactions are poisoned by sulfur.

Evaluating the tests with hydrogen, the slopes of the iV-curves increase most when adding 2 ppm  $\text{H}_2\text{S}$  (circle and cross curves in figure 3a), while they do not change as significantly when the  $\text{H}_2\text{S}$  concentration was increased further (figure 3a), i.e. the poisoning effect is levelling off. This indicates that the largest poisoning effect occurs already at smaller  $\text{H}_2\text{S}$  concentrations. This trend is in line with the results of conventional poisoning tests in hydrogen, even though they were performed with cells of different anode and cathode compositions and at constant current density (6).

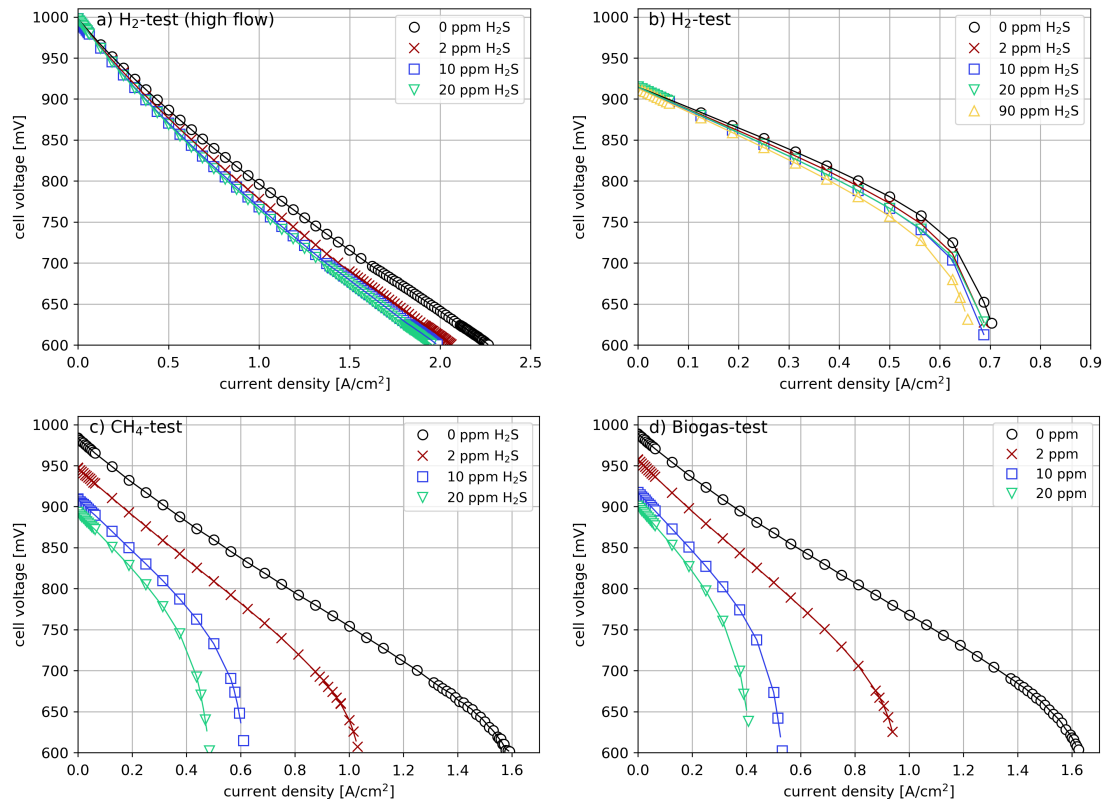


Figure 3. Linear interpolated iV-curves with various sulfur concentrations (0 ppm-90 ppm) fueled with a)  $\text{H}_2$ , (high flow), b)  $\text{H}_2$  (low flow), c)  $\text{CH}_4$  and d) pre-mixed biogas at 850 °C and 140 l/h air on the cathode side. Further specifications are given in table 1.

In tests shown in figure 3b)-d), with the same anode flow rates of 10 l/h also significant diffusion losses were observed at high current densities. When comparing the test in figure 3a) conducted with an anode flow rate of 24 l/h and figure 3b) with only hydrogen/steam fuel, this observation is related to the hydrogen content. The small share of hydrogen initially present in the fuel in test figure 3b) and the lower anode fuel flow rate leads to a faster fuel starvation already in the absence of H<sub>2</sub>S. In tests figure 3c) and d) the starvation is in addition related to the poisoning of the reforming reaction, which leads to smaller in-situ formed hydrogen with increasing degree of poisoning.

The obtained results of the iV-curves were further evaluated in terms of the more common approach of estimating the immediate voltage drops ( $\Delta U$ ) and ASR increase as consequence of the addition of sulfur. This was achieved by subtracting iV-curves under H<sub>2</sub>S from the one without H<sub>2</sub>S in the fuel. The results are shown in figure 4 as a function of the current density. The data were taken from the measured iV-curves (see figure 3) after linear interpolation as a first approximation.

Using hydrogen/steam fuel in the regime where no fuel starvation occurs (linear range in figure 3a, b), the resulting cell voltage drop (delta voltage) are superimposed, i.e. the poisoning effect is the same (line a) and b) in fig. 4). These results indicate that the total flow rate in the range between 24 l/h (test a)) and 10 l/h (test b)) has no influence on the degree of H<sub>2</sub>S poisoning because the ratio of p(H<sub>2</sub>S) and p(H<sub>2</sub>) is the determining parameter and not the flow rate. As soon as the regime of fuel starvation is reached, the poisoning effect becomes more significant, not only affecting the anode reaction but also diffusion.

The voltage drops of test c) and d) increased with increasing current density, which points to a critical effect of fuel starvation with progressing poisoning of the reforming reaction caused by the low flow rate of hydrogen and CO. The voltage drop increased more in test d) than in test c). The reason for this could be the lower hydrogen amount (10% vs. 13%, respectively) and the larger share of CO<sub>2</sub> in the initial fuel stream of test d). For the tests with CH<sub>4</sub> and biogas (test c) and d)), two poisoning regimes can be distinguished as function of current density, one at low current density (more flat slope) and one at high current density (steep slope). The poisoning regime at lower current densities (more flat slope) is observed in the H<sub>2</sub> fuel as well (test a) and b)).

These two regions become even more apparent when calculating the increase of ASR due to H<sub>2</sub>S addition (18). In figure 5 the immediate ASR value increases as a function of the current density are shown using the results obtained in this study. The curves were derived by taking the gradient of the immediate voltage drop curves shown in figure 4 and applying a Savitzky-Golay filter for smoothing the data.

There has been a discussion of the effect of current on the sulfur poisoning, with arguments in favor of current (12) (19) (20) (21) (22) (23) (24) and against an effect (25) (26). Interestingly, when looking at the region where the iV-curves are linear (compare to figure 3c) and d)), there is basically no change of the immediate ASR increase as function of current density. In figure 5 the curves a) and b) show no change of the ASR up to current density of ca. 0.5 A/cm<sup>2</sup> and curve c) up to ca 0.2 A/cm<sup>2</sup>. On the other hand, the ASR values increase steeply at higher current density (see figure 5). Hagen et al. (18) found that current has no effect on the increase of ASR due to H<sub>2</sub>S poisoning in the low-

current region, where the poisoning effect is mainly due to poisoning of the anode polarization. However, at higher current density, where fuel starvation due to the poisoning of the reforming reaction occurs more severely, there is an increase of ASR with increasing current density. The results in this study, which were obtained through a different approach, completely support these findings.

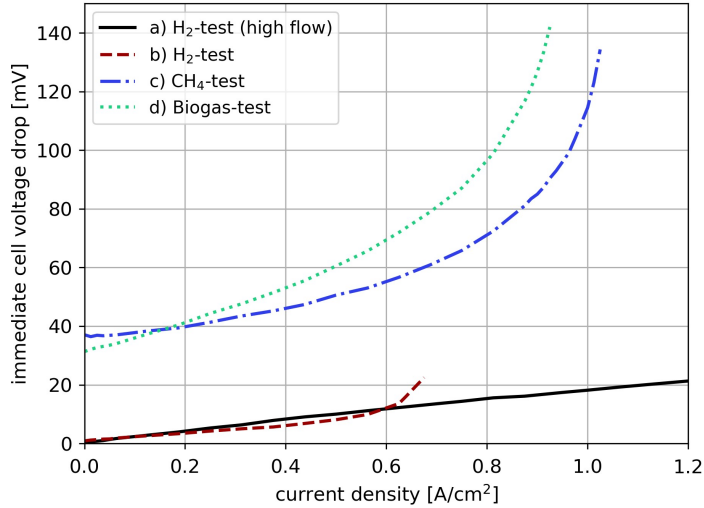


Figure 4. Immediate voltage drops for 2 ppm H<sub>2</sub>S in relation to 0 ppm H<sub>2</sub>S as a function of the current density in fuels a) to d). The curves were derived from the interpolated iV-curves shown in figure 3.

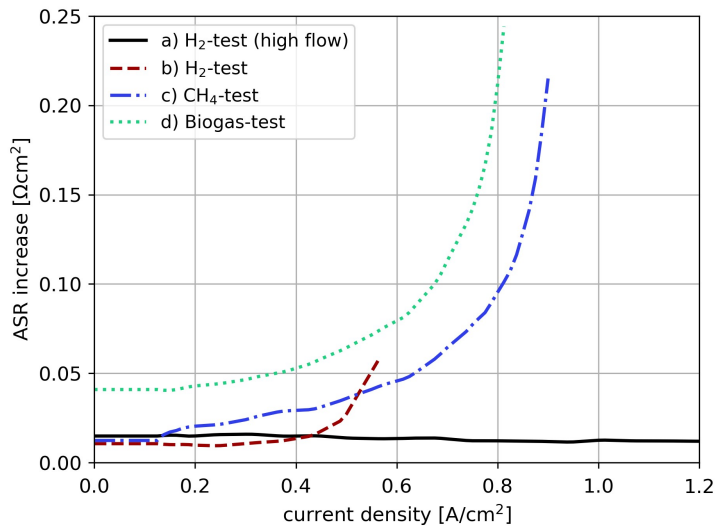


Figure 5. Area specific resistance (ASR) increase for 2 ppm H<sub>2</sub>S in relation to 0 ppm H<sub>2</sub>S as a function of the current density in fuels a) to d). Curves were derived by taking the gradient of the immediate voltage drop curves shown in figure 4. Furthermore a Savitzky-Golay filter was applied for smoothing the data.

## Comparative Test to Validate the H<sub>2</sub>S iV-Curve Approach

The current study suggests that it is possible to determine cell voltage drops and increase of ASR due to H<sub>2</sub>S poisoning by analyzing iV-curves (figure 4, 5), which is significantly faster than the conventional approach that measures under steady state conditions – as long as reversible changes occur.

In order to validate the results and compare to values obtained with the traditional poisoning tests, a test with pre-mixed biogas as fuel was carried out with a constant current density of 0.5 A/cm<sup>2</sup>. Figure 6 shows the cell voltage and the serial resistance ( $R_s$ ) and polarization resistance ( $R_p$ ) which were determined from EIS spectra over time. In the absence of sulfur, the cell voltage was 871 mV and thus close to the expected value of 868 mV from the iV-curve (see figure 3d)). After addition of 2 ppm H<sub>2</sub>S the cell voltage dropped (for values see table 2) by 61.9 mV. This value is very close to the one calculated from the iV-curves; the relative error is only 2.2% (see table 2, figure 4). This confirms the validity of the cell voltage drop values obtained with the faster iV-curve approach.

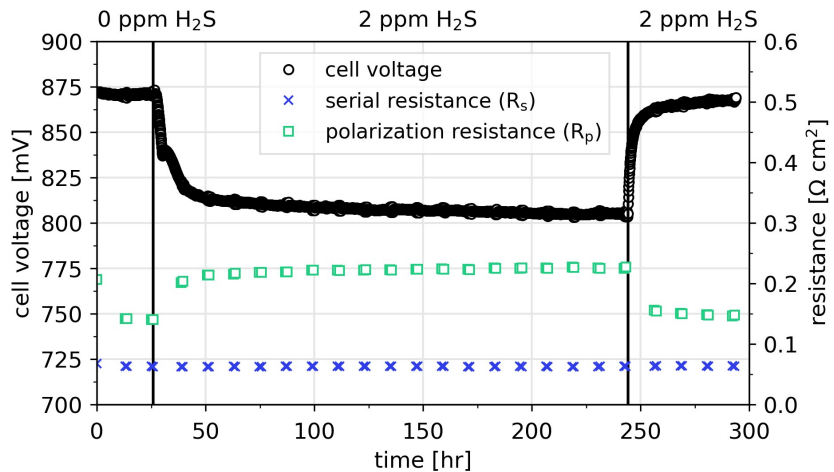


Figure 6. Steady state test with pre-mixed biogas at 0.5 A/cm<sup>2</sup>, 850 °C. Cell voltage (circle, left-axis) and serial resistance  $R_s$  (cross, right-axis), polarization resistance  $R_p$  (square, right-axis) before and after addition of 2 ppm H<sub>2</sub>S.

**TABLE II.** Expected (see fig. 4) and measured (after 61 hours of test, figure 6) cell voltage drop after addition of 2 ppm H<sub>2</sub>S to pre-mixed biogas fuel at 850 °C and 0.5 A/cm<sup>2</sup>.

Expected Voltage Drop [mV]	Measured Voltage Drop [mV]	Relative Error [%]
60.9	61.9	2.2

The  $R_p$  and  $R_s$  values for the EIS recorded over time as presented in figure 6 show that  $R_p$  is increasing (and decreasing) when H<sub>2</sub>S is added (or removed) from the fuel, while  $R_s$  remains constant. This is a clear indication of a reversible poisoning effect. In figure 7, selected EIS spectra are shown. They confirm that the serial resistance remained constant. The  $R_p$  increased and two main contributions to this increase can be clearly identified (see figure 7 bottom). There is an increase of impedance at lower (4 Hz, diffusion) and higher (800 Hz, anode reaction) frequencies. The result confirms the expectations from the iV-curves in figure 3d), where a current density of 0.5 A/cm<sup>2</sup> is

located in a regime where the anode reaction is poisoned and also fuel starvation (increased diffusion impedance) due to the degree of poisoning starts to occur.

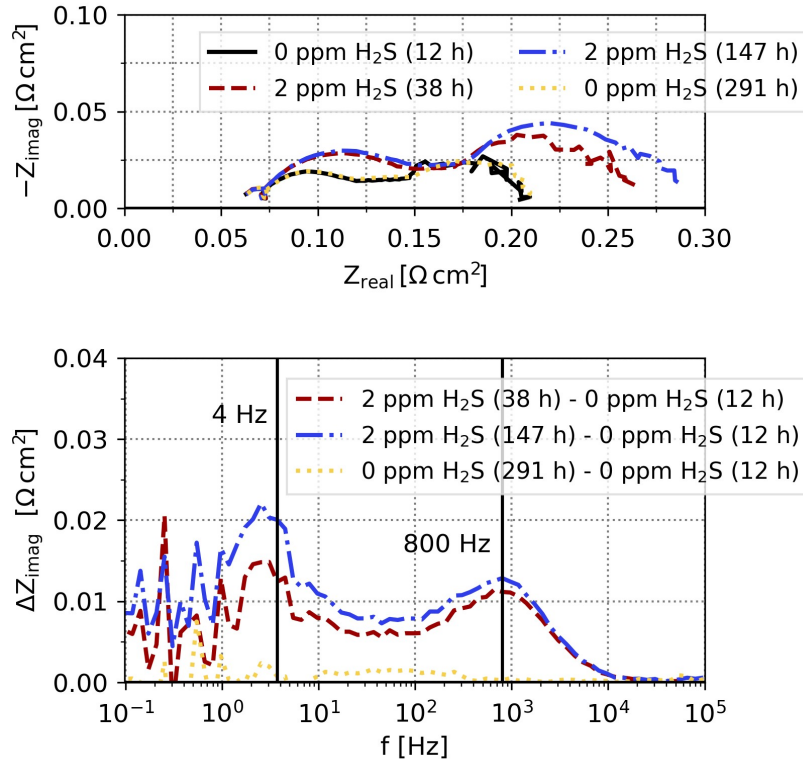


Figure 7. Nyquist (top) and differences (bottom) plot (bode plot) of the pre-mixed biogas before and after addition of 2 ppm H<sub>2</sub>S sulfur in pre-mixed biogas, 850 °C, 0.5 A/cm<sup>2</sup>.

## Conclusion

A new approach of testing SOFC in regard to sulfur poisoning was introduced. This approach is significantly less time consuming as compared to the traditional steady state approach of starting SOFC operation, adding of a certain H<sub>2</sub>S concentration, observing a steady state response, removing the H<sub>2</sub>S and awaiting recovery, followed by the H<sub>2</sub>S addition of the next concentration and later on other variations of operating parameters such as current density. In this study it was demonstrated that a fast approach is to compare iV-curves recorded at a certain H<sub>2</sub>S concentration in the fuel with sulfur free conditions. The comparison of the iV-curves with and without sulfur allows for the calculation of the well-known voltage drop due to H<sub>2</sub>S poisoning. The values are in the same range as obtained by the traditional steady state approach.

The magnitudes of the voltage drops were seen to change with current density. In addition to a general increase of the voltage drop with increasing current density, also the differentiation between two major poisoning regimes, one at low and one at higher current densities was possible. These regimes are related to the poisoning of the anode reaction and the increase of fuel starvation, respectively.

Apart from evaluating the cell voltage drop as parameter for the degree of H<sub>2</sub>S poisoning, also the increase of ASR was evaluated based on the iV-curves. It was shown that the ASR increase due to H<sub>2</sub>S poisoning is independent on the current density as long as there is no severe fuel starvation. In the operating regime of severe fuel starvation, the ASR increase grows with increasing current density.

### Acknowledgments

The authors would like to say thank you to X. Sun, J. Nielsen for the scientific support and to O. Hansen, H. Henriksen for their technical assistance.

### References

1. T. Abbasi, S. M. Tauseef and S. A. Abbasi, "Biogas energy," Biogas Energy, pp. 1-169, 2012.
2. EurObserv'ER, Biogas Barometer 2017, EurObserv'ER, Ed., 2017.
3. H. Chum, A. Faaij, J. Moreira, G. Berndes, P. Dhamija, H. Dong, B. Gabrielle, A. Goss Eng, W. Lucht, M. Mapako, O. Masera Cerutti, T. McIntyre, T. Minowa, K. Pingoud, Bioenergy, in IPCC Special Report on Renewable Energy Sources and Climate Change Mitigation (Eds. O. Edenhofer, R. Pichs-Madruga, Y. Sokona, K. Seyboth, P. Matschoss, S. Kadner, T. Zwickel, P. Eickemeier, G. Hansen, S. Schlömer, C. von Stechow), Cambridge University Press, Cambridge, United Kingdom and New York, NY, USA, 2011.
4. J. R. Rostrup-Nielsen, J. Sehested and J. K. Norskov, "Hydrogen and synthesis gas by steam- and CO<sub>2</sub> reforming," Advances in Catalysis, vol. 47, pp. 65-139, 2002.
5. J. Larminie, Fuel cell systems explained, Chichester [u.a.] : Wiley, 2003.
6. J. F. B. Rasmussen and A. Hagen, "The effect of H<sub>2</sub>S on the performance of Ni-YSZ anodes in solid oxide fuel cells," Journal of Power Sources, vol. 191, pp. 534-541, 2009.
7. A. Lanzini, D. Ferrero, D. Papurello and M. Santarelli, "Reporting Degradation from Different Fuel Contaminants in Ni-anode SOFCs," Fuel Cells, vol. 17, pp. 423-433, 2017.
8. A. Hagen, J. F. B. Rasmussen and K. T. S. Thydén, "Durability of solid oxide fuel cells using sulfur containing fuels," Journal of Power Sources, vol. 196, pp. 7271-7276, 2011.
9. A. Weber, S. Dierickx, A. Kromp and E. Ivers-Tiffée, "Sulfur poisoning of anode-supported SOFCs under reformate operation," Fuel Cells, vol. 13, pp. 487-493, 2013.
10. D. K. Niakolas, "Sulfur poisoning of Ni-based anodes for Solid Oxide Fuel Cells in H/C-based fuels," Applied Catalysis A: General, vol. 486, pp. 123-142, 2014.
11. K. Sasaki, K. Susuki, A. Iyoshi, M. Uchimura, N. Imamura, H. Kusaba, Y. Teraoka, H. Fuchino, K. Tsujimoto, Y. Uchida and N. Jingo, "H<sub>2</sub>S poisoning of solid oxide fuel cells," Journal of the Electrochemical Society, vol. 153, pp. 009611JES, A2023-A2029, 2006.

12. J. Bøgild Hansen and J. Rostrup-Nielsen, "Sulfur poisoning on Ni catalyst and anodes," in *Handbook of Fuel Cells*, Wiley Online Library, 2009.
13. A. Hagen, "Sulfur Poisoning of the Water Gas Shift Reaction on Anode Supported Solid Oxide Fuel Cells," *Electrochemical Society Journal*, vol. 160, pp. F111-F118, 2013.
14. J. F. B. Rasmussen and A. Hagen, "The Effect of H<sub>2</sub>S on the Performance of SOFCs using Methane Containing Fuel," *Fuel Cells*, vol. 10, pp. 1135-1142, 2010.
15. A. Hagen, A. Winiwarter, H. Langnickel and G. Johnson, "SOFC Operation with Real Biogas," *Fuel Cells*, vol. 17, pp. 854-861, 2017.
16. A. Hauch and M. B. Mogensen, "Testing of Electrodes, Cells and Short Stacks," *Cism International Centre for Mechanical Sciences*, vol. 574, pp. 31-76, 2017.
17. C. R. Graves, RAVDAV data analysis software, version 0.9.7, 2012.
18. A. Hagen, G. B. Johnson and P. Hjalmarsson, "Electrochemical evaluation of sulfur poisoning in a methane-fuelled solid oxide fuel cell: Effect of current density and sulfur concentration," *Journal of Power Sources*, vol. 272, pp. 776-785, 2014.
19. J. B. Hansen, "Direct reforming fuel cells," in *Fuel Cells: Technologies for Fuel Processing*, Elsevier, 2011, pp. 409-450.
20. Z. Cheng, S. Zha and M. Liu, "Influence of cell voltage and current on sulfur poisoning behavior of solid oxide fuel cells," *Journal of Power Sources*, vol. 172, pp. 688-693, 2007.
21. S. Zha, Z. Cheng and M. Liu, "Sulfur poisoning and regeneration of Ni-based anodes in solid oxide fuel cells," *Journal of the Electrochemical Society*, vol. 154, pp. B201-B206, 2007.
22. Z. Cheng, "Investigations into the interactions between sulfur and anodes for solid oxide fuel cells," 2008.
23. E. Brightman, D. G. Ivey, D. J. L. Brett and N. P. Brandon, "The effect of current density on H<sub>2</sub>S-poisoning of nickel-based solid oxide fuel cell anodes," *Journal of Power Sources*, vol. 196, pp. 7182-7187, 2011.
24. D. S. Monder and K. Karan, "Coverage Dependent Thermodynamics for Sulfur Poisoning of Ni Based Anodes," *ECS Transactions*, vol. 57, pp. 2449-2458, 10 2013.
25. S. J. Xia and V. I. Birss, "Deactivation and Recovery of Ni-YSZ Anode in H<sub>2</sub> Fuel Containing H<sub>2</sub>S," *ECS Proceedings Volumes*, Vols. 2005-07, pp. 1275-1283, 1 2005.
26. T. Yoshizumi, C. Uryu, T. Oshima, Y. Shiratori, K. Ito and K. Sasaki, "Sulfur Poisoning of SOFCs: Dependence on Operational Parameters," 2011.

### **C.3 Efficiency analysis of 50 kW<sub>e</sub> SOFC systems fueled with biogas from waste water**

## Efficiency analysis of 50 kWe SOFC systems fueled with biogas from waste water

Hendrik Langnickel, Markus Rautanen, Marta Gandiglio, Massimo Santarelli, Tuomas Hakala, Marco Acri, Jari Kiviahio

### Keywords

Biogas, Waste water treatment, Solid oxide fuel cell system, High electric efficiencies, High total efficiencies, Electric power modulation

### Abstract

Solid oxide fuel cell systems (SOFCs) are able to convert biogas from e.g. waste water plants highly efficiently into electricity and heat. An efficiency study of industrial sized SOFC systems installed at a waste water treatment plant is presented. The site consist of a biogas cleaning unit, two Convion C50 SOFC systems and a heat recovery section. The electric and total efficiencies of the systems are analyzed as a function of the electric net power output. The two SOFC systems achieved consistently high electric (50-55%) and total (80-90%) efficiencies in an electric net power output range between 25 kW and 55 kW. The study also shows that the high system efficiencies are independent of the CH<sub>4</sub> content in the biogas. The results indicate that fuel cell systems are able to perform power modulation according to the power demand, while achieving constant high efficiencies. This is a clear benefit in comparison to micro turbines and combustion engines which are normally used for converting biogas into electricity and heat.

### 1. Introduction

Efficient utilization of waste is an important step towards circular economy and reduction of greenhouse gas emissions. Biogas is generated in e.g. waste water treatment and municipal waste management plants. Anaerobic digestion of biomass results in biogas consisting of mainly CH<sub>4</sub> and CO<sub>2</sub>. Biogas often also includes contaminants like sulfur compounds and siloxanes depending on feedstock [1]. In 2016 the total biogas energy production was 190 TWh in Europe. The electricity production from biogas in Europe was in 2016 approximately 63 TWh [2]. Around 17% of the used biogas was produced from landfill and 9% from waste water. The other 74% was produced by different industrial plants like decentralized agricultural plants and methanation plants. One way to reduce the emissions and increase the efficiency of waste management systems is to utilize the produced biogas for electricity and heat production on-site, thus reducing the required external energy input of the plant. Conventional approach to convert biogas into electricity and heat has been to utilize internal combustion engines or micro-turbines. This has the disadvantage of low electric efficiencies and air pollution with nitrogen oxides and small particles [3]. An alternative option is the use of fuel cell systems. A fuel cell is a chemical converter which converts hydrogen based fuels highly efficiently into electricity and heat. The use of fuel cells for converting biogas into electric energy has been discussed and demonstrated on different levels in a broad range ([4]-[16]). The potential of biogas fed fuel cells for producing electricity and heat was analyzed by Torija et al. [4] and Van herle et al. [5]. The advantages of fuel cells for emission reduction and increasing the efficiency of waste management systems has been investigated for example by Lombardi et al. [6] and Gandiglio et al. [7]. Successful operations and analysis at cell level for a solid oxide fuel cell (SOFC) fueled with real biogas from landfill was reported by Hagen et al. [8] [9]. Successful 500 hours operation of a SOFC short stack fueled with pre-mixed dry biogas and including the use of a cleaning unit and a pre-reformer was presented by Papurello et al. [10]. A review about dealing

1 with fuel contaminants in the biogas for operation of biogas fueled SOFC's and molten carbonate fuel cells  
 2 (MCFC) is provided by Lanzini et al. [11]. In comparison to other fuel cell types SOFCs have the advantage of  
 3 fuel flexibility and can be operated directly with hydrocarbon fuels such as biogas [9]. Furthermore this type  
 4 of fuel cell is more robust to impurities in the fuel because of the high operation temperature.

5 One of the first field tests of a commercial fuel cell system at a landfill gas site using a phosphoric acid fuel  
 6 cell (PAFC) is reported by Spiegel et al. [12]. The first installation of a fuel cell system in Europe for converting  
 7 biogas from a waste water plant into electricity and heat was demonstrated in Germany [13]. The system  
 8 was based on a 200 kW PAFC system. The biogas was pre-cleaned by a two-phase purification phase and an  
 9 adsorption step using an activated carbon filter. Furthermore, a reformer unit was used for converting the  
 10 biogas into a H<sub>2</sub> rich gas. The first use of a MCFC system for converting biogas from a waste water plant in  
 11 Europe is reported by Krumbeck et al. [14]. The first 20 kW SOFC based system fueled with biogas from landfill  
 12 was demonstrated by Wärtsilä in Finland [15] [16].

13 The DEMOSOFC project is the first industrial sized SOFC site operated at a waste water plant [17]. The project  
 14 aims to install and operate a biogas fed 174 kW electric SOFC site at the SMAT Collegno waste water plant  
 15 close to Turin in Italy. The project should illustrate the technical and economical practicability of SOFC  
 16 systems operated at a waste water plant. Furthermore, the increase of the overall waste water plant  
 17 efficiency and reduction of the environmental plant emissions is demonstrated in the project. A detailed  
 18 description and first results of the SOFC site at the Turin waste water plant have been reported by Gandiglio  
 19 et al. [18] and M. Santarelli et al. [19].

20 The aim of this article is to analyze the performance of the biogas fed SOFC systems from October 2017 until  
 21 the end of 2019. It is expected that the SOFC systems will be operated at least until the end of 2020 to gain  
 22 further experience of the installation and operation.

## 31 2. Experimental

32 The data was recorded at the biogas fed SOFC site located at the SMAT Collegno waste water plant close to  
 33 Turin in Italy. The site can be divided into three sections: biogas cleaning and compression, SOFC framework  
 34 and heat recovery. Commercial impregnated activated carbon filters are used for the biogas cleaning. The  
 35 SOFC section consists of two C50 SOFC power systems and one C60 SOFC power system from the company  
 36 Convion [20]. The systems have an electric net power output of 40 to 60 kW each. A heat recovery unit is  
 37 included in the systems. At the end of 2019, the two C50 systems have been installed, while the C60 system  
 38 is planned to be installed in 2020. Except of the implemented SOFC stack technology the two C50 systems  
 39 are identical. In the heat recovery section the heat provided by the SOFC systems is transferred to the waste  
 40 water plant. The operation of the biogas fed SOFC site is monitored by different sensors. The sensors are  
 41 located at various positions on the site.

42 Data for the analysis is coming both from the plant site sensors, installed by the end user, and SOFC system  
 43 specific sensors, installed within the system control volume. Some measurements are done both by the end  
 44 user and the SOFC producer, for example the power production, the heat recovery rate, the biogas flow rate  
 45 consumed. All the values are logged at a 10-minutes interval by the PLC and stored in the onsite operator  
 46 panel. The data is exported from the operator panel by POLITO and/or SMAT personnel and is shared through  
 47 a dedicated cloud with VTT personnel responsible for the analysis. More detailed descriptions concerning the  
 48 set-up of the SOFC site are given in reference [18] and [19].

49 The data has been recorded from beginning of October 2017 until the end of 2019. For the analysis the data  
 50 were interpolated to one hour time steps. Results like the electric and total efficiencies of the C50 systems  
 51 were calculated according to the international standard IEC 62282-3-200 for stationary fuel cell power

systems. In addition stable operation conditions for the C50 systems were defined based on the guideline as well [21]. An overview about the data analysis is given in figure 1.

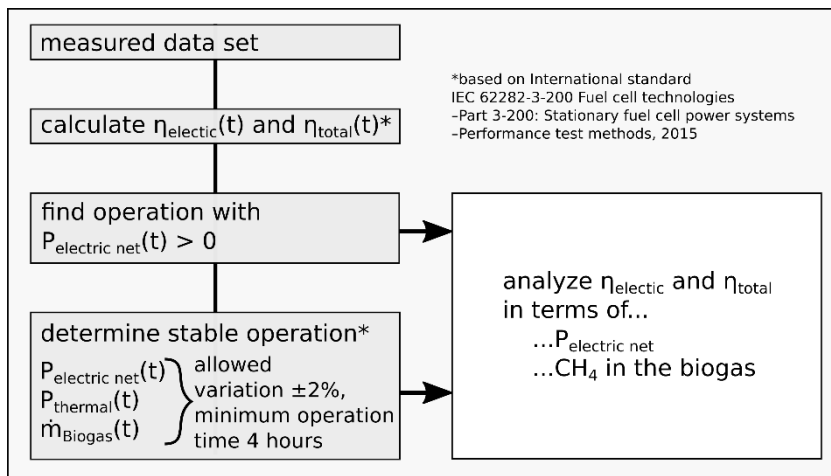


Figure 1: Illustration of the data analysis procedure which is based on the International standard IEC 62282-3-200 Fuel cell technologies – Part 3-200: Stationary fuel cell power systems – Performance test methods, 2015 [21].

### 3. Results and discussion

The first system and the second system have been operating in total for 9113 hours providing electricity and heat to the plant.

In Figure 2 the data analysis results of the first system are shown. In Figure 2a) the total electric efficiency and the total efficiency in terms of the electric net power output from 0 to 55 kW are illustrated. The red squares in Figure 2a) represent the mean values of the electric efficiencies of the corresponding electric net power output segment during stable operation. The SOFC system was operated stable in an electric net power output range between 25 kW and 55 kW. In this range the electric efficiency stayed stable between 50% and 55%. The black crosses show the total efficiency mean values which were between 67% and 87% during stable operation. The larger deviation of the total efficiency in comparison to the electric efficiency was caused by heat recovery flow rates not being optimized in the beginning of the operation. The stable and high electric efficiencies over the operating net power output range (25-55 kW) illustrate an advantage of fuel cell technology in comparison to micro turbines and internal combustion engines. The results show that power modulation according to the site demand is possible with high efficiencies using SOFC systems. The decreasing efficiencies (black dashed and dotted lines) during non-stable operation at electric net power outputs lower than 25 kW are caused by lower fuel utilization.

In Figure 2b) the normalized distribution of the electric net power output is shown. Two main electric net power output operation regions can be identified. The first one between 45 and 55 kW with 88% of the stable operation time which corresponds to 442 hours. And the second one between 25 and 30 kW at which system one was operating for around 12% of the stable operation time. The rest of the time the system was operating in the range 45 to 50 kW and 30 to 35 kW.

During stable operation the electric efficiency was between 45% and 60%. (see Figure 2c)). For the majority of the time (79%) the electric efficiency was between 50% and 55%. Around 2% of the time the electric efficiency was even higher with values between 55% and 60%. The total efficiency variation was with values from 65% up to 95% broader than the variation of the electric efficiency. Three main areas can be identified in terms of the total efficiency of the first system. Firstly, the total efficiency was between 75% and 85% for 70% of the stable operation time. Secondly, 17% of the stable operation time the total efficiency was

between 65% and 75%. Finally for 12% of the stable operation time the first system reached a total efficiency between 85% and 95%.

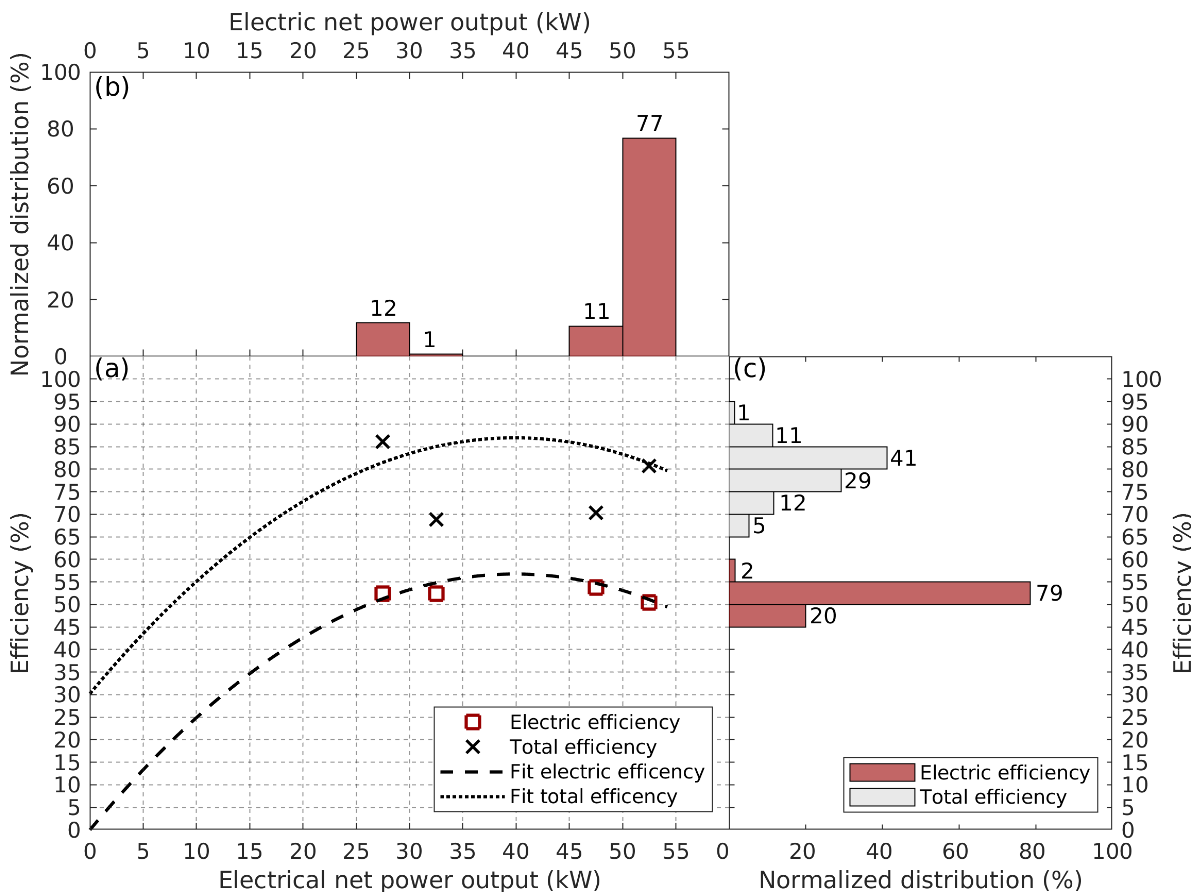


Figure 2: Electric and total efficiencies of the first Convia C50 SOFC system as function of the electrical net power output and corresponding normalized distributions. a) Electric (red squares) and total (black crosses) efficiency mean values for electrical net power output segments during stable operation. Segments are represented by the vertical dashed lines. Black dashed and dotted lines represent second order polynomial fits of the electric and total efficiencies for electric net power output values greater zero. b) Normalized distribution of the electric net power output. c) Normalized distribution of the electric and total efficiencies. Combined standard uncertainties were around 3% for the electric and around 6% for the total efficiency.

In Figure 3 the data analysis of the second system is illustrated. Similar to the first system, the electric efficiency stayed stable with values in the range of 48% to 53% (red squares Figure 3a)). The total efficiency stayed steady between 82% and 92% (black crosses, Figure 3a)). The maximum achieved electrical net power output during stable operation was 45 kW. The lower electric net power output was caused by the fact that the systems were not identical in terms of the stack implementation. The stacks were from different manufacturers and the number of stacks implemented in the hot box were different. The similar achieved efficiencies of the systems are an indication for similar stack performances. The lower net power output of the second system was due to a lower number of stacks implemented in the hot box in comparison to the first system. The dashed and dotted black lines which represent the electric efficiency and total efficiency as a function of the electrical net power output have a similar shape as the corresponding lines of the first system (compare Figure 2a)).

The normalized distribution of the electric net power output shown in Figure 3b) illustrates that the second system was operated for around 69% (~1040 hours) of the stable operation time between 40 kW to 45 kW. The rest of the time the unit was operated in the ranges 35-40 kW and 25-30 kW. This shows that the second

system was operating more at one specific electric net power output than the first system which was operating in a larger range. Around 59% of the stable operation time the electric efficiency of the second system was between 50%-60% (see Figure 3c)). This is similar with the observed electric efficiency distribution of system one. The rest of the operation time the electric efficiency was mainly between 45% and 50%. A similar behavior can be observed for the total efficiency of system one: for 52% of the stable operation time the total efficiency was between 85% and 90%. The rest of the time the total efficiency was mainly between 80-85% and 90-95%. Therefore it can be stated that the second system was operating steadier at a higher total efficiency as the first system.

In general the second system was operating more stable at one specific operation point than the first system. In terms of the electric efficiency similar values could be achieved. Concerning the total efficiencies the values of the second system were around 5 to 10% higher compared to the first system. This shows that the system maturity in terms of operation monitoring and controlling was improved from the first system to the second system. Additionally the site operation was improved with less interruptions caused by the site auxiliary equipment and more optimized heat recovery loop control, which resulted in a more stable total efficiency of the second system in comparison to the first system. These are good indications for future installations.

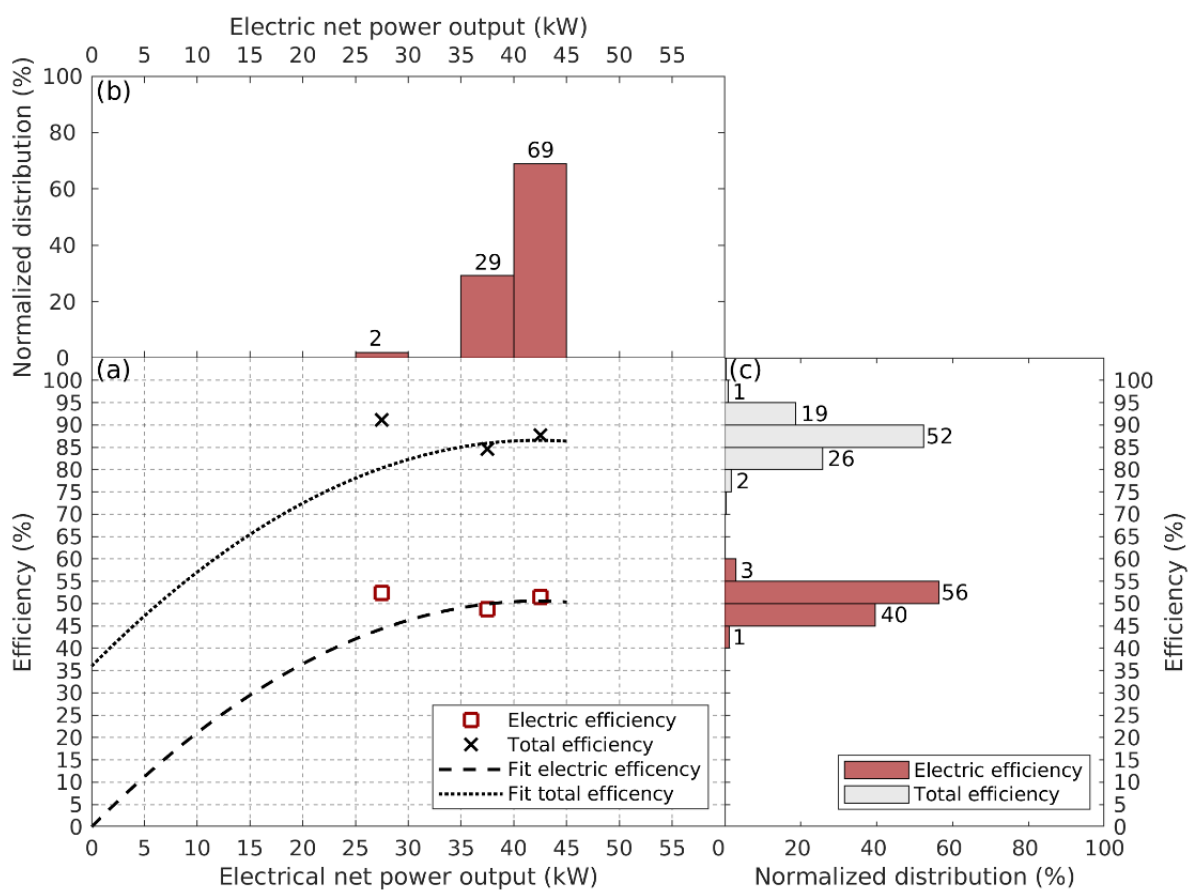
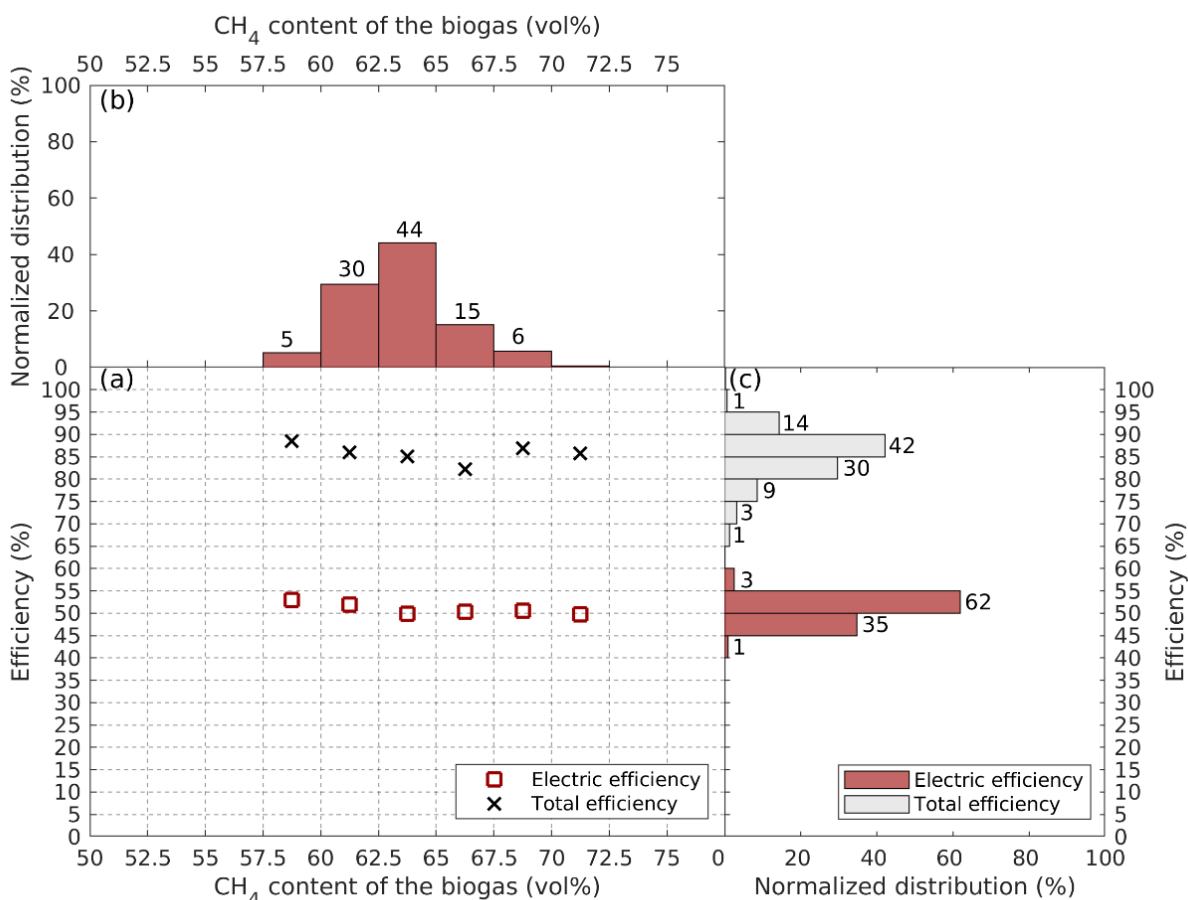


Figure 3: Electric and total efficiencies of the second Convion C50 SOFC system as function of the electrical net power output and corresponding normalized distributions. a) Electric (red squares) and total (black crosses) efficiency mean values for electrical net power output segments during stable operation. Segments are represented by the vertical dashed lines. Black dashed and dotted lines represent second order polynomial fits of the electric and total efficiencies for electric net power output values greater zero. b) Normalized distribution of the electric net power output. c) Normalized distribution of the electric and total efficiencies. Combined standard uncertainties were around 3% for the electric and around 6% for the total efficiency.

System efficiency as a function of CH<sub>4</sub> content of the fuel gas was analyzed for both systems (see Figure 4). Due to the fact that the systems were supplied with biogas from the same source both systems were

1  
2  
3  
4  
5  
6  
7  
8  
9  
10  
11  
12  
13  
14  
15  
16  
17  
18  
19  
20  
21  
22  
23  
24  
25  
26  
27  
28  
29  
30  
31  
32  
33  
34  
35  
36  
37  
38  
39  
40  
41  
42  
43  
44  
45  
46  
47  
48  
49  
50  
51  
52  
53  
54  
55  
56  
57  
58  
59  
60  
61  
62  
63  
64  
65  
considered together in this case. The CH<sub>4</sub> content in the biogas was variating from 58% up to 71% as shown in Figure 4. The mean values of the electric efficiency (red squares in Figure 4a)) and total efficiency (black crosses in Figure 4a)) stayed constant with values around 50 to 52% and 82% to 88% respectively. This indicates that high electric and total efficiencies can be achieved by the SOFC systems with varying CH<sub>4</sub> content in biogas. This is supported by the normalized distribution plots of the system efficiencies shown in Figure 4c). The electric efficiency was for 97% of the stable operation time between 45% and 55%. Furthermore the total efficiency was for 72% of the stable operation time between 80% and 90%. Additionally the normalized CH<sub>4</sub> content distribution in Figure 4b) shows that the CH<sub>4</sub> content was mainly between 60% and 65% in the biogas during the stable operation time.



44  
45  
46  
47  
48  
49  
50  
51  
52  
53  
54  
55  
56  
57  
58  
59  
60  
61  
62  
63  
64  
65  
Figure 4: Electric and total efficiencies of both Convion C50 systems as function of the CH<sub>4</sub> content of the biogas and corresponding normalized distributions. a) Electric (red squares) and total (black crosses) efficiency mean values for CH<sub>4</sub> content of the biogas segments during stable operation. Segments are represented by the vertical dashed lines. b) Normalized distribution of the CH<sub>4</sub> content of the biogas. c) Normalized distribution of the electric and total efficiencies. Combined standard uncertainties were around 3% for the electric and around 6% for the total efficiency.

## 4. Conclusion

Electric and total efficiency data of two industrial sized Convion C50 SOFC systems installed at the same waste water plant were presented. During stable operation the SOFC systems were operating in an electric net power output range between 25 kW and 55 kW. The two SOFC systems fed with biogas were constantly achieving high electric efficiencies in the range of 50% to 55% and total system efficiencies in the range of 80% to 90%. Moreover it was shown that the high electric and high total efficiencies were independent of the CH<sub>4</sub> content in the biogas.

This study points out that high electric and total efficiencies can be achieved with biogas fed SOFC systems. The high efficiencies are stable at varying electric net power output and changing CH<sub>4</sub> content of the biogas. This is a clear advantage of the SOFC technology in comparison to micro turbines and combustion engines. The results underline the fact that fuel cell systems are able to perform power modulation according to the power demand, while achieving constant high efficiencies. In addition the improvement of the site and system maturity which was achieved during this investigation are promising indications for further installations.

## 5. Acknowledgments

This project has received funding from the Fuel Cells and Hydrogen 2 Joint Undertaking under grant agreement No 671470. This Joint Undertaking receives support from the European Union's Horizon 2020 research and innovation programme, Hydrogen Europe and Hydrogen Europe research.

## 6. References

- [1] Naskeo-Environnement, "Biogas composition," 2009. [Online]. Available: [http://www.biogas-renewable-energy.info/biogas\\_composition.html](http://www.biogas-renewable-energy.info/biogas_composition.html).
- [2] EurObserv'ER, "Biogas Barometer 2017," 1 11 2017. [Online]. Available: <https://www.eurobserv-er.org/pdf/biogas-barometer-2017-en/>.
- [3] J. Merkisz and J. Pielecha, "Particulate Matter Emissions during Engine Start-Up," in *Nanoparticle Emissions From Combustion Engines*, Cham, Springer International Publishing, 2015, pp. 47-60.
- [4] S. Torija, A. Castillo-Castillo and N. P. Brandon, "The Prospects for Biogas Integration with Fuel Cells in the United Kingdom," *Fuel Cells*, vol. 16, pp. 55-79, 2016.
- [5] J. Van herle, Y. Membrez and O. Bucheli, "Biogas as a fuel source for SOFC co-generators," *Journal of Power Sources*, vol. 127, pp. 300-312, 2004.
- [6] L. Lombardi, E. Carnevale and A. Corti, "Greenhouse effect reduction and energy recovery from waste landfill," *Energy*, vol. 31, pp. 3208-3219, 2006.
- [7] M. Gandiglio, A. Lanzini, A. Soto, P. Leone and M. Santarelli, "Enhancing the Energy Efficiency of Wastewater Treatment Plants through Co-digestion and Fuel Cell Systems," *Frontiers in Environmental Science*, vol. 5, 2017.
- [8] A. Hagen, A. Winiwarter, H. Langnickel and G. Johnson, "SOFC Operation with Real Biogas," *Fuel Cells*, vol. 17, pp. 854-861, 2017.
- [9] A. Hagen, H. Langnickel and X. Sun, "Operation of solid oxide fuel cells with alternative hydrogen carriers," *International Journal of Hydrogen Energy*, vol. 44, pp. 18382-18392, 2019.
- [10] D. Papurello, R. Borchiellini, P. Bareschino, V. Chiodo, S. Freni, A. Lanzini, F. Pepe, G. A. Ortigoza and M. Santarelli, "Performance of a Solid Oxide Fuel Cell short-stack with biogas feeding," *Applied Energy*, vol. 125, pp. 254-263, 2014.
- [11] A. Lanzini, H. Madi, V. Chiodo, D. Papurello, S. Maisano, M. Santarelli and J. Van Herle, "Dealing with fuel contaminants in biogas-fed solid oxide fuel cell (SOFC) and molten carbonate fuel cell (MCFC)

1 plants: Degradation of catalytic and electro-catalytic active surfaces and related gas purification  
2 methods," *Progress in Energy and Combustion Science*, vol. 61, pp. 150-188, 2017.

3 [12] R. J. Spiegel, J. C. Trocciola and J. L. Preston, "Test results for fuel-cell operation on landfill gas," *Energy*,  
4 vol. 22, pp. 777-786, 1997.

5 [13] U. Langnickel, "First European fuel cell application using digester gas," *Fuel Cells Bulletin*, 2000.

6 [14] M. Krumbeck, T. Klinge and B. Döding, "First European fuel cell installation with anaerobic digester gas  
7 in a molten carbonate fuel cell," *Journal of Power Sources*, vol. 157, pp. 902-905, 2006.

8 [15] E. Fontell, "Fuel cell fed with landfill biogas provides power," *Industrial Bioprocessing*, vol. 30, p. 10,  
9 2008.

10 [16] M. Noponen, T. Hottinen and C. Sandstrom, "WFC20 biogas unit operation," in *Proceedings of the 9th*  
11 *European Solid Oxide Fuel Cell Forum*, 2010.

12 [17] DEMOSOFC, "DEMOFC project official website," 11 2019. [Online]. Available:  
13 <http://www.demosofc.eu/>.

14 [18] M. Gandiglio, A. Lanzini, M. Santarelli, M. Acri, T. Hakala and M. Rautanen, "Results from an industrial  
15 size biogas-fed SOFC plant (the DEMOSOFC project)," *International Journal of Hydrogen Energy*, 2019.

16 [19] M. Santarelli, M. Gandiglio, M. Acri, T. Hakala, M. Rautanen and A. Hawkes, "Results from industrial size  
17 biogas-fed SOFC plant (DeMosofC project)," *Ecs Transactions*, vol. 91, pp. 107-116, 2019.

18 [20] Convion, "Convion fuel cell - official website," 11 2019. [Online]. Available: <http://convion.fi/products/>.

19 [21] *International standard IEC 62282-3-200 Fuel cell technologies –Part 3-200: Stationary fuel cell power*  
20 *systems – Performance test methods*, 2015.

1  
2  
3  
4  
5  
6  
7  
8  
9  
10  
11  
12  
13  
14  
15  
16  
17  
18  
19  
20  
21  
22  
23  
24  
25  
26  
27  
28  
29  
30  
31  
32  
33  
34  
35  
36  
37  
38  
39  
40  
41  
42  
43  
44  
45  
46  
47  
48  
49  
50  
51  
52  
53  
54  
55  
56  
57  
58  
59  
60  
61  
62  
63  
64  
65